AIX-MARSEILLE UNIVERSITÉ
ECOLE DOCTORALE 352 - PHYSIQUE ET SCIENCES DE LA MATIÈRE
FACULTÉ DES SCIENCES
LABORATOIRE D'ASTROPHYSIQUE DE MARSEILLE

Thèse présentée pour obtenir le grade universitaire de docteur

Discipline : PHYSIQUE ET SCIENCES DE LA MATIERE
Spécialité : Astrophysique et Cosmologie

Mario BONAMIGO

# Triaxial galaxy clusters

Soutenue le 22/09/2016 devant le jury :

| | | |
|---|---|---|
| Monique ARNAUD | CEA | Rapporteur |
| Mauro SERENO | Università di Bologna | Rapporteur |
| Philippe AMRAM | LAM | Examinateur |
| Marceau LIMOUSIN | LAM | Directeur de thèse |
| Geneviève SOUCAIL | IRAP | CoDirecteur de thèse |

# Résumé

Les amas de galaxies sont reconnus comme étant de puissantes sondes cosmologiques. En particulier, l'évolution de la fonction de masse des amas en fonction du redshift est sensitive à certains paramètres cosmologiques. Cependant, l'hypothèse standard de symétrie sphérique pour la matière noire et le gas de l'amas est incorrecte et porte à confusion. En effet, il est bien établit théoriquement et observationnellement que les amas de galaxies ne sont pas des objets sphériques, et qu'ils sont beaucoup mieux décrits par la géométrie triaxiale. Malgré cela, les travaux sur la forme tri-dimensionnelle des amas de galaxies sont encore très rares. L'objet de cette thèse est de contribuer à cette problématique naissante. L'originalité de ce travail est d'aborder ce sujet théoriquement et observationnellement.

Dans une première partie, j'introduit le contexte cosmologique et j'explique comment il est possible d'obtenir des contraintes sur la forme des halos en combinant différentes sondes du potentiel gravitationnel, notamment lentilles gravitationnelles et rayons X.

Dans une seconde partie, je présente une analyse des simulations numériques à grand nombre de particules "Millenium XXL" et "Sbarbine". J'y étudie la forme des halos de matière noire qui se forment dans ces simulations, et propose des prédictions sur 5 ordres de grandeur en masse. C'est la première fois que ce type de prédictions sont disponibles pour les halos d'amas de galaxies massifs. Auparavant, la communauté utilisait des extrapolations provenant d'études effectuées sur des halos moins massifs.

Ensuite, je m'intéresse aux amas simulés qui génèrent des phénomènes de lentilles gravitationnelles fortes, afin de caractériser cette classe d'objets. Je trouve que ces objets constituent une population biaisée de halos triaxiaux dont le grand axe tend à être aligné avec notre ligne de visée, ce qui, par effet de projection, tend à accroître la probabilité de générer un effet de lentilles fortes. De plus, j'étudie aussi comment la forme des halos varie avec la distance au centre de l'amas.

Dans le quatrième chapitre, je présente un algorithme que j'ai développé et qui se propose d'ajuster de façon simultanée des données en lentilles gravitationnelles et en rayons X afin de contraindre une distribution de masse triaxiale. Une fois la méthode introduite, je l'illustre sur un modèle très simple. Puis je présente en détails les équations pertinentes et le cadre Bayesien de l'analyse combinée. Ce modèle est utilisé afin de générer des données simulées, qui sont utilisées pour tester et caractériser l'algorithme. L'algorithme permet de retrouver les valeurs d'entrées utilisées pour obtenir des données simulées, et il est prêt pour être utilisé sur de vrais données.

Dans le dernier chapitre, je présente l'analyse en données rayons X de l'amas

de galaxies Abell 1703, pour lequel 80 ks d'observations obtenues avec le télescope Chandra sont disponibles. A partir de ces données, je construit un profil de masse dans une hypothèse de symétrie sphérique. Ce profil n'est pas en accord avec l'analyse en lentilles gravitationnelles, ce qui laisse supposer que la géométrie sphérique ne convient pas. Dans un futur proche, j'envisage de combiner les analyses en lentilles gravitationnelles et en rayons X dans un cadre triaxial afin de contraindre la géométrie de l'amas.

Mots clés : cosmologie, amas de galaxies, Structure tri-dimensionnelle, lentilles gravitationnelles, simulations N-body, inference Bayesien

# Abstract

While clusters of galaxies are considered one of the most important cosmological probes, the standard spherical modelling of the dark matter and the intra-cluster medium is only a rough approximation. Indeed, it is well established both theoretically and observationally that galaxy clusters are much better approximated as triaxial objects. However, investigating the asphericity of galaxy clusters is still in its infancy. This thesis focuses on the three dimensional shape of galaxy clusters. The originality of my approach is to tackle the problem both theoretically and observationally.

Firstly, the cosmological context and the relevance of going beyond the spherical assumption is discussed. I also explain how it is possible to combine complementary probes of the gravitational potential in order to constrain the three dimensional shape of a galaxy cluster.

Then, I present an analysis of the "Millenium XXL" and "Sbarbine" N-body simulations. I investigate the shape of galaxy clusters forming in these simulations, providing predictions for shapes of dark matter halo in a mass range of over 5 orders of magnitude. In particular, this is the first time predictions are drawn for massive, cluster-scale, dark matter haloes. Later, I investigate which numerically simulated clusters do generate strong lensing features; characterising the strong lensing population, finding that they constitute a biased class of objects whose major axis tend to be aligned with our line of sight. Besides, I also investigate how the shape of dark matter haloes vary with cluster-centric distance.

In the fourth chapter of this thesis, I present an algorithm that I developed aimed at fitting simultaneously lensing and X-ray data in order to constrain a triaxial mass distribution. After discussing the idea of the method, I illustrate it on a toy model. Then I present in details the relevant equations and the Bayesian framework of the joint analysis. The model is used to generate mock observational data, which are fitted using the algorithm. This allows us to test and characterise the algorithm, which is found to be able to recover the input parameters.

In the last part, I present the X-ray analysis of galaxy cluster Abell 1703, for which 80 ks of Chandra observation is available. I present the source spectral analysis, discuss the issues related to background modelling and systematic errors. Using the spherical assumption, I derive a mass profile from X-ray data. It is found to disagree with the lensing based mass profile, suggesting the need to go beyond the spherical assumption. The prospect is then to combine the X-ray analysis with the existing lensing analysis of Abell 1703 in order to investigate its shape.

Keywords : Cosmology, galaxy cluster, Three dimensional structure, gravita-

tional lensing, N-body simulations, Bayesian inference

# Contents

# List of Figures



# List of Tables

# 1. Introduction

## 1.1. Cosmology & Galaxy Clusters

### 1.1.1. Cosmology: Emergence of the Dark Sector

Cosmology is the branch of astrophysics concerned with the study of the Universe *as a whole*, a field of investigation that is likely to be as old as humankind. However, the modern physically motivated cosmology is relatively young. With the observation of the Universe through the first telescopes and the development of mathematics and physics, cosmology has left the territory of philosophers and religions to enter the modern physical cosmology era. This transition happened less than one century ago, in particular with the works of Einstein, Friedman, Lemaître and De Sitter. The development of more and more powerful telescopes (on the ground and in space) has revolutionised our understanding of the cosmos providing an ever growing amount of data.

Nowadays, cosmological multi-wavelength observations are driving cosmology, and challenging new theories. In the last century, astronomers have revealed that we knew very little of the content of our Universe. Indeed, observational evidences led us to describe our Universe as dominated by two mysterious components: (i) *Dark Matter* (DM) which represents about 80% of the mass density of our Universe and is made of non-baryonic particles, yet to be identified. Although the CERN Large Hadron Collider may still challenge the standard particle physics models by discovering/weighting new particles, many investigations on the nature of Dark Matter can be undertaken by cosmologists to unravel some of its properties. (ii) Furthermore, at the end of the last century, physicists and astronomers have identified that *Dark Energy* (DE) represents about 75% of the mass-energy budget of the Universe. This cosmological concordance model is referred as $\Lambda$CDM: $\Lambda$ for the Dark Energy component, and CDM for "Cold Dark Matter" (upper panel of Fig. 1.1). Investigating this "Dark Sector" is fundamental in modern cosmology, and many projects are underway to unravel these mysteries using different instruments and telescopes (*e.g.* DES, BigBOSS, LSST, EUCLID)

#### Dark Energy:

With the measurement of the Hubble diagram of type Ia SNe (Riess, Filippenko, et al., 1998; Perlmutter, Aldering, et al., 1999), complemented by the observation of the Cosmological Microwave Background (with the *Planck* mission), and the detection of the Baryonic Acoustic Oscillation (BAO) in the SDSS-II survey (Eisenstein, Zehavi, et al., 2005), we have some evidences in favour of a cos-

mological model that includes a component with a similar effect as Einstein's cosmological constant (called $\Lambda$). In particular, this component must be responsible for an acceleration of the Universe expansion seen in recent times. The generic name for such a component is Dark Energy (DE) and it represent about 75% of the mass-energy budget in the Universe. Despite more than ten years of speculations and development of new theories, DE remains today one of the biggest mystery for fundamental physics and cosmology.

## Dark Matter:

The Dark Matter story began in 1933 when Fritz Zwicky (using cluster galaxies as test particles in order to probe the mass distribution of the Coma galaxy cluster), noticed that the virial mass of Coma was much larger than the stellar mass in its galaxies. This puzzling observation led him to postulate the existence of a new invisible substance in the Universe. At the end of the Seventies, using high quality velocity measurements of the neutral hydrogen gas at large distance from galactic centres, the evidence for flat rotation curves of galaxies firmly established the need for DM, thus confirming Zwicky's hypothesis.

More recent measurement of the mass distribution in massive galaxy clusters using velocity dispersion of cluster members, X-ray, Sunyaev Zel'dovich (SZ) observations and gravitational lensing, all conclude that baryonic matter represent *only* at best 20% of the total mass of a cluster. In some exceptional cases of merging clusters, the detailed mapping of the X-ray gas and the mass distribution probed by gravitational lensing showed a clear separation of the baryonic and DM components (*e.g.* Clowe, Bradač, et al., 2006) thus giving the best observational proof of the existence of DM and evidence for it being non-collisional, hence *Cold* Dark Matter (CDM).

Although direct laboratory measurements will continue to make progress and improve or refute claim(s) of DM particles detection, astrophysical observations and particularly *galaxy cluster* observations will provide ways of constraining with high accuracy the DM mass distribution.

## N-body Simulations:

From a theoretical point of view, N-body simulations constitute a *powerful cosmological tool*, allowing to *compare* observational results to theoretical expectations, therefore providing a way to *test* the input cosmology used in the simulations. Actually, it is possible to simulate large portions of the Universe with increasing resolution and complexity. On galaxy cluster scales (lower panel of Fig. 1.1), N-body simulations indicate that DM haloes aggregate with a typical mass density profile characterised by a Navarro, Frenck & White profile (Navarro, C. S. Frenk, et al., 1996, hereafter NFW). Its three dimensional density profile is characterised by a scale radius $r_s$, where the density is proportional to $r^{-2}$ and

beyond which falls as $r^{-3}$. On smaller scales, the 3D density profile of the DM is described using a cuspy profile, and dark matter only simulations predict a logarithmic slope of 1 for $r \rightarrow 0$. Besides, the concentration parameter $c$ is defined as the ratio between the virial radius and the scale radius.

### 1.1.2. Galaxy Clusters: Vertices of the Cosmic Web

Large spectroscopic galaxy redshift surveys and numerical N-body simulations have revealed a large scale distribution of matter in the Universe featuring a complex network of interconnected filamentary galaxy associations. Vertices, i.e. intersections among the filaments, correspond to the very dense compact nodes within this *cosmic web* where one can find massive galaxy clusters. Being the most massive collapsed structures in the Universe, they constitute powerful cosmological probes. They form the high-mass end of the mass function of collapsed haloes, whose development as a function of redshift is a basic test of the hierarchical structure formation scenario and depends sensitively on a number of cosmological parameters (*e.g.* Voit, 2005). The structure of the cosmic web is illustrated on Fig. 1.2.

### 1.1.3. The Mass Spectrum

When observing the structures of the Universe, we detect individual galaxies, whose masses is of order $10^{12}$ solar masses; galaxy groups, whose masses are of order $10^{13}$ solar masses, and galaxy clusters, with masses exceeds $10^{14}$ solar masses (upper panel of Fig. 1.3). The number density of clusters of galaxies at a given mass (i.e. the mass function) can be predicted analytically from linearised models of the evolution of the density field with a simple prescription for the formation of gravitationally bound objects. This is the Press-Schechter approach which has been extended in various ways over the years (Press and Schechter, 1974; Bond, Cole, et al., 1991; Lacey and Cole, 1993). The results have been confirmed and refined with numerical simulations (Sheth and Tormen, 1999; Sheth, Mo, et al., 2001; Jenkins, C. S. Frenk, et al., 2001; G. Despali, C. Giocoli, R. E. Angulo, et al., 2016). The cluster mass function and its evolution depend strongly on the cosmological parameters (lower panel of Fig. 1.3): measurements of the local mass function constrain the normalisation of the matter power spectrum, $\sigma_8$, if an independent estimate of the mean mass density in the Universe, $\Omega_{\rm M}$, is used. The evolution of the mass function breaks the degeneracy between $\sigma_8$ and $\Omega_{\rm M}$, and provides strong leverage for the determination of $\Omega_{\rm M}$. Measurements of the evolution of the cluster mass function form therefore a cornerstone of current and future research in cosmology.

Investigating the mass spectrum requires to be able to weight the structures. Cluster masses cannot be measured directly, so that investigation of the predictions depends on the measurement of other observables which are related to

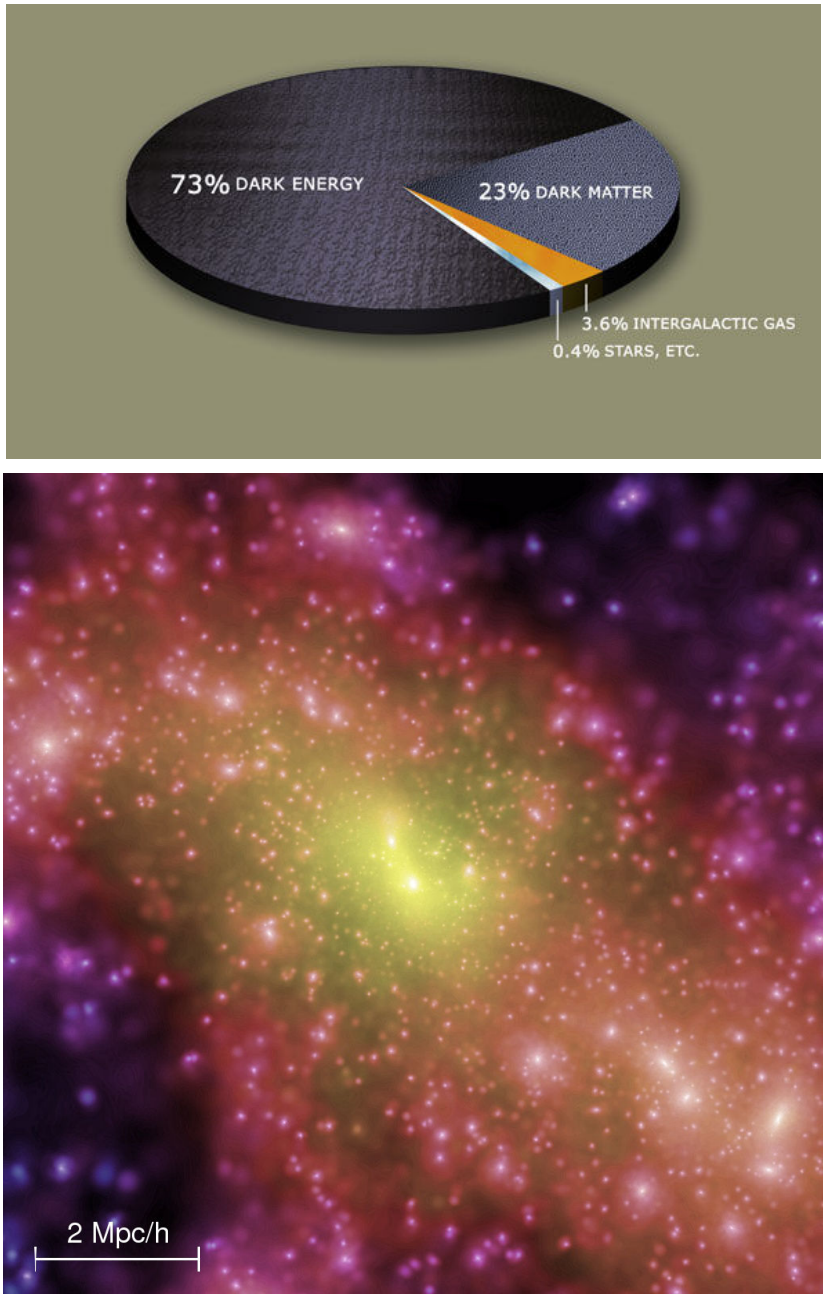


Figure 1.1.: Up: A pie diagram summarising the basic constituents of mass-energy today. The nature and properties of dark energy and dark matter is currently unknown and is the subject of ambitious prospective ground and space-based projects. The studies presented in this manuscript aim at a better understanding of the dark matter component. Down: A simulated galaxy cluster, showing the distribution of individual galaxies and how they cluster to form a larger gravitationally bound structure called a galaxy cluster. [Credits: Millennium simulation]

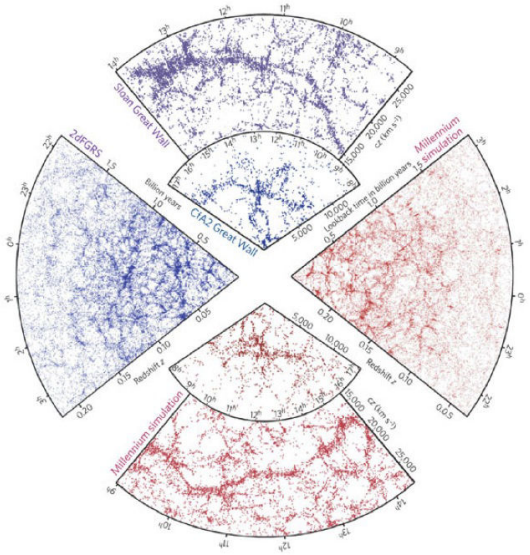


Figure 1.2.: Slices of the Universe. Each dot represents a galaxy: observed (blue and purple) and simulated (red and orange). Galaxies do cluster along certain directions. We can appreciate the structure of the Universe on large scale and how it displays the so called cosmic web.

mass. Weighting galaxy clusters is precisely the motivation of this PhD work.

## 1.2. How can we measure masses?

There are different methods of measuring masses that I briefly describe below.

### 1.2.1. Galaxy Dynamics

Observation of the internal dynamics of clusters, based on the virial theorem and using the cluster galaxies as test particles of the cluster potential, is the historical approach which provided early evidence for the existence of "missing" (now called "dark") matter (Zwicky, 1937). However, clusters of galaxies may be sometimes far from being simple relaxed systems and their structural complexity makes analysis of the velocity field difficult, especially in the presence of substructures.

### 1.2.2. X-ray emission of the Intracluster Gas

An efficient way to derive the total mass of a cluster of galaxies is to use the X-ray emission of the intracluster gas (see Ettori, Donnarumma, et al., 2013, for

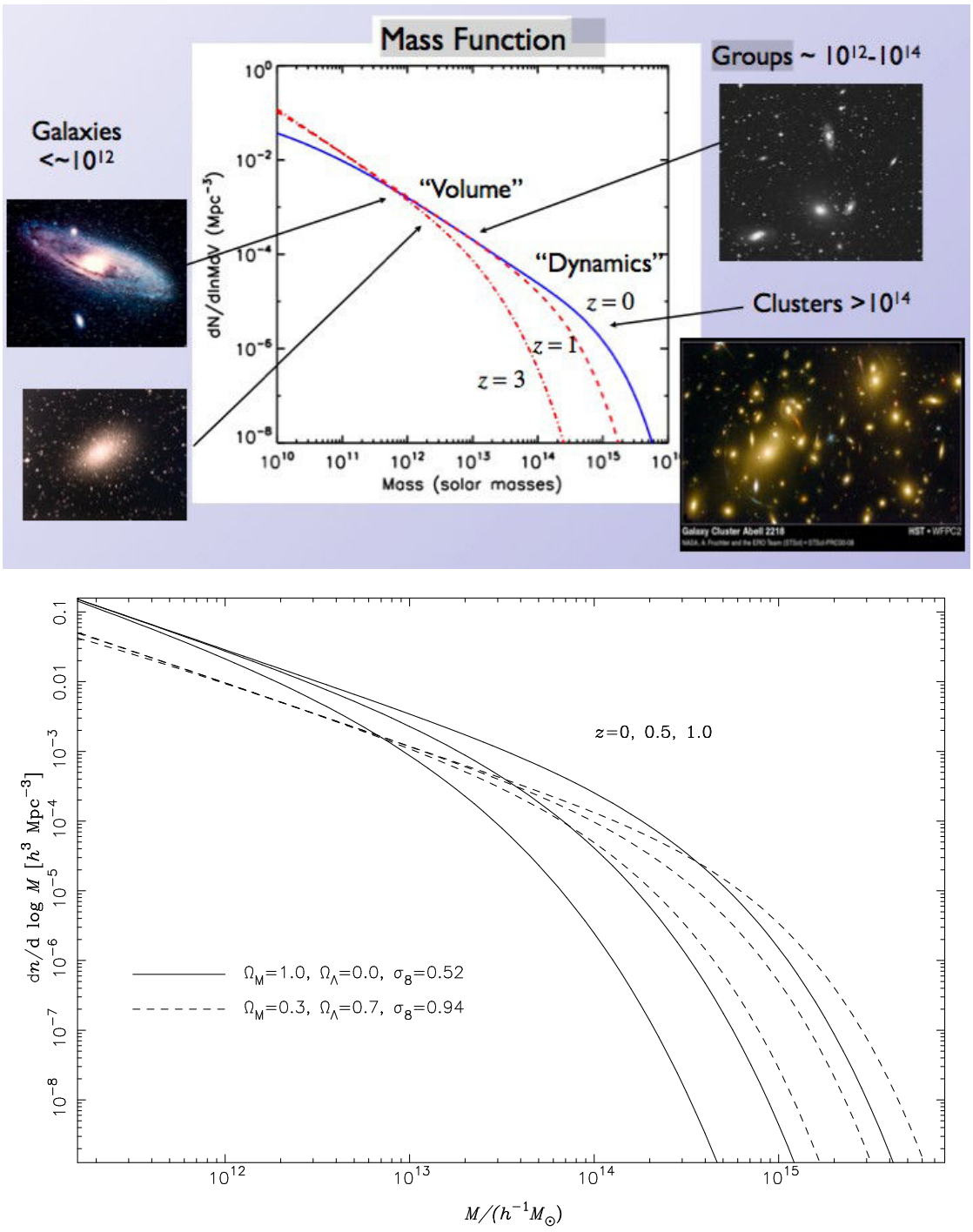


Figure 1.3.: Mass function of the structures of the Universe. Up: its evolution with redshift. Bottom: The halo mass function is shown at three redshifts for two background cosmologies, the Einstein-de Sitter model and the Λ-dominated flat model. The lower curves in each family are at higher redshift.

a detailed review on the subject). Rich clusters of galaxies are permeated by a hot tenuous plasma with temperatures of order $10^7/10^8$ K and number densities of order $n_g \sim 10^{-3}/$ cm$^3$. This gas emits radiation at X-ray energies through the thermal bremsstrahlung mechanism: clusters of galaxies are amongst the brightest known X–ray emitters. Assuming hydrostatic equilibrium of the X-ray emitting gas in the cluster potential, it is possible to derive the DM potential shape and therefore its mass. These masses can suffer systematics effects from non relaxed objects or from non thermal pressure support (although some current X-ray analysis take this component into account into a generalised hydrostatic equilibrium equation, see Section 4.1.2). Because of these systematics, masses tend to be underestimated by 10-15% as seen in numerical simulations (Nagai, Vikhlinin, et al., 2007; Lau, A. V. Kravtsov, et al., 2009; Meneghetti, Rasia, et al., 2010) and suggested by observational results (Mahdavi, Hoekstra, et al., 2008).

### 1.2.3. Sunyaev-Zel'dovich effect

Another efficient technique to characterise galaxy clusters is mapping the distortion of the Cosmic Microwave Background spectrum. This is due to the inverse Compton scattering induced from the high-energy electrons present in the hot intra-cluster medium (ICM). Clear detection of these features (named Sunyaev-Zel'dovich, SZ, effect) occurred in the late 90's (see the review by Carlstrom, 2002) and many survey over wide areas of the sky have started to produce interesting results (the South Pole Telescope; the Atacama Cosmology Telescope and more recently the Planck collaboration has presented the first sample of 189 high signal-to- noise clusters in January 2011). The integrated SZ signal, being proportional to the ICM pressure along the line-of-sight, can be used as proxy of the total cluster mass.

### 1.2.4. Gravitational Lensing: A Direct Probe of the Total Projected Mass Distribution

The deflection of light in the vicinity of large masses is one of the central predictions of Einstein's theory of general relativity. Close to large masses space time can be curved to such an extent that there are multiple null geodesics which connect an observer to the distant light source; in this case the observer sees multiple images of the same source. At larger distances from the deflecting mass, light rays emerging from the source are (partially) focused and sheared and the image of the source, as seen by an observer, is distorted and magnified or de-magnified. All these effects are observed in the form of multiply imaged QSOs, giant arcs and arclets in clusters and groups of galaxies (strong lensing), or a statistical distortion pattern in galaxies behind groups and clusters of galaxies (weak lensing, Bartelmann and P. Schneider, 2001), and are subsumed under

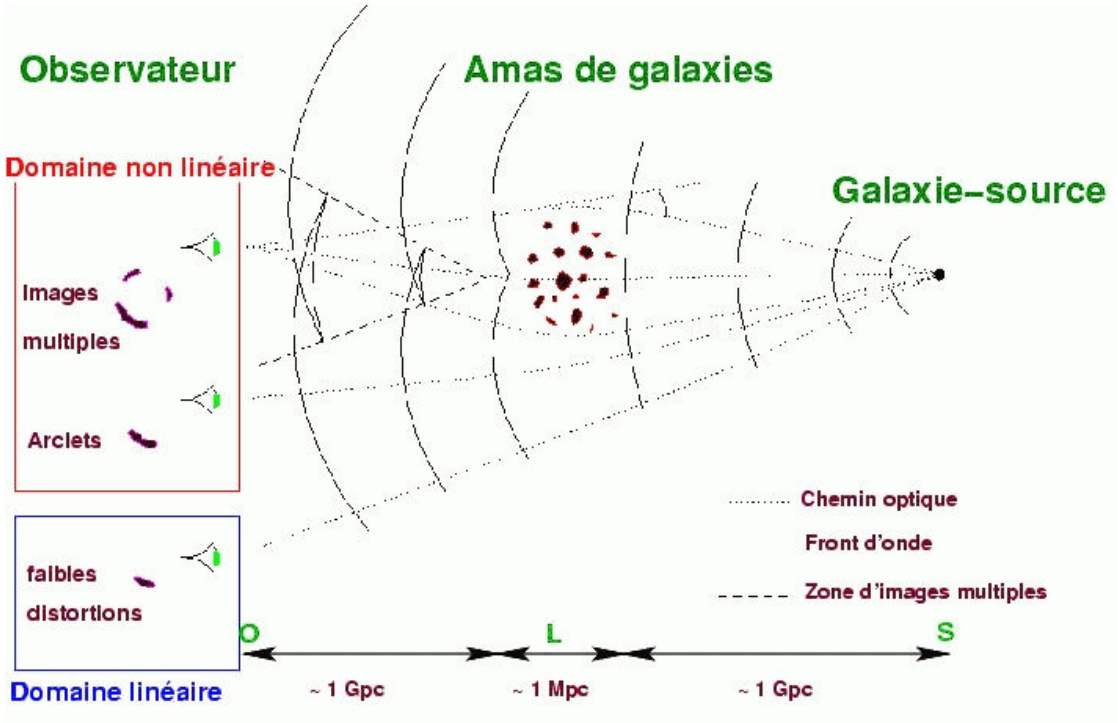


Figure 1.4.: Illustration of different regimes of gravitational lensing. Considering the light coming from a distant background source; if the light rays are passing through the cluster core where the matter density is very high, one is within the non linear strong lensing regime and we observe strongly distorted multiple images of the background galaxy. If the light is travelling at larger cluster-centric distance where the matter density is lower than the critical density required to generate strong lensing feature, the shape of the background galaxy will be slightly and linearly distorted. Both regimes are complementary since they probe the cluster potential on different scales.

the term gravitational lensing. Because the lensing effects depend directly on the mass distribution between the source and the observer without regard to its dynamical state or composition (baryonic or non-baryonic), gravitational lensing has become a very valuable tool for cosmological research, especially in the field of galaxy clusters (Kneib and Natarajan, 2011, for an in depth review).

The two regimes of gravitational lensing (strong and weak) are illustrated on Fig. 1.4. One limitation of gravitational lensing is that it is sensitive to *all* the mass between the source and the observer. Therefore, the lensing signal is likely to be contaminated by structures which are not correlated with the object of interest, and suffers from projection effects.

## 1.3. The three dimensional shape of galaxy clusters

For more than thirty years it has been known that galaxy clusters are not spherical objects. This can be seen in all their different components: from the distribution of galaxies in optical images (Binggeli, 1982); to the measured gas density in X-ray (Fabricant, Rybicki, et al., 1984) and Sunyaev-Zel'dovich (Sayers, Golwala, et al., 2011a) observations and finally in the total mass that comes from strong (Soucail, Fort, et al., 1987) and weak (Oguri, Takada, et al., 2010) gravitational lensing analyses. Whichever probe one considers, the observed projected quantities are not circular, a result that is incompatible with a simple spherical shape for galaxy clusters.

Moreover, the triaxiality of dark matter haloes has been observed in numerical simulations since C. S. Frenk, White, et al., (1988) and many studies have expanded our knowledge of the shape of simulated haloes (C. S. Frenk, White, et al., 1988; Dubinski and Carlberg, 1991; Warren, Quinn, et al., 1992; Cole and Lacey, 1996; Y. Jing and Y. Suto, 2002; Hopkins, Bahcall, et al., 2005; Bailin and Steinmetz, 2005; Kasun and Evrard, 2005; Paz, Lambas, et al., 2006; Allgood, R. A. Flores, et al., 2006; Bett, Eke, et al., 2007; Muñoz-Cuartas, Macciò, et al., 2011; Gao, Navarro, et al., 2012; M. D. Schneider, C. S. Frenk, et al., 2012; G. Despali, Tormen, et al., 2013). Additionally, the asphericity of haloes is a straightforward result of a very basic assumption in the theory of large scale structures formation: the fluctuations in the initial density field are independent along the three dimensions. Therefore it is very unlikely for a density peak to be spherically symmetric and host a spherical halo at later times.

When measuring the mass distribution of a galaxy clusters using any of the method presented above, a shape for the object has to be assumed. Naturally, the first choice adopted was spherical symmetry: this simplified the modelling and it provided a sufficiently good description of galaxy clusters, given the poor quality of data available at the time. In addition, the individual probes suffer from intrinsic degeneracies with the shape and only by combining them in a multi-wavelength analysis it is possible to actually measure the 3D shape of the clusters (see Section 1.3.1).

The spherical assumption has also the problem of introducing biases in analyses. For instance, galaxy cluster Abell 1689 shows some puzzling properties: it has an extremely high concentration (up to $15$, Umetsu, Birkinshaw, et al., 2009) and a very large Einstein radius (Broadhurst, Benítez, et al., 2005) both which are in contrast with predictions from the standard $\Lambda$CDM model (Neto, Gao, et al., 2007; Duffy, Schaye, et al., 2008); furthermore the mass estimates from X-ray data is only half of what can be measured with strong gravitational lensing. However, by adopting a more general triaxial framework, it is possible to solve both problems so that the masses from complementary probes are in agreement

and the values of concentration and Einstein radius are reconciled with the theoretical predictions. The full details of this analysis can be found in M. Limousin, A. Morandi, et al., (2013), where similar results have been obtained for three additional clusters.

### 1.3.1. How to get access to the third dimension

As the quality of data improved, the initial approximation that galaxy clusters could be described as spherical objects became less necessary. Many authors have then proposed methods that assume axial symmetry or triaxial ellipsoids to model the shape; some relied on theoretical priors, other chose to combine multi-wavelength observations to infer the three dimensional mass distribution of galaxy clusters. A more detailed review on the methods available in the literature can be found in M. Limousin, A. Morandi, et al., (2013).

Even with the latest progress in data quality and modelling techniques, the spherical assumption is still very popular in many analyses. This is because the problem of deprojection is the curse of astronomy: every image we obtain is projected on the plane of the sky; we can measure angular distances with beautiful precision, but in many cases we have to deal with measurements in the perpendicular direction that are order of magnitudes worse.

Deprojection is typically an under-constrained problem. For instance, the gravitational lensing effect arises from the full path of a photon through a gravitational potential (see section 1.2.4), therefore we can only measure the integrated impact of a mass on the light coming from background objects. In other words, it can only constrain the 2D projected mass density and any 3D model will be intrinsically degenerate, since lensing can rarely give full information on the line of sight distribution of the mass. The only way to break the degeneracies introduced by the projection is to combine different observables.

Recently two frameworks have been proposed to simultaneously fit complementary datasets with a triaxial model; they have been presented respectively in A. Morandi and M. Limousin, (2012) and in Sereno, Ettori, et al., (2012). They both exploit the idea that different probes have different dependence on the density: for example, X-ray surface brightness is proportional to the square of the electron density integrated along the line of sight; while the Sunyaev Zel'dovich effect only depend on the integral of the electron density times the temperature. As an example, we present a simple toy model that can be very useful to get a better understanding on why combined analysis is able to constrain the shape of an halo.

First of all, we restrict the model to a prolate halo oriented along the line of sight, so that the radius is given by $R^2 = (x^2 + y^2)/s^2 + z^2$, where $s$ is the axis ratio. Moreover we use a simple isothermal density profile $\rho(R) = AR^{-2}$, where $A$ is a normalisation constant; in this toy model $s$ and $A$ are the only free parameters. By projecting the density along the $z$ axis we can obtain the lensing

observable $L$, while to obtain the X-Ray surface brightness $X$ we need to make an additional very strong simplification: we will assume that the gas follows exactly the dark matter (DM) distribution so that the electron density is proportional to $\rho(R)$:

$$\begin{aligned} L &\propto \int \rho(R)\mathrm{d}z, \\ X &\propto \int \rho^2(R)\mathrm{d}z. \end{aligned} \tag{1.1}$$

We would like to stress that this is not physical and we will use these assumptions only in this section for illustration purposes. Alternatively, one can consider only baryons and combine X-Ray with Sunyaev-Zel'dovich (similarly to what is done in Sereno, Ettori, et al., 2012). Within the limits of this toy model the two approaches are identical: by assuming a constant temperature and using the isothermal profile as the electron density $n_e$, the SZ observable is proportional to the lensing as defined in eq 1.1: $SZ \propto \int n_e T \mathrm{d}z = T \int n_e \mathrm{d}z = T \int \rho(R)\mathrm{d}z$.

If we substitute the definition of $\rho(R)$ into eq. 1.1 we can see how the two observables, taken separately, are not sufficient to measure the shape even of such a simple model:

$$\begin{aligned} L &\propto \int \frac{As^2\mathrm{d}z}{x^2+y^2+(sz)^2} = As\int \frac{\mathrm{d}(sz)}{x^2+y^2+(sz)^2} = As\int \frac{\mathrm{d}t}{x^2+y^2+t^2}, \\ X &\propto \int \frac{A^2s^4\mathrm{d}z}{\left[x^2+y^2+(sz)^2\right]^2} = A^2s^3\int \frac{\mathrm{d}(sz)}{\left[x^2+y^2+(sz)^2\right]^2} = A^2s^3\int \frac{\mathrm{d}t}{(x^2+y^2+t^2)^2}. \end{aligned} \tag{1.2}$$

In the last step, we changed the integration variable to $t = sz$ to underline the fact that all the information on the elongation along the line of site is lost and the equation is indistinguishable from a spherical case. It is also clear that the normalisation is inversely proportional to the axis ratio and therefore by solving only one of the two equations it is not possible to break the degeneracy between the variables: both observables are needed in order to obtain the 3D shape.

Finally, we have used this simple toy model to generate a set of mock surface density and X-Ray surface brightness. Having added to each pixel a Gaussian noise with standard deviation of $10\%$, we have computed the posterior probability drawing samples from flat priors (simple Monte Carlo) to constrain $A$ and $s$; the resulting distributions are shown in Figure 1.5. Blue, green and red contours represent three different analysis respectively: lensing only, X-Ray only and combined modelling. Dark contours show the areas that contain $39.3\%$ of the volume, lighter contours contain $86.4\%$; these are the values that correspond to $1$ and $2$ sigma for a 2D normal distribution. A Gaussian filter has been applied to the resulting histograms for graphical purposes only.

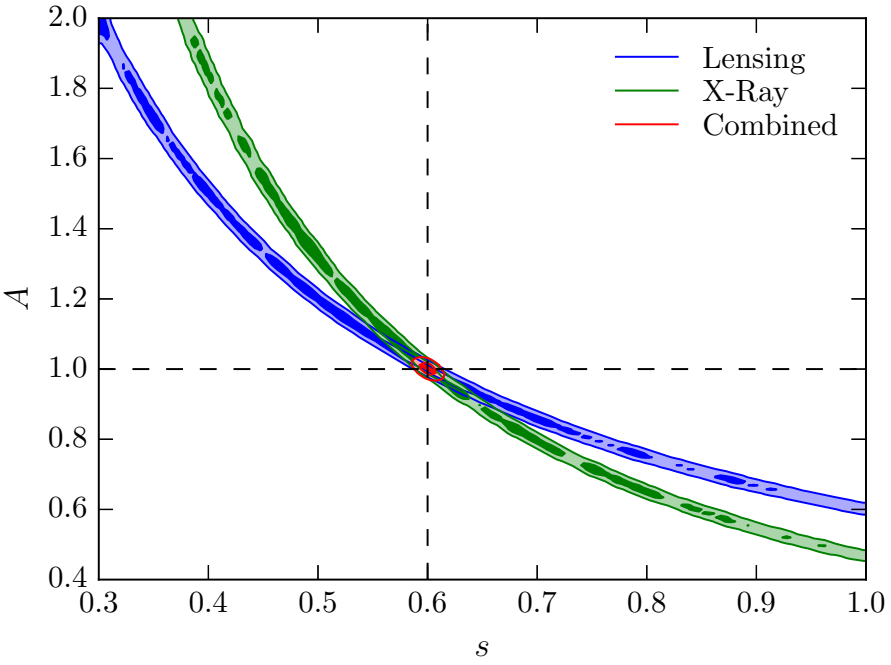


Figure 1.5.: Posterior probability distributions for axis ratio $s$ and normalisation $A$ of the toy model. Blue contours refer to lensing only analysis, green to X-Ray and red to combined analysis. The dashed vertical and horizontal lines show the input values of the parameters.

As expected, both lensing and X-Ray only analyses can not break the projection degeneracy; moreover the logarithmic slopes of the contours are exactly what it has been derived in equations 1.2. On the other hand, when combining the two probes it is possible to recover the 3D shape by exploiting the different dependence on the density of lensing and X-Ray.

## 1.4. Plan of the thesis

This work is meant to advance our knowledge of the 3D shape of galaxy clusters. Its originality is to tackle the problem both theoretically and observationally.

In the first part of this PhD (Chapter 2), I undertake an investigation of the shape of numerically simulated clusters (Bonamigo, G. Despali, et al., 2015; G. Despali, C. Giocoli, Bonamigo, et al., 2016; C. Giocoli, Bonamigo, et al., 2016) The motivation of this project is to update the predictions by Y. P. Jing and Y. Suto, (2002). Indeed, regarding the predictions on the triaxial shape of simulated haloes (in particular the axis ratio), we still rely on the works by Y. P. Jing and Y. Suto, (2002, JS 02 hereafter). JS 02 predictions are based on (dark matter only) simulations with $512^3$ particles in a box of side 100 Mpc that have been performed in 2001. Given the small side of the box, the statistics for massive haloes is extremely poor, having *no* haloes with mass larger than $5\times10^{14}$ solar masses. Therefore, cluster scale triaxial predictions rely on *extrapolation* from smaller (more numerous) haloes and may be inaccurate. In order to perform meaningful comparisons between observations and simulations, is it therefore important to update the results by JS 02 using state-of-the-art N-body simulations, with the goal of characterising the statistics of halo non-sphericity with an unprecedented precision.

To this end, I have considered the Millenium-XXL dark matter only simulation, the best suited simulation to address this important issue. Performed in 2011, it follows $6720^3$ particles in a cosmological box of side 4.1 Gpc (R. E. Angulo, V. Springel, et al., 2012a), featuring 464 haloes more massive than $2\times10^{15}$ solar masses.

The skill I have developed in manipulating the large amount of data of the Millenium-XXL simulation allowed me to participate actively (as second and third author) in two related projects: (i) characterising the strong lensing clusters (work presented in Chapter 3 and published in C. Giocoli, Bonamigo, et al., 2016); (ii) and studying the evolution of the shape as a function of cluster-centric distance (G. Despali, C. Giocoli, Bonamigo, et al., 2016).

In the second part (from Chapter 4), I present a parametric algorithm aimed at fitting simultaneously lensing and X-ray data sets within a triaxial framework. It follows the general approach of the algorithm developed by A. Morandi and M. Limousin, (2012), but goes beyond it implementing a more advanced Montecarlo-Markov chain sampler and a more accurate likelihood function. Im-

portantly, it is tested on mock data sets, which allows me to characterise it and acknowledge its performances and biases. Moreover, it has been coded in a way that simplifies the extension to other data sets, such as Sunyaev-Zel'dovich, and to models beyond the assumed NFW density profile. Finally, the code is released under open source licence: the field of galaxy clusters modelling needs some standard code to analyse multi-wavelength data and hopefully this algorithm will help to start a discussion for a more widespread tool.

The aim of this algorithm is to be applied on observational data sets, therefore in the last part, I present an ongoing work on galaxy cluster Abell 1703. Firstly, I introduce an X-ray analysis from deep Chandra data and then I model them in a spherical framework, showing the need for a more realistic triaxial description.

# 2. What we can learn from simulations

In this chapter, we aim to characterise the shape of numerically simulated clusters, described within a triaxial framework. As mentioned in Section 1.4, most analyses of galaxy clusters that include non-spherical geometry still rely on the predictions of Y. Jing and Y. Suto, (2002). However, those results where obtained from a relatively small simulated region, which means that only a few haloes would have a mass higher than $10^{14}$ $M_{\odot}$. Later works (Y. Jing and Y. Suto, 2002; Allgood, R. a. Flores, et al., 2006; Macciò, Dutton, et al., 2008; Muñoz-Cuartas, Macciò, et al., 2011; G. Despali, Tormen, et al., 2013; G Despali, C. Giocoli, et al., 2014) expanded the explored mass range; but, until recently, it was not possible to run a large enough simulation that had both the required resolution and number of objects. The Millennium XXL (MXXL) simulation (R. E. Angulo, V. Springel, et al., 2012b) satisfies such requirements, allowing us to study in details the three dimensional shape of massive galaxy clusters.

Having developed a code that measures the triaxial shape of an halo (similar to the one presented in G. Despali, Tormen, et al., 2013), I applied it to haloes extracted from the MXXL and the SBARBINE (G. Despali, C. Giocoli, R. E. Angulo, et al., 2016) simulations. The former gives as a very large number of massive galaxy clusters ($\approx$ 500 with $M > 2 \times 10^{15}$ $M_{\odot}h^{-1}$); while the latter, being a collection of different box size simulations, allows us to extend the analysis to nearly six orders of magnitude in mass, from $10^{10}$ to almost $10^{16}$ $M_{\odot}h^{-1}$). The task of measuring the shape of each halo in the MXXL simulation is not a trivial one, considering that one has to analyse 3TB of data; it required a very fast code and the implementation of parallelisation techniques.

I have approximate the mass distribution of each halo with a triaxial ellipsoid and then computed the corresponding mass, centre of mass, axis ratios and orientation. As I am using a single component to describe haloes, I had to remove objects that are not unimodal; this was accomplished by selecting only those which had the centre of mass close to the minimum of potential (within 5% of their virial radius). In the literature, additional constrains are used, such as the amount of mass in substructures and the ratio of kinetic to potential energy. However, all situations where the additional criteria fail are either unlikely (extremely symmetrical configurations), or not relevant for the current analysis (massive substructures in the centre) which is focused on the large scale shape of the halo.

Once the unrelaxed objects have been removed, I have looked at the probability distribution functions (PDF) of the axis ratios.

- In the context of cluster scale haloes, one can rescale the minor to major

axis ratio using function of mass proxy, the density peak height $\nu$, to obtain a single PDF which can be approximated by a single lognormal distribution. Moreover, the parameters of the fitted PDF do not depend on mass, redshift or cosmology as the rescaling is done as function of $\nu$.

- For lower mass haloes, a lognormal distribution is not able to approximate the minor to major axis ratio PDF. We have then adopted a beta distribution whose parameters depend on the mass (via $\nu$); as before the dependence on $\nu$ assures that the fitting distribution can be applied to different cosmologies and redshifts.

- In addition, the probability distribution function of the intermediate to major axis ratio depends only on the other axis ratio and not on the mass of the halo. We have used a beta distribution to model this PDF and given a fit for its parameters as function of the minor to major axis ratio.

By studying the haloes from the MXXL and the SBARBINE simulations, I have derived an analytic description of the probability distribution function of the two axis ratios of an halo. These results are important for both theoretical and observational studies:

- on the theory side, the adopted parametrisation fits in the more general view that properties of an halo depend, at first order, only on its mass;

- the proposed PDF can be used as priors when modelling observations of galaxy clusters in a three dimensional framework;

- finally, it is possible to generate mock haloes with shapes that are consistent with numerical simulations.

For a more detailed presentation of the results of this analysis, I include the corresponding published paper in the next section.

## 2.1. Universality of dark matter haloes shape over six decades in mass: insights from the Millennium XXL and SBARBINE simulations

M. Bonamigo, G. Despali, et al. “Universality of dark matter haloes shape over six decades in mass: insights from the Millennium XXL and SBARBINE simulations”. In: *MNRAS* 449 (May 2015), pp. 3171–3182. DOI: 10.1093/mnras/stv417. arXiv: 1410.0015

Monthly Notices of the ROYAL ASTRONOMICAL SOCIETY
MNRAS **449,** 3171–3182 (2015) doi:10.1093/mnras/stv417

# Universality of dark matter haloes shape over six decades in mass: insights from the Millennium XXL and SBARBINE simulations

Mario Bonamigo,[1]★ Giulia Despali,[2] Marceau Limousin,[1] Raul Angulo,[3] Carlo Giocoli[4,5,6] and Geneviève Soucail[7,8]

[1]*Aix Marseille Université, CNRS, LAM (Laboratoire d'Astrophysique de Marseille) UMR 7326, F-13388 Marseille, France*
[2]*Dipartimento di Fisica e Astronomia, Università degli Studi di Padova, vicolo dell'Osservatorio 3, I-35122 Padova, Italy*
[3]*Centro de Estudios de Física del Cosmos de Aragón (CEFCA), Plaza San Juan 1, Planta-2, E-44001 Teruel, Spain*
[4]*Dipartimento di Fisica e Astronomia, Alma Mater Studiorum Università di Bologna, viale Berti Pichat, 6/2, I-40127 Bologna, Italy*
[5]*INAF - Osservatorio Astronomico di Bologna, via Ranzani 1, I-40127 Bologna, Italy*
[6]*INFN - Sezione di Bologna, viale Berti Pichat 6/2, I-40127 Bologna, Italy*
[7]*Université de Toulouse, UPS-OMP, Institut de Recherche en Astrophysique et Planétologie (IRAP), F-31400 Toulouse, France*
[8]*CNRS, IRAP, 14 Avenue Edouard Belin, F-31400 Toulouse, France*

Accepted 2015 February 23. Received 2015 January 14; in original form 2014 September 29

**ABSTRACT**

For the last 30 yr many observational and theoretical evidences have shown that galaxy clusters are not spherical objects, and that their shape is much better described by a triaxial geometry. With the advent of multiwavelength data of increasing quality, triaxial investigations of galaxy clusters is gathering a growing interest from the community, especially in the time of 'precision cosmology'. In this work, we aim to provide the first statistically significant predictions in the unexplored mass range above $3 \times 10^{14}$ $M_{\odot}h^{-1}$, using haloes from two redshift snapshots ($z = 0$ and $z = 1$) of the Millennium XXL simulation. The size of this cosmological dark matter-only simulation (4.1 Gpc) allows the formation of a statistically significant number of massive cluster scale haloes (≈500 with $M > 2\times 10^{15}$ $M_{\odot}\,h^{-1}$, and 780 000 with $M > 10^{14}$ $M_{\odot}\,h^{-1}$). Besides, we aim to extend this investigation to lower masses in order to look for universal predictions across nearly six orders of magnitude in mass, from $10^{10}$ to almost $10^{16}$ $M_{\odot}\,h^{-1}$. For this purpose we use the SBARBINE simulations, allowing us to model haloes of masses starting from $\approx 10^{10}$ $M_{\odot}\,h^{-1}$. We use an elliptical overdensity method to select haloes and compute the shapes of the unimodal ones (approximately 50 per cent), while we discard the more unrelaxed. The minor to major and intermediate to major axis ratio distributions are found to be well described by simple universal functional forms that do not depend on cosmology or redshift. Our results extend the findings of Jing & Suto to a higher precision and a wider range of mass. This 'recipe' is made available to the community in this paper and in a dedicated web page.

**Key words:** methods: numerical – galaxies: clusters: general – galaxies: haloes – cosmology: theory – dark matter.

## 1 INTRODUCTION

Spectroscopic galaxy redshift surveys and numerical *N*-body simulations have revealed a large-scale distribution of matter in the Universe featuring a complex network of interconnected filamentary galaxy associations. Vertices, i.e. intersections among the filaments, correspond to the very dense compact nodes within this *cosmic web* where one can find massive galaxy clusters.

These objects have been first assigned a spherical geometry, being the easiest way to characterize a shape in three dimensions; at the time this fitted the available data well enough. Nowadays, with the advent of multiwavelength data of increasing quality, there is a growing interest from the community to go beyond the spherical assumption, which is inaccurate and misleading. At first, clusters of galaxies have been characterized as spherical objects, a model that fitted well enough the limited data available at the time. Nowadays, with the advent of multiwavelength data of increasing quality, there is a growing interest from the community to go beyond the spherical assumption.

★ E-mail: mario.bonamigo@lam.fr

Many observational evidences have been collected showing that clusters are not spherical objects; in particular from the non-circular projection of various probes; density of cluster galaxies (Carter & Metcalfe 1980; Binggeli 1982); X-Ray surface brightness (Fabricant, Rybicki & Gorenstein 1984; Buote & Canizares 1992, 1996; Kawahara 2010; Lau et al. 2012); Sunyaev Zel'dovich pressure maps (Sayers et al. 2011); strong gravitational lensing (Soucail et al. 1987) and weak gravitational lensing (Evans & Bridle 2009; Oguri et al. 2010, 2012).

Recently, an azimuthal variation of galaxy kinematics has been detected in a stacked sample of 1 743 galaxy clusters from the SDSS (Skielboe et al. 2012). The line-of-sight velocity dispersion of galaxies lying along the major axis of the central galaxy is found to be larger than those along the direction of the minor axis, further evidence supporting the asphericity of galaxy clusters.

On the numerical side, haloes forming in cosmological simulations have been found to be triaxial in shape, with a preference for prolateness over oblateness (Frenk et al. 1988; Dubinski & Carlberg 1991; Warren et al. 1992; Cole & Lacey 1996; Jing & Suto 2002; Bailin & Steinmetz 2005; Hopkins, Bahcall & Bode 2005; Kasun & Evrard 2005; Allgood et al. 2006; Paz et al. 2006; Bett et al. 2007; Muñoz-Cuartas et al. 2011; Gao et al. 2012; Schneider, Frenk & Cole 2012; Despali, Tormen & Sheth 2013). These simulations also predict an evolution of the shape with mass and redshift; low-mass haloes appear more spherical than high-mass haloes, essentially because high-mass haloes have formed later on (Despali, Giocoli & Tormen 2014).

Finally, it can be shown (Doroshkevich 1970) that triaxial collapse is a straightforward prediction of structure growth driven by self-gravity of Gaussian density fluctuations.

These evidences shows that the triaxial framework, though still an approximation, encapsulates halo shapes much more accurately than the spherical counterpart.

Besides, it has been shown that cluster properties (mass, concentration parameter, slope of the inner dark matter density profile, strong lensing cross-section) can differ significantly depending on the shape assumed in the analysis (see, e.g. the discussion in Limousin et al. 2013, regarding Abell 1689); see also Giocoli et al. (2012a,b). Even the galaxy correlation function can be affected by wrong assumptions on the triaxiality of haloes (van Daalen, Angulo & White 2012).

Since the mentioned properties constitute key ingredients of important cosmological tests, this suggests that triaxial modelling is the next milestone in the road map of 'precision cosmology' with galaxy clusters.

In this paper, we aim to characterize the shape of numerically simulated clusters, described within a triaxial framework. Apart from the three Euler angles, a triaxial geometry is characterized by three axes ($a < b < c$), hence two axial ratios: minor to major ($s = a/c$ in the following) and intermediate to major ($q = b/c$).

Shape of triaxial haloes have been investigated theoretically in a number of works which aim to characterize the dependence of shapes on mass, redshift, radius and so on. Most of the works agree on the fact that massive haloes are on average more elongated than low-mass haloes (Jing & Suto 2002; Allgood et al. 2006; Muñoz-Cuartas et al. 2011; Despali et al. 2013, 2014), since they form at later times and thus still retain memory of their original shape; which is influenced by the direction of the surrounding filaments or of the last major merger. Moreover, shapes depend also on redshift with haloes of all masses having on average smaller axial ratios at higher $z$; even though, the rank in mass is maintained at all times (Muñoz-Cuartas et al. 2011; Despali et al. 2014). Other works have investigated halo shapes as a function of radius, measuring axial ratios of shells at different distances from the centre and the alignment between shells (Warren et al. 1992; Jing & Suto 2002; Bailin & Steinmetz 2005; Allgood et al. 2006; Schneider et al. 2012); haloes are more elongated in the central regions, while the outskirts are more rounded, probably due to interactions with the surrounding environment. Obviously the available number of haloes increased in parallel with computational resources; the analysis of Jing & Suto (2002) was based on simulations with $512^3$ particles in a 100 Mpc $h^{-1}$ box, which contained hardly any halo above $10^{14}$ $M_\odot$ $h^{-1}$ and some higher resolution runs which provided only 12 haloes with more than $10^6$ particles. On the other hand more recent works, i.e. Schneider et al. (2012), have been able to analyse larger data sets like the Millennium I and II simulations (Springel 2005; Boylan-Kolchin et al. 2009). The mass range between $10^{12}$ and $10^{14}$ $M_\odot$ $h^{-1}$ has been widely explored in all these works, while only recently small haloes down to $10^{10}$ $M_\odot$ $h^{-1}$ (Muñoz-Cuartas et al. 2011; Schneider et al. 2012) and some massive haloes of $10^{15}$ $M_\odot$ $h^{-1}$ (Despali et al. 2014) have been included in this kind of analysis. So far, no statistically significant predictions are available above $3 \times 10^{14}$ $h^{-1}$ $M_\odot$ and we rely on extrapolations from lower mass haloes when it comes to predict the shapes of massive galaxy clusters. With about 300 billion particles and a box size of 3 Gpc $h^{-1}$, the Millennium XXL (MXXL) simulation (Angulo et al. 2012) fills the range of high masses and explore the properties of cluster size haloes.

In this work our aims are twofold:

(i) using cluster scale haloes ($M > 10^{14}$ $M_\odot$ $h^{-1}$) from the MXXL simulation, we aim to provide predictions for the shape of massive clusters.

(ii) Then, we extend the mass range by considering haloes from the SBARBINE simulations, applying similar methods in order to investigate the shapes of haloes and provide predictions over five decades in mass, from $\sim 3 \times 10^{10}$ to $\sim 4 \times 10^{15}$ $M_\odot$ $h^{-1}$.

This paper is organized as follows: in Section 2, we present the simulations and the methodology used to extract haloes and measure their shapes. In Section 3, we present our results for the massive cluster scale haloes, then in Section 4 we extend our analysis to a broader mass range. In Section 5, we compare our findings with previous works. We discuss our results and conclude in Section 6.

## 2 HALO CATALOGUE

We have derived the shape of galaxy clusters from the MXXL simulation (Angulo et al. 2012). To generalize our analysis to lower masses, we used a new set of simulations (Despali et al., in preparation), which extended the mass range to more than five orders of magnitudes. From both simulations, we have analysed haloes from two redshifts: $z = 0$ and 1. The main features of the simulations are described in the following sections and summarized in Table 1.

### 2.1 MXXL simulation

With a box side of 3 Gpc $h^{-1}$ (4.1 Gpc), this simulation was especially tailored to study massive haloes which can be only found in very large volumes, because of their nature of extremely rare objects and due to the dampening of large fluctuation modes in smaller boxes. The $6720^3 \approx 3 \times 10^{11}$ dark matter particles have a mass of $6.174 \times 10^9$ $M_\odot$ $h^{-1}$; the Plummer-equivalent softening length is $\epsilon = 13.7$ kpc. For reasons of consistency with the previous Millennium runs, the adopted ΛCDM cosmology is the *Wilkinson*

**Table 1.** Main features of the simulations used in this work. The last two columns report the total number of haloes with more than 1000 particles ($N_{\rm h}$) and the corresponding fraction of 'regular' haloes ($N_{\rm reg}$), at redshift $z = 0$.

| | Box (Mpc $h^{-1}$) | $z_i$ | $m_{\rm p}$($M_\odot$ $h^{-1}$) | Soft (kpc $h^{-1}$) | $N_{\rm h}(z=0)$ | $N_{\rm reg}(z=0)$ |
|---|---|---|---|---|---|---|
| **Ada** | 62.5 | 129 | $1.94 \times 10^7$ | 1.5 | 39 445 | 28 005 |
| **Bice** | 125 | 99 | $1.55 \times 10^8$ | 3 | 49 100 | 32 107 |
| **Dora** | 500 | 99 | $9.92 \times 10^9$ | 12 | 66 300 | 33 970 |
| **Emma** | 1000 | 99 | $7.94 \times 10^{10}$ | 24 | 46 665 | 20 696 |
| **Flora** | 2000 | 99 | $6.35 \times 10^{11}$ | 48 | 7754 | 2997 |
| **MXXL** | 3000 | 63 | $6.17 \times 10^9$ | 18.8 | 937 755 | 568 477 |

*Microwave Anisotropy Probe* one: total matter density $\Omega_{\rm m} = 0.25$, baryons density $\Omega_{\rm b} = 0.045$, cosmological constant $\Omega_\Lambda = 0.75$, power spectrum normalization $\sigma_8 = 0.9$ and dimensionless Hubble parameter $h = 0.73$. The main properties of the simulation are summarized in Table 1.

Due to the huge number of haloes in the simulation (almost 68 millions at redshift 0), we restricted the analysis to only a random subsample; for each logarithmic mass bin of size 0.2 [mass inside a spherical overdensity (SO) of $200\Omega_{\rm crit}$] we chose either $10^5$ random objects or all, for the higher masses where the number of haloes in the bin is lower. This cut happens at a logarithmic mass of about 14.4 and 14.0 $M_\odot$ $h^{-1}$ for redshifts 0 and 1, respectively. We have then re-identified haloes at redshift $z = 1$ and 0 using an ellipsoidal halo finder, which will be described in Section 2.3.

### 2.2 LE SBARBINE simulations

With the purpose of comparing different data sets and extending the available mass range, we use (from Section 4 on) the results from five cosmological simulations which have been run in Padova using the publicly available code GADGET-2 (Springel 2005); these are part of a series of new simulations which will be presented in a subsequent work ('LE SBARBINE' simulations, Despali et al., in preparation). The adopted cosmology follows the recent Planck results (Planck Collaboration XVI 2014): $\Omega_{\rm m} = 0.307$, $\Omega_\Lambda = 0.693$, $\sigma_8 = 0.829$ and $h = 0.677$. The initial power spectrum was generated with the code CAMB (Lewis, Challinor & Lasenby 2008) and initial conditions were produced perturbing a glass distribution with N-GenIC (http://www.mpa-garching.mpg.de/gadget). They all follow $1024^3$ particles in a periodic box of variable length. Table 1 shows some of the main characteristics of these simulations. Haloes were identified using a SO algorithm (Tormen, Moscardini & Yoshida 2004; Giocoli, Tormen & van den Bosch 2008) and then the best-fitting ellipsoid was found using an ellipsoidal overdensity method, already presented in Despali et al. (2013, 2014) and similar to the one used on the MXXL haloes and described in the next section; the two codes produce equivalent results. We selected only haloes with more than 1000 particles to ensure a good resolution and to have a good comparison with the haloes of the MXXL simulation.

### 2.3 Ellispoidal halo finder

It is known that Friends Of Friends finders tend to connect together multiple virialized haloes via thin bridges of particles (Jing & Fang 1994); thus, to characterize halo shapes more precisely, we used a second halo finder that iteratively selects particles inside an ellipsoid and then uses their mass distribution to compute the ellipsoid for the next step in the iteration. A more detailed description of the 'ellipsoidal halo finder' in general and of the iterative procedure can be found in Despali et al. (2013)

We start with a traditional SO algorithm which selects particles inside a sphere of given overdensity, namely the value from the spherical collapse model at $z = 0$: $\Delta_{\rm vir} = 359.7$ times the background density (Eke, Cole & Frenk 1996), and centred in the particle with lowest potential (most bound particle). We then compute the mass tensor[1]

$$\mathcal{M}_{\alpha\beta} = \sum_{i=1}^{N_V} \frac{m_i\, r_{i,\alpha}\, r_{i,\beta}}{M_{\rm TOT}} \qquad (1)$$

of the particles inside the virial radius of the sphere of mass $M_{\rm TOT}$, where $r_i$ is the distance of the $i$th particle, of mass $m_i$, from the most bound particle. The tensor's eigenvectors give the direction of the ellipsoid that approximate the mass distribution, while the square roots of the eigenvalues are proportional to the axes length ($c > b > a$).

Having derived the triaxial distribution of dark matter for the SO, we use it to select particles inside an ellipsoid. This technique has been already adopted in the literature (Allgood et al. 2006; Schneider et al. 2012; Despali et al. 2013); however, different authors use different criteria to define the ellipsoid. We select particles inside an ellipsoid, centred in the most bound particle, that encloses an overdensity equal to the virial one, as provided by the spherical collapse model $\Delta_{\rm vir}$; we do not fix the mass, the volume or the major axis to be equal to the spherical values, as has been done in previous works. We then recompute the mass tensor with the new subset and we iterate this procedure until both the ratios of minor to major axis $s = a/c$ and intermediate to major axis $q = b/c$ converge within a 0.5 per cent of error. This method allows us to adopt a more general description while being still close to theoretical predictions and is the simplest possible extension of the SO, which actually becomes just the first step in our iteration. The mass difference between the spherical and the ellipsoidal identifications goes from 2 per cent at $10^{13}$ $M_\odot$ $h^{-1}$ to 5 per cent for very massive haloes of $5.5 \times 10^{15}$ $M_\odot$ $h^{-1}$. On the other hand the change in the measured shapes is about 30 per cent and cannot be ignored, as shown also by Despali et al. (2013). Ellipsoidal masses are in general larger than the spherical ones, since a triaxial shape is expected to follow the actual distribution of matter better than a sphere, and so follow the overdense regions, adding more particles. The difference in the following results between using the mass inside a sphere or an ellipsoid is negligible.

[1] Not to be confused with the inertia tensor (Bett et al. 2007).

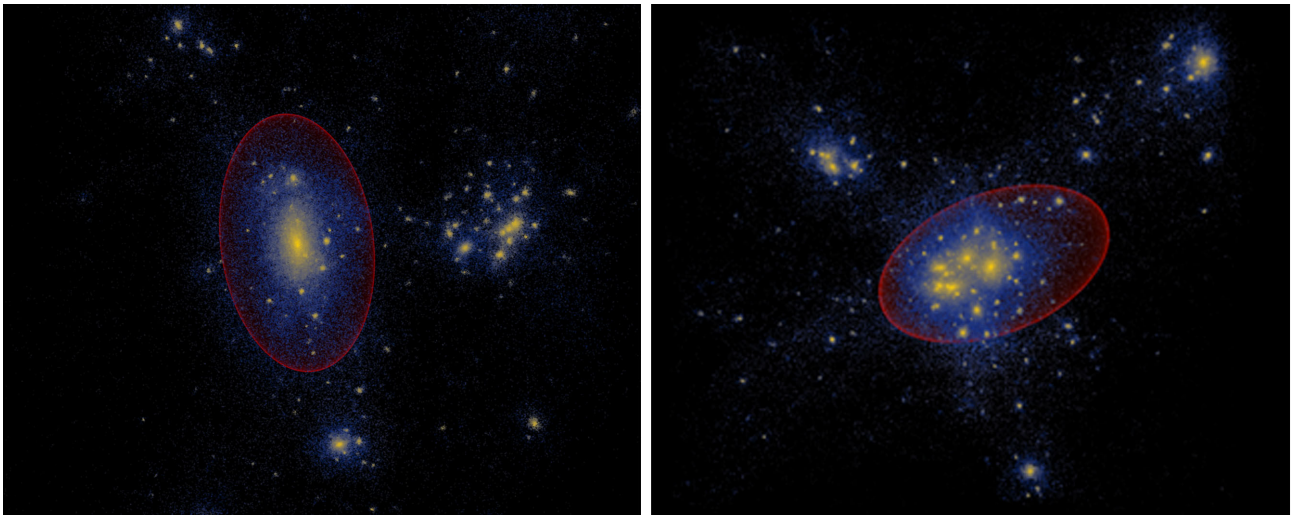

**Figure 1.** Density distribution (colour scale) of dark matter particles inside a 10 Mpc $h^{-1}$ side cube centred in two different haloes and the respective computed ellipsoids (red) that approximate the mass distribution of the halo. The halo shown on the left-hand panel has a virial mass of $5.29 \times 10^{14}$ $M_{\odot}$ $h^{-1}$, the one on the right has a mass of $6.90 \times 10^{14}$ $M_{\odot}$ $h^{-1}$. These represent two families of objects: a 'regular' haloes (left) and a perturbed one (right), due to the large amount of substructures the latter has to be discarded, as it cannot be well described by a triaxial approximation.

### 2.4 Halo selection

Fig. 2 shows the mass function of all haloes (upper panel). Data from redshift $z = 0$ and $z = 1$ are indicated by red squares and blue circles, respectively. As previously explained, we have analysed only a random sample of the entire halo catalogue of the MXXL simulation; this is causing the flattening at the mass bins which have more than $10^5$ objects in the entire box ($\approx 10^{14}$ $M_{\odot}$ $h^{-1}$). To avoid any resolution effect, we have kept only haloes with at least 1000 particles within the ellipsoid (vertical dashed line) in both simulations.

For our analysis, we cleaned the halo catalogue from many unrelaxed systems. As an example, Fig. 1 shows the density distribution of dark matter of two haloes (colour scale) and, in red, the computed ellipsoid which encloses an overdensity of $\Delta_{\rm vir}$. The object on the left has a virial mass of $5.29 \times 10^{14}$ $M_{\odot}$ $h^{-1}$ and represent a relaxed halo; the mass of the one on the right is $6.90 \times 10^{14}$ $M_{\odot}$ $h^{-1}$ and it is clearly multimodal. The ellipsoid seems to capture quite well the overall three-dimensional matter distribution of the relaxed halo; though it fails, as expected, with the perturbed one. This system is highly asymmetrical and lacks of a well-defined centre, therefore it cannot be described using a single triaxial model. Since triaxial multimass modelling is beyond the purpose of this paper we decided to not consider for our analysis multimodal haloes, like the one on the right-hand panel.

In general, defining relaxed and unrelaxed haloes is not a trivial task; there is no absolute definition and the limiting criteria depend on the model that must be tested. In our case, where we are interested in haloes shapes, we would like at least to be able to describe them with a single ellipsoid. In particular, we need to well define their centres as well as their symmetry, up to a certain degree.

A possible way to discriminate this kind of objects is to look at the offset between centre of mass and geometrical centre of the ellipsoid, which is one of the commonly used criteria for the selection of relaxed haloes. While the latter is associated with the minimum of the potential (most bound particle) of the most massive substructure (Springel et al. 2001), the other represents the centre of mass of the whole particle distribution. This means that, if a significant number of massive substructures is present and perturbs the whole halo distribution, there will be an offset between the centre of the ellipsoid and the centre of mass. We decided to select only haloes for which the offset is less than 5 per cent of their virial radius,

$$\frac{|\bar{x}_{\rm MBP} - \bar{x}_{\rm cm}|}{R_{\rm vir}} < 0.05. \quad (2)$$

The lower panel of Fig. 2 shows the percentage of cleaned haloes as a function of the mass. As expected, the number of perturbed haloes increases with the mass, due to more massive haloes being assembled recently (Giocoli et al. 2007). At high redshift (blue circles), the percentage of 'regular' haloes was lower and more constant with mass, than at $z = 0$ (red squares). For cluster masses the percentage is roughly 50 per cent.

Generally, 'relaxed' haloes are selected using both this and two other criteria: the amount of mass in substructures and the ratio of kinetic to potential energy as measurements of the dynamical state of a halo (Meneghetti et al. 2014). For this reason, we choose to call our cleaned sample of haloes 'regular' and not relaxed haloes. However, as can be seen in Neto et al. (2007), the selection in the centre offset is responsible for the majority of the rejected haloes; this means that our selection is still able to eliminate the most unrelaxed and irregular objects. Ludlow et al. (2012) used a similar selection ($N_{200} > 5000$ and spherically defined haloes) and found different results: the fraction of objects with an offset less than 5 per cent is 0.536, while, combining all the three relaxation criteria, the fraction of selected haloes is 0.285. In comparison with their work, our selection is still able to capture approximately 65 per cent of all perturbed haloes.

Thus, the choice of the criteria to distinguish between relaxed and unrelaxed haloes is still different in different works. Since we are interested in the overall shape of haloes, we decided to use only the centre offset as a selection criterion, since it is able to exclude very irregular haloes which could not be well fitted by an ellipsoid; we believe that adding the other two criteria would not change our results more than a few percent. Moreover, our choice is motivated also by the fact that we do not want to restrict our analysis to a very limited and regular sample, since our future plans include a

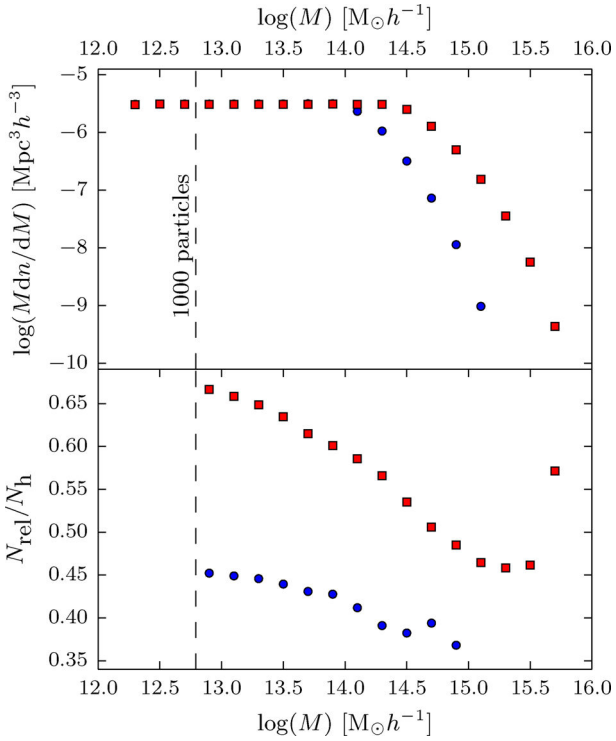


**Figure 2.** Mass function and halo selection of the MXXL sample at redshift $z = 0$ (red squares) and $z = 1$ (blue circles) obtained with the ellipsoidal overdensity. The vertical dashed line indicates the mass of a halo with 1000 particles. Top panel: points show the mass function of the whole selected halo catalogue. The cut at low masses is clearly visible. Bottom panel: points show the percentage of regular haloes in each mass bin (i.e. objects with a centre offset smaller than 5 per cent of their virial radius).

comparison with observational results, which are far from being homogeneous and regular.

Another used criterion is the rms of the fit adopting an NFW profile (Macciò et al. 2007; Muñoz-Cuartas et al. 2011) as reference. As we are only interested in the overall shape of a halo, this does not play an important role; it is also interesting to mention that the halo profile may vary for the simple NFW predictions (Navarro et al. 2004; Prada et al. 2012; Klypin et al. 2014). This can be seen, for example, in fig. 6 of Macciò et al. (2007), where the authors compare the dependence of shape on mass for different selection criteria. A selection only on centre offset (as done here) correspond to what the authors called GOOD and NOISY halo samples (offset less than 4 per cent) and differ only by the goodness of the NFW fit. The two curves in the plot are almost identical, while there is a noticeable difference when compared with the BAD and UGLY sample (offset larger than 4 per cent).

These methods for selecting regular haloes have also been applied to the five SBARBINE simulations, obtaining a catalogue equivalent to the MXXL haloes. The selected number haloes for both simulations at redshift $z = 0$ is shown in Table 1.

## 3 TRIAXIAL SHAPES OF MASSIVE GALAXY CLUSTERS FROM MXXL

### 3.1 MXXL results

In this first analysis we are mostly interested in the clusters mass range, therefore we will use only a portion of the available MXXL

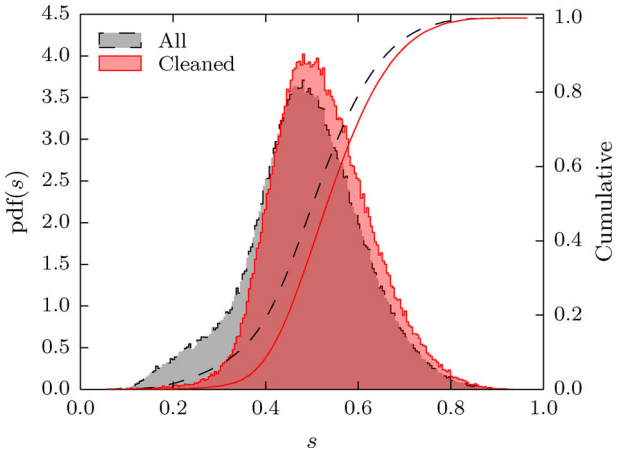


**Figure 3.** Probability distribution functions – differential and cumulative – of $s = a/c$. The distributions for the entire haloes population is shown in grey (and with dashed lines), while the red (solid) ones refer to the cleaned population.

**Table 2.** Number of haloes in each logarithmic mass bin(in $\log(M/\mathrm{M}_\odot h)$) and percentage of regular haloes for redshifts $z = 0$ and 1.

| | $z = 0$ | | $z = 1$ | |
|---|---|---|---|---|
| $\log(M)[\mathrm{M}_\odot\, h^{-1}]$ | $N_\mathrm{h}$ | $N_\mathrm{reg}/N_\mathrm{h}$ | $N_\mathrm{h}$ | $N_\mathrm{reg}/N_\mathrm{h}$ |
| 14.0–14.2 | 57 759 | 58.56 per cent | 30 823 | 41.19 per cent |
| 14.2–14.4 | 56 083 | 56.61 per cent | 13 271 | 39.11 per cent |
| 14.4–14.6 | 42 951 | 53.52 per cent | 3914 | 38.24 per cent |
| 14.6–14.8 | 20 715 | 50.60 per cent | 919 | 39.39 per cent |
| 14.8–15.0 | 7823 | 48.50 per cent | 134 | 36.81 per cent |
| 15.0–15.2 | 2305 | 46.46 per cent | 6 | 19.35 per cent |
| 15.2–15.4 | 523 | 45.84 per cent | | |
| 15.4–15.6 | 84 | 46.15 per cent | | |

data. By taking the ratio of minor to major axis $s = a/c$ we can measure the degree of triaxiality of a halo; the closer $s$ is to 0, the less spherical the object is. If we combine this information with the value of the intermediate to major axis ratio $q = b/c$, we can infer how much prolate or oblate the halo is. In Fig. 3, the distribution of $s$ is shown for the entire halo catalogue (dashed grey curves), and for the regular one (solid red curves). The filled histograms represent the differential distributions, while the curves are cumulative distributions of the two different samples. In the original population there is a noticeable bump at low $s$ which corresponds to highly aspherical objects; clearly this is the case of unrelaxed or merging clusters. As it can be seen in the red histogram, the selection criteria we adopted have helped to remove this unwanted feature, since modelling them is beyond the goal of this work. We have divided our sample in eight logarithmic mass bins, from $10^{14}$ to $3.98 \times 10^{15}$ $\mathrm{M}_\odot\, h^{-1}$. Table 2 reports the total number of haloes $N_\mathrm{h}$ and the percentage of regular ones $N_\mathrm{rel}/N_\mathrm{h}$ for each mass bin for both redshifts of the MXXL. As expected, the number of clusters at high redshift is lower and we do not have any halo in the highest mass bins. As noted before, the percentage of regular haloes is higher at low masses, which formed earlier and thus had more time to reach an equilibrium state.

It has already been established (Jing & Suto 2002; Allgood et al. 2006; Bett et al. 2007; Schneider et al. 2012) that the axis ratio $s$ depends on the mass of the halo, however this dependence has not been tested at the high masses available in large simulation boxes such as the MXXL. Fig. 4 shows the distributions of $s$ for different mass bins in our sample – only five mass bins of Table 2,

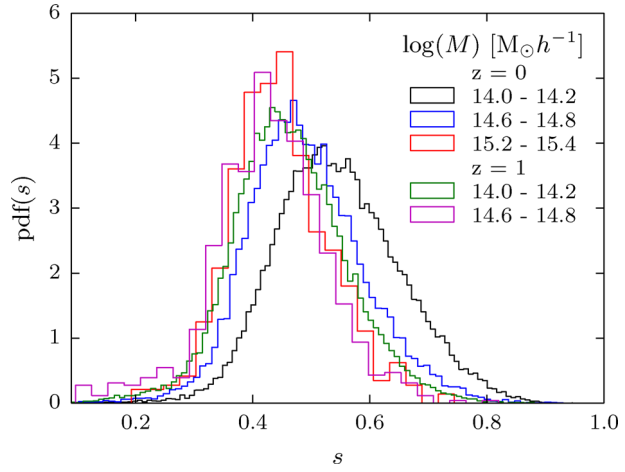


**Figure 4.** Probability distribution function of $s = a/c$ binned in mass using a fixed bin of 0.2 $M_\odot\, h^{-1}$ for both redshifts. For clarity, we show the results for only five of the mass bins reported in Table 2.

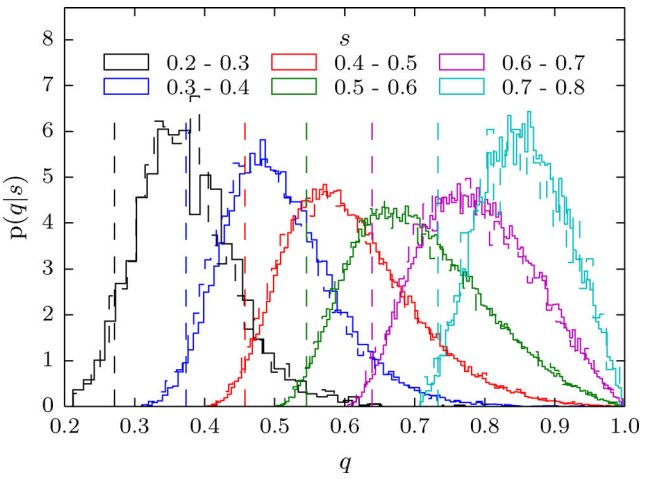


**Figure 5.** Conditional distributions $p(q|s)$, with $q = b/c$. Different colours represent the distributions for six bins in $s$; solid and dashed histogram shows data from redshift 0 and 1, respectively. The vertical dashed lines of corresponding colour show the median value of $s$ for each bin.

to avoid an overcrowded plot; as halo mass increases, the median value of the axis ratio becomes smaller, that is, the halo is less spherical. This effect is barely visible at redshift $z = 1$. Moreover the dispersion in $s$ is larger in the lower bins. It is also noticeable that the distributions are not symmetric, particularly they are skewed to low values of the axis ratio. To fully describe the shape of haloes, we need also the conditional probability distribution function $p(q|s)$, which is the distribution of $q$ for a given value of $s$. Fig. 5 shows the conditional distributions obtained for six bins in $s$: solid histogram for $z = 0$ and dashed for $z = 1$. The two redshifts are almost indistinguishable, which hints at the universality of the conditional distribution that will be discussed later on. For any interval, the median value of $b/c$ is fairly close to the median of $a/c$ (dashed vertical lines); although still fully triaxial, haloes tend to be prolate rather than oblate. For example, in the case of a 'disc-like' object, all the distributions would have been prominently shifted to values close to unity, because, in this case, $b \approx c$ independently of the minor axis $a$.

### 3.2 Minor to major axis ratio distribution: functional form

We aim to obtain a functional form to describe the axial ratio distributions at different masses. Due to the low statistic, Jing & Suto (2002) were not able to fully resolve the shape of the distribution and therefore assumed a Gaussian distribution. On the other hand, Schneider et al. (2012) claimed to be able to fit all the masses with a single beta distribution, although, even after a rescaling of $s$, they mention some residual mass dependence. Thanks to the large statistic in the MXXL simulation we are able to reconstruct the distributions with greater detail, even at large masses. Moreover, we are only interested in clusters, so we do not need the same level of generalization of the previous authors (see Section 4 for broader analysis). These two conditions allow us to simplify the analysis and obtain a better fit of the axial ratio distributions.

As shown by various authors (Press & Schechter 1974; Bond et al. 1991; Lacey & Cole 1993) the mass function written as a function of peak height $\nu = \delta_c(z)/\sigma(M)$ does not depend on redshift nor on cosmology (see appendix A for the details on how to compute $\nu$). It can be understood as follows: $\delta_c(z)$ is the critical overdensity of the spherical collapse model (initial density required for a fluctuation to collapse at redshift $z$), it increases with $z$; $\sigma(M)$ is the variance in the initial density field smoothed on a scale of a uniform sphere of mass $M$ and is higher for small masses. Then, since at high-redshift haloes were less massive, the dependences on time of the two quantities compensate with each other. For example, $\nu(M_\star, z) = 1$ at every redshift, and $\nu > 1$ always represent a halo with a mass larger than the typical haloes collapsing at that time, even though the exact value of $M_\star$ changes with redshift.

Fig. 6 shows the logarithm of $s$ versus the logarithm of peak height (≈mass) for the selected haloes. Medians of $\log(s)$ for the two redshifts are shown in red squares and blue circles; the redshift dependence seen in Fig. 4 has disappeared completely. As already shown by Despali et al. (2014, fig. 5), the universality of haloes properties seems to extend also to the shape when using $\nu$ instead of mass. The change of variable allows us to provide results that are independent of the redshift and valid for different cosmologies. This idea was already in the original Jing & Suto (2002) paper, as the mass was given in units of $M_\star$, but the use of $\nu$ is more

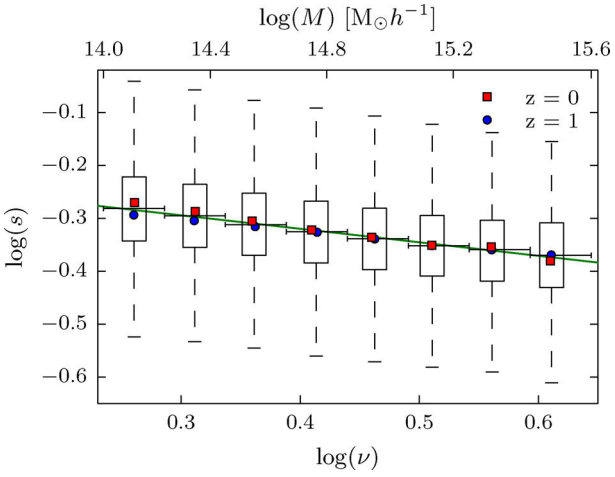


**Figure 6.** (logarithmic) Distribution of $s$ as function of peak height: the black boxes and whiskers represent the quartiles and 1.5 the quartiles range of the combined distributions. The horizontal error shows the different bins, while the green solid line is the linear fit to the medians. Red squares and blue circles are redshift 0 and 1 subsamples. As reference, the corresponding mass for MXXL cosmology at $z = 0$ is shown in the top axis.

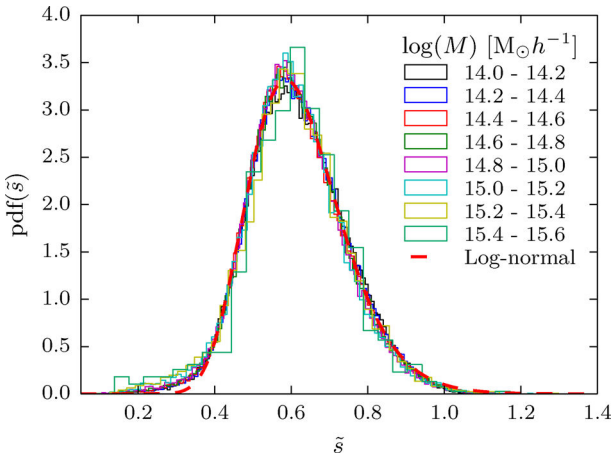


**Figure 7.** Distribution of the scaled axial ratio $\tilde{s}$ for masses shown in Table 2. It can be easily seen that the distributions at all masses are well represented by an unique fitting function.

general and gives a more direct connection to the theory of structure formation. As a result, we can safely treat the two data sets as a single population, shown by the box and whiskers plot for a given $\nu$ bin (horizontal error bars). This plot confirms the previously mentioned trend: more massive haloes (higher $\nu$) are more aspherical. We have looked for a linear relation between $\nu$ and axis ratio in the log–log space (green line in Fig. 6) and obtained an inclination $a = -0.257 \pm 0.01$ and an intercept $b = -0.219 \pm 0.005$. The intercept is the logarithm of the median axis ratio at $M_\star$: $\tilde{s}(M_\star) = 10^b = 0.604 \pm 0.006$, which however does not enter directly in the following relations. The relation translate to a rescaling similar to the one adopted by previous authors: $\log(s) = a \log(\nu) + b \Rightarrow \tilde{s} = 10^b = 10^{\log s - a \log(\nu)} = s\,\nu^{-a}$. Therefore

$$\tilde{s} = s\nu^{0.257} \tag{3}$$

as $\nu$ takes care of any time and cosmology dependence, this rescaling is valid also for different redshifts and cosmologies. As Fig. 7 shows, distributions of the rescaled axis ratios (coloured histograms) are nearly indistinguishable from each other, meaning that we have eliminated all the dependence on the mass, in contrast with the findings of Schneider et al. (2012). Moreover, we were not able to fit the histogram of $\tilde{s}$ with a beta distribution. As it can be seen in Fig. 7, the distributions are non-zero at values greater than $\tilde{s} = 1$; this does not mean that there are haloes with axis ratio greater than 1: $\tilde{s}$ is not a physical quantity, this effect is due to the rescaling. Nevertheless, one can argue that $\tilde{s}$ represents the physical axis ratio at $\nu = 1$ ($M = 5.8 \times 10^{12}\ \mathrm{M}_\odot\, h^{-1}$); still, this rescaling has been obtained only for $M > 10^{14}\ \mathrm{M}_\odot\, h^{-1}$, leaving the unscaled axis ratio well within the physically meaningful boundaries. We have chosen to fit the minor to major axis ratio using a lognormal distribution

$$p(x, \mu, \sigma) = \frac{1}{x\sqrt{2\pi}\sigma} \exp\left(-\frac{(\ln x - \mu)^2}{2\sigma^2}\right), \tag{4}$$

which corresponds to the probability distribution function of a variable which is normally distributed in the logarithmic space. The parameters of the fitted function are the following:

$$\mu = -0.49$$
$$\sigma = 0.20; \tag{5}$$

they can be converted to more familiar quantities

$$\text{median} = e^\mu = 0.61,$$
$$\text{std} = \sqrt{(e^{\sigma^2} - 1)e^{2\mu+\sigma^2}} = 0.13. \tag{6}$$

In this framework, for a simple analysis, one can just use the scaled median value $\tilde{s} = e^\mu = 0.61$ with asymmetric quartiles at 0.53 and 0.70; then use equation (3) to obtain the physical value. On the other hand, it is possible to use the fit to obtain the whole distribution for a given mass. For example, to use it as a prior distribution of the minor to major axis ratio, one draws a value $x$ from a normal (Gaussian) distribution with mean $\mu = -0.49$ and standard deviation $\sigma = 0.20$, the scaled axis ratio is then $e^x$ (or directly extract $\tilde{s}$ from a lognormal distribution); inverting the rescaling relation one can obtain the axis ratio of the halo at a given peak height, which can be subsequently converted in mass for a given cosmology at a given redshift.

### 3.3 Intermidiate to major axis ratio distribution: functional form

Once we are able to describe $s$ as a function of mass we can look at the correlation between the two axial ratios. For construction, $q$ is always greater (or equal) than $s$; also it is always less than 1. These limits have the effect of distorting the distribution of intermediate to major axis ratio in a way that depends directly on $s$. To avoid this problem, we use the rescaled quantity $\tilde{q} = (q - s)/(1 - s)$ instead of the simple axial ratio (Schneider et al. 2012), eliminating the issues of a limited interval; the correlation between the rescaled second axial ratio and $s$ can be seen in the left-hand panel of Fig. 8, where medians (red error bars) and quartiles (box and whiskers plot) for different values of the first axis ratio are shown. We have divided $\tilde{q}$ in bins of different $s$ and extracted the distributions $p(\tilde{q}|s)$ (right-hand panel of Fig. 8). From both plots, it is quite evident that $\tilde{q}$ strongly depends on the first axial ratio, with higher values at higher $s$, which is in agreement with haloes that tend to be prolate. Moreover the scatter is larger at higher $s$, though this is mostly due to the rescaling which extends the allowed interval of $\tilde{q}$.

Because of the strong correlation between $\tilde{q}$ and $s$, we cannot just give $\tilde{q}$ as a function of mass to obtain the second axis ratio distribution for a given mass, we have to describe $p(\tilde{q}|s)$ and then get the first axis ratio from its distribution at different masses (as shown in Section 3.2). Given the large differences in the shapes of the distributions of $\tilde{q}$ at a given $s$, the rescaling needed to reduce them to a single one needs to be much more complex than the one adopted in the last section. Therefore, we fit each single histogram with a different beta distribution, which has the following analytical expression:

$$p(x, \alpha, \beta) = \frac{1}{B(\alpha, \beta)} x^{\alpha-1}(1 - x)^{\beta-1}. \tag{7}$$

This function has two shape parameters $\alpha$ and $\beta$; the factor $1/B(\alpha, \beta)$ is a normalization constant that can be computed by requiring that the integral of the probability distribution function is equal to unity.

From the fitting procedure, we obtained a pair of parameters for each bin in $s$; however, $\alpha$ has a complicated dependence on the first axial ratio (almost constant with an average value of $\alpha = 2.15$), while the mean value of the beta distributions $\mu = 1/(1 + \beta/\alpha)$ follows a linear relation. Fig. 9 shows the dependence of the mean $\mu$ (red squares on left-hand panel) and $\beta$ parameter (blue circles on right-hand panel) of the fitted beta functions on the first axial ratio

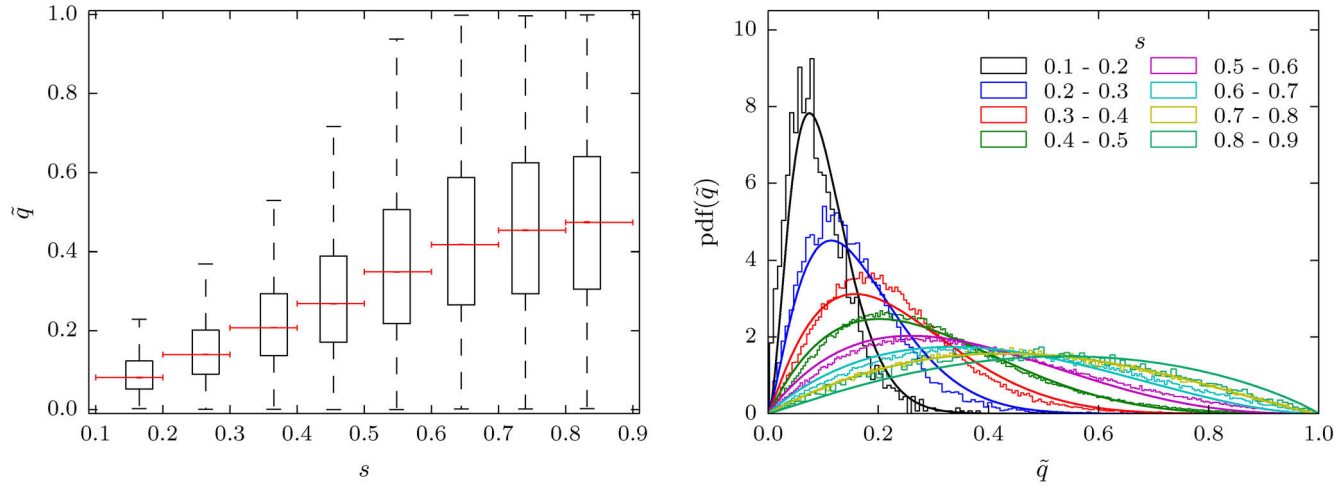


**Figure 8.** Distribution of $\tilde{q} = (q - s)/(1 - s)$ as function of $s$: the black boxes and whiskers represent the quartiles and 1.5 the quartiles range, respectively. The horizontal red error bars represent the bin inside which the medians have been computed. Right: distributions of $\tilde{q}$ for different values of $s$ (histograms) and fitting function resulting from the model presented in the section (curves).

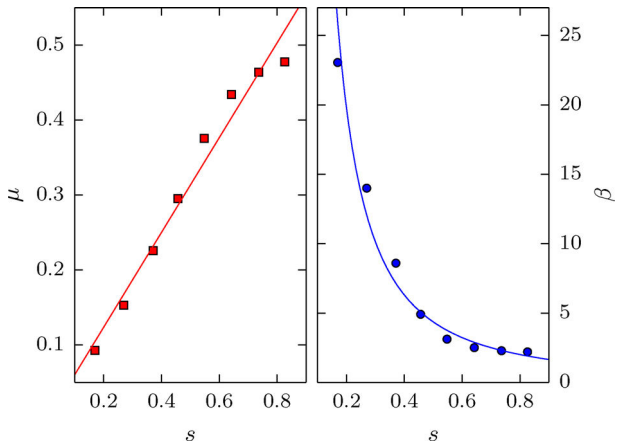


**Figure 9.** Parameters of the fitted beta functions. Red is the mean of the distribution, in blue the second parameter $\beta$.

$s$. The coloured lines in each respective panel show a fit of these two parameters:

$$\mu(s) = 0.633 s^{-0.007}$$
$$\beta(s) = 1.389 s^{-1.685}. \quad (8)$$

These two equations give us a functional form of $p(\tilde{q}|s)$: starting from a value of $s$, one can retrieve the mean $\mu$ and $\beta$ from which the other parameter can be computed $\alpha = \beta/(1/\mu + 1)$. This gives what is needed to reconstruct the distribution of $\tilde{q}$ of a given $s$ and the scatter, if needed. The final step is to revert the change of coordinates and compute the physical axial ratio $q$.

## 4 EXPLODING THE MASS RANGE TO FIVE ORDERS OF MAGNITUDE

The next step of our work is to explode the recipes for dark matter halo shapes to lower masses; in the following sections we describe how to generalize the axial ratio distribution to a wider mass range. To do so, we combined the MXXL data with the SBARBINE simulations, a set of cosmological simulations that will allow us to study the shape of dark matter haloes from $3 \times 10^{10}$ to $6 \times 10^{15}$ $M_\odot\, h^{-1}$.

As before, we express the mass dependence in terms of peak height $\nu$. By doing this, it is possible to treat homogeneously data from different redshifts and cosmologies, such as the SBARBINE and the MXXL simulations.

### 4.1 Axis ratio distribution: minor to major

On left-hand panel of Fig. 10, the logarithm of the minor to major axial ratio $s$ is shown as a function of the logarithm of $\nu$. As before, horizontal error bars represent the interval in $\nu$ and the box and whiskers are the quartiles and 1.5 the quartiles range for the combined sample, while coloured points are medians of individual catalogues. Again, there is no difference in the medians between redshifts, neither between the single simulations. It can be seen that $s$ has a nearly linear dependence on $\log(\nu)$, with a hint of flattening at both high and low masses.

For each bin, we extracted the probability distribution function of $\log(s)$ (right-hand panel of Fig. 10). The resulting curves exhibit an interesting pattern: high and low $\nu$ histograms are mirrored with respect to a central symmetric distribution which corresponds to $\nu \simeq 1.21$ ($M \approx M_*$). The rescaling adopted in Section 3.2 for cluster-size haloes does not compensate this large variation in the form of the distributions and it is not able to remove entirely the mass dependence. Instead of using a different rescaling relation to obtain a single probability distribution function (pdf), we decided to follow the same recipe we used for the second axial ratio; first of all we separately fit each distribution and then we relate the resulting parameters to the binning quantity. This is shown in Fig. 11, where we fit the mean (left-hand panel) and $\beta$ parameter (right-hand panel) of the Beta distributions we derived by fitting the histograms of the right-hand panel of Fig. 10. In order to keep the procedure simple we fit with a linear relation both $\mu$ and $\log\beta$,

$$\mu(\nu) = -0.322 \log\nu + 0.620$$
$$\log(\beta(\nu)) = 0.560 \log\nu + 0.836. \quad (9)$$

As before, the dependence of $\alpha$ is difficult to describe and it is almost constant with a value of about 11.21.

Using this fits we are now able to approximate the probability distribution function of the first axial ratio with a Beta function with parameters $\alpha = \beta/(1/\mu - 1)$ and $\beta$, over a range in mass of almost

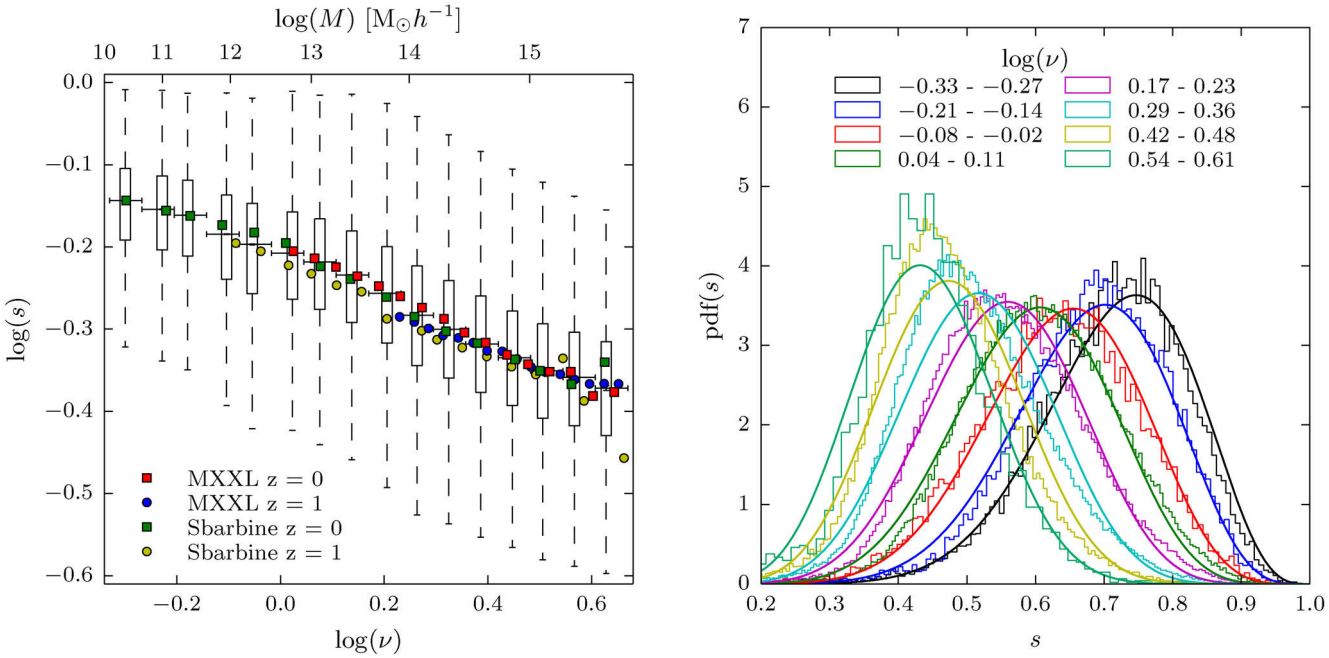


**Figure 10.** Left: distribution of $s$ as function of peak height for all the haloes selected from both redshifts the two simulations; the black boxes and whiskers represent the quartiles and 1.5 the quartiles range, respectively, computed within the bins shown by the horizontal error bars. The coloured points represent the medians for individual redshifts for the two simulations. Right: differential distribution of $s$ for 8 bin in $\nu$ (histograms) and the respective approximating functions obtained as shown in section 4.1 (curves).

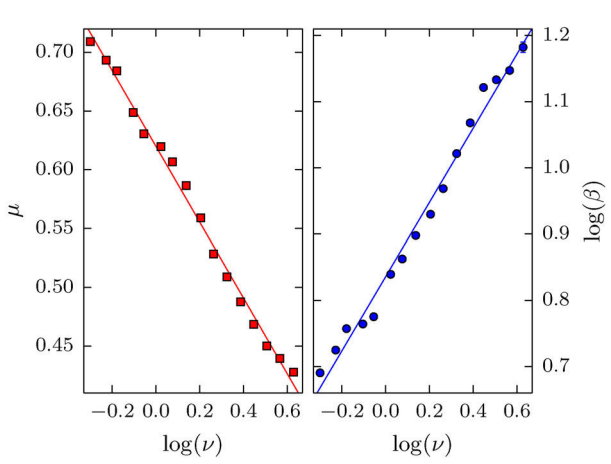


**Figure 11.** Parameters of the fitted beta functions. Red is the mean of the distribution, in blue the second parameter $\beta$.

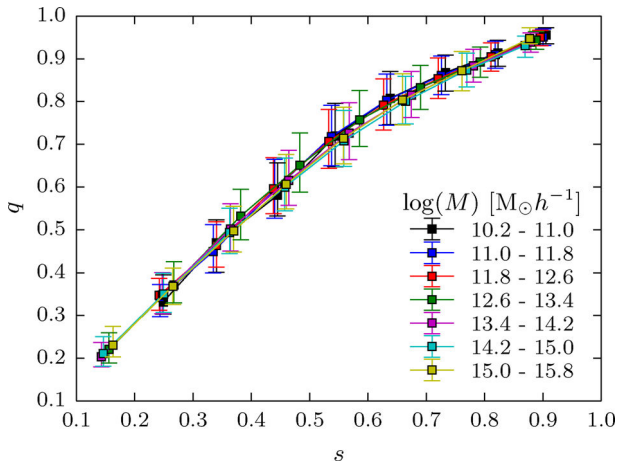


**Figure 12.** Axis ratio $q$ as function of $s$ for different masses, represented by the points of different colours. Since there is no residual mass dependence in the conditional distribution, we get the same result as in the MXXL with all the simulations, confirming that this relation is universal.

six orders of magnitudes. Moreover the use of $\nu$ allows us to extend these results to different cosmologies and different redshifts.

### 4.2 Axis ratio distribution: intermediate to major

Finally, to fully describe a triaxial halo of a given mass the intermediate to major axis ratio has to be parametrized. As Fig. 12 shows, the relation between $q$ and $s$ at redshift $z = 0$ does not depend on the mass; the curves of different colours represent different mass bins and still trace the same relation. The fact that all the mass dependence is already inside $s$, allows us to use for $p(q|s)$ the same functional form of Section 3.3, independently of the mass we choose. The same applies to different redshifts (not shown here, but see Fig. 5 for a limited comparison), with the relation between the two quantities being indistinguishable from the one in Fig. 12. Moreover, this independence of the conditional distribution from both mass and redshift is in agreement with the theoretical predictions from Rossi, Sheth & Tormen (2011).

## 5 COMPARISON WITH PREVIOUS WORKS

We have compared our results with measurement of axis ratios from other authors (Fig. 13). The data from both redshifts of the MXXL and SBARBINE simulations are shown with red squares, the median result form the analysis on cluster masses (Section 3.2) is the blue solid line and the green solid line is from the combined

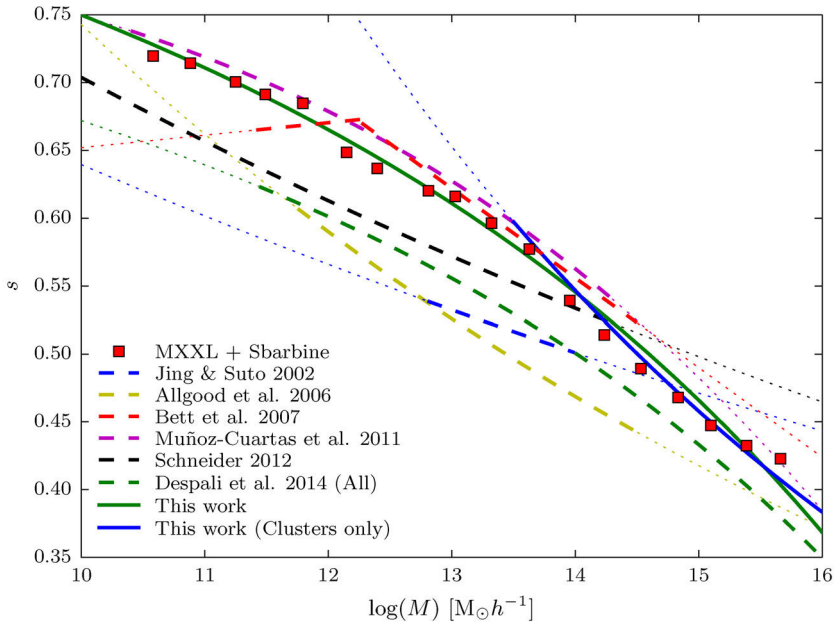


**Figure 13.** Comparison between previous works (dashed lines) and the results of this paper (solid lines). Red squares represent the data from both redshifts of the MXXL and the SBARBINE simulations, converted to redshift $z = 0$ for the Millennium cosmology. The blue solid line is the model for clusters shown in Section 3.2; the green solid line is the fit for the entire mass interval from section 4.1. The dotted parts of the curves show the mass ranges outside where the relations have been derived from.

data sets (Section 4.1). Results from other authors are shown with dashed lines in the mass range where their analysis was carried out and with dotted lines when extrapolated beyond it. Moreover all data and predictions have been converted to redshift $z = 0$ for the Millennium cosmology, when necessary. As it can be seen, there is a general agreement in the dependence of $s$ on the mass, with more massive haloes being less spherical. Although there seems to be a scatter of about 15 per cent, this is due more to the differences in the method of measuring shapes (different finders, radius, cleaning procedure), than an error on the measurement. It must be noticed that instead of the spherical mass, we used the mass within the ellipsoid for consistency reasons; yet, this does not substantially alter the findings presented here.

The most important difference comes from the radius at which the shape is measured. Jing & Suto (2002, blue dashed line) used particles of the isodensity surface corresponding to $2500\delta_c$, roughly at a radius of $0.3R_{\rm vir}$; this analysis is different from all the following authors, as it reflects the shape of an ellipsoidal shell, and not of all the mass inside the ellipsoid. Their mass range $6 \times 10^{12}$–$10^{14}$ $M_\odot\, h^{-1}$ was also quite small compared to later analysis.

Studying a larger mass interval, $6 \times 10^{11}$–$3 \times 10^{14}$ $M_\odot\, h^{-1}$, Allgood et al. (2006, yellow dashed line) derived axis ratios of particles distribution inside $0.3R_{\rm vir}$ diagonalizing the normalized mass tensor (weighted by the distance from the centre); because of this their measure reflects the shape at an even closer radius.

On the other hand, Schneider et al. (2012, black dashed line) extended the analysis up to the virial radius, nevertheless the use of the normalized tensor prevents a meaningful comparison with our results.

All of these results are lower than what we derived, which can be explained by the fact that the shapes were measured at inner radii, where the particle distribution is supposed to be more elongate. However, if we restrict the comparison to works that used particles within the virial radius the agreement becomes much more strong. This is the case of Muñoz-Cuartas et al. (2011, magenta dashed line), who studied shapes with an ellipsoidal overdensity algorithm similar to the one adopted in this work; their results agree with ours much more than any other work.

Finally, using a different type of halo finder, Bett et al. (2007, red dashed line) measured $s$ for a set of particles that represent all the bounded particles of a halo without assuming any particular shape; the finder also clean the sample for irregular haloes. The agreement with our results is another indication that the adopted selection criteria are justified and ellipsoids are a good approximation for regular haloes.

The other difference can arise from the cleaning of the sample; the green dashed line show the prediction from Despali et al. (2014), which is obtained from all haloes, regardless of their state of relaxation. As expected the values are lower, since the more unrelaxed haloes are typically irregular and so they appear more elongated with lower axial ratios. The difference is greater for less massive haloes.

## 6 SUMMARY AND CONCLUSIONS

We have studied the triaxiality of dark matter haloes from the MXXL simulation, which enabled us to characterize the shape of haloes with extremely good statistic in the galaxy clusters mass range, from $10^{14}$ to $4 \times 10^{15}$ $M_\odot\, h^{-1}$. Using the SBARBINE simulations, we have extended our analysis to lower masses down to $3 \times 10^{10}$ $M_\odot\, h^{-1}$, thus increased the mass range by more than five orders of magnitude. The main results of our analysis are the following:

(i) dark matter haloes are triaxial with a tendency of being prolate and in particular more massive objects are less spherical; as shown in Fig. 3 very unrelaxed haloes have the effect of artificially increasing the axis ratios and cannot be described by this simple ellipsoidal model, which is unimodal by construction;

(ii) for clusters, the distribution of the rescaled minor to major axis ratio is well described by a lognormal distribution, in contrast to previous extrapolations from lower masses that found a simple Gaussian fit;

(iii) over the whole examined mass range, $s$ can be approximated by a beta distribution that depends only on the peak height $\nu$;

(iv) the conditional intermediate to major axis ratio distribution $p(q|s)$ can also be described by a beta distribution that depends only on the first axis ratio and not on the mass, thus the same approach can be used for both clusters and the whole mass range of haloes;

(v) overall, the pdf of the shape of a dark matter halo is given by one single parameter $\nu$, related to its mass, that incorporates the dependence on redshift and cosmology. This goes in support of methods that allows us to change the cosmology of a numerical simulation (Angulo & White 2010), as within good approximation most of halo properties depend only on $\nu$.

In the recipe that we provide, a halo shape is determined only by its mass and can be changed to different cosmologies and redshifts. Depending on the level of precision desired, it is possible to choose different approximations,

(i) for a simpler analysis that is focused on the entire mass range, Section 4.1 presents a single method that can be applied to masses from $10^{10}$ up to $10^{16}$ $M_\odot\, h^{-1}$. If restricted to masses lower than $10^{14}$ $M_\odot\, h^{-1}$, this is actually a very accurate description of haloes shapes;

(ii) if the interest is only on clusters shapes, then Section 3.2 gives a more precise model;

(iii) finally, it is possible to combine the two description and just use the most suitable one given the mass of the halo, although losing the universality of the description.

A simple implementation of this model can be found on a dedicated website.[2]

In Section 5, we have compared our results with previous findings. There is a general agreement with previous works within a 15 per cent scatter that is due to the different methods used and especially to the radius at which the shape is measured. However, the picture is clear; dark matter haloes are triaxial objects and this effect is more prominent in clusters where the spherical model is quite far from being able to realistically represent the matter distribution.

## ACKNOWLEDGEMENTS

This work has been carried out thanks to the support of the OCEVU Labex (ANR-11-LABX-0060) and the A*MIDEX project (ANR-11-IDEX-0001-02) funded by the 'Investissements d'Avenir' French government programme managed by the ANR. ML acknowledges the Centre National de la Recherche Scientifique (CNRS) for its support. This study also benefited from the facilities offered by CeSAM (Centre de donnéeS Astrophysiques de Marseille http://lam.oamp.fr/cesam/). The 3D visualization was performed with GLNEMO2 program, developed by Jean-Charles LAMBERT at CeSAM – (http://projets.lam.fr/projects/glnemo2). GD has been partially financed by the Strategic Research Project *AACSE* (Algorithms and Architectures for Computational Science and Engineering) of the University of Padova. CG's research is part of the project GLENCO, funded under the European Seventh Framework Programme, Ideas, Grant Agreement no. 259349. CG and RA thank LAM for supporting their visits during which part of this work has been done. GD and CG thank the whole cosmology group of the University of Padova with whom the SBARBINE simulations were designed; in particular, we thank Giuseppe Tormen for providing the computational resources and Giacomo Baso for running *Ada*.

[2] http://wiki.lam.fr/triaxial

## REFERENCES

Allgood B., Flores R. A., Primack J. R., Kravtsov A. V., Wechsler R. H., Faltenbacher A., Bullock J. S., 2006, MNRAS, 367, 1781
Angulo R. E., White S. D. M., 2010, MNRAS, 405, 143
Angulo R. E., Springel V., White S. D. M., Jenkins A., Baugh C. M., Frenk C. S., 2012, MNRAS, 426, 2046
Bailin J., Steinmetz M., 2005, ApJ, 627, 647
Bett P., Eke V., Frenk C. S., Jenkins A., Helly J., Navarro J., 2007, MNRAS, 376, 215
Binggeli B., 1982, A&A, 107, 338
Bond J. R., Cole S., Efstathiou G., Kaiser N., 1991, ApJ, 379, 440
Boylan-Kolchin M., Springel V., White S. D. M., Jenkins A., Lemson G., 2009, MNRAS, 398, 1150
Buote D. A., Canizares C. R., 1992, ApJ, 400, 385
Buote D. A., Canizares C. R., 1996, ApJ, 457, 565
Carroll S. M., Press W. H., Turner E. L., 1992, ARA&A, 30, 499
Carter D., Metcalfe N., 1980, MNRAS, 191, 325
Cole S., Lacey C., 1996, MNRAS, 281, 716
Despali G., Tormen G., Sheth R. K., 2013, MNRAS, 431, 1143
Despali G., Giocoli C., Tormen G., 2014, MNRAS, 443, 3208
Doroshkevich A. G., 1970, Astrophysics, 6, 320
Dubinski J., Carlberg R. G., 1991, ApJ, 378, 496
Eke V. R., Cole S., Frenk C. S., 1996, MNRAS, 282, 263
Evans A. K. D., Bridle S., 2009, ApJ, 695, 1446
Fabricant D., Rybicki G., Gorenstein P., 1984, ApJ, 286, 186
Frenk C. S., White S. D. M., Davis M., Efstathiou G., 1988, ApJ, 327, 507
Gao L., Navarro J. F., Frenk C. S., Jenkins A., Springel V., White S. D. M., 2012, MNRAS, 425, 2169
Giocoli C., Moreno J., Sheth R. K., Tormen G., 2007, MNRAS, 376, 977
Giocoli C., Tormen G., van den Bosch F. C., 2008, MNRAS, 386, 2135
Giocoli C., Meneghetti M., Bartelmann M., Moscardini L., Boldrin M., 2012a, MNRAS, 421, 3343
Giocoli C., Meneghetti M., Ettori S., Moscardini L., 2012b, MNRAS, 426, 1558
Hopkins P. F., Bahcall N. A., Bode P., 2005, ApJ, 618, 1
Jing Y.-P., Fang L.-Z., 1994, ApJ, 432, 438
Jing Y., Suto Y., 2002, ApJ, 574, 538
Kasun S. F., Evrard A. E., 2005, ApJ, 629, 781
Kawahara H., 2010, ApJ, 719, 1926
Klypin A., Yepes G., Gottlober S., Prada F., Hess S., 2014, preprint (arXiv:1411.4001)
Lacey C., Cole S., 1993, MNRAS, 262, 627
Lau E. T., Nagai D., Kravtsov A. V., Vikhlinin A., Zentner A. R., 2012, ApJ, 755, 116
Lewis A., Challinor A., Lasenby A., 2008, ApJ, 2, 2
Limousin M., Morandi A., Sereno M., Meneghetti M., Ettori S., Bartelmann M., Verdugo T., 2013, Space Sci. Rev., 177, 155
Ludlow A. D., Navarro J. F., Li M., Angulo R. E., Boylan-Kolchin M., Bett P. E., 2012, MNRAS, 427, 1322
Macciò A. V., Dutton A. A., van den Bosch F. C., Moore B., Potter D., Stadel J., 2007, MNRAS, 378, 55
Meneghetti M. et al., 2014, ApJ, 797, 34
Muñoz-Cuartas J. C., Macciò A. V., Gottlöber S., Dutton A. A., 2011, MNRAS, 411, 584
Navarro J. F. et al., 2004, MNRAS, 349, 1039
Neto A. F. et al., 2007, MNRAS, 381, 1450
Oguri M., Takada M., Okabe N., Smith G. P., 2010, MNRAS, 405, 2215
Oguri M., Bayliss M. B., Dahle H., Sharon K., Gladders M. D., Natarajan P., Hennawi J. F., Koester B. P., 2012, MNRAS, 420, 3213
Paz D. J., Lambas D. G., Padilla N., Merchán M., 2006, MNRAS, 366, 1503

Planck Collaboration XVI, 2014, A&A, 571, A16
Prada F., Klypin A. A., Cuesta A. J., Betancort-Rijo J. E., Primack J., 2012, MNRAS, 423, 3018
Press W. H., Schechter P., 1974, ApJ, 187, 425
Rossi G., Sheth R. K., Tormen G., 2011, MNRAS, 416, 248
Sayers J., Golwala S. R., Ameglio S., Pierpaoli E., 2011, ApJ, 728, 39
Schneider M. D., Frenk C. S., Cole S., 2012, J. Cosmol. Astropart. Phys., 2012, 030
Skielboe A., Wojtak R., Pedersen K., Rozo E., Rykoff E. S., 2012, ApJ, 758L, 16
Soucail G., Fort B., Mellier Y., Picat J. P., 1987, A&A, 172, L14
Springel V., 2005, MNRAS, 364, 1105
Springel V., White S. D. M., Tormen G., Kauffmann G., 2001, MNRAS, 328, 726
Tormen G., Moscardini L., Yoshida N., 2004, MNRAS, 350, 1397
van Daalen M. P., Angulo R. E., White S. D. M., 2012, MNRAS, 424, 2954
Warren M. S., Quinn P. J., Salmon J. K., Zurek W. H., 1992, ApJ, 399, 405

## APPENDIX A: DENSITY PEAK HEIGHT

In this appendix, we describe step by step how to compute density peak height $\nu$ for a virialized halo with mass $M$ at redshift $z$ for a given cosmological model. Its definition is the following:

$$\nu \equiv \frac{\delta_c(z)}{\sigma(M)}, \tag{A1}$$

where $\delta_c(z)$ is the critical overdensity of the spherical collapse model, the initial density required for a fluctuation to collapse at redshift $z$. This in turn can be expressed as the collapse overdensity at redshift $z = 0$ rescaled to a given time: $\delta_c(z) = \delta_c/D(z)$, with $D(z)$ being the linear growth rate of a density fluctuation normalized to unity at $z = 0$. The overdensity $\delta_c$ depends only on redshift and not on the mass; on the other hand, the denominator $\sigma(M)$, depends on the mass but not on redshift. It is the variance in the initial density field smoothed on a linear scale $R$, which corresponds to the radius of a uniform sphere of mass $M$. Therefore, only the linear growth rate $D(z)$ and the initial power spectrum $P(k)$ are needed.

From the linear perturbation theory, it is possible to compute $D(z)$

$$D(z) \propto H(t) \int_0^t \frac{\mathrm{d}t'}{a^2(t')H^2(t')}, \tag{A2}$$

which has to be solved numerically. Fortunately, there is an approximated solution (Carroll, Press & Turner 1992) that can be expressed as $D(z) \propto g(z)/(1+z)$, where

$$g(z) = \frac{5/2\,\Omega_m(z)}{\Omega_m^{4/7} - \Omega_\Lambda(z) + [1+\Omega_m(z)/2]\,[1+\Omega_\Lambda(z)/70]}. \tag{A3}$$

Additionally, the collapse overdensity has an extremely weak dependence on cosmology: $\delta_c \approx 1.686[\Omega_m(t_c)]^{0.0055}$; for realistic cosmologies this can be approximated to $\delta_c \approx 1.69$. Therefore, at $z = 0$ the collapse overdensity is $\delta_c$ and it increases with redshift, due to $D(z)$.

The other quantity required, the variance $\sigma^2(M)$, is defined from the power spectrum as

$$\sigma^2(M) = \frac{1}{2\pi^2} \int_0^\infty P(k)\tilde{W}^2(kR)k^2\mathrm{d}k; \tag{A4}$$

where $\tilde{W}$ is the Fourier transform of a window function. Typically, $W$ is a Top Hat (sphere) in the coordinates space, so that its Fourier transform $\tilde{W}$ is

$$\tilde{W}(kR) = 3\frac{\sin(kR) - kR\cos(kR)}{(kR)^3}; \tag{A5}$$

with the radius $R$ given by $M = \rho_b 4\pi/3R^3$. The power spectrum $P(k)$ of the density fluctuations is the main input; given a set of cosmological parameters it can be computed from a software like CAMB (Lewis et al. 2008). As it is function of initial conditions only, $\sigma(M)$ needs to be computed only once for a given cosmology; all the redshift dependence is inside $D(z)$.

Finally, for a halo of mass $M$, using equation (A4) it is possible to compute $\sigma(M)$ and combine it with the value of $D(z)$ from equation (A3) to obtain the correct density peak height $\nu$.

This paper has been typeset from a TEX/LATEX file prepared by the author.

# 3. Simulating gravitational lensing observations with MOKA

Strong gravitational lensing systems represent a biased population. In order to form multiple images or visibly deform background sources, a high surface mass density is required (or lucky alignments of the background object); this threshold can be reached by haloes that have large mass, high concentration or special orientation (Hennawi, Dalal, et al., 2007). Therefore it is clear that a sample of galaxy cluster selected because of their gravitational lensing does not represent the overall population.

Many studies have characterised the different systematics that can influence the appearance and strength of gravitational lensing effects (Hennawi, Dalal, et al., 2007; Meneghetti, Fedeli, et al., 2010; Redlich, Bartelmann, et al., 2012; Waizmann, Redlich, et al., 2012, for example); however the limited size of the simulations prevented the formation of a large number of very massive objects.

The analysis presented in the previous chapter provided us with a catalogue of triaxial shape and orientation of all the haloes in the Millennium XXL (MXXL) simulation. In this chapter we have exploited these data to investigate the properties of galaxy clusters that generate strong gravitational lensing and how they are influenced by shape and orientation of the halo. I have done so by selecting haloes from the MXXL simulation and then computing their lensing properties using the MOKA software (C. Giocoli, Meneghetti, et al., 2012). Even though the catalogue with properties of haloes was already available, I had to generate surface mass density maps for each selected cluster; I also had to modify MOKA to accept mass maps as input to measure the Einstein radius and produce the convergence and shear maps.

For each halo, I have produced outputs for six different orientations: three along the $x$, $y$ and $z$ axis; and three along the main axes of the halo. The first three orientations correspond to random rotations of the object; while the latter allows us to quantify the boost in strong lensing signal caused by the alignment of the axes with the line of sight, in particular by looking at the Einstein radius of the different orientations. Moreover, I have compared the distribution of minor to major axis ratio of strong lensing clusters with the overall population for different values of the Einstein radius.

Finally, I have checked that in our analysis the effect of correlated structures along the line of sight are negligible by comparing the results with what is obtained by using larger regions in the projected direction.

The main results of our analysis can be summarised as following:

- projection effects play an important role in biasing strong lensing clusters;

- orientation effects can boost the Einstein radius by more than a factor of two when an halo is aligned with its major axis along the line of sight;
- there is a small but non-negligible difference in the distribution of the minor to major axis ratio between the strong lensing clusters and the overall population.

The results of this work are shown in Section 2.1 ("Strong lensing of Clusters in the Millennium-XXL Simulation") of the paper included in the following section. The paper has been accepted for publication in MNRAS.

## 3.1. Characterising Strong Lensing Galaxy Clusters using the Millennium-XXL and MOKA simulations

C. Giocoli, M. Bonamigo, et al. "Characterising Strong Lensing Galaxy Clusters using the Millennium-XXL and MOKA simulations". In: *ArXiv e-prints* (Apr. 2016). arXiv: 1604.03109

Mon. Not. R. Astron. Soc. **000**, 000–000 (2016) Printed July 12, 2016 (MN LATEX style file v2.2)

# Characterising Strong Lensing Galaxy Clusters using the Millennium-XXL and MOKA simulations

Carlo Giocoli[1⋆], Mario Bonamigo[1], Marceau Limousin[1], Massimo Meneghetti[2,3], Lauro Moscardini[4,2,3], Raul E. Angulo[5], Giulia Despali[1,6], Eric Jullo[1]

[1] *Aix Marseille Université, CNRS, LAM (Laboratoire d'Astrophysique de Marseille) UMR 7326, 13388 Marseille, France*
[2] *INAF - Osservatorio Astronomico di Bologna, via Ranzani 1, 40127 Bologna, Italy*
[3] *INFN - Sezione di Bologna, viale Berti Pichat 6/2, 40127 Bologna, Italy*
[4] *Dipartimento di Fisica e Astronomia, Alma Mater Studiorum Università di Bologna, viale Berti Pichat, 6/2, 40127 Bologna, Italy*
[5] *Centro de Estudios de Física del Cosmos de Aragón (CEFCA), Plaza San Juan 1, Planta-2, 44001 Teruel, Spain*
[6] *Max Planck Institute for Astrophysics, Karl-Schwarzschild-Strasse 1, 85740 Garching, Germany*



July 12, 2016

**ABSTRACT**

In this paper we investigate the strong lensing statistics in galaxy clusters. We extract dark matter haloes from the Millennium-XXL simulation, compute their Einstein radius distribution, and find a very good agreement with Monte Carlo predictions produced with the MOKA code. The distribution of the Einstein radii is well described by a log-normal distribution, with a considerable fraction of the largest systems boosted by different projection effects. We discuss the importance of substructures and triaxiality in shaping the size of the critical lines for cluster size haloes. We then model and interpret the different deviations, accounting for the presence of a Bright Central Galaxy (BCG) and two different stellar mass density profiles. We present scaling relations between weak lensing quantities and the size of the Einstein radii. Finally we discuss how sensible is the distribution of the Einstein radii on the cosmological parameters $\Omega_M - \sigma_8$ finding that cosmologies with higher $\Omega_M$ and $\sigma_8$ possess a large sample of strong lensing clusters. The Einstein radius distribution may help distinguish Planck13 and WMAP7 cosmology at $3\sigma$.

**Key words:** Gravitational lensing: strong lensing – galaxy clusters; Numerical methods: simulations; Galaxies: clusters

## 1 INTRODUCTION

Spectroscopic galaxy redshift surveys and numerical $N$-body simulations have revealed a large-scale distribution of matter in the Universe featuring a complex network of interconnected filamentary galaxy associations (Tormen et al. 2004; Springel et al. 2005; The Dark Energy Survey Collaboration 2005; Sousbie et al. 2008, 2011; Guzzo et al. 2014; Percival et al. 2014; Le Fèvre et al. 2015; Codis et al. 2015). Vertices, i.e. interconnections among the filaments, correspond to the very dense compact nodes within this *cosmic web* where one can find massive galaxy clusters (Tormen 1998; Bryan & Norman 1998; Shaw et al. 2006; Borgani & Kravtsov 2011; Bellagamba et al. 2011).

The mass density distribution in clusters can be inferred using different wavelength observations (Meneghetti et al. 2010b; Donnarumma et al. 2011; Donahue et al. 2016). In particular, optical and near-infrared data provided by, for instance, the Subaru and the Hubble Space telescopes (HST) are allowing to indirectly infer the total projected matter density distribution in clusters through its effect of gravitationally bending the light of background galaxies (Jullo et al. 2007; Merten et al. 2015; Limousin et al. 2015). Gravitational lensing, as predicted by the Einstein's General Relativity, deflects light rays once they get close to a deep potential well (Einstein 1918; Landau & Lifshitz 1971). Light-rays from distant galaxies travelling in the space-time of our Universe can be weakly or strongly bent when they approach a galaxy cluster (Bartelmann & Schneider 2001; Bartelmann 2010). The weak lensing regime happens when the light-rays travel far from the centre of the cluster. In this case, the shapes of background galaxies are only slightly altered and, for a good determination of the signal, it is usually necessary to average over a large sample of background systems (Hoekstra et al. 2012, 2013; Giocoli et al. 2014; Radovich et al. 2015; Formicola et al. 2016). The strong lensing regime

⋆ E-mail: carlo.giocoli@lam.fr

takes place when the light-rays transit close to the centre of the cluster, and the mass density becomes critical: the lensing event in this case is non-linear and images of background galaxies may be multiplied and/or appear stretched and elongated. Depending on the quality of the data and on their availability, weak and strong lensing data can be used separately or jointly for a better reconstruction of the projected mass from the very central region to the outskirts of the cluster. In the following, we will concentrate on the strong lensing regime and on the objects that originate it, which we will refer to as Strong Lensing Clusters (SLCs).

SLCs may constitute a peculiar class of objects. While their existence is a natural consequence of General Relativity, "giant arcs" – extremely distorted images of background galaxies – hosted in clusters have been discovered only 30 years ago in the core of Abell 370, independently by Lynds & Petrosian (1986) and Soucail et al. (1987). This observation was recognised by Paczynski (1987) as the result of strong gravitational lensing, a hypothesis later confirmed by the measurement of the redshift of the arc (Soucail et al. 1988a,b).

Since then, SLCs have led to many important advances in cosmology: (*i*) being a direct and precise probe of the two-dimensional projected mass density, Strong Lensing (SL) has provided accurate mass maps, constraining structure formation properties and evolution scenarios (for example: Broadhurst et al. 2000; Sand et al. 2002; Saha & Williams 2006; Bradač et al. 2006; Zitrin et al. 2009a; Zitrin & Broadhurst 2009b; Newman et al. 2011; Verdugo et al. 2011; Sharon et al. 2014); (*ii*) producing a natural gravitational amplification, SL has allowed to push the frontier of our telescopes (for example: Richard et al. 2006; Coe et al. 2013; Atek et al. 2014; Zitrin et al. 2014); (*iii*) providing a method to probe the dark energy equation of state, since images position depends on the underling cosmology (for example: Soucail et al. 2004; Jullo et al. 2010).

SLCs are now well established as a promising class of objects that cannot be ignored in cosmology, and their future is extremely promising, since future facilities are expected to detect thousands of SLCs (Laureijs et al. 2011; Boldrin et al. 2012, 2016; Serjeant 2014), and the exquisite resolution of the *James Webb Space Telescope* (JWST) will deliver unique multi-colour data sets for some of them. The growing importance of SLCs has been recently illustrated by the CLASH program (Postman et al. 2012) which has been awarded of 500 HST orbits to observe 25 massive SLCs. More recently, the Hubble Deep Fields Initiative has unanimously recommended a "Frontier Field" program of six deep fields concentrated on SL clusters (together with six deep "blank fields") in order to advance our knowledge of the early epochs of galaxy formation and to eventually offer a glimpse of JWST's universe (http://www.stsci.edu/hst/campaigns/frontier-fields). Each cluster will be imaged with 140 orbits, leading to a total of 840 orbits dedicated to the Frontier Field Initiative.

Very encouraging is also the work performed by Zitrin et al. (2011c) on reconstructing the mass density distribution and the Einstein radius (which estimates the size of the SL region) of a large sample of SDSS clusters. In this case, the "blind' approach based on the assumption that light traces mass has allowed to establish that the Einstein radius distribution of clusters with $0.1 < z_l < 0.55$ has a log-normal shape. Furthermore, a visual inspection has revealed that approximately 20 percent of SLCs are boosted by various projection effects.

Given the significance of SLCs, characterising this peculiar class of object is crucial and this has been the focus of many studies (for example: Hennawi et al. 2007; Meneghetti et al. 2010a; Redlich et al. 2012; Waizmann et al. 2012). This is also the motivation of the present work, where we aim at characterising which clusters do generate strong lensing features. Our approach is twofold: (*i*) first we will use the large sample of cluster statistics afforded by the Millennium -XXL simulation (Angulo et al. 2012) – exploiting its large size (3 Gpc/$h$ box side), that allows to follows the formation of many massive haloes; (*ii*) second we will complement the statistics with a cosmological study based on clusters modelled using the MOKA code (Giocoli et al. 2012a).

We want to spend few words about the fact that the Einstein radius of lenses is not a direct observable quantity. The Einstein radius, defined by the location of the tangential critical lines (more will be discussed about this in the first section) is a byproduct of the mass reconstruction pipeline by mean of parametric algorithms that typically assume that mass traces the light (Jullo et al. 2007; Zitrin et al. 2011) or adaptively reconstruct the mass density distribution using non-parametric approaches (Merten 2014).

The paper is organised as follows: in Section 2 we present the numerical simulations and the pseudo-analytical methods we adopt as bases for our analyses; in Section 3 we discuss the scaling relations between the size of the Einstein radius and weak lensing-derived quantities; in Section 4 we present how the Einstein radius distribution depends on the matter content of the universe and on the initial normalisation of the power spectrum. Finally in Section 5 we summarise and discuss our results.

## 2 METHODS

In this paper we aim at studying the strong lensing properties of galaxy clusters – through the size of their Einstein radius – extracted from a very large cosmological box. However, the limitation of possessing the simulation only for one cosmological model in addition to the fact that the run has been performed only using collisionless dark matter particles forced us to complement the analyses using a pseudo-analytic approach to simulate convergence maps of triaxial clusters. This latter method allows us, in a more flexible way, to investigate which properties of clusters mainly contribute in shaping the Einstein radius, to quantify the contribution of the stellar component and to understand how the Einstein radius distribution of clusters may depend on specific cosmological parameters.

### 2.1 Strong lensing of Clusters in the Millennium-XXL Simulation

With a box side of 3 Gpc/$h$, the Millennium-XXL (M-XXL) simulation (Angulo et al. 2012) was especially tailored to study massive haloes which can be only found in very large volumes, because of their nature of extremely rare objects. The $6720^3 \sim 3 \times 10^{11}$ dark matter particles have a mass of $6.174 \times 10^9 M_\odot/h$; the Plummer-equivalent softening length

is $\epsilon = 13.7$ kpc. For reasons of consistency with the previous Millennium runs (Springel et al. 2005; Boylan-Kolchin et al. 2009), the adopted ΛCDM cosmology as the following parameters total matter density $\Omega_M = 0.25$, baryons density $\Omega_b = 0.045$, cosmological constant $\Omega_\Lambda = 0.75$, power spectrum normalisation $\sigma_8 = 0.9$ and dimensionless Hubble parameter in $H_0/100$ km$/s/$Mpc $h = 0.73$. We remind the reader that the simulated volume of the M-XXL is equivalent to the whole observable Universe up to redshift $z = 0.72$.

At each simulation snapshot, haloes have been identified using a FoF algorithm. For each FoF-group, starting from the particle with the minimum potential, we then compute $M_{200}$ as the mass enclosing a sphere 200 times denser than the critical density $\rho_c$ at that redshift. In our analysis – for the motivation we will underline later – we will consider the halo catalogue at $z = 1$ and the corresponding snapshot files. Due to the large number of haloes identified in the simulation volume we restrict our analysis only to the ones more massive than $3\times10^{14} M_\odot/h$ – corresponding to 3135 systems. For each halo respecting this criterion we store all the particles enclosed in a cube of $8\,\mathrm{Mpc}/h$ by side and project them in a 2D-mass map resolved with $2048 \times 2048$ pixels using the Triangular Shape Cloud technique, along six different directions. In the first three cases we consider three projections along the cartesian axes, which are then *random* with respect to the cluster morphology, we then consider three *peculiar projections* i.e. along the ellipsoid axes as computed in Bonamigo et al. (2015): major, intermediate and minor axes. In placing the particles on the grid, to avoid particle noise effects (Rau et al. 2013; Angulo et al. 2014) due to the discreteness of the dark matter density, we apply a Gaussian filter with a scale of 3.25 kpc$/h$, which corresponds to approximately one third of the simulation Plummer-equivalent softening.

From the constructed mass density maps $\Sigma(x_1, x_2)$ – where $x_1$ and $x_2$ are the two cartesian coordinates on the 2D map projected in the plane of the sky – we compute the convergence $\kappa(x_1, x_2)$ as:

$$\kappa(x_1, x_2) = \frac{\Sigma(x_1, x_2)}{\Sigma_{\rm crit}} \tag{1}$$

with

$$\Sigma_{\rm crit} \equiv \frac{c^2}{4\pi G}\frac{D_l}{D_s D_{ls}} \equiv \frac{c^2}{4\pi G}\frac{1}{D_{lens}} \tag{2}$$

where $c$ represents the speed of light and $G$ the universal gravitational constant; $D_l$, $D_s$ and $D_{ls}$ are the angular diameter distances between observer-lens, observer-source and source-lens, respectively; we also define the lensing distance $D_{lens} \equiv D_{ls}D_s/D_l$. We assume clusters to be located at $z_l = 0.5$ and sources at $z_s = 2.5$, computing the distances assuming the cosmological parameters in agreement with the Planck13 results (Planck Collaboration et al. 2014): the matter density parameter $\Omega_M = 0.307$, the contribution of Λ $\Omega_\Lambda = 0.693$, the normalised Hubble constant $h = 0.6777$ and the normalisation of the initial power spectrum $\sigma_8 = 0.829$. We do so because, even if the M-XXL simulation has been run with a different set of cosmological parameters, we assume to be able to rescale those clusters at $z = 1$ from a M-XXL cosmology to a sample at $z = 0.5$ in a Planck13 cosmology. This is supported by the fact that the halo properties at $z = 1$ in the M-XXL cosmology are very similar to those at $z = 0.5$ in a Planck13 cosmology (Sheth & Tormen 1999; Macciò et al. 2008; Zhao et al. 2009; Giocoli et al. 2012b; Despali et al. 2015); even if the two mass functions for haloes more massive than $3 \times 10^{14} M_\odot/h$ may be different by more than 50%, the two concentration-mass relations deviate by less than 5%.

From the convergence we can define the effective lensing potential as:

$$\Phi(x_1, x_2) \equiv \frac{1}{\pi}\int \kappa(\mathbf{x}') \ln|\mathbf{x} - \mathbf{x}'| \mathrm{d}^2\mathbf{x}', \tag{3}$$

with $\mathbf{x} \equiv (x_1, x_2)$, and then the pseudo-vector field of the shear $\gamma = \gamma_1 + i\gamma_2$ as:

$$\gamma_1(x_1, x_2) = \frac{1}{2}\left(\Phi_{11} - \Phi_{22}\right), \tag{4}$$

$$\gamma_2(x_1, x_2) = \Phi_{12} = \Phi_{21} \tag{5}$$

with $\Phi_{ij}$ representing the $i$ and $j$ derivatives of the effective lensing potential (Bartelmann & Schneider 2001; Bacon et al. 2010). At first order, gravitational lensing induces distortion and stretch on background sources: typically a circular source is mapped through gravitational lensing into an ellipse when both $k$ and $\gamma$ are different from zero. These effects are described by the Jacobian matrix:

$$A = \begin{pmatrix} 1-\kappa-\gamma_1 & -\gamma_2 \\ -\gamma_2 & 1-\kappa+\gamma_1 \end{pmatrix}. \tag{6}$$

The magnification is quantified as the inverse determinant of the Jacobian matrix that can be read as:

$$\mu \equiv \frac{1}{\det A} = \frac{1}{(1-\kappa)^2 - \gamma^2}; \tag{7}$$

the inverse of the eigenvalues of the Jacobian matrix measure the amplification in radial and tangential direction of background sources:

$$\mu_r = \frac{1}{1-\kappa+\gamma} \tag{8}$$

$$\mu_t = \frac{1}{1-\kappa-\gamma}. \tag{9}$$

For circularly symmetric lenses, the regions in the image plane where the denominator of the relations above is equal to zero define where the source images are infinitely radially and tangentially magnified, respectively. In particular images forming close to the tangential critical curve are strongly distorted tangentially to it.

The definition of critical curves is more complex and non trivial in asymmetric, substructured and triaxial clusters. From each convergence map the lensing potential and the shear are numerically computed in Fourier space [1] where derivatives are easily and efficiently calculated. To avoid artificial boundary effects each map is enclosed in a zero-padded region of 1024 pixels. We have tested the impact of the size of the zero-padded regions on the weak and strong lensing properties of individual non-periodic cluster maps and find that artefact mirror clusters do not appear when the size of the zero region is at least half of the considered field of view. To define the Einstein radius of the cluster we identify in the cluster maps points of infinite tangential



[1] using the FFTW libraries: http://www.fftw.org

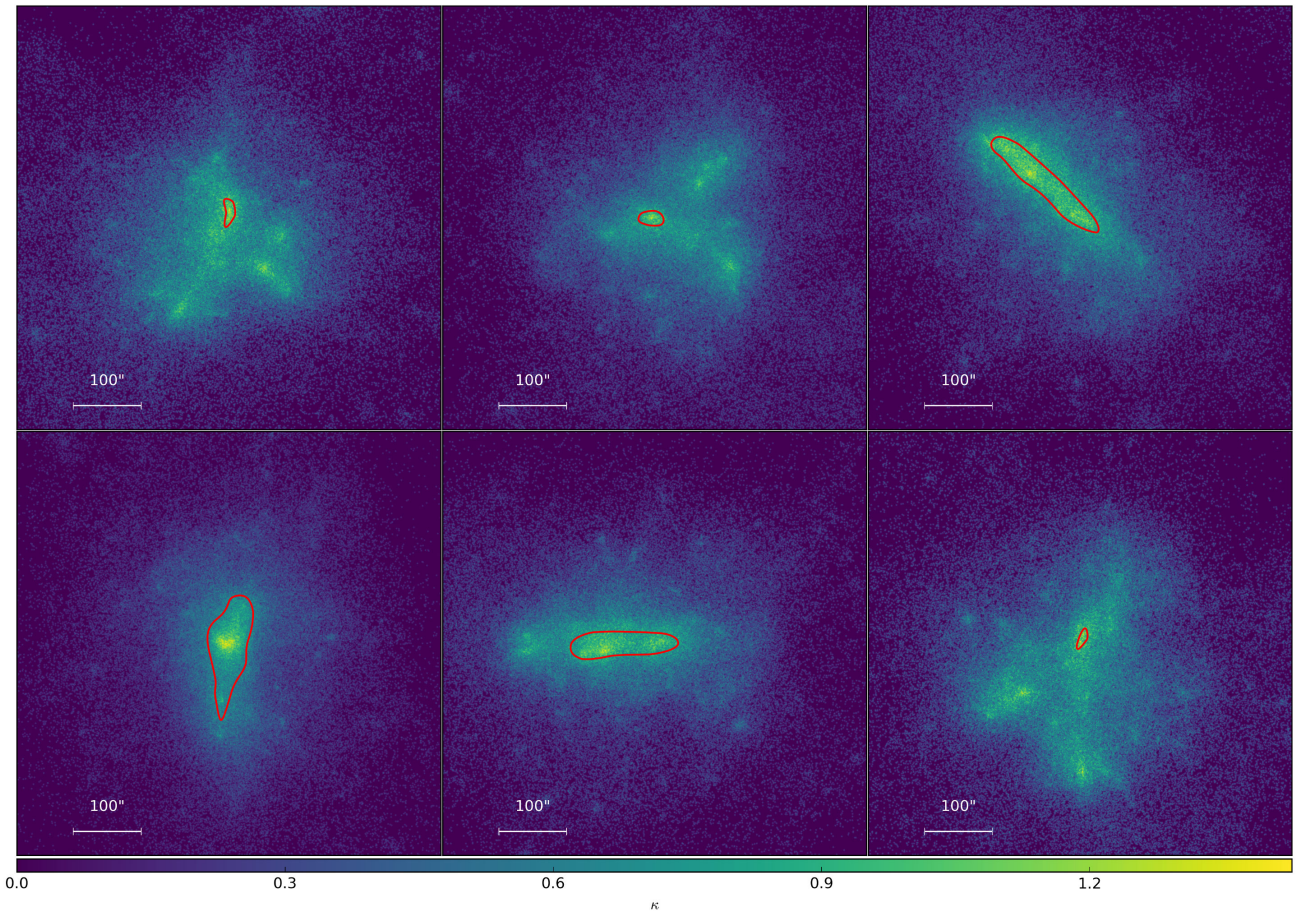


**Figure 1.** Convergence maps of different projections of a halo extracted from the Millennium-XXL simulation with mass $M_{200} = 1.2 \times 10^{15} M_{\odot}/h$. The red curves in each panel represent the tangential critical lines from which we compute the median Einstein radii. The top-three images show the three projections along the cartesian axes (i.e. *random* with respect to the cluster morphology), while the bottom ones from left to right, are the projections along the major, intermediate and minor axes, respectively. This particular cluster has the peculiarity of having in one projection (namely the one in the left bottom panel) the largest Einstein radius in our sample: 75 arcsec.

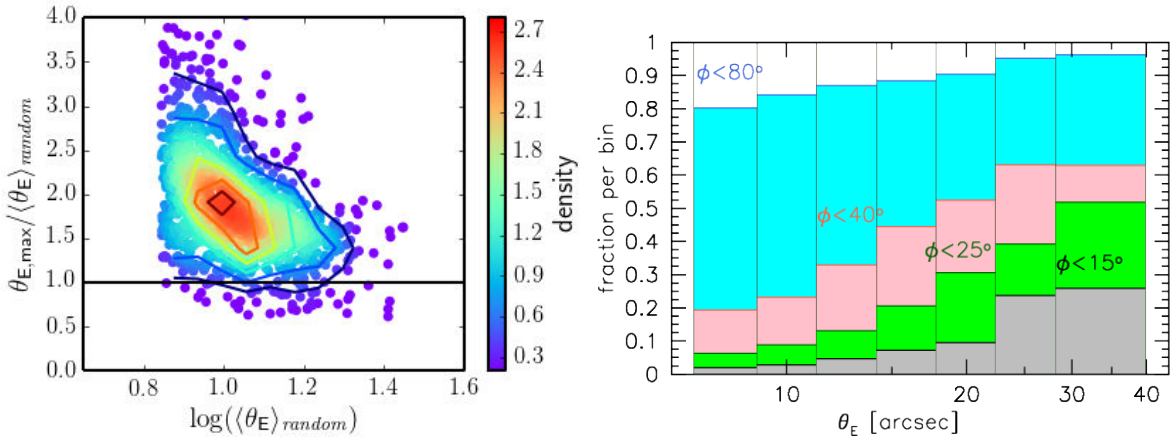


**Figure 2.** Left panel: scatter plots of the relative size of the Einstein radii when the cluster major axis of the ellipsoid is oriented along the line-of-sight with compared to the average value of the three *random* projections: $\langle\theta_E\rangle_{random}$. Right panel: Fraction i of clusters with an angle $\phi$ between the direction of the major axis of the mass ellipsoid and the line-of-sight smaller than 80°, 40°, 25° and 10° as a function of the Einstein radius.

**Table 1.** Percentage of the projections along which M-XXL clusters have the largest Einstein radius for the *random* and the *peculiar* projections, respectively.

| projection | % (*random*) |
|---|---|
| $x$ | 34% |
| $y$ | 32% |
| $z$ | 34% |
| **projection** | **% (*peculiar*)** |
| major axis of the ellipsoid | 86% |
| intermediate | 12% |
| minor | 2% |

magnification $\theta_t$ and define the Einstein radius $\theta_E$ as the median distance of these points from the cluster centre:

$$\theta_E \equiv \mathrm{med}\left\{ \sqrt{(\theta_{i,x_1} - \theta_{c,x_1})^2 + (\theta_{i,x_2} - \theta_{c,x_2})^2} \mid \theta_i \in \theta_t \right\} . \quad (10)$$

We define the center of the cluster $\theta_c$ as the position of the particle with minimum potential and the connected region defined by the tangential critical points $\theta_t$, when they exist, have to enclose the cluster centre; this ensures that the critical points are not eventually assigned to a substructure present in the field of view. The robustness of this definition has already been tested and discussed in a series of works (Meneghetti et al. 2008, 2010a; Redlich et al. 2012; Giocoli et al. 2014) to which we remind the reader for more details. The size of the Einstein radius defines a measure of the strong lensing region and, for an axially symmetric lens, permits to estimate the mass enclosed within it using the equation:

$$\theta_E = \left( \frac{4GM(<\theta_E)}{c^2} \frac{D_{ls}}{D_l D_s} \right)^{1/2} \quad (11)$$

assuming that all mass is located at the centre of the lens. By geometrically measuring the area $A$ enclosed by the tangential critical curve it is possible to define the effective Einstein radius as $\theta_{E,eff} = \sqrt{A/\pi}$. However, we will rely on the median Einstein radius definition that – as noticed by Meneghetti et al. (2011) and Giocoli et al. (2014) – better captures the presence of asymmetries of the matter distribution towards the cluster centre.

In Figure 1 we show the six considered projections of the halo which in one them has the largest Einstein radius (75 arcsec) in our constructed catalogue – namely in the bottom left panel. The top panels show the $x$, $y$ and $z$ projections, while the bottom ones the projections along the major, intermediate and minor axis of the halo ellipsoid, from left to right respectively. In each panel, the red curves represent the tangential critical curves, i.e. where images of background galaxies would appear highly tangentially magnified if located close to the optical axis of the lens system. From the figure we notice that the largest Einstein radius occurs, in this case – as in most of the cases, when the major axis of the cluster ellipsoid is oriented along the line-of-sight; the opposite holds when the minor axis points towards the observer. From the measured Einstein radius of each of the six projections of all clusters in the M-XXL we can summarise (as it can be read in Table 1) that in the *random projections* the probability of having the largest Einstein radius is uniform in the three cases as expected. However, considering the *peculiar projections*, sample we notice that in 86% of the cases the largest Einstein radius appears when the major axis of the ellipsoid is oriented along the line-of-sight and in 12% (2%) of the cases when the orientation is the intermediate (minor) axis. We have investigated those latter cases and they arise either ($i$) when there is a merging event which manifests in the presence of a massive substructure projected in correspondence of the cluster centre and/or ($ii$) when the cluster ellipsoid is very elongated in the plane of the sky.

In the left panel of Figure 2 we quantify by how much the Einstein radius grows when the cluster is oriented along the major axis of its mass ellipsoid. We consider all clusters having at least an Einstein radius of 7 arcsec along one of the considered projections[2]. In this case we compare the size of the Einstein radius computed when the cluster is oriented along the major axis with respect to the average value measured from its three *random projections*. From the figure we observe that the typical size of an Einstein radius may grow up to a factor of two/three when the cluster is aligned along the line of sight with respect to a random orientation; we also notice some cases where the Einstein radius computed in a *random projection* is larger than the value measured when the mass ellipsoid is oriented along the line-of-sight; as discussed previously we verified that those cases are merging clusters or very elongated ellipsoids in the plane of the sky. All this brings more light to the general picture that most of the strong lensing clusters may possess their dark matter halo major axis preferentially pointing close to the line-of-sight (Oguri & Blandford 2009). This is more evident in the right panel of the same figure where we show the fraction of SLCs per different bins in $\theta_E$ that possess an angle $\phi$ between the major axis of the ellipsoid and the line-of-sight smaller than a given value: 65% of SLCs with $30 < \theta_E < 40$ have an angle $\phi$ between the direction of their major axis and the line-of-sight smaller than 40 degrees. Our finding are quite consistent with the results presented by Oguri et al. (2005) where the authors also discuss that the apparent steep observed mass profile can be reconciled with theoretical models if the triaxial ellipsoid of the dark matter halo is preferentially oriented with the major axis along the line-of-sight.

However, when looking at random projections in the plane of the sky, the sole effect of triaxiality is less obvious. Figure 3 shows the difference that might arise in the distribution of shapes – namely minor to major axis ratio $s$ – by selecting clusters that are strong lenses (blue histograms) instead of the general population (black histograms). Haloes have been subdivided in bins of Einstein radius $\theta_E$, each shown in a different panel. Even though, as previously found by Hennawi et al. (2007), the distribution of the axis ratio of SLCs does not seem to differ from the distribution of the overall population, the mean values (vertical dashed lines) vary up to 5%, in particular for very large $\theta_E$. A Kolmogorov-Smirnov test showed that we can reject the hypothesis that the samples are taken from the same distri-

[2] The value of 7 arcsec ensures that the measurement of the size of the Einstein radius of the cluster is not affected nor by particle noise neither by the finite grid size of the map.

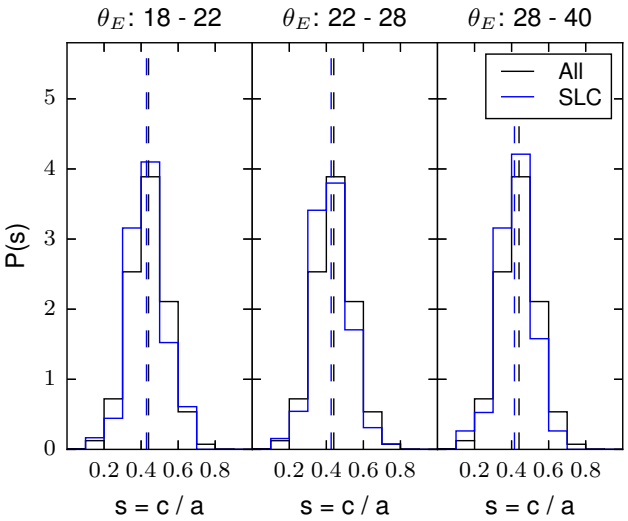


**Figure 3.** Probability distribution functions of the minor to major axis ratio of the overall M-XXL cluster population (black histogram) and of the SLCs (blue histogram), with each panel representing a different bin in $\theta_E$. Vertical dashed lines indicate the mean of the corresponding sample.

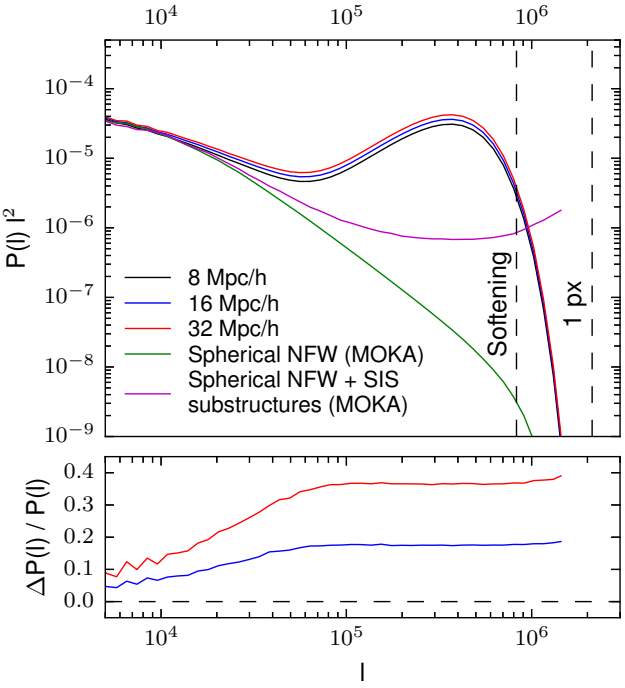


**Figure 4.** Average convergence power spectrum of haloes of the M-XXL simulation. Black, blue and red curve show the average power spectrum derived extracting the particles contained in a region of 8, 16 and 32 Mpc/$h$ along the line-of-sight; in the plane of the sky in all three cases we have considered particles in a square of 8 Mpc/$h$ of side. The green curve shows the prediction from smooth NFW spherical haloes, while the purple one presents the prediction for spherical MOKA haloes with substructures modelled with a Singular Isothermal Sphere (SIS) profile. The bottom panel shows the relative residuals of the average power spectra measured using 16 and 32 Mpc/$h$ with respect to the one computed assuming 8 Mpc/$h$ as box side along the line-of-sight.

bution at significance level of 10%, meaning that there is a low probability that SLC have the same shape properties of the overall population. This suggests that the concentration is mainly responsible in driving the correlation of the cluster Einstein radii.

It is important to underline that the effect of correlated and uncorrelated large scale structures may also impact the lensing properties of galaxy clusters and boost their strong lensing cross section as well as the size of the Einstein radius (Puchwein & Hilbert 2009). Usually to quantify the impact of uncorrelated structures along the line-of-sight it is necessary to run expensive multi-plane ray-tracing lensing simulations of clusters and matter extracted from cosmological runs (Hilbert et al. 2008; Petkova et al. 2014; Giocoli et al. 2015), things that are beyond the purpose of this paper. However the effect of correlated structures on the lensing properties can be studied selecting for each cluster projection a larger region along the line-of-sight, and quantify how these changes on the determination of the Einstein radius. To do so, we have produced two other sets of convergence maps, one selecting particles from a region of 16 Mpc/$h$ and another from 32 Mpc/$h$ along the line-of-sight, and projecting all of them into a single lens plane. We still keep the size of the region in the plane of the sky to be 8 Mcp/$h$ of a side. As an example, in Figure 4 we show the average convergence power spectra of the *random projections* sample considering a region of 8, 16 and 32 Mpc/$h$ along the line-of-sight in black, blue and red, respectively. In the bottom panel we present the relative residuals of the last two cases with respect to the 8 Mpc/$h$ reference one. We notice that the inclusion of more matter along the line-of-sight tends to increase the convergence power spectrum at small scales of about 20 percent for 16 Mpc/$h$ and almost 40 percent for 32 Mpc/$h$, which however contains 4 times the volume. In the figure we show also for comparison the prediction from a smooth NFW halo (green curve) and the power spectrum of a spherical halo (with the same large scale normalisation) with substructures (in magenta): both curves are obtained by averaging produced using MOKA haloes (see below), with the same masses and NFW concentrations of the M-XXL sample. In this case we observe that the presence of substructures in a halo tends to increase the small scale power of more than one order of magnitude for $l \gtrsim 3 \times 10^4$ with respect to a smooth case. The other interesting behaviour is that while the power spectrum of haloes extracted from the M-XXL are characterised at small scales by the particle noise and finite grid size of the maps (Vale & White 2003), MOKA haloes are particle noise-free and the only numerical limitation at small scale is set by the desired grid size of the map.

Puchwein & Hilbert (2009) have shown that the presence of uncorrelated structures tends to boost both the strong lensing cross-section for giant arcs and the size of the Einstein radii. As discussed, an accurate description of the contribution of uncorrelated large-scale structures needs expensive multi-plane ray-tracing simulations and is beyond the purpose of this paper. However in order to give a hint on how much the Einstein radii change including more matter along the line-of-sight, in Figure 5 we show the relative size of the Einstein radius – with respect to the case in which we select a region of 8 Mpc/$h$ along the line-of-sight – computed selecting a region of 16 Mpc/$h$ (left) and 32 Mpc/$h$

the unique results that will be available from the next-generation wide field surveys from space.

## ACKNOWLEDGMENTS

CG thanks CNES for financial support. ML acknowledges the Centre National de la Recherche Scientifique (CNRS) for its support. This work was performed using facilities offered by CeSAM (Centre de donneS Astrophysique de Marseille-(http://lam.oamp.fr/cesam/). This work was granted access to the HPC resources of Aix-Marseille Universite financed by the project Equip@Meso (ANR-10-EQPX-29-01) of the program "Investissements d'Avenir" supervised by the Agence Nationale pour la Recherche (ANR). This work was carried out with support of the OCEVU Labex (ANR- 11-LABX-0060) and the A*MIDEX project (ANR-11-IDEX-0001-02) funded by the "Investissements d'Avenir" French government program managed by the ANR. We acknowledge support from the Programme National de Cosmologie et Galaxie (PNCG). MM acknowledges support from Ministry of Foreign Affairs and International Cooperation, Directorate General for Country Promotion, from INAF via PRIN-INAF 2014 1.05.01.94.02, and from ASI via contract ASI/INAF/I/023/12/0. LM acknowledges the grants ASI n.I/023/12/0 "Attività relative alla fase B2/C per la missione Euclid", MIUR PRIN 2010-2011 "The dark Universe and the cosmic evolution of baryons: from current surveys to Euclid" and PRIN INAF 2012 "The Universe in the box: multiscale simulations of cosmic structure". REA acknowledges support from AYA2015-66211-C2-2. EJ acknowledge CNES support. CG thanks Mauro Sereno, Jesus Vega and Michele Boldrin for useful discussions and python stratagems. We also thank Giuseppe Tormen and Vincenzo Mezzalira for giving us the possibility to use their computer facilities on which part of the MOKA simulations have been run.

This paper has been typeset from a TEX/ LATEX file prepared by the author.

## References

Angulo R. E., Chen R., Hilbert S., Abel T., 2014, MNRAS, 444, 2925

Angulo R. E., Springel V., White S. D. M., Jenkins a., Baugh C. M., Frenk C. S., 2012, MNRAS, 426, 2046

Atek H., Richard J., Kneib J.-P., Clement B., Egami E., Ebeling H., Jauzac M., Jullo E., Laporte N., Limousin M., Natarajan P., 2014, ApJ, 786, 60

Bacon D. J., Amara A., Read J. I., 2010, MNRAS, 409, 389

Bartelmann M., 2010, Classical and Quantum Gravity, 27, 233001

Bartelmann M., Schneider P., 2001, Physics Reports, 340, 291

Bellagamba F., Maturi M., Hamana T., Meneghetti M., Miyazaki S., Moscardini L., 2011, MNRAS, 413, 1145

Blumenthal G. R., Faber S. M., Flores R., Primack J. R., 1986, ApJ, 301, 27

Boldrin M., Giocoli C., Meneghetti M., Moscardini L., 2012, MNRAS, 427, 3134

Boldrin M., Giocoli C., Meneghetti M., Moscardini L., Tormen G., Biviano A., 2016, MNRAS, 457, 2738

Bonamigo M., Despali G., Limousin M., Angulo R., Giocoli C., Soucail G., 2015, MNRAS, 449, 3171

Borgani S., Kravtsov A., 2011, Advanced Science Letters, 4, 204

Boylan-Kolchin M., Springel V., White S. D. M., Jenkins A., Lemson G., 2009, MNRAS, 398, 1150

Bradač M., Clowe D., Gonzalez A. H., Marshall P., Forman W., Jones C., Markevitch M., Randall S., Schrabback T., Zaritsky D., 2006, ApJ, 652, 937

Broadhurst T., Huang X., Frye B., Ellis R., 2000, ApJ, 534, L15

Bryan G. L., Norman M. L., 1998, ApJ, 495, 80

Choi J.-H., Weinberg M. D., Katz N., 2007, MNRAS, 381, 987

Codis S., Pichon C., Pogosyan D., 2015, MNRAS, 452, 3369

Coe D., Zitrin A., Carrasco M., Shu X., Zheng W., Postman M., Bradley L., Koekemoer et al. 2013, ApJ, 762, 32

Cooray A., Sheth R., 2002, Physics Reports, 372, 1

De Lucia G., Kauffmann G., Springel V., White S. D. M., Lanzoni B., Stoehr F., Tormen G., Yoshida N., 2004, MNRAS, 348, 333

Despali G., Giocoli C., Angulo R. E., Tormen G., Sheth R. K., Baso G., Moscardini L., 2015, ArXiv e-prints

Despali G., Giocoli C., Tormen G., 2014, MNRAS, 443, 3208

Donahue M., Ettori S., Rasia E., Sayers J., Zitrin A., Meneghetti M., Voit G. M., Golwala S., Czakon N., Yepes G., Baldi A., Koekemoer A., Postman M., 2016, ApJ, 819, 36

Donnarumma A., Ettori S., Meneghetti M., Gavazzi R., Fort B., Moscardini L., Romano A., Fu L., Giordano F., Radovich M., Maoli R., Scaramella R., Richard J., 2011, A&A, 528, A73

Einstein A., 1918, Sitzungsberichte der Königlich Preußischen Akademie der Wissenschaften (Berlin), Seite 448-459.

Eke V. R., Cole S., Frenk C. S., 1996, MNRAS, 282, 263

Formicola I., Radovich M., Meneghetti M., Mazzotta P., Grado A., Giocoli C., 2016, MNRAS

Gao L., White S. D. M., Jenkins A., Stoehr F., Springel V., 2004, MNRAS, 355, 819

Giocoli C., Jullo E., Metcalf R. B., de la Torre S., Yepes G., Prada F., Comparat J., Goettlober S., Kyplin A., Kneib J.-P., Petkova M., Shan H., Tessore N., 2015, ArXiv e-prints

Giocoli C., Meneghetti M., Bartelmann M., Moscardini L., Boldrin M., 2012a, MNRAS, 421, 3343

Giocoli C., Meneghetti M., Metcalf R. B., Ettori S., Moscardini L., 2014, MNRAS, 440, 1899

Giocoli C., Tormen G., Sheth R. K., 2012b, MNRAS, 422, 185

Giocoli C., Tormen G., Sheth R. K., van den Bosch F. C., 2010a, MNRAS, 404, 502

Giocoli C., Tormen G., van den Bosch F. C., 2008, MNRAS, 386, 2135

Gnedin O. Y., Ceverino D., Gnedin N. Y., Klypin A. A., Kravtsov A. V., Levine R., Nagai D., Yepes G., 2011, ArXiv e-prints

Guzzo L., Scodeggio M., Garilli B., Granett B. R., Fritz A., Abbas U., Adami C., Arnouts et al. 2014, A&A, 566, A108
Hayashi E., Navarro J. F., Taylor J. E., Stadel J., Quinn T., 2003, ApJ, 584, 541
Hennawi J. F., Dalal N., Bode P., Ostriker J. P., 2007, ApJ, 654, 714
Hernquist L., 1990, ApJ, 356, 359
Hilbert S., White S. D. M., Hartlap J., Schneider P., 2008, MNRAS, 386, 1845
Hoekstra H., Bartelmann M., Dahle H., Israel H., Limousin M., Meneghetti M., 2013, Space Sci.Rev., 177, 75
Hoekstra H., Mahdavi A., Babul A., Bildfell C., 2012, MNRAS, 427, 1298
Jaffe W., 1983, MNRAS, 202, 995
Jing Y. P., Suto Y., 2002, ApJ, 574, 538
Jullo E., Kneib J.-P., Limousin M., Elíasdóttir Á., Marshall P. J., Verdugo T., 2007, New Journal of Physics, 9, 447
Jullo E., Natarajan P., Kneib J.-P., D'Aloisio A., Limousin M., Richard J., Schimd C., 2010, Science, 329, 924
Katayama H., Hayashida K., Takahara F., Fujita Y., 2003, ApJ, 585, 687
Keeton C. R., 2001, ApJ, 561, 46
Keeton C. R., 2003, ApJ, 584, 664
Koopmans L. V. E., Bolton A., Treu T., Czoske O., Auger M. W., Barnabè M., Vegetti S., Gavazzi R., Moustakas L. A., Burles S., 2009, ApJ, 703, L51
Koopmans L. V. E., Treu T., Bolton A. S., Burles S., Moustakas L. A., 2006, ApJ, 649, 599
Landau L. D., Lifshitz E. M., 1971, The classical theory of fields
Laureijs R., Amiaux J., Arduini S., Augueres J. ., Brinchmann J., Cole R., Cropper M., Dabin C., Duvet L., et al. 2011, arXiv:1110.3193
Le Fèvre O., Tasca L. A. M., Cassata P., Garilli B., Le Brun V., Maccagni D., Pentericci L., Thomas et al. 2015, A&A, 576, A79
Limousin M., Richard J., Jullo E., Jauzac M., Ebeling H., Bonamigo M., Alavi A., Clement B., Giocoli C., Kneib J. P., Verdugo T., Natarajan P., Siana B., 2015, ArXiv e-prints
Lynds R., Petrosian V., 1986, in Bulletin of the American Astronomical Society Vol. 18 of BAAS, Giant Luminous Arcs in Galaxy Clusters. p. 1014
Macciò A. V., Dutton A. A., van den Bosch F. C., 2008, MNRAS, 391, 1940
Meneghetti M., Bartelmann M., Moscardini L., 2003, MNRAS, 346, 67
Meneghetti M., Fedeli C., Pace F., Gottlöber S., Yepes G., 2010a, A&A, 519, A90
Meneghetti M., Fedeli C., Zitrin A., Bartelmann M., Broadhurst T., Gottlöber S., Moscardini L., Yepes G., 2011, A&A, 530, A17
Meneghetti M., Melchior P., Grazian A., De Lucia G., Dolag K., Bartelmann M., Heymans C., Moscardini L., Radovich M., 2008, A&A, 482, 403
Meneghetti M., Rasia E., Merten J., Bellagamba F., Ettori S., Mazzotta P., Dolag K., Marri S., 2010b, A&A, 514, A93+
Merritt D., 1985, ApJ, 289, 18
Merten J., 2014, ArXiv e-prints
Merten J., Meneghetti M., Postman M., Umetsu K., Zitrin A., Medezinski E., Nonino M., Koekemoer A., Melchior P., Gruen D., et al. 2015, ApJ, 806, 4
Metcalf R. B., Madau P., 2001, MNRAS, 563, 9
More A., Cabanac R., More S., Alard C., Limousin M., Kneib J.-P., Gavazzi R., Motta V., 2012, ApJ, 749, 38
Navarro J. F., Frenk C. S., White S. D. M., 1996, ApJ, 462, 563
Navarro J. F., Frenk C. S., White S. D. M., 1997, ApJ, 490, 493
Newman A. B., Treu T., Ellis R. S., Sand D. J., 2011, ApJ, 728, L39+
Oguri M., Blandford R. D., 2009, MNRAS, 392, 930
Oguri M., Takada M., Umetsu K., Broadhurst T., 2005, ApJ, 632, 841
Paczynski B., 1987, Nature, 325, 572
Percival W. J., Ross A. J., Sánchez A. G., Samushia L., Burden A., Crittenden R., Cuesta A. J., et al. 2014, MNRAS, 439, 2531
Petkova M., Metcalf R. B., Giocoli C., 2014, MNRAS, 445, 1954
Planck Collaboration Ade P. A. R., Aghanim N., Alves M. I. R., Armitage-Caplan C., Arnaud M., Ashdown M., Atrio-Barandela F., Aumont J., Aussel H., et al. 2014, A&A, 571, A1
Postman M., Coe D., Benítez N., Bradley L., Broadhurst T., Donahue M., Ford H., Graur et al. 2012, ApJS, 199, 25
Puchwein E., Hilbert S., 2009, MNRAS, 398, 1298
Radovich M., Formicola I., Meneghetti M., Bartalucci I., Bourdin H., Mazzotta P., Moscardini L., Ettori S., Arnaud M., Pratt G. W., Aghanim N., Dahle H., Douspis M., Pointecouteau E., Grado A., 2015, A&A, 579, A7
Rau S., Vegetti S., White S. D. M., 2013, MNRAS, 430, 2232
Redlich M., Bartelmann M., Waizmann J.-C., Fedeli C., 2012, A&A, 547, A66
Richard J., Pelló R., Schaerer D., Le Borgne J.-F., Kneib J.-P., 2006, A&A, 456, 861
Rozo E., Wechsler R. H., Rykoff E. S., Annis J. T., Becker M. R., Evrard A. E., Frieman J. A., Hansen et al. 2010, ApJ, 708, 645
Saha P., Williams L. L. R., 2006, ApJ, 653, 936
Sand D. J., Treu T., Ellis R. S., 2002, ApJ, 574, L129
Sanderson A. J. R., Edge A. C., Smith G. P., 2009, MNRAS, 398, 1698
Sartoris B., Biviano A., Fedeli C., Bartlett J. G., Borgani S., Costanzi M., Giocoli C., Moscardini L., Weller J., Ascaso B., Bardelli S., Maurogordato S., Viana P. T. P., 2015, arXiv:1505.02165
Serjeant S., 2014, ApJ, 793, L10
Sharon K., Gladders M. D., Rigby J. R., Wuyts E., Bayliss M. B., Johnson T. L., Florian M. K., Dahle H., 2014, ApJ, 795, 50
Shaw L. D., Weller J., Ostriker J. P., Bode P., 2006, ApJ, 646, 815
Sheth R. K., Tormen G., 1999, MNRAS, 308, 119
Soucail G., Fort B., Mellier Y., Picat J. P., 1987, A&A, 172, L14
Soucail G., Kneib J.-P., Golse G., 2004, A&A, 417, L33
Soucail G., Mellier Y., Fort B., Cailloux M., 1988b, A&AS, 73, 471
Soucail G., Mellier Y., Fort B., Mathez G., Cailloux M.,

1988a, A&A, 191, L19
Sousbie T., Pichon C., Colombi S., Novikov D., Pogosyan D., 2008, MNRAS, 383, 1655
Sousbie T., Pichon C., Kawahara H., 2011, MNRAS, 414, 384
Springel V., White S. D. M., Jenkins A., Frenk C. S., Yoshida N., Gao L., Navarro J., Thacker R., Croton D., Helly J., Peacock J. A., Cole S., Thomas P., Couchman H., Evrard A., Colberg J., Pearce F., 2005, Nature, 435, 629
Springel V., White S. D. M., Tormen G., Kauffmann G., 2001b, MNRAS, 328, 726
The Dark Energy Survey Collaboration 2005, ArXiv Astrophysics e-prints
Tormen G., 1998, MNRAS, 297, 648
Tormen G., Moscardini L., Yoshida N., 2004, MNRAS, 350, 1397
Vale C., White M., 2003, ApJ, 592, 699
van den Bosch F. C., Tormen G., Giocoli C., 2005, MNRAS, 359, 1029
Verdugo T., Motta V., Muñoz R. P., Limousin M., Cabanac R., Richard J., 2011, A&A, 527, A124
von der Linden A., Allen M. T., Applegate D. E., Kelly P. L., Allen S. W., Ebeling H., Burchat P. R., Burke D. L., Donovan D., Morris R. G., Blandford R., Erben T., Mantz A., 2014, MNRAS, 439, 2
Waizmann J.-C., Redlich M., Bartelmann M., 2012, A&A, 547, A67
Waizmann J.-C., Redlich M., Meneghetti M., Bartelmann M., 2014, A&A, 565, A28
Wang L., Li C., Kauffmann G., De Lucia G., 2006, MNRAS, 371, 537
Wu X.-P., Fang L.-Z., Xu W., 1998, A&A, 338, 813
Xu B., Postman M., Meneghetti M., Seitz S., Zitrin A., Merten J., Maoz D., Frye B., Umetsu K., Zheng W., Bradley L., Vega J., Koekemoer A., 2015, ArXiv e-prints
Zhang Y., Miller C., McKay T., Rooney P., Evrard A. E., Romer A. K., Perfecto R., Song J., et al. 2016, ApJ, 816, 98
Zhao D. H., Jing Y. P., Mo H. J., Bnörner G., 2009, ApJ, 707, 354
Zitrin A., Broadhurst T., 2009b, ApJ, 703, L132
Zitrin A., Broadhurst T., Barkana R., Rephaeli Y., Benítez N., 2011, MNRAS, 410, 1939
Zitrin A., Broadhurst T., Bartelmann M., Rephaeli Y., Oguri M., Benítez N., Hao J., Umetsu K., 2011c, ArXiv e-prints
Zitrin A., Broadhurst T., Umetsu K., Coe D., Benítez N., Ascaso B., Bradley L., Ford H., Jee J., Medezinski E., Rephaeli Y., Zheng W., 2009a, MNRAS, 396, 1985
Zitrin A., Zheng W., Broadhurst T., Moustakas J., Lam D., Shu X., Huang X., Diego J. M., Ford H., Lim J., Bauer F. E., Infante L., Kelson D. D., Molino A., 2014, ApJ, 793, L12

# 4. A Bayesian framework for multi-wavelength galaxy clusters

In the literature, there are two different, and complementary, approaches which have been developed and applied to lensing, X-Ray and SZ data within a full triaxial framework. One is described in A. Morandi and M. Limousin, (2012), the other in Sereno, Ettori, et al., (2012). While the former focuses on strong lensing and X-Ray to study the inner regions of a cluster, the latter exploits weak lensing and SZ to model the halo on a larger scale; however both algorithms can (and do) use all available observables. The main difference between the two codes is in how they compute the projected quantities: the algorithm presented in Sereno, Ettori, et al., (2012) leverages the symmetries of the problem to express analytically the integrals along the line of sight, while the approach of A. Morandi and M. Limousin, (2012) is to compute values on a grid and then project it on the plane of the sky. A grid-based code is much slower than an analytical evaluation of the integrals; however the advantage is that it allows for an arbitrary complex (and even multi-object) model as it does not rely on any simplifying assumption. Nevertheless, in the current implementation A. Morandi and M. Limousin, (2012) assumes the intra-cluster medium (ICM) to be in hydrostatical equilibrium, while the method of Sereno, Ettori, et al., (2012) can be used to test this hypothesis. When applied to the same cluster, the two codes give comparable results (M. Limousin, A. Morandi, et al., 2013). These approaches have never been tested on mock data sets. We are therefore unaware of the possible bias of the algorithms.

In this chapter, we present a new algorithm, based on the works published by Andrea Morandi and collaborators (A. Morandi, K. Pedersen, et al., 2010; A. Morandi, K. Pedersen, et al., 2011a; A. Morandi, M. Limousin, Rephaeli, et al., 2011b; A. Morandi and M. Limousin, 2012; A. Morandi, M. Limousin, Sayers, et al., 2011), which combines consistently lensing and X-ray (with the possibility of adding SZ data) within a triaxial framework. However, on the technical point of view, the algorithm is different from the one used in A. Morandi and M. Limousin, (2012). Although the original code has been successfully applied to a four observed clusters of galaxies (Fig. 4.1), and it has shown that the triaxial model reduces tensions between observations and theoretical predictions; it has never been tested on simulated data. In this work, we test the new version of the algorithm on mock data sets in order to characterise its behaviour. We have also made the source code available to the community under a free license (MIT) at https://bitbucket.org/marioaieie/mcclusters.

This chapter is organised as follows. In Section 4.1, we present the physical model currently implemented in the code, giving explicitly the equations

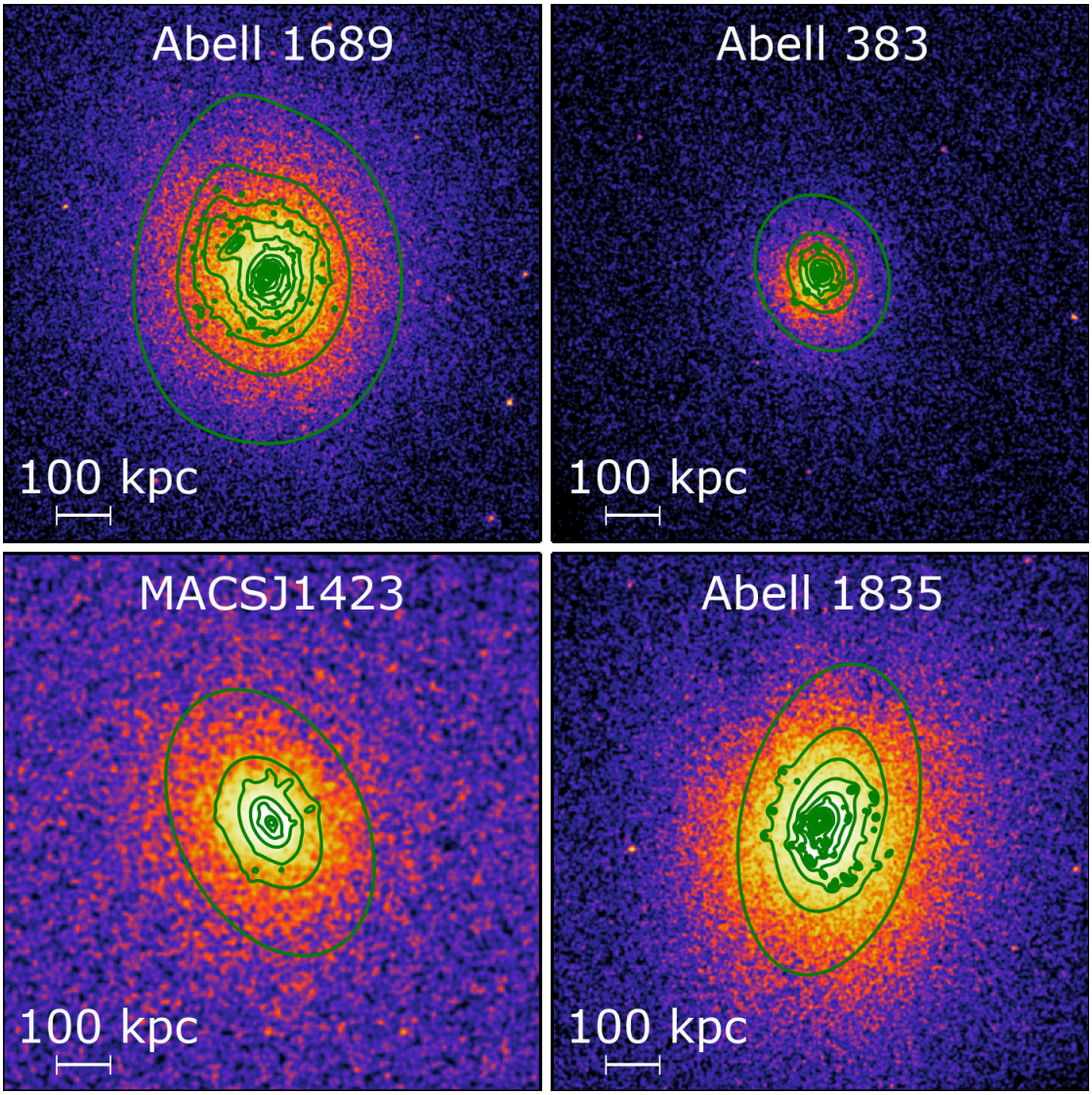


Figure 4.1.: X-Ray surface brightness (colour map) of the four clusters studied by Andrea Morandi and collaborators (M. Limousin, A. Morandi, et al., 2013). Over-plotted in green are the contours of the projected mass maps.

entering the lensing, X-ray and SZ analyses, and the corresponding likelihoods to be combined. In Section 4.2, we use the aforementioned equations in order to generate analytically mock data sets used to pursue a test of the algorithm and investigate the degeneracies, and possible biases, between the different parameters. We test the model in a triaxial first and subsequently in a spherical framework, showing the systematical effects introduced by such assumption.

## 4.1. Methodology

In this Section we summarise the astrophysical model used in the current implementation of the code, for a more detailed review see M. Limousin, A. Morandi, et al., (2013). We also present the choices made for the likelihoods and introduce the new sampler used to perform the Montecarlo-Markov chain (MCMC).

### 4.1.1. Lensing Equations

In the model we describe the DM and ICM as ellipsoids oriented in an arbitrary direction on the sky. We introduce two Cartesian coordinate systems, $\mathbf{x} = (x, y, z)$ and $\mathbf{x}' = (x', y', z')$, which represent respectively the principal coordinate system of the triaxial cluster and the observer's coordinate system, with the origins set at the centre of the halo. We assume that the $z'$-axis points along the line of sight direction of the observer and that the $x', y'$ axes identify the directions of West and North, respectively, on the plane of the sky. We also assume that the $x, y, z$-axes point along the minor, intermediate and major axes, respectively, of the DM halo. In our model, $x, y, z$ also represent the axes of the ICM distribution. We define $\psi$, $\theta$ and $\phi$ as the rotation angles about the $x$, $y$ and $z$ axis, respectively. Then the relation between the two coordinate systems can be expressed in terms of the rotation matrix $M$ as $\mathbf{x}' = M(\psi, \theta, \phi)\mathbf{x}$, where $M$ represents the orthogonal matrix corresponding to counter-clockwise/right-handed rotations.

We define the radius $R$ as the major axis of ellipsoid:

$$R^2 = c^2 \left( \frac{x^2}{a^2} + \frac{y^2}{b^2} + \frac{z^2}{c^2} \right), \qquad (a \leq b \leq c); \tag{4.1}$$

therefore, minor-major and intermediate-major axis ratios are $s_{DM} = a/c$ and $q_{DM} = b/c$, respectively.

In order to parametrise the cluster mass distribution, we consider a triaxial generalised Navarro, Frenk & White model (gNFW, *e.g.* Y. P. Jing and Y. Suto, 2002):

$$\rho(R) = \frac{\delta_c \rho_{c,z}}{(R/R_S)^{\alpha} \left(1 + R/R_S\right)^{3-\alpha}}, \tag{4.2}$$

where $R_S$ is the scale radius, $\alpha$ represents the inner slope of the density profile,

$\rho_{c,z} \equiv 3H(z)^2/8\pi G$ is the critical density of the universe at redshift $z$ and $\delta_c$ is the dimensionless characteristic density contrast:

$$\delta_c = \frac{200}{3} \frac{c_{200}^3}{F(c_{200}, \alpha)} \ , \tag{4.3}$$

where $c_{200} \equiv R_{200}/R_S$ is the concentration parameter and with (Wyithe, Turner, et al., 2001): $F(y, \alpha) \equiv \int_0^y x^{2-\alpha}(1+x)^{\alpha-3}\mathrm{d}x$.

Finally, the two-dimensional surface mass density $\mathbf{\Sigma}$ is derived by projecting the three dimensional density $\rho(R)$ along the direction of the line of sight $z'$. We also calculated the covariance matrix $\mathbf{C}$ among all the pixels of the reconstructed surface mass (see A. Morandi, M. Limousin, Rephaeli, et al., 2011b, for further details).

### 4.1.2. X-ray Equations

For small eccentricities, the gravitational potential of a gNFW halo (Eq. 4.2) can be approximated as follows (Lee and Y. Suto, 2003):

$$\begin{aligned} \Phi(\mathbf{u}) \simeq & C_0 \ F_1(u) + C_0 \ \frac{e_b^2 + e_c^2}{2} F_2(u) \\ & + C_0 \ \frac{e_b^2 \sin^2\theta \sin^2\phi + e_c^2 \cos^2\theta}{2} F_3(u), \end{aligned} \tag{4.4}$$

with $\mathbf{u} \equiv \mathbf{r}/R_S$, $C_0 = 4\pi G \delta_c \rho_c(z) R_S^2$, and the functions $F_1(u), F_2(u)$, and $F_3(u)$ as defined in A. Morandi, K. Pedersen, et al., (2010); finally $e_b$ and $e_c$ are the eccentricity of DM with respect to the major axis (e.g. $e_b = \sqrt{1-(b/c)^2}$). The work of Lee and Y. Suto, (2003) showed that the iso-potential surfaces of the triaxial dark halo are well approximated by a sequence of concentric triaxial distributions of radius $R_{ICM}$ with different and non-constant eccentricity (see A. Morandi, K. Pedersen, et al., 2010, for further details).

If we assume hydrostatic equilibrium (HE), the iso-potential surfaces of the triaxial halo coincide also with the iso-density (pressure, temperature) surfaces of the intracluster gas. This is simply a direct consequence of the *X-ray shape theorem* (Buote and Canizares, 1994); the HE equation (4.6) yields

$$\nabla P \times \nabla \Phi = \nabla \rho_{gas} \times \nabla \Phi = 0. \tag{4.5}$$

For the X-ray analysis we rely on a generalisation of the HE equation (A. Morandi, M. Limousin, Rephaeli, et al., 2011b), which accounts for the non-thermal pressure $P_{nT}$ and reads:

$$\nabla P_{TOT} = -\rho_{gas} \nabla \Phi \tag{4.6}$$

where $\rho_{gas}$ is the gas mass density, $\Phi$ is the gravitational potential, $P_{TOT} = P_T + P_{nT}$. We implemented a model where $P_{nT}$ is a fraction of the total pressure $P_{TOT}$, and we set this fraction to be a power law with respect to the radius (Shaw, Nagai, et al., 2010):

$$\frac{P_{nT}}{P_{TOT}} = \xi \, (R/R_{200})^n \ . \tag{4.7}$$

Note that X-ray data probe only the thermal component of the gas $P_T = n_e \, k_B T$, $k_B$ being the Boltzmann constant. From Equations (4.6) and (4.7) we point out that neglecting $P_{nT}$ (i.e. $P_{TOT} = P_T$) systematically biases low the determination of cluster mass profiles. This effect increases at larger radii, where the contribution of the gas motion is larger.

Solving Eq. (4.6), gives the model temperature $T$, however given that this is a first order differential equation, we need a boundary condition on the pressure, $P_0$, and it is an unknown parameter to be determined.

To model the electron density profile in the triaxial ICM halo, we use the following fitting function, which corresponds to a simplified version of the function given by Vikhlinin, A. Kravtsov, et al., (2006):

$$n_e(R_{ICM}) = n_0 \, (R_{ICM}/r_c)^{-\delta} (1 + R_{ICM}^2/r_c^2)^{-3/2\,\varepsilon + \delta/2} \tag{4.8}$$

with parameters $(n_0, r_c, \varepsilon, \delta)$. We compute the theoretical three-dimensional temperature $T$ by numerically integrating the equation of the HE (Equation 4.6), assuming triaxial geometry and a functional form of the gas density given by Equation (4.8).

The observed X-Ray surface brightness $S_X$ is given by:

$$S_X = \frac{1}{4\pi(1+z)^4} \Lambda(T^*_{proj}, Z) \int n_e n_p \, dz' \ , \tag{4.9}$$

where $\Lambda(T^*_{proj}, Z)$ is the cooling function. Since the projection on the sky of the plasma emissivity gives the X-ray surface brightness, the latter can be geometrically fitted with the model $n_e(R_{ICM})$ of the assumed distribution of the electron density (Equation 4.8) by applying Equation (4.9). This has been accomplished via simulated *Chandra* spectra, where the current model is folded through response curves (ARF and RMF) and then added to a background file, and with absorption, temperature and metallicity measured in that neighbouring ring in the spectral analysis. In order to calculate $\Lambda(T^*_{proj}, Z)$, we adopted a MEKAL model for the emissivity.

### 4.1.3. Bayesian combined analysis

In our analysis, we want to infer the values of parameters of a model given the observations we have. Using Bayes theorem, this probability $P(\boldsymbol{\theta}|\mathbf{d})$ can be expressed as:

$$P(\boldsymbol{\theta}|\mathbf{d}) = \frac{P(\mathbf{d}|\boldsymbol{\theta})P(\boldsymbol{\theta})}{P(\mathbf{d})}, \tag{4.10}$$

where $\boldsymbol{\theta}$ and $\mathbf{d}$ are the parameters and observations vectors, $P(\boldsymbol{\theta}|\mathbf{d})$ is the likelihood $\mathcal{L}$, $P(\boldsymbol{\theta})$ is the priors probability distribution and $P(\mathbf{d})$ is just a normalisation factor that can be used to compare different models. In the rest of this work, we will ignore $P(\mathbf{d})$.

If the observations vector $\mathbf{d}$ is composed of independent data sets then the joint likelihood can be expressed as the product of independent likelihoods (Marshall, Hobson, et al., 2003). Therefore, we can assume in our combined analysis $\mathcal{L} = \mathcal{L}_\Sigma \, \mathcal{L}_T \, \mathcal{L}_{S_X}$, where the independent likelihoods are:

- for the lensing constraint, the two-dimensional projected mass density $\boldsymbol{\Sigma}$ is described by a Gaussian likelihood

$$\mathcal{L}_\Sigma \propto \exp\left[-\frac{1}{2}(\boldsymbol{\Sigma} - \boldsymbol{\Sigma}^*)^T \mathbf{C}^{-1} (\boldsymbol{\Sigma} - \boldsymbol{\Sigma}^*)\right], \tag{4.11}$$

  where $\mathbf{C}$ is the covariance matrix, $\boldsymbol{\Sigma}^*$ are the observed measurements of the two-dimensional projected mass density in the $i$th pixel, and $\boldsymbol{\Sigma}$ is the theoretical 2D model;

- for the temperature $T$ in the spectral analysis, the likelihood is

$$\mathcal{L}_T \propto \exp\left[-\frac{1}{2}\sum_{i=1}^{n_T} \frac{(T_{proj,i} - T^*_{proj,i})^2}{\sigma^2_{T^*_{proj,i}}}\right], \tag{4.12}$$

  $T^*_{proj,i}$ being the observed projected temperature profile in the $i$th circular ring and $T_{proj,i}$ the azimuthally-averaged projection (following Mazzotta, Rasia, et al., 2004) of the theoretical three-dimensional temperature $T$; the latter is the result of solving the HE equation, with the gas density $n_e(R_{ICM})$;

- for the X-ray surface brightness, given that the number of counts in each cell might be small ($< 5$), we cannot assume that the distribution from which the counts are sampled has a nearly Gaussian shape; the likelihood of a Poisson distribution can be approximated as

$$\mathcal{L}_{S_X} \propto \exp\left[-2\sum_{i=1}^{N_S} S_{X,i} - S^*_{X,i}\log(S_{X,i}) - S^*_{X,i} + S^*_{X,i}\log(S^*_{X,i})\right] \tag{4.13}$$

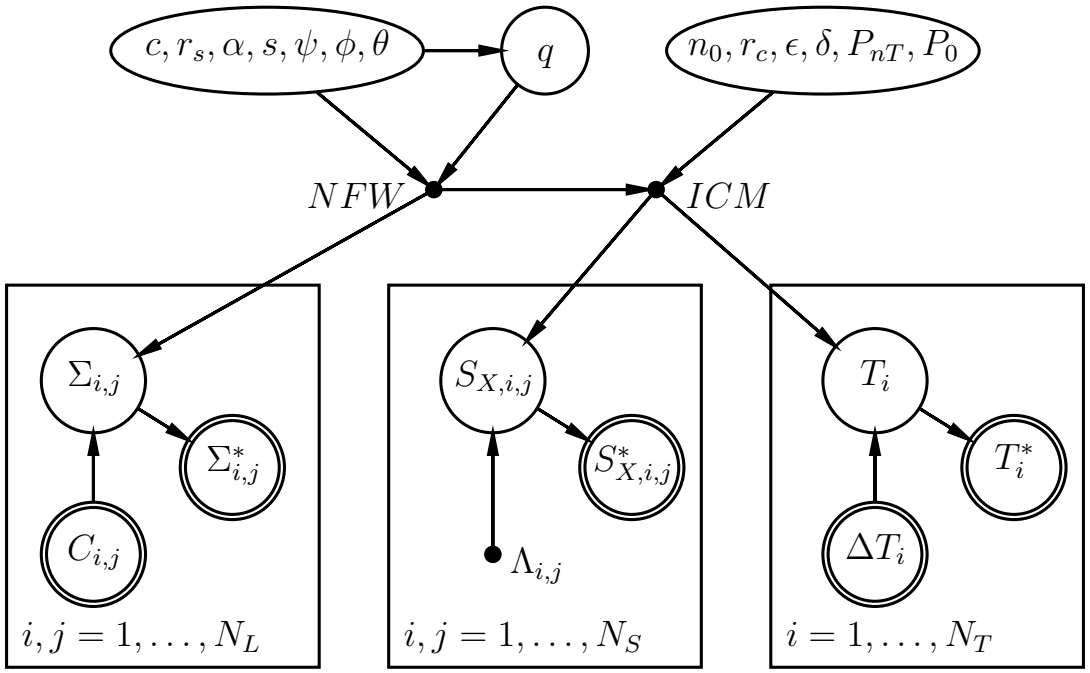


Figure 4.2.: Probabilistic graphical model (PGM) of the framework presented. In this notation, ellipses and circles represent random variables drawn from probability distribution. A double circle means that the value is observed, therefore fixed. A point represent a deterministic quantity and rectangle enclose operations that apply on vectors. Finally arrows show the conditional dependence of the variables.

with $S_{X,i}$ and $S^*_{X,i}$ theoretical and observed counts in the $i$th pixel of the image.

The whole framework can be summarised in a probabilistic graphical model (PGM), shown in figure 4.2. In this notation, ellipses and circles represent random variables drawn from probability distribution. A double circle means that the value is observed, therefore fixed. A point represents a deterministic quantity, a rectangle encloses operations that apply on vectors and an arrow shows conditional dependence of two variables. The PGM makes it easy to visualise the relations between variables in the model:

- the axis ratio $q$ is conditional on the value of $s$ (they are ordered), so it is shown in a separate circle connected with an arrow to the other parameters;
- only some variables are used to generate the NFW density profile which itself is the only ingredient used to generate the lensing data;
- the NFW profile and additional parameters are then used to generate the

ICM model which is used to derive the surface brightness and temperature profiles;

- the rectangles show that each observable is compared pixel per pixel using the corresponding distribution.

Finally, the prior probability distributions $P(\boldsymbol{\theta})$ have to be specified for each analysis as the contain the prior knowledge on the parameters; in table 4.1 we show the priors used in this work.

### 4.1.4. New implementation

We present here a new implementation of the code used in A. Morandi, M. Limousin, Sayers, et al., (2011). It has been completely rewritten in python to use a more advanced MCMC sampler called *emcee* (Foreman-Mackey, Hogg, et al., 2013), much faster and easy to run in parallel. One of the main advantages of the new version is its modularity: we maintained a very clear distinction between astrophysical model and statistical inference sections of the code, which leads to easier implementation of alternative models and data-sets. Another addition to the original algorithm is the full implementation of prior probability distributions. It is now possible to define custom functions or use predefined distributions from standard libraries.

The code has been made available to the community with an open source license. It can be found at `https://bitbucket.org/marioaieie/mcclusters`.

## 4.2. Testing the Algorithm

In order to test our algorithm, we generate mock data from the model itself, *i.e.* using the equations given in the previous Section. We use values for the parameters (see Table 4.1) which are modelled on those of galaxy cluster MACS J1423 presented in M. Limousin, A. Morandi, et al., (2013). These do not need to be really representative of the cluster population: the scope of this analysis is to test the reconstruction algorithm, not the astrophysical model.

The values for $c_{200}$ and $R_{200}$ are in the typical range for clusters of galaxies (Duffy, Schaye, et al., 2008) and $\alpha = 1$ means that the halo is a simple NFW, even though we still consider it as a free parameter in the analysis (Table 4.1). The same applies for the gas density profile: even though we have used a simpler model to generate the data ($\delta = 0$ and $P_{nT} = 0$), we treat these as unknown variables and we fit the complete model. In absence of weak lensing and SZ, $P_0$ is a nuisance parameter (the pressure in the outskirts of the cluster), therefore we have chosen a value that produces a temperature in the last bin that is at least $1keV$. At last, the angle between the major axis of the halo and the line of sight is justified by the fact that strong lensing cluster are preferentially found

| Name | Prior | True |
|---|---|---|
| $c_{200}$ | *Uniform* [1, 12] | 4.00 |
| $R_{200}$ [kpc] | *Uniform* [$5 \times 10^2$, $8 \times 10^3$] | 2400 |
| $\alpha$ | *Uniform* [0, 3] | 1.00 |
| $s$ | *Uniform* [0.2, 1] | 0.60 |
| $q$ | *Uniform* [$s$, 1] | 0.70 |
| $\psi$ [deg] | *Uniform* [$-180$, 180] | $-68.75$ |
| $\phi$ [deg] | *Uniform* [$-180$, 0] | $-34.38$ |
| $\theta$ [deg] | *Uniform* [0, 90] | 28.65 |
| $n_0$ [cm$^{-3}$] | *Uniform* [$10^{-3}$, 1] | 0.10 |
| $r_c$ [kpc] | *Uniform* [10, 200] | 30.00 |
| $\epsilon$ | *Uniform* [0, 1] | 0.55 |
| $\delta$ | *Uniform* [0, 1] | 0.00 |
| $P_{nT}$ | $\exp(-x/10)$ with $x < 1$. | 0.00 |
| $P_0$ [$10^4$ keV cm$^{-3}$] | *Uniform* [0, 10] | 3.74 |

Table 4.1.: True values and priors of the parameters of the triaxial joint model

with their major axis close to the line of sight: around $50\%$ of the clusters with an Einstein radius larger than $20''$, have an inclination angle lower than $30$ degrees (Figure 2 in C. Giocoli, Bonamigo, et al., 2016).

We generated 7 sets of mock observations with increasing minor to major axis ratio $s$, from $0.4$ to $1$ with linear bins of $0.1$; the intermediate to minor axis ratio $q$ is then fix to $q = (1 + s)/2$, which gives an halo in-between a prolate and an oblate one (prolateness equal to zero). This is an arbitrary condition used only to generate the mock data-set from a mono-dimensional binning in shape; it is not forced in the actual fitting of the observables. In the following, we will use $10 \times s$ to identify the different mock haloes (e.g. *halo 4* has $s = 0.4$).

### 4.2.1. Generating mock observables

Figure 4.3 shows the generated data sets, from *halo 4* to *9* (left to right and top to bottom). The colour maps show the X-Ray surface brightness, while the contours correspond to the projected mass maps (lensing data). For each of the halo, we have projected the observable to produce an image similar to what have been used to analyse the real clusters (*lenstool* 2D mass maps and Chandra images). We have then added noise independently with the following procedure.

For the strong lensing, we used a $200'' \times 200''$ image with $50$ pixels per side, that gives a resolution of $4''$/pixel. Normally, strong lensing analysis has a higher resolution, and this procedure would degrade the accuracy with which strong lensing is typically able to reconstruct mass distributions in the core ($\sim 150 - 200$ kpc). This is not a problem here since the purpose of our analysis is to model the main mass clump with a single triaxial halo, ignoring any substructures; we

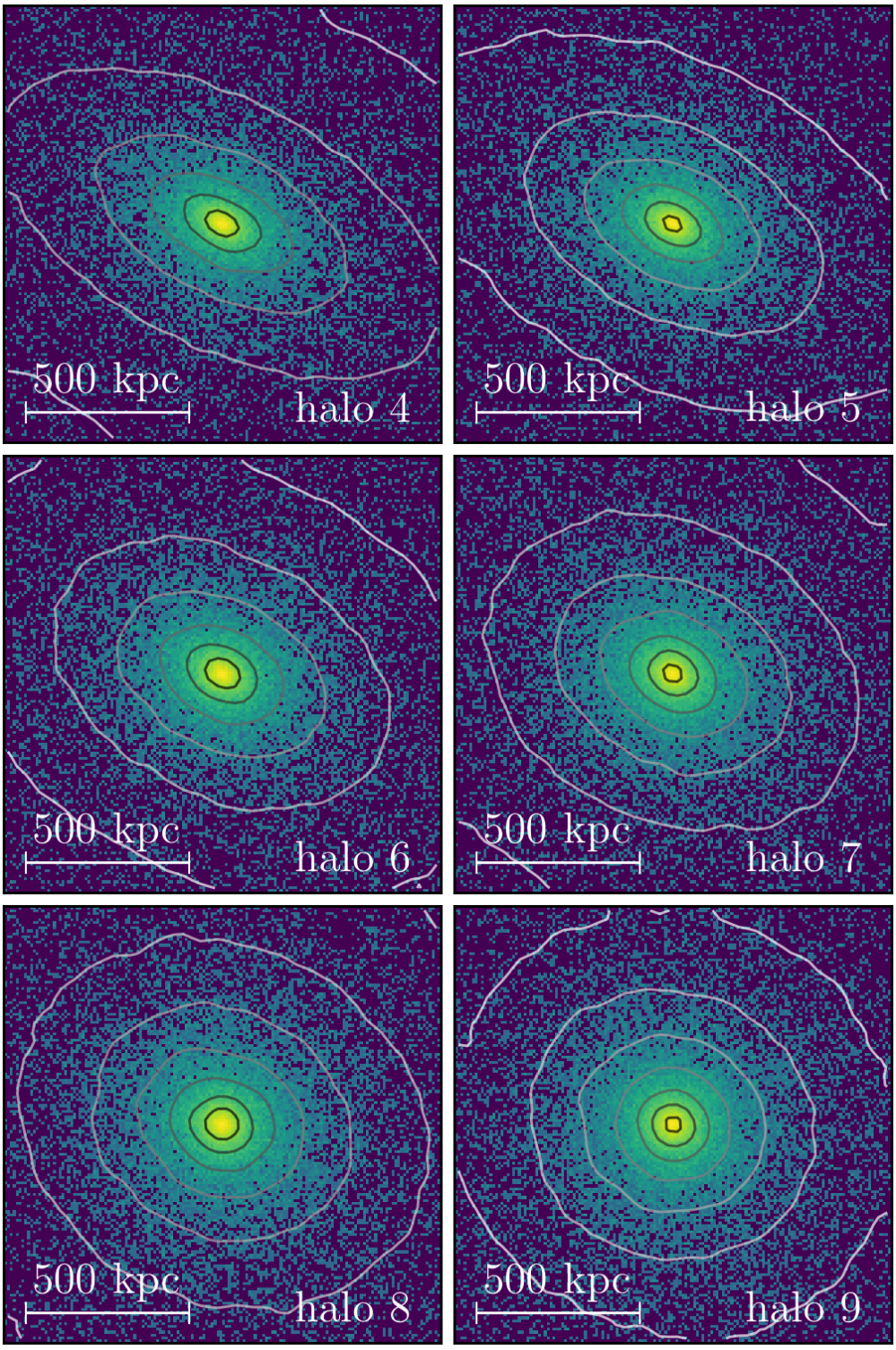


Figure 4.3.: X-Ray surface brightness (colour map) of the mock clusters presented in this chapter (from halo 4 to halo 9). Over-plotted are the contours of the projected mass maps that correspond to the lensing data in this analysis.

are also not working with images positions but only with the projected mass map, which does not require the same level of spatial resolution. Then, we have projected the NFW profile and added independently to each pixel a Gaussian noise with $\sigma_\Sigma = 5\%\,\Sigma$; because of this, the lensing likelihood is not a multivariate Gaussian (eq. 4.11) anymore, but simply the product of independent Gaussian functions.

Similarly, for the X-Ray temperature, we have averaged the model's 2D temperature in 8 circular annuli and added Gaussian noise with $\sigma_T = 5\%\,T$. To simplify the procedure of generating the X-Ray surface brightness, we have used a constant cooling function $\Lambda(T^*_{proj}, Z)$ (eq. 4.9); this is possible because in our code it is treated as a rescaling factor that is only function of the observed temperature. Therefore, the mock surface brightness was obtained by rescaling the projected electron density in Chandra-like images: $1024 \times 1024$ pixels (then reduced to $256 \times 256$ pixels for convenience reasons) with a side of about $8.4'$ plus a uniform background of $0.1$ cts/s/arcmin$^2$. Finally, we used the surface brightness to extract the photon counts per pixel from a Poisson distribution.

### 4.2.2. Triaxial analysis

As shown in Table 4.1, we have used uniform prior distributions for all parameters except for the non-thermal pressure $P_{nT}$ for which we adopted a decreasing exponential with scale of $0.1$ and truncated at $1$. In addition, the lower limit of the distribution of $q$ is set to the value of $s$, to maintain the correct order in the axis ratios.

One of the more difficult aspect of using *emcee* is choosing a good initial guess from which starting to explore the parameter space (Foreman-Mackey, Hogg, et al., 2013). Although the suggested technique is to start from a tight N-dimensional ball close to the point of maximum probability, we have found that in our case traditional maximum likelihood methods do not give correct results. This is possibly due to the large number of variables in the model or the complex correlations between the observables. Therefore, we decided to use a spherical NFW halo to find a first guess of the model parameters (see sub-section 4.2.3 for biases introduced by a spherical analysis): the reduced number of variables allows us to start *emcee* from the maximum likelihood fit. We then set the starting values of the angles to zero and of the axis ratios to $s = 0.5$ and $q = 0.65$, typical values for cluster scale haloes (see chapter 2). We have also decided to fit $R_{200}$ instead of the scale radius to avoid the strong correlation with the concentration that can be problematic, at times, for samplers like *emcee*.

Figure 4.4 shows the mock observables of *halo 4* and *halo 10*, namely: one dimensional profiles of surface density, X-Ray surface brightness and X-Ray temperature, from top to bottom panel. The red line corresponds to the true values of the parameters; the green one with error bars is obtained by adding noise to the true profiles, as described in the previous section; and the blue lines are

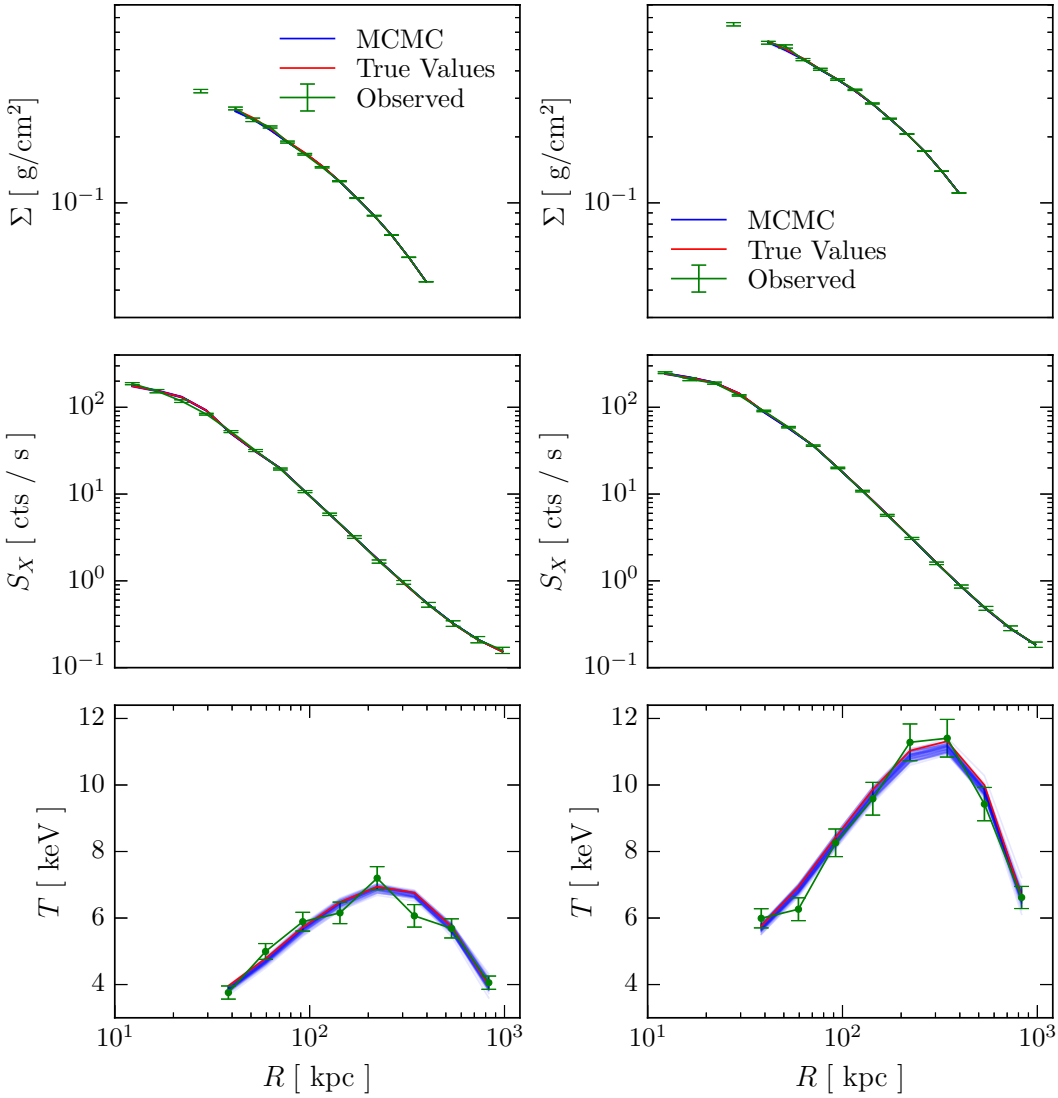


Figure 4.4.: Results from the triaxial analysis of halo 4 (left panel) and halo 10 (right panel) combining all available probes. Each panel shows three profiles from top to bottom: projected 2D mass, X-Ray surface brightness and X-Ray temperature. Red lines represent the input data, while green points are the observed values including noise. Finally, blue lines are a subset of the MCMC chain obtained by fitting the data in green. As a remainder, the fit is done in 2D for all observables but for the X-Ray temperature; these one dimensional profiles are only used for visualisation.

the Montecarlo-Markov chains. This figure is just for illustration purposes, given that the fit is done comparing pixel by pixel the 2D images of lensing and X-Ray surface brightness; the temperature is the only observables that is actually modelled from the one dimensional profile.

We have also computed the residuals of the projected mass (Figure 4.5 ) and X-Rays surface brightness (Figure 4.6) maps comparing the fitted model with the noise-less data. Clearly the visible symmetric patterns tell us to expect some biases in the shape and orientation of the recovered halo, however the residual signal is around $1$-$2\%$, well below the assumed noise ($5\%$ for the projected mass). This is also seen in the ratio between the $\chi^2$ of the fit and the one computed using the true parameters: for every analysed halo this value is always unity within $1$ part out of $10^3$. The reduced $\chi^2$ are actually lower than 1, for example, for *halo 4* the value is 0.720; this is because we have used a Poisson distribution for the X-Ray surface brightness, which means that the common rule of reduced $\chi^2$ being one for a good fit does not apply. Moreover, in a Bayesian framework the idea is to maximise the posterior distribution, not minimise the $\chi^2$.

In summary, it is clear that the algorithm was able to converge to values that reproduce the input observations within the given uncertainties.

The posterior probability distributions obtained by the MCMC analysis for *halo 4* are shown in Figure 4.10 as blue 2D filled contours and histograms. Dark contours show the areas that contain $39.3\%$ of the volume, lighter contours contain $86.4\%$; these are the values that correspond to $1$ and $2$ sigma for a 2D normal distribution. In the one dimensional histograms, dashed vertical lines show the median, $16\%$ and $84\%$ percentiles; these values are also shown in Table 4.2. As it can be seen, all parameters are constrained even though some degeneracies are still present, for examples between angles and axis ratios. Overall, most of the true values (green lines) are recovered within 1 or 2 sigma.

As the aim of this analysis is to measure the 3D shape of galaxy clusters, we show in Figure 4.7 the marginalised posterior distributions of the axis ratios for the 7 mock haloes. As before, contours show the areas that would correspond to 1 and 2 sigma in a 2D Gaussian distribution. The colours correspond to the different values of minor to major axis ratio as indicated in the legend and the white stars show the true value of the parameters. While there is a good recovery of the principal axis ratio $s$ (almost always within one sigma of the true value), the intermediate to major axis ratio is not constrained as accurately. More precisely, in the two more elongated haloes, the posterior distribution of $q$ are more than three sigmas away from the correct value. This could be due to the algorithm finding only a local maximum or to unfavourable initial conditions for the MCMC sampler which might not be adequate to deal with strong correlations between variables like shape, orientation and radius of the cluster. We are investigating alternative techniques to start the algorithm and eventually different MCMC samplers.

Even though we still can not recover accurately the full 3D shape (at least

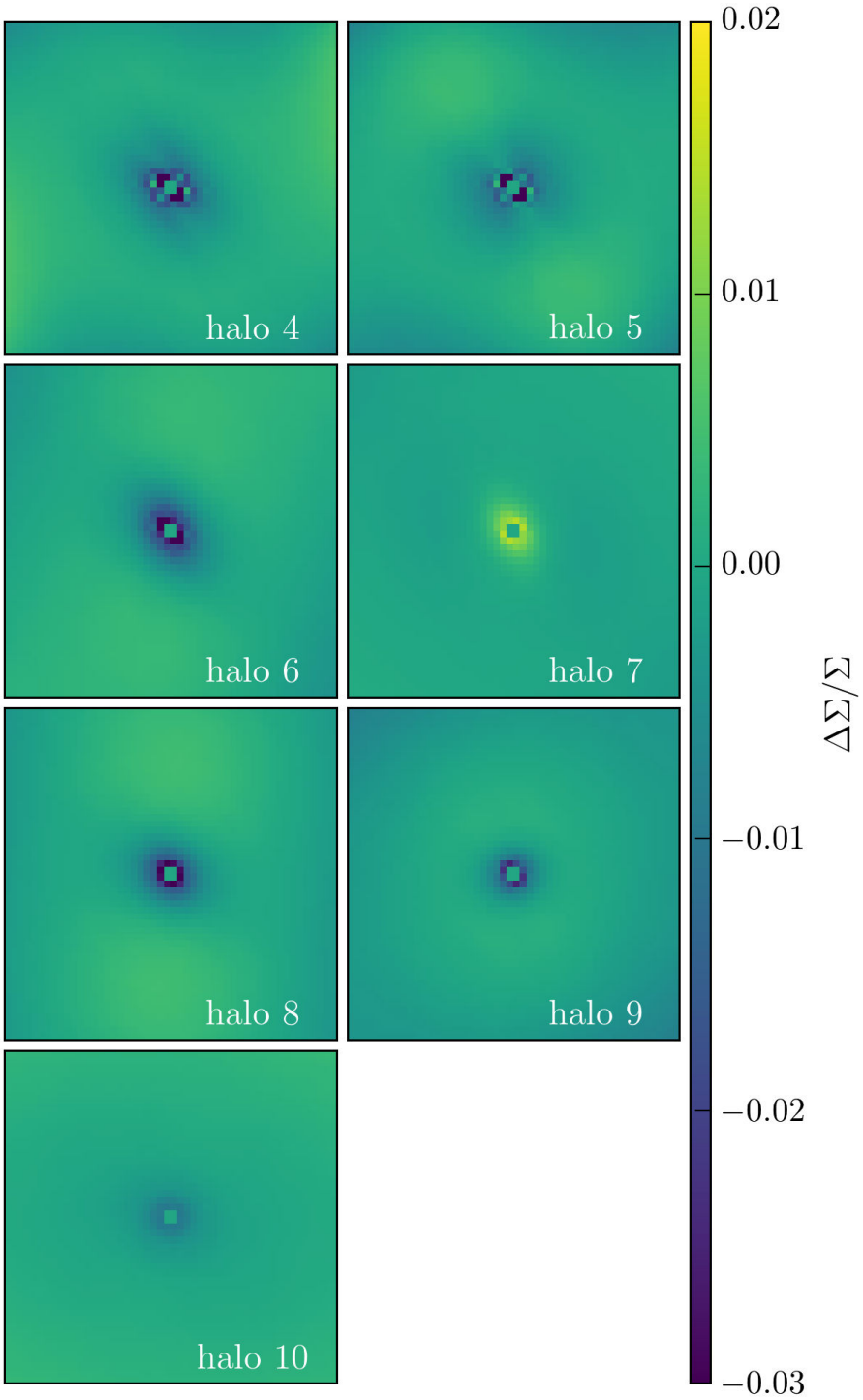


Figure 4.5.: Projected mass maps residuals of the triaxial fit from the noise-less image. Each pannel show a different halo.

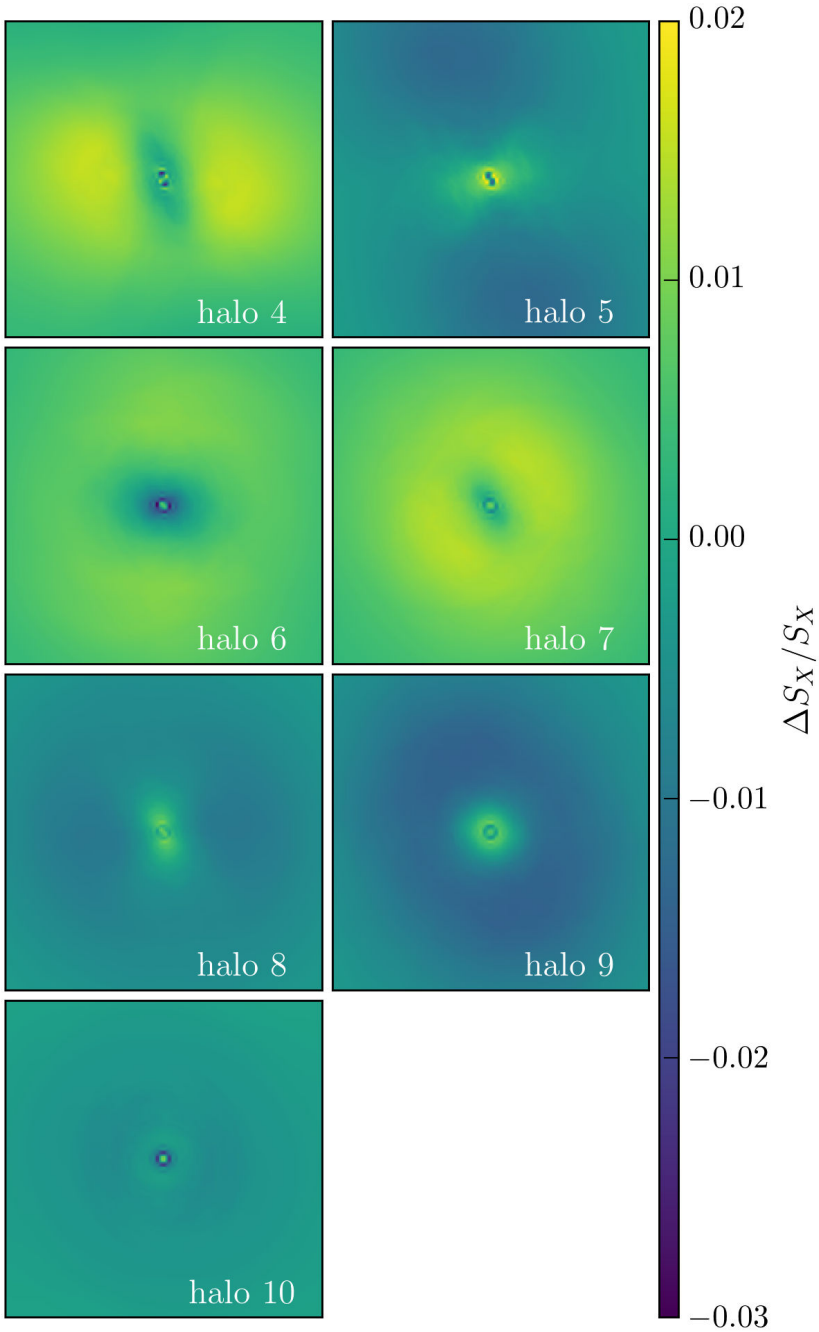


Figure 4.6.: X-Ray surface brightness maps residuals of the triaxial fit from the noise-less image. Each panel show a different halo.

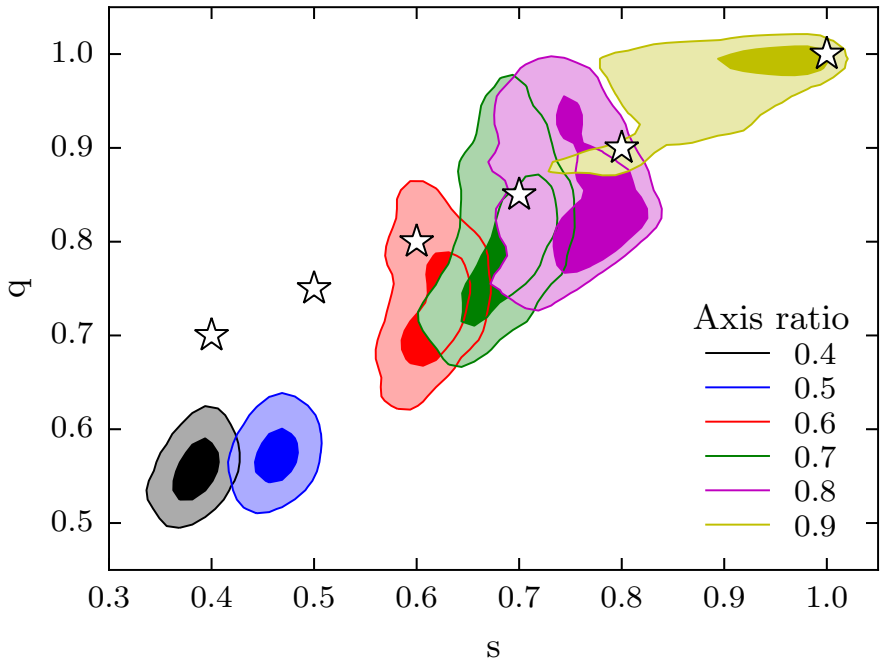


Figure 4.7.: Marginalised distributions of shape parameters obtained with the triaxial model. Contours show one and two sigmas and each colour represents a different halo, with the minor to major axis ratio indicated in the legend. Stars show the input value of the parameters. We have omitted halo 9 from the plot for clarity reasons, as its contour would have overlapped with other ones.

given the assumption of this work), we are able to reproduce the combined data-set within the errors of current observations. As well as improving the fitting procedure, the addition of Sunyaev-Zel'dovich data and higher precision measurement of the X-ray and lensing signals could help reducing the systematic effects we have seen. Finally, even with the presence of an offset in the shape measurements, we are capable of constraining the cluster mass with extremely good precision and accuracy (see Figure 4.9 for a comparison with the spherical case).

### 4.2.3. Spherical analysis

In this subsection we aim at quantifying the bias induced by assuming a spherical approach. To this end, we consider the same data-sets generated with the triaxial model and fit the mock data using a spherical halo.

In Figure 4.11 we show the output of the spherical analysis for *halo 5* (same as Figure 4.10). The median values and relative errors are summarised in table 4.2. The resulting marginalised distributions show that:

- regarding the gas distribution, both the non-thermal pressure $P_{nT}$ and the pressure $P_0$ (the boundary condition of the HE) are highly biased;
- other parameters are recovered correctly within 1-2 sigma, namely concentration $c_{200}$, gNFW inner slope $\alpha$, gas density normalisation $n_0$ and slopes $\varepsilon$ and $\delta$;
- finally, the radii of the two profiles, $R_{200}$ and $r_c$, are offset by more than 3 sigma.

The marginalised distributions of all mock haloes are shown in Appendix A.

An interesting trend is the bias of the concentration as function of the axis ratio $s$ of the cluster, shown in Figure 4.8. In this box and whiskers plot, the boxes enclose the quartiles, while error bars are drawn at $1.5$ times the interquartile range (between 2 and 3 sigma for a Gaussian distribution). It is clear that the more elongated the halo, the more the concentration is over-estimated by a spherical analysis. For an average cluster with $s = 0.5$ this bias can at the 3 sigma level.

A similar trend can be seen in both radii of the model, where for example the measured scale radius of *halo 4* is only half of the true value. However, it is important to note that a comparison between a spherical and an ellipsoidal radius depends always on definitions (G. Despali, Tormen, et al., 2013; Bonamigo, G. Despali, et al., 2015) and no unambiguous correspondence exists. We therefore prefer to compare the total mass of a cluster, given that this is also the most (cosmologically) relevant property of the object. The probability distributions of the total mass ($M_{200}$) are shown in Figure 4.9; these are computed respectively with the triaxial (top panel) and the spherical model (bottom panel) for

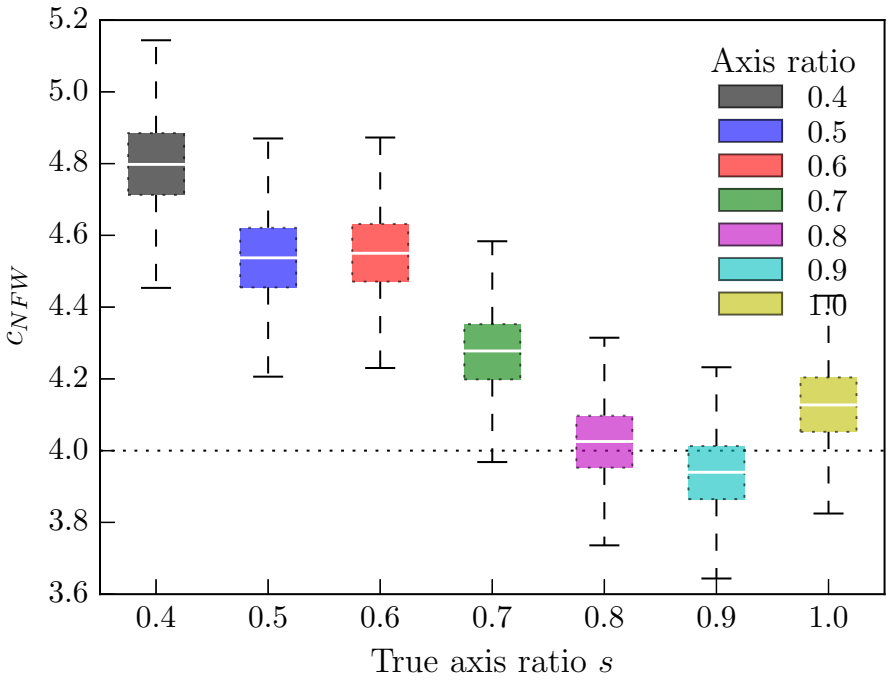


Figure 4.8.: Values of concentration obtained with the spherical model. Each colour represents a different halo, with the minor to major axis ratio indicated in the legend. The boxes enclose the quartiles, while error bars are drawn at 1.5 times the interquartile range.

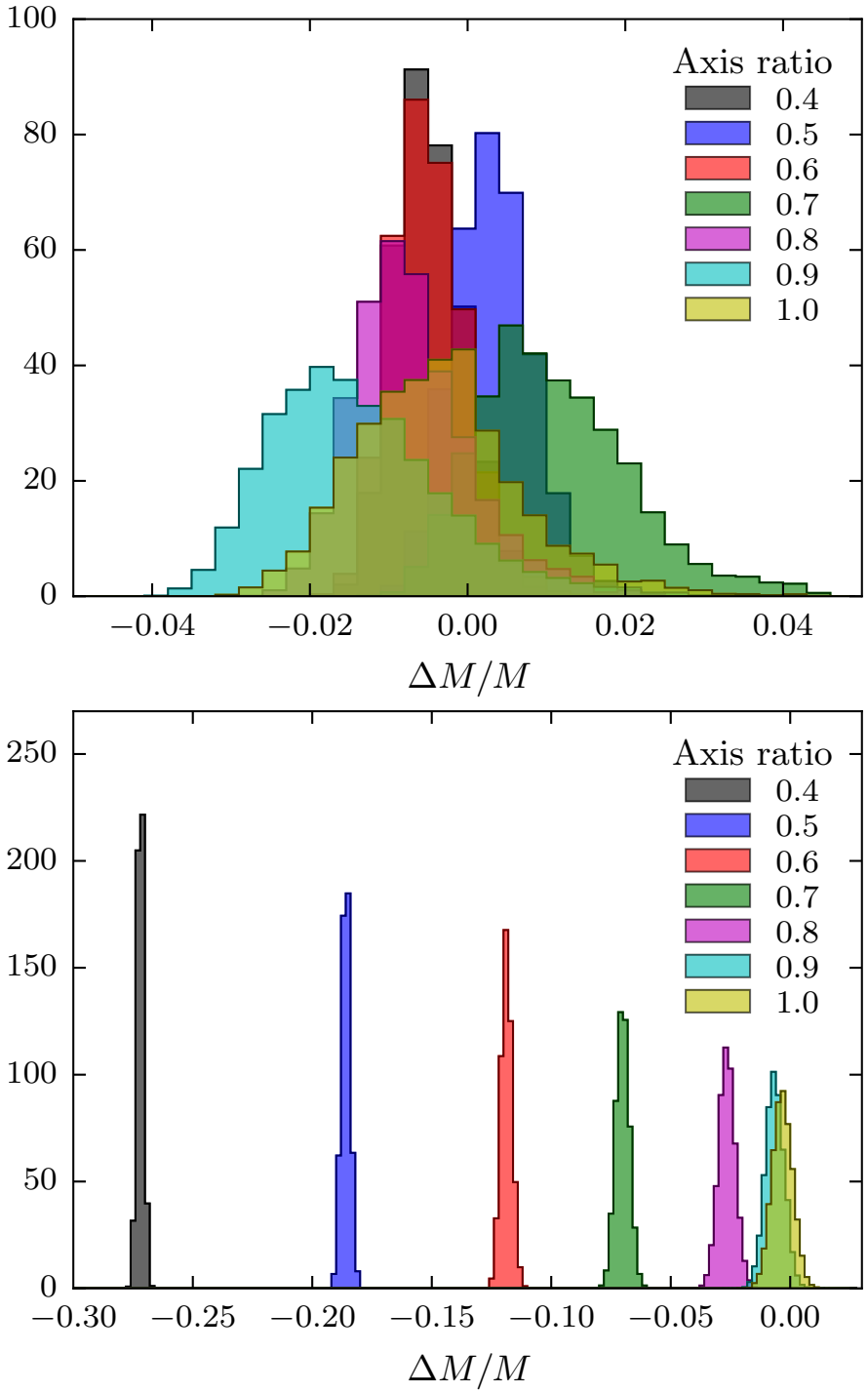


Figure 4.9.: Relative error in mass ($M_{200}$) for the triaxial model (top) and for the spherical model (bottom). Each colour represents a different halo, with the minor to major axis ratio indicated in the legend.

all haloes (shown in different colours). While in the triaxial analysis we are able to retrieve the input mass within $1\%$ accuracy and precision; in the spherical model it can be underestimated by up to $30\%$ for a very elongated halo (but not particularly uncommon (Bonamigo, G. Despali, et al., 2015)), similarly to what happens with the concentration. Although slightly concerning in the context of precision cosmology, this result should be considered as a limit case as it depends on the particular orientation of the considered cluster.

## 4.3. Summary and Conclusions

In this chapter, we have presented an algorithm aimed at fitting simultaneously complementary data sets of galaxy clusters within a triaxial framework. We have first introduced the physical model which describes the lensing and X-ray data sets. The algorithm is implemented in an open source code that is available to the community and that, thanks to its modularity, can be easily improved to incorporate additional probes, such as SZ data, or dynamics of cluster members.

We have generated mock data sets in order to characterise the algorithm and we find that overall the input parameters are well retrieved. However there are some biases present in the shape measured for some haloes; the origin of such systematic effects is not clear and improvement to the whole framework are being investigated. However, the observables are reproduced within the assumed errors and we are able to constrain the input mass within a few percents.

Moreover, we have also quantified the bias arising from using a spherical framework to fit triaxial data sets, showing that recovered masses can be biased by up to $\sim 30\%$. This is another demonstration that the current (widely adopted) spherical model is not adequate for the coming era of $1\%$ precision cosmology with clusters of galaxies.

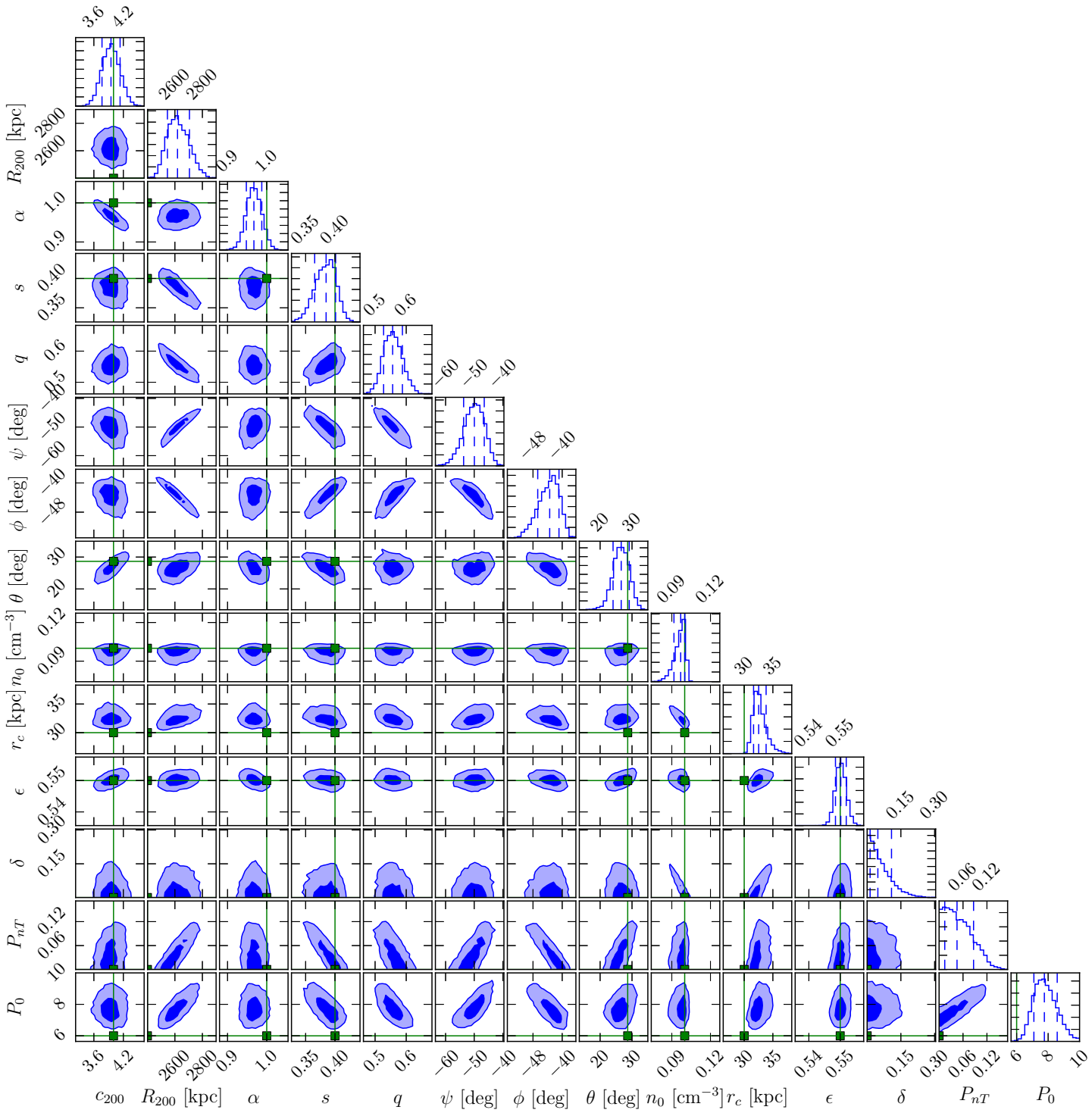


Figure 4.10.: Marginalised posterior probability distributions for the triaxial joint model parameters of halo 4

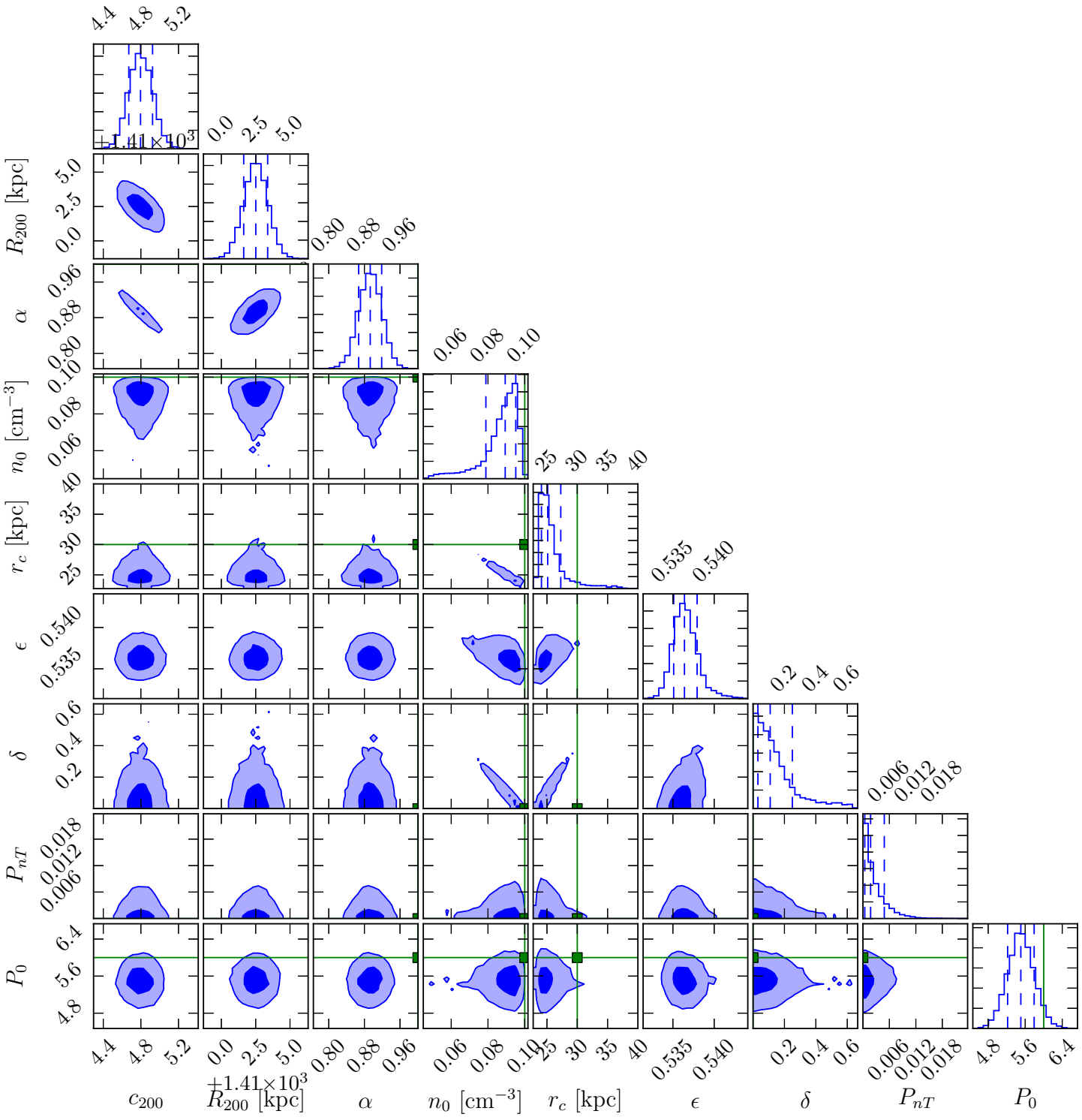


Figure 4.11.: Marginalised posterior probability distributions for the spherical joint model parameters of halo 4

| Name | True | Triaxial 4 | Triaxial 5 | Triaxial 6 | Triaxial 7 | Triaxial 8 | Triaxial 9 | Triaxial 10 |
|---|---|---|---|---|---|---|---|---|
| $c_{200}$ | 4.00 | $3.99^{+0.39}_{-0.21}$ | $3.82^{+0.49}_{-0.23}$ | $4.24^{+0.27}_{-0.26}$ | $3.65^{+0.32}_{-0.34}$ | $4.41^{+0.29}_{-0.30}$ | $4.42^{+0.45}_{-0.37}$ | $4.35^{+0.42}_{-0.48}$ |
| $R_{200}$ [kpc] | 2400.00 | $2609.51^{+103.45}_{-111.29}$ | $2656.22^{+103.19}_{-277.21}$ | $2395.03^{+101.94}_{-57.30}$ | $2463.11^{+186.37}_{-97.93}$ | $2503.32^{+112.17}_{-87.34}$ | $2773.35^{+131.41}_{-128.60}$ | $2663.22^{+224.23}_{-116.08}$ |
| $\alpha$ | 1.00 | $0.97^{+0.02}_{-0.04}$ | $0.99^{+0.02}_{-0.03}$ | $0.95^{+0.03}_{-0.03}$ | $1.04^{+0.03}_{-0.03}$ | $0.93^{+0.03}_{-0.02}$ | $0.95^{+0.03}_{-0.03}$ | $0.97^{+0.04}_{-0.03}$ |
| $s$ | — | $0.39^{+0.03}_{-0.02}$ | $0.47^{+0.02}_{-0.02}$ | $0.61^{+0.03}_{-0.04}$ | $0.66^{+0.03}_{-0.06}$ | $0.74^{+0.04}_{-0.07}$ | $0.67^{+0.07}_{-0.06}$ | $0.78^{+0.07}_{-0.14}$ |
| $q$ | — | $0.56^{+0.18}_{-0.03}$ | $0.60^{+0.21}_{-0.04}$ | $0.78^{+0.07}_{-0.06}$ | $0.82^{+0.09}_{-0.10}$ | $0.83^{+0.07}_{-0.05}$ | $0.81^{+0.04}_{-0.04}$ | $0.92^{+0.06}_{-0.08}$ |
| $\psi$ [deg] | $-68.75$ | $-50.07^{+4.09}_{-5.22}$ | $-46.97^{+4.07}_{-16.01}$ | $-67.58^{+12.00}_{-15.79}$ | $-50.94^{+11.20}_{-19.00}$ | $-46.04^{+15.96}_{-25.12}$ | $-5.57^{+7.44}_{-10.00}$ | $-0.27^{+1.19}_{-3.19}$ |
| $\phi$ [deg] | $-34.38$ | $-43.72^{+2.96}_{-5.27}$ | $-42.73^{+6.58}_{-5.77}$ | $-33.49^{+4.17}_{-6.95}$ | $-36.56^{+5.51}_{-13.81}$ | $-49.30^{+16.24}_{-30.33}$ | $-107.38^{+22.38}_{-15.88}$ | $-74.94^{+50.66}_{-62.05}$ |
| $\theta$ [deg] | 28.65 | $26.95^{+3.42}_{-3.47}$ | $23.86^{+6.42}_{-5.03}$ | $26.21^{+5.65}_{-6.10}$ | $26.76^{+7.20}_{-8.24}$ | $39.78^{+14.15}_{-9.48}$ | $47.72^{+8.00}_{-6.93}$ | $52.56^{+14.35}_{-13.60}$ |
| $n_0$ [cm$^{-3}$] | 0.10 | $0.097^{+0.004}_{-0.006}$ | $0.095^{+0.003}_{-0.006}$ | $0.095^{+0.006}_{-0.008}$ | $0.096^{+0.004}_{-0.007}$ | $0.097^{+0.003}_{-0.005}$ | $0.093^{+0.005}_{-0.007}$ | $0.090^{+0.008}_{-0.007}$ |
| $r_c$ [kpc] | 30.00 | $32.31^{+1.44}_{-15.12}$ | $33.12^{+1.53}_{-2.99}$ | $30.79^{+1.66}_{-1.50}$ | $31.07^{+1.85}_{-1.72}$ | $31.59^{+1.19}_{-1.27}$ | $34.52^{+2.05}_{-1.82}$ | $33.73^{+2.11}_{-2.84}$ |
| $\epsilon$ | 0.55 | $0.551^{+0.003}_{-0.002}$ | $0.553^{+0.003}_{-0.002}$ | $0.548^{+0.003}_{-0.002}$ | $0.549^{+0.003}_{-0.002}$ | $0.554^{+0.002}_{-0.002}$ | $0.558^{+0.003}_{-0.002}$ | $0.555^{+0.004}_{-0.002}$ |
| $\delta$ | 0.00 | $0.05^{+0.06}_{-0.04}$ | $0.04^{+0.06}_{-0.03}$ | $0.07^{+0.08}_{-0.06}$ | $0.05^{+0.07}_{-0.04}$ | $0.03^{+0.05}_{-0.03}$ | $0.08^{+0.07}_{-0.06}$ | $0.11^{+0.07}_{-0.08}$ |
| $P_{nT}$ | 0.00 | $0.04^{+0.04}_{-0.03}$ | $0.02^{+0.03}_{-0.02}$ | $0.02^{+0.03}_{-0.02}$ | $0.02^{+0.03}_{-0.02}$ | $0.03^{+0.03}_{-0.02}$ | $0.06^{+0.04}_{-0.04}$ | $0.06^{+0.04}_{-0.04}$ |
| $P_0$ [$10^4$ keV cm$^{-3}$] | 6.00 | $7.60^{+0.86}_{-4.39}$ | $7.70^{+0.90}_{-2.08}$ | $5.73^{+0.65}_{-0.79}$ | $6.31^{+1.27}_{-1.28}$ | $6.41^{+0.82}_{-1.17}$ | $7.66^{+1.24}_{-1.46}$ | $7.85^{+1.27}_{-1.48}$ |

| Name | True | Spherical 4 | Spherical 5 | Spherical 6 | Spherical 7 | Spherical 8 | Spherical 9 | Spherical 10 |
|---|---|---|---|---|---|---|---|---|
| $c_{200}$ | 4.00 | $4.80^{+0.13}_{-0.13}$ | $4.54^{+0.13}_{-0.12}$ | $4.55^{+0.12}_{-0.12}$ | $4.28^{+0.11}_{-0.11}$ | $4.03^{+0.11}_{-0.11}$ | $3.94^{+0.11}_{-0.11}$ | $4.13^{+0.11}_{-0.11}$ |
| $R_{200}$ [kpc] | 2400.00 | $1412.52^{+0.88}_{-0.88}$ | $1616.00^{+1.21}_{-1.25}$ | $1801.60^{+1.59}_{-1.54}$ | $1970.23^{+2.03}_{-2.01}$ | $2131.90^{+2.55}_{-2.46}$ | $2272.91^{+3.08}_{-2.91}$ | $2397.34^{+3.45}_{-3.38}$ |
| $\alpha$ | 1.00 | $0.89^{+0.03}_{-0.03}$ | $0.93^{+0.02}_{-0.03}$ | $0.91^{+0.02}_{-0.02}$ | $0.96^{+0.02}_{-0.02}$ | $0.99^{+0.02}_{-0.02}$ | $1.01^{+0.02}_{-0.02}$ | $0.97^{+0.02}_{-0.02}$ |
| $n_0$ [cm$^{-3}$] | 0.10 | $0.090^{+0.005}_{-0.008}$ | $0.092^{+0.005}_{-0.007}$ | $0.091^{+0.005}_{-0.008}$ | $0.095^{+0.004}_{-0.007}$ | $0.093^{+0.007}_{-0.009}$ | $0.096^{+0.003}_{-0.007}$ | $0.080^{+0.007}_{-0.006}$ |
| $r_c$ [kpc] | 30.00 | $24.97^{+1.54}_{-0.92}$ | $26.12^{+1.49}_{-0.86}$ | $27.69^{+1.75}_{-0.93}$ | $28.68^{+1.37}_{-0.72}$ | $29.43^{+2.04}_{-1.35}$ | $29.97^{+1.42}_{-0.74}$ | $34.97^{+1.79}_{-1.81}$ |
| $\epsilon$ | 0.55 | $0.536^{+0.001}_{-0.001}$ | $0.540^{+0.001}_{-0.001}$ | $0.543^{+0.001}_{-0.001}$ | $0.549^{+0.001}_{-0.001}$ | $0.546^{+0.001}_{-0.001}$ | $0.549^{+0.001}_{-0.001}$ | $0.554^{+0.001}_{-0.001}$ |
| $\delta$ | 0.00 | $0.10^{+0.10}_{-0.07}$ | $0.09^{+0.10}_{-0.06}$ | $0.08^{+0.10}_{-0.06}$ | $0.06^{+0.08}_{-0.04}$ | $0.12^{+0.11}_{-0.08}$ | $0.06^{+0.08}_{-0.04}$ | $0.24^{+0.07}_{-0.08}$ |
| $P_{nT}$ | 0.00 | $0.00^{+0.00}_{-0.00}$ | $0.00^{+0.00}_{-0.00}$ | $0.00^{+0.00}_{-0.00}$ | $0.00^{+0.01}_{-0.00}$ | $0.01^{+0.01}_{-0.01}$ | $0.01^{+0.02}_{-0.01}$ | $0.02^{+0.02}_{-0.01}$ |
| $P_0$ [$10^4$ keV cm$^{-3}$] | 6.00 | $5.51^{+0.29}_{-0.29}$ | $5.42^{+0.29}_{-0.30}$ | $5.03^{+0.30}_{-0.29}$ | $5.40^{+0.32}_{-0.30}$ | $5.43^{+0.36}_{-0.34}$ | $5.67^{+0.38}_{-0.35}$ | $5.60^{+0.42}_{-0.38}$ |

Table 4.2.: Fitted parameters of the triaxial (upper table) and spherical (lower table) analysis. The first two columns show the name of the parameter and the true value. In the remaining columns are presented the median and 16% - 84% percentiles (1 sigma).

# 5. An X-Ray study of galaxy cluster Abell 1703

In this chapter we present two Chandra observations of galaxy cluster Abell 1703. The cluster is located at redshift $0.2836$ and it is considered to be a relaxed and unimodal object. In the chapter, we have adopted a flat $\Lambda$CDM cosmology with the following parameters: total matter density $\Omega_m = 0.3$, cosmological constant $\Omega_\Lambda = 0.3$ and Hubble constant $H_0 = 70$ km s$^{-1}$ Mpc$^{-1}$.

## 5.1. X-Ray data and spectral analysis

We have analysed data from two Chandra observations of galaxy cluster Abell 1703: 15123 (P.I. Christine Jones) and 16126 (P.I. Fabio Gastaldello). Both data-sets are taken with the ACIS-I camera with exposure times of 29130 ks and 48246 ks respectively.

Having reduced both observation following a standard Chandra analysis using the CIAO software, we extracted the source spectrum form concentric annuli. The radii are chosen so that every region contains 7 000 counts (cluster plus background). Figure 5.1 shows counts rate from observation 16126 (colour bar), with the position of the CCD during observation 15123 superimposed (white mask); magenta annuli show the binning used to measure the source spectrum. Background emission has been modelled on red and blue circles from observation 15123 and 16126 respectively, as explained in the following section.

For the cluster emission spectrum we adopted an APEC model with a photo-electric absorption (phabs) from the Galaxy. The hydrogen column density is taken from the LAB Survey of Galactic HI and correspond to $n_H = 1.32 \times 10^{20}$ cm$^{-2}$ and the spectrum is fitted between $0.7$ and $7$ keV.

### 5.1.1. Background modelling and systematics

To model the background signal, we have adopted a simplified version of the one proposed by Bartalucci, Mazzotta, et al., (2014). First of all we implemented continuum emissions for sky and the instrumental noise (nxb):

```
model  1:sky apec + (apec + powerlaw)phabs
model  2:nxb expdec + powerlaw
```

From the fit residuals, at least three lines were visible, respectively at $2.165$, $7.5$ and $9.72$ KeV; we used fixed single Gaussian to describe these lines instead of the position-dependent mother-daughter systems adopted by the authors. We performed the analysis in the range between $0.3$ and $11$ keV.

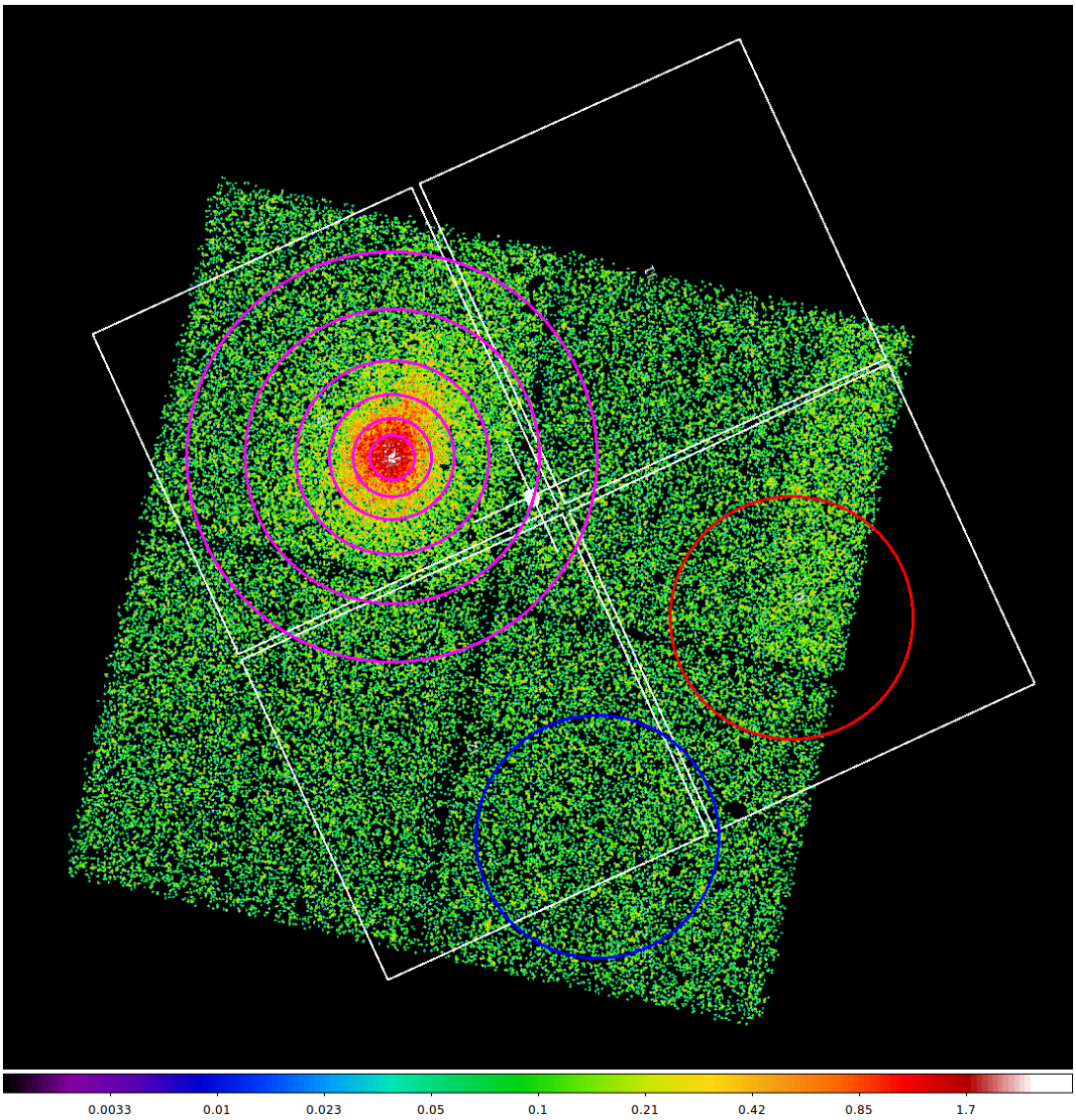


Figure 5.1.: Counts rate from observation 16126 (colour bar) and position of CCD during observation 15123 (white mask). Magenta annuli show the binning used to measure the source spectrum (Section 5.1). Red and blue circles are the regions used for the background modelling in Section 5.1.1.

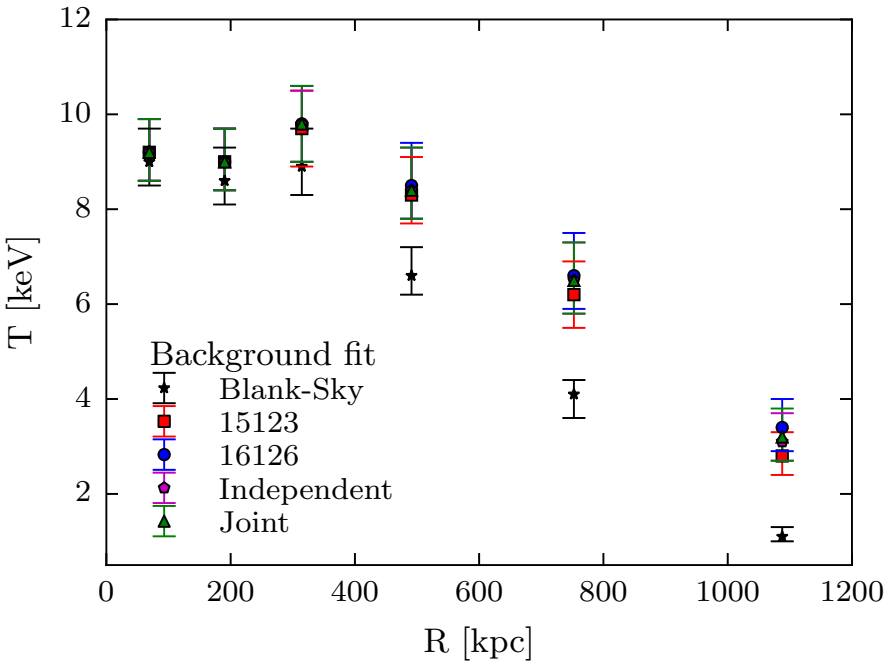


Figure 5.2.: Cluster temperature profile for different background assumptions. Black stars correspond to blank-sky file subtraction. Red squares and blue circles show the case where the source-free region is modelled only on one observation and then applied to both; while in case of magenta pentagons each background is applied to the corresponding data-set. For green triangles, the background is jointly measured on both observations.

In order to check if the normalisation of the model are constant between the two data-sets, we measured it on single observations separately. Due to the different position angles, it was not possible to use exactly the same region on the sky; however they cover, roughly, the same portion of the detector.

Figure 5.2 shows how the cluster profile temperature (and one sigma errors) changes with different assumptions on the background. As reference, black stars represent the data obtained by using a blank-sky background. Red squares are computed by modelling the source-free region only on observation 15123 (red circle in Fig. 5.1) and then use it as background for both data-sets. The same applies to blue circles with observation 16126. Magenta pentagons correspond to the case where each modelled background is used on the corresponding observation. Finally, green triangles are the adopted background, where normalisation are assumed to be constant between data-sets; therefore the two source-free regions can be used together to obtain a single background model. There is very little difference between magenta and green points; this confirms our assumption that the background does not change much, in normalisation, between the two observations. However, when using only one data-set to model the source-

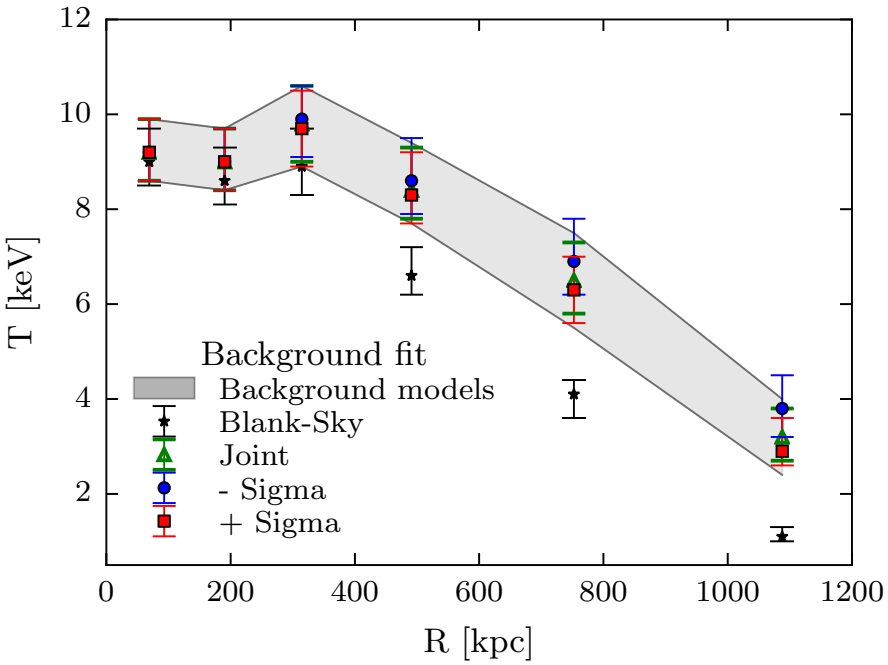


Figure 5.3.: Systematics effect on the temperature profile. Black stars correspond to blank-sky file subtraction. Green triangles and shaded region are the adopted model and the most extreme errors of the different choices in the background. Blue circles and red squares represent the temperature profile measured using a background with normalisation of minus and plus one sigma respectively.

free region, the resulting temperature are slightly offset; this can arise from problems in the data reduction. For instance the fit to the source-free region of observation 15123 (black lines) seems to fail at line 9.72 keV;this will cause an over estimation of the background, which in turn will give a lower temperature for the outskirts of the cluster, as observed in Fig. 5.2.

To better assess the systematic errors we measured the cluster temperature profile using normalisation for the nxb at plus and minus one sigma from the model; these are shown in Fig. 5.3 as red squares and blue circles respectively. In addition, blank-sky background modelling is shown in black stars and the adopted background as green empty triangles. The grey shaded area show the maximum errors on the temperature corresponding to different choices in the background modelling (top panel). Although quite similar, the errors are slightly dominated by systematics effects in the outer regions of the cluster.

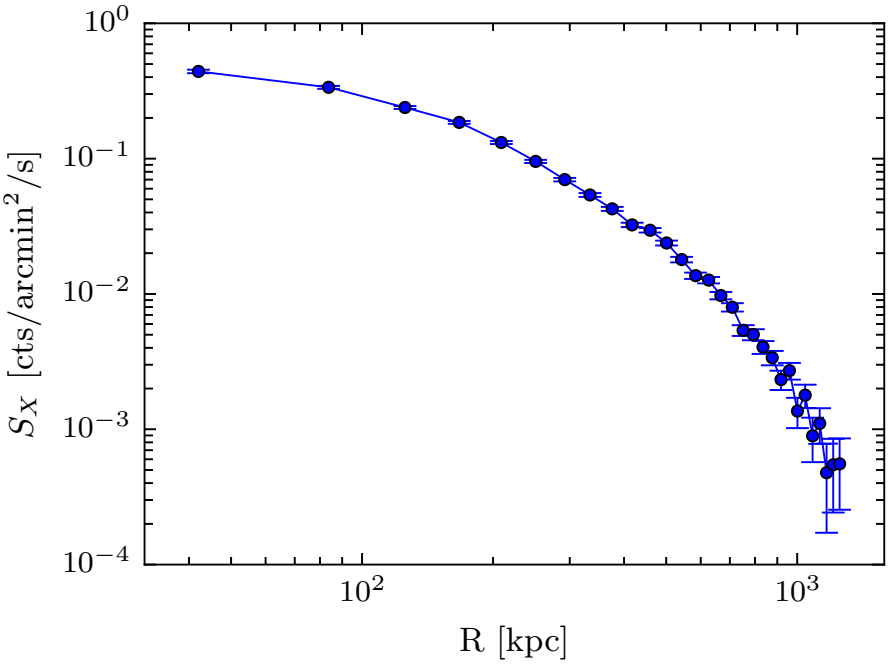


Figure 5.4.: Surface brightness profile measured from 30 concentric annuli up to a radius of 600 px (295.2 arcsec).

### 5.1.2. Observed profiles

Additionally, we measured the surface brightness from the combined data-set on 30 concentric annuli, up to a radius of 600 px (295.2 arcsec). The background is measured on the subsequent annulus, with a width of 30 px (14.76 arcsec). The result is shown in Fig. 5.4, where the error bars are drawn at $1\sigma$.

Finally, Figure 5.5 shows the resulting profiles of temperature (upper panel), metallicity (middle panel) and normalisation (lower panel), all using the reference background model. Error bars represent statistical errors at $1\sigma$.

## 5.2. Strong lensing mass model

We here present briefly the strong lensing analysis of Abell 1703, performed using the parametric Lenstool software (Jullo, Kneib, et al., 2007). For more details, we refer to M. Limousin, Richard, Kneib, et al., (2008) and Richard, Pei, et al., (2009). During this PhD, we have updated the published mass model, in particular by performing the optimisation in the image plane instead of source plane, which is known to be more reliable. Our approach is parametric: we describe the cluster using a smooth large scale dark matter halo on top of which we add the individual cluster galaxies. More details about our analysis approach is given in Jullo, Kneib, et al., (2007). We use as constraints 53 multiple images,

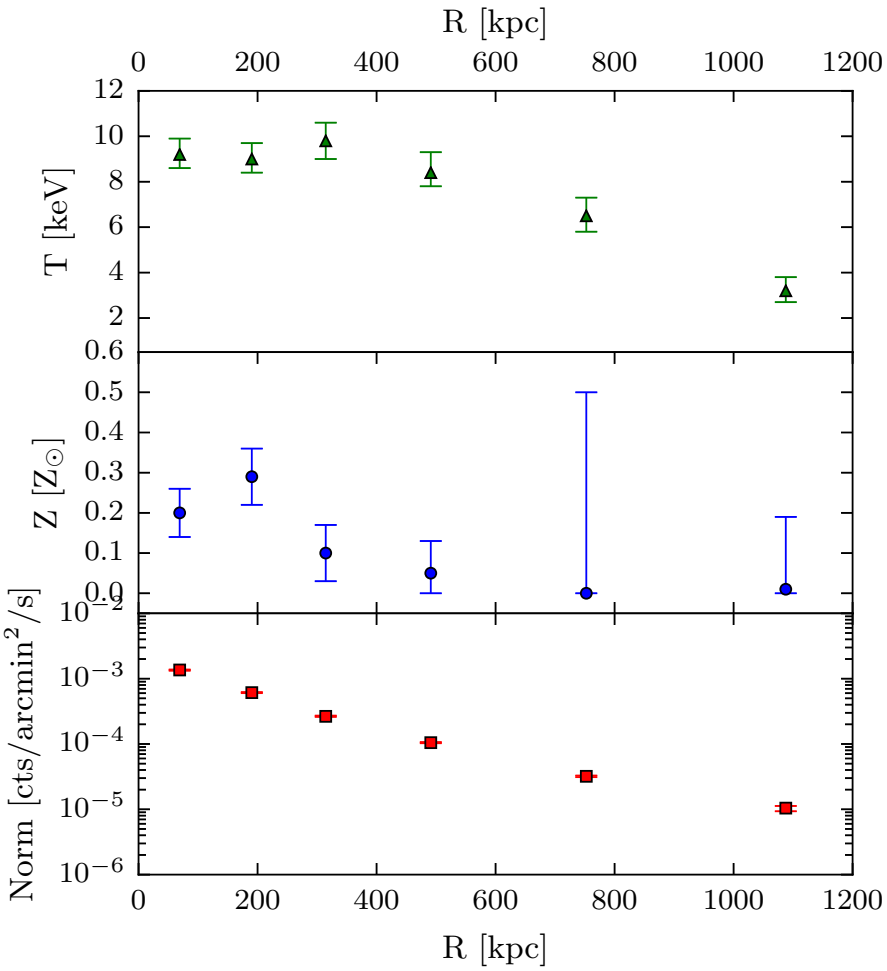


Figure 5.5.: Measured profiles as function of radius: temperature (upper panel), metallicity (middle panel) and normalisation (lower panel).

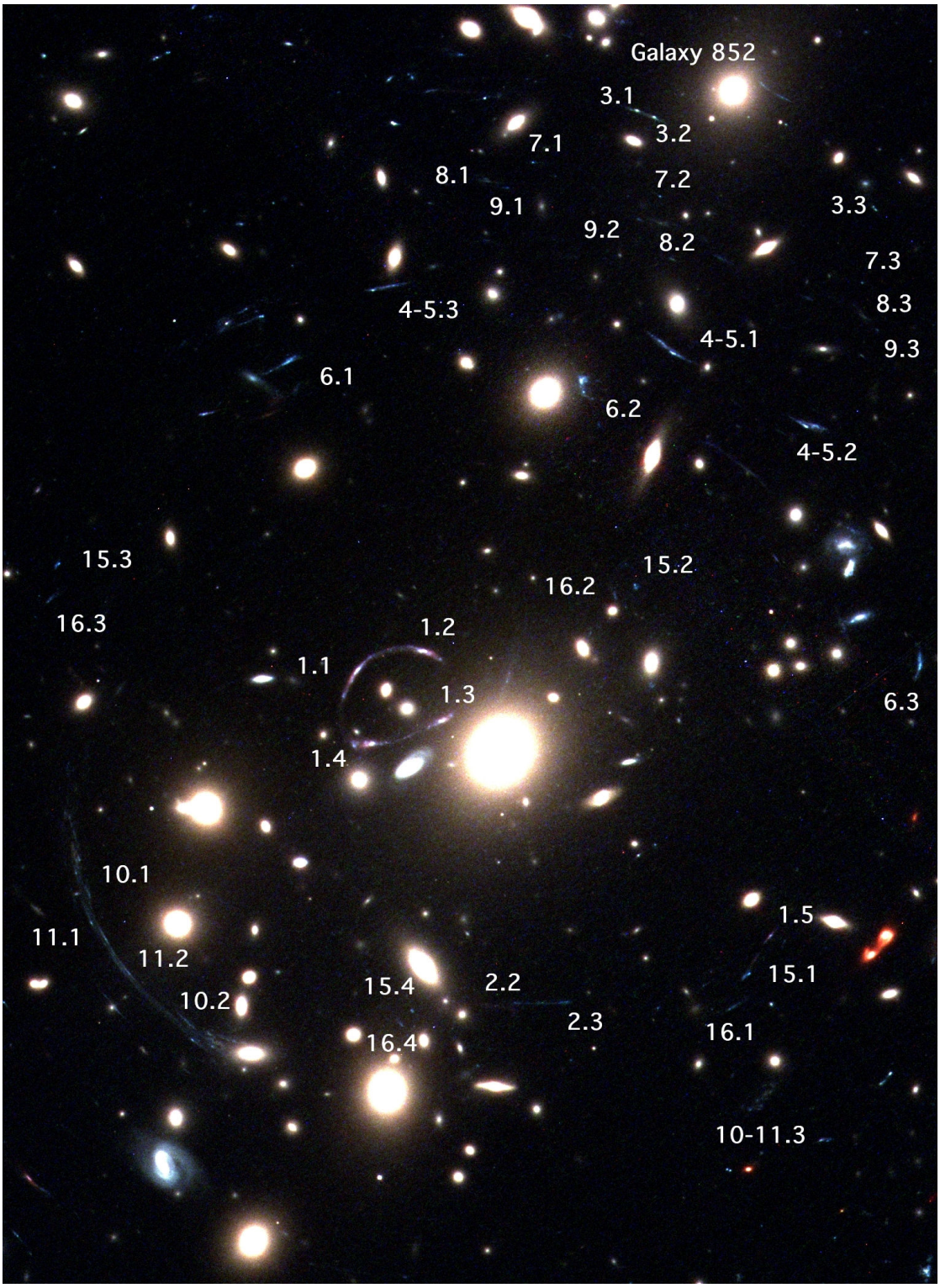


Figure 5.6.: Location of the 53 multiple images used in this work.

belonging to 16 multiply imaged systems (Fig. 5.6), of which 9 are spectroscopically confirmed. The result of the optimisation are some parameters describing the mass distribution. From these parameters, we can derive a two dimensional mass map with the associated error bars. This is this output from the lensing analysis which is used as an input in our combined analysis.

## 5.3. Spherical Modelling

In this section, we apply the algorithm presented in the previous chapter to the X-ray data-set. We have decided to start with a spherical framework and later, in a following work, increase the complexity of the model, to better understand the systematics introduced by a spherical X-ray only analysis. This also allows us to compare the parameters measured by our code with the ones presented in Gastaldello, Bonamigo et al. (in prep), obtained with the algorithm developed by Stefano Ettori and collaborators (Ettori, Gastaldello, et al., 2010). For this reason, we describe the electron density with the following analytic function (Vikhlinin, A. Kravtsov, et al., 2006):

$$n_e(R_{ICM}) = n_0 \, (1 + R^2_{ICM}/r^2_{c_1})^{-3/2\,\varepsilon} (1 + R^3_{ICM}/r^3_{c_2})^{-\upsilon/3}; \tag{5.1}$$

where $r_{c_2}$ and $\upsilon$ are the characteristic radius and slope of the profile at large scales; these additional parameters were not considered in the previous chapter (eq. 4.8). We have also set $\delta$ to zero, as the cluster does not show the presence of a cool core both in the temperature and surface brightness profile. Finally, we assume zero non-thermal pressure $P_{nT}$ and the boundary condition of the hydrostatic equilibrium $P_0$ is set by deprojecting the density in the outermost annulus $P_0 = 1.622 \times 10^{-4}\,\mathrm{keV\,cm^{-3}}$ at a distance from the centre of the cluster of $R = 1.684\,\mathrm{Mpc}$. All these simplifying assumptions have been chosen in order to compare the results of this work with the values presented in Gastaldello, Bonamigo et al. (in prep).

As previously stated, we have adopted a Poisson likelihood for the surface brightness map (eq. 4.13) and a Gaussian function for the X-ray temperature profile (eq. 4.12). We then simply multiply the two likelihoods without adding artificial weights to the fitting procedure. The background in the surface brightness map is assumed to be constant and it has been measured in an area of the image not contaminated by the cluster emission. Moreover, we have chosen flat prior distribution for all parameters, as shown in Table 5.1.

In this analysis, we have started the algorithm from a set of values obtained by a maximum likelihood method and then spread the walkers using a N-dimensional Gaussian with standard deviations equal to 10% of the priors support.

The result of the MCMC sampling are presented in Figure 5.7, where darker contours show the areas that contain $39.3\%$ of the volume, lighter contours con-

| Parameter name | Prior distribution |
|---|---|
| $c_{200}$ | *Uniform* [1, 12] |
| $R_{200}$ [kpc] | *Uniform* [600, 3000] |
| $n_0$ [cm$^{-3}$] | *Uniform* [$10^{-3}$, 1] |
| $r_{c_1}$ [kpc] | *Uniform* [10, 300] |
| $\varepsilon$ | *Uniform* [0, 1] |
| $r_{c_2}$ [kpc] | *Uniform* [300, 2000] |
| $\upsilon$ | *Uniform* [0, 4] |

Table 5.1.: Priors used in the analysis of Abell 1703

tain $86.4\%$; these are the values that correspond to $1$ and $2$ sigma for a 2D normal distribution. In the one dimensional histograms, dashed vertical lines show the median, $16\%$ and $84\%$ percentiles; these values are also shown in Table 5.1. The green lines show the reference values presented in Gastaldello, Bonamigo et al. (in prep). The fit gives a $\chi^2$ of 47185, with 51467 degrees of freedom; this corresponds to a reduced $\chi^2$ of 0.92: however, as the surface brightness can not be described by a Gaussian likelihood function, the popular rule of thumb of having a value close to the unity does not hold anymore and there is no real "aim-to number" (for large number counts the $\chi^2$ should tend to one, thanks to the central limit theorem). Individually, the two observables have $\chi^2$ of 47171 and 12.85 and a reduced value of 0.9165253 and 2.14244893. Here we have divided only by the corresponding number of data points, as it is not straightforward to compute separately the degrees of freedom in a combined analysis: for example the X-ray temperature profile has 6 values and the model has 7 fitted parameters).

Almost all parameters are in agreement within $1$ sigma; however it has to be noticed that even though the physical model is the same, the two analysis differ in the fitting procedure. While we have inferred all the parameters from a joint analysis of the surface brightness map and the temperature profile; the reference method only fits the temperature profile using the observed electron density (obtained by deprojecting the surface brightness). Moreover, the parameter of the Vikhlinin profile have been derived from a one dimensional fit, as opposed to our 2D map fit.

Having derived the parameters of the NFW profile from an X-ray only spherical analysis, we can use them to predict the projected mass measured by the gravitational lensing. This is possible because, having assumed hydrostatical equilibrium, the X-ray is sensitive to the gravitational potential generated by the total mass distribution. The upper panel of Figure 5.8 shows the projected mass profile from the lensing data presented in Section 5.2, while the second and third panels show the surface brightness and X-ray temperature profile, respectively. We remind the reader that in the algorithm we use the surface brightness map and that the 1-D profile is shown here just for illustration purposes. The

green points with error bars are the observed values; while blue lines are the Montecarlo-Markov chains. Both X-ray profiles are very well recovered by the fitting procedure, however the model is not able to predict the lensing data: a spherical X-ray only analysis of Abell 1703 under-estimates the mass of the galaxy cluster, similarly with what has been found in Abell 1689 (A. Morandi, K. Pedersen, et al., 2011b).

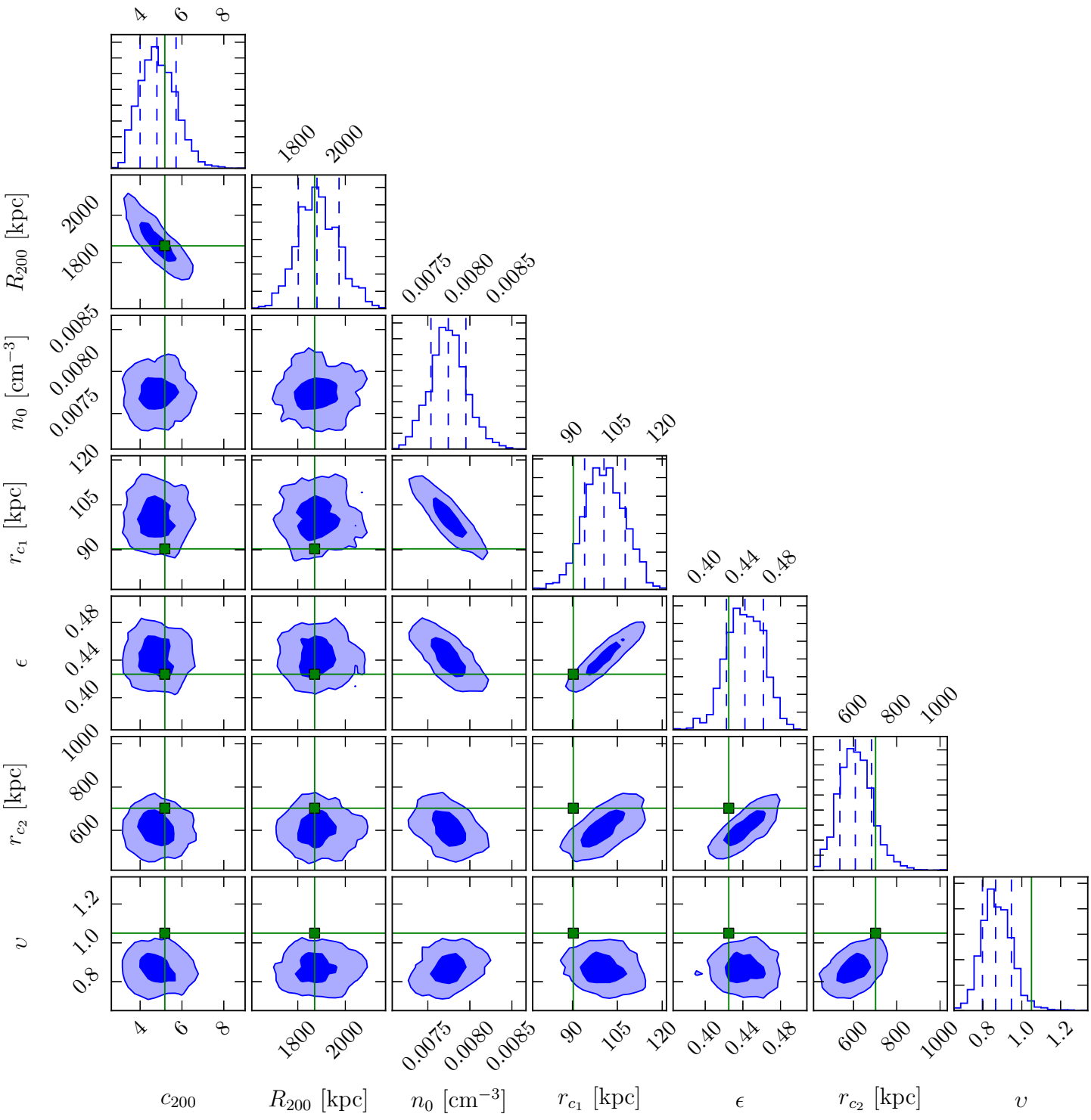


Figure 5.7.: Marginalised posterior probability distributions for the model parameters of Abell 1703

## 5.4. Summary and Conclusions

In this chapter, we have presented a set of two Chandra X-ray observations of the cluster of galaxies Abell 1703 which correspond to a total of almost 80ks of exposure. We have modelled the X-ray background and the instrumental noise with a simplified version of the framework proposed by Bartalucci, Mazzotta, et al., (2014) and then checked how the resulting temperature profile depend on the method of combining the two data-sets. This systematic effect turns out to be about the same order of magnitude of the statistical errors.

We have then used the algorithm presented in the previous chapter to model the X-ray observations and obtained parameters that are consistent with what has been derived by a reference pipeline (Ettori, Gastaldello, et al., 2010). However the adopted spherical framework predicts a projected mass that is lower than the one observed with strong gravitational lensing. Clearly this spherical model is not able to reconcile the observed X-ray data with the measured lensing signal and a combined triaxial analysis might be needed to obtain a consistent description of cluster of galaxy Abell 1703.

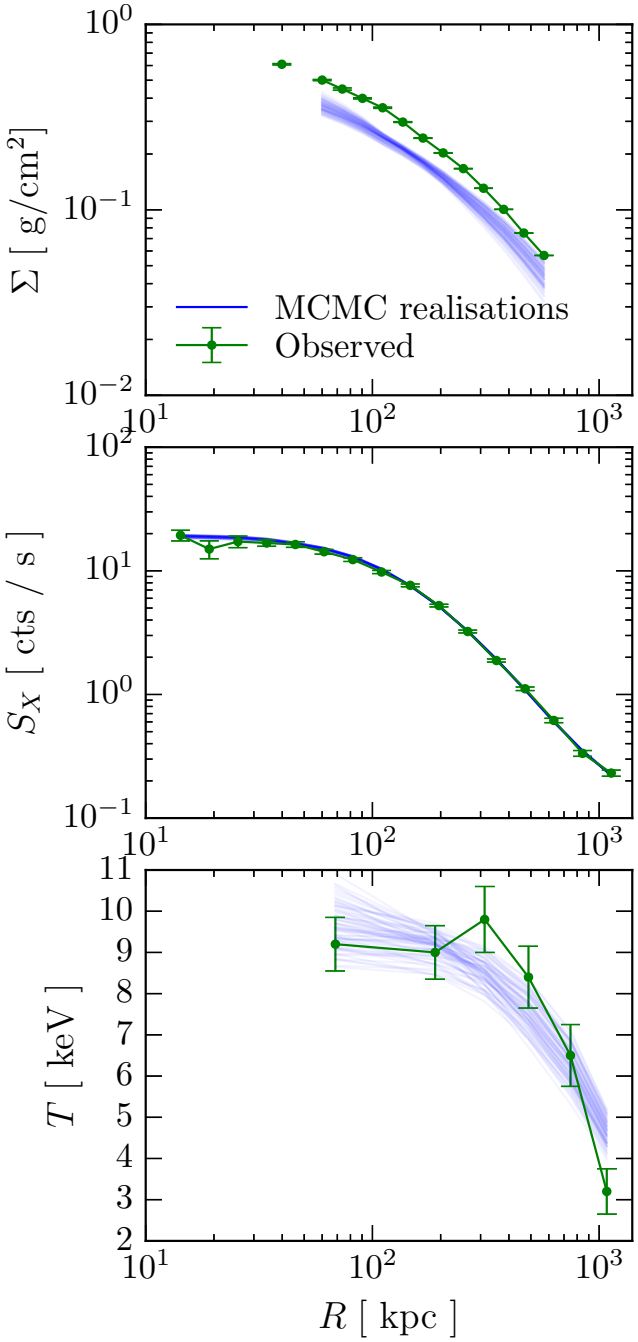


Figure 5.8.: Results from the spherical X-ray only analysis of Abell 1703. Each panel shows three profiles from top to bottom: projected 2D mass, X-Ray surface brightness and X-Ray temperature . The green points with error bars are the observed values; while blue lines are the Montecarlo-Markov chains. As a remainder, the fit is done in 2D for all observables but the X-Ray temperature; these one dimensional profiles are only used for visualisation.

# Conclusion

The study of clusters of galaxies is one of the most promising tools of astrophysics of the next decade. Thanks to the large surveys that will be conducted in the near future, we will be able to collect enough of these objects to have constraints on the cosmological parameters that are competitive with other, more traditional, probes. Such a large quantity of data will bring the modelling of galaxy clusters in a regime where the statistical errors are comparable if not smaller than the current systematics; therefore it is extremely important to improve the models we use to avoid biased results.

One of the many possible ways to enhance our description of these objects is to renounce to the inaccurate approximation that clusters of galaxies are spherical objects and move one step further by using triaxial ellipsoids to describe their shape. This has been possible only recently due to the improvement of both numerical simulations and observations. On one side, it is now possible to simulate with high spatial and mass resolution extremely large volumes, a fundamental requirement for the study of a statistically significant sample of dark matter haloes. These state of the art simulations enable very detailed descriptions of the inner structure and, in particular, of the shape of the dark matter distribution in galaxy clusters. The other advancement is the availability of deep optical and X-ray observations from telescopes like the Hubble Space Telescope and the Chandra X-ray observatory; with these powerful tools, it is now possible to constrain the properties of cluster of galaxies with unprecedented precision. In this thesis, I have exploited both these recent improvement in order to advance our understanding of the three dimensional shape of galaxy clusters.

First of all, I started by looking at what N-body simulations can tell us about the 3D structure of such objects (Chapter 2). By studying the particle distribution of more than half a million of dark matter haloes extracted from the Millennium XXL simulation (R. E. Angulo, V. Springel, et al., 2012b), I was able to:

- provide to the community distributions of the axis ratios of haloes hosting massive galaxy clusters, a mass regime previously unexplored;
- confirm the theoretical expectations that more massive objects are less spherical and that in general they tend to be prolate rather than oblate;
- show that distributions of the axis ratios can be described by analytical functions that only depend on a single parameter (density peak height $\nu$) and not on the cosmology or on the redshift.

These novel results are particularly useful to generate realistic mock haloes or as priors in the analysis of clusters of galaxies.

By using mock observations it is possible to study more in details possible systematic effects of a given measurement technique. In Chapter 3 I have looked at the MXXL clusters through the gravitational lensing effect generated by the *MOKA* code. The main conclusions of the study quantities what was already expected: strong gravitational lenses represent a biased population that is preferentially aligned along the line of sight. This special orientation is very important when studying galaxy clusters and it has to be kept into consideration, as it causes an higher concentration in the 2D radial density profile.

The other main result of this thesis is the modelling of multi-wavelength observations of galaxy clusters:

- firstly in the Introduction, I have presented a simple toy model to illustrate, both analytically and numerically, how the combination of complementary data-sets can help to solve the projection problem;
- then in Chapter 4, having introduced the real physical model, I have tested the triaxial reconstruction on mock analytical observations;
- finally, I have compared the results with what I have obtained, on the same data, with a spherical analysis.

In particular, the joint analysis of gravitational lensing and X-ray data is required to brake the degeneracies introduced by the projection into two dimensional observables. This is done in the new algorithm presented in Chapter 4. The test on mock data has shown that the new code is able to recover the original 3D shape from projected noisy observables although some systematic effects are still present at this level of noise. Moreover, the spherical model applied to triaxial data has given biased results with mass and concentration that can be off even by $30\%$.

In the last chapter of this thesis (Chapter 5), I have reduced and analysed two Chandra X-ray observations of the cluster of galaxies Abell 1703. I have first subtracted the X-ray background and the instrumental noise using a model that consider the continuum emission and three prominent lines. Then I have applied the code presented in the previous chapter to model the X-ray emission with a spherically symmetric distribution. When using the fitted parameters to predict the total mass, the X-ray only spherical analysis under-estimates the projected mass measured by gravitational lensing, suggesting that a more accurate triaxial parametrisation should be applied to the galaxy cluster.

With this thesis, I have tried to contribute to an advance in both the theoretical and the observational side of the study of galaxy cluster in a triaxial framework. The field is still in its early phases; however it is a necessary step in the direction of an accurate description of clusters of galaxies in the coming era of precision cosmology.

# Bibliography


[1] B. Allgood, R. A. Flores, et al. “The shape of dark matter haloes: dependence on mass, redshift, radius and formation”. In: *MNRAS* 367 (Apr. 2006), pp. 1781–1796. DOI: 10.1111/j.1365-2966.2006.10094.x. eprint: arXiv:astro-ph/0508497 (cit. on p. 18).

[2] B. Allgood, R. a. Flores, et al. “The shape of dark matter haloes: dependence on mass, redshift, radius and formation”. In: *MNRAS* 367.4 (Apr. 2006), pp. 1781–1796. ISSN: 0035-8711. DOI: 10.1111/j.1365-2966.2006.10094.x. URL: http://mnras.oxfordjournals.org/cgi/doi/10.1111/j.1365-2966.2006.10094.x (cit. on p. 24).

[3] R. E. Angulo, V. Springel, et al. “Scaling relations for galaxy clusters in the Millennium-XXL simulation”. In: *ArXiv e-prints* (Mar. 2012). arXiv: 1203.3216 [astro-ph.CO] (cit. on p. 22).

[4] R E Angulo, V Springel, et al. “Scaling relations for galaxy clusters in the Millennium-XXL simulation”. In: *MNRAS* 426.3 (Nov. 2012), pp. 2046–2062. ISSN: 00358711. DOI: 10.1111/j.1365-2966.2012.21830.x. URL: http://arxiv.org/abs/1203.3216$%5Cbackslash$nhttp://mnras.oxfordjournals.org/cgi/doi/10.1111/j.1365-2966.2012.21830.x (cit. on pp. 24, 92).

[5] J. Bailin and M. Steinmetz. “Internal and External Alignment of the Shapes and Angular Momenta of ΛCDM Halos”. In: *ApJ* 627 (July 2005), pp. 647–665. DOI: 10.1086/430397. eprint: arXiv:astro-ph/0408163 (cit. on p. 18).

[6] I. Bartalucci, P. Mazzotta, et al. “Chandra ACIS-I particle background: an analytical model”. In: *A&A* 566, A25 (June 2014), A25. DOI: 10.1051/0004-6361/201423443. arXiv: 1404.3587 [astro-ph.IM] (cit. on pp. 79, 90).

[7] M. Bartelmann and P. Schneider. “Weak gravitational lensing”. In: *Physics Reports* 340 (Jan. 2001), pp. 291–472. DOI: 10.1016/S0370-1573(00)00082-X. eprint: astro-ph/9912508 (cit. on p. 16).

[8] P. Bett, V. Eke, et al. “The spin and shape of dark matter haloes in the Millennium simulation of a Λ cold dark matter universe”. In: *MNRAS* 376 (Mar. 2007), pp. 215–232. DOI: 10.1111/j.1365-2966.2007.11432.x. eprint: arXiv:astro-ph/0608607 (cit. on p. 18).

[9] B. Binggeli. “The shape and orientation of clusters of galaxies”. In: *A&A* 107 (Mar. 1982), pp. 338–349 (cit. on p. 18).

[10] M. Bonamigo, G. Despali, et al. “Universality of dark matter haloes shape over six decades in mass: insights from the Millennium XXL and SBARBINE simulations”. In: *MNRAS* 449 (May 2015), pp. 3171–3182. DOI: 10.1093/mnras/stv417. arXiv: 1410.0015 (cit. on pp. 22, 25, 72, 75).

[11] J. R. Bond, S. Cole, et al. “Excursion set mass functions for hierarchical Gaussian fluctuations”. In: *ApJ* 379 (Oct. 1991), pp. 440–460. DOI: 10.1086/170520 (cit. on p. 12).

[12] T. Broadhurst, N. Benítez, et al. “Strong-Lensing Analysis of A1689 from Deep Advanced Camera Images”. In: *ApJ* 621 (Mar. 2005), pp. 53–88. DOI: 10.1086/426494. eprint: astro-ph/0409132 (cit. on p. 18).

[13] D. A. Buote and C. R. Canizares. “Geometrical evidence for dark matter: X-ray constraints on the mass of the elliptical galaxy NGC 720”. In: *ApJ* 427 (May 1994), pp. 86–111. DOI: 10.1086/174123. eprint: arXiv:astro-ph/9311073 (cit. on p. 59).

[14] J. E. Carlstrom. “Cosmology with the Sunyaev-Zel’dovich Effect”. In: *APS April Meeting Abstracts*. Apr. 2002 (cit. on p. 16).

[15] D. Clowe, M. Bradač, et al. “A Direct Empirical Proof of the Existence of Dark Matter”. In: *ApJ* 648 (Sept. 2006), pp. L109–L113. DOI: 10.1086/508162. eprint: astro-ph/0608407 (cit. on p. 11).

[16] S. Cole and C. Lacey. “The structure of dark matter haloes in hierarchical clustering models”. In: *MNRAS* 281 (July 1996), p. 716. eprint: arXiv:astro-ph/9510147 (cit. on p. 18).

[17] G. Despali, C. Giocoli, R. E. Angulo, et al. “The universality of the virial halo mass function and models for non-universality of other halo definitions”. In: *MNRAS* 456 (Mar. 2016), pp. 2486–2504. DOI: 10.1093/mnras/stv2842. arXiv: 1507.05627 (cit. on pp. 12, 24).

[18] G. Despali, C. Giocoli, M. Bonamigo, et al. “A look to the inside of haloes: a characterisation of the halo shape as a function of overdensity in the Planck cosmology”. In: *ArXiv e-prints* (May 2016). arXiv: 1605.04319 (cit. on pp. 22, 134).

[19] G Despali, Carlo Giocoli, et al. “Some like it triaxial: the universality of dark matter halo shapes and their evolution along the cosmic time”. In: *arXiv preprint arXiv:1404.6527* 11.May (2014), pp. 1–11. arXiv: arXiv:1404.6527v2. URL: http://arxiv.org/abs/1404.6527 (cit. on p. 24).

[20] G. Despali, G. Tormen, et al. “Ellipsoidal halo finders and implications for models of triaxial halo formation”. In: *MNRAS* 431.2 (Mar. 2013), pp. 1143–1159. ISSN: 0035-8711. DOI: 10.1093/mnras/stt235. URL: http://mnras.oxfordjournals.org/cgi/doi/10.1093/mnras/stt235 (cit. on pp. 18, 24, 72).

[21] J. Dubinski and R. G. Carlberg. “The structure of cold dark matter halos”. In: *ApJ* 378 (Sept. 1991), pp. 496–503. DOI: 10.1086/170451 (cit. on p. 18).

[22] A. R. Duffy, J. Schaye, et al. “Dark matter halo concentrations in the Wilkinson Microwave Anisotropy Probe year 5 cosmology”. In: *MNRAS* 390 (Oct. 2008), pp. L64–L68. DOI: 10.1111/j.1745-3933.2008.00537.x. arXiv: 0804.2486 (cit. on pp. 18, 63).

[23] D. J. Eisenstein, I. Zehavi, et al. “Detection of the Baryon Acoustic Peak in the Large-Scale Correlation Function of SDSS Luminous Red Galaxies”. In: *ApJ* 633 (Nov. 2005), pp. 560–574. DOI: 10.1086/466512. eprint: astro-ph/0501171 (cit. on p. 10).

[24] S. Ettori, A. Donnarumma, et al. “Mass Profiles of Galaxy Clusters from X-ray Analysis”. In: *Space Sci.Rev.* 177 (Aug. 2013), pp. 119–154. DOI: 10.1007/s11214-013-9976-7. arXiv: 1303.3530 (cit. on p. 14).

[25] S. Ettori, F. Gastaldello, et al. “Mass profiles and c-$M_{DM}$ relation in X-ray luminous galaxy clusters”. In: *A&A* 524, A68 (Dec. 2010), A68. DOI: 10.1051/0004-6361/201015271 (cit. on pp. 86, 90).

[26] D. Fabricant, G. Rybicki, et al. “X-ray measurements of the nonspherical mass distribution in the cluster of galaxies A2256”. In: *ApJ* 286 (Nov. 1984), pp. 186–195. DOI: 10.1086/162586 (cit. on p. 18).

[27] D. Foreman-Mackey, D. W. Hogg, et al. “emcee: The MCMC Hammer”. In: *PASP* 125 (Mar. 2013), pp. 306–312. DOI: 10.1086/670067. arXiv: 1202.3665 [astro-ph.IM] (cit. on pp. 63, 66).

[28] C. S. Frenk, S. D. M. White, et al. “The formation of dark halos in a universe dominated by cold dark matter”. In: *ApJ* 327 (Apr. 1988), pp. 507–525. DOI: 10.1086/166213 (cit. on p. 18).

[29] L. Gao, J. F. Navarro, et al. “The Phoenix Project: the dark side of rich Galaxy clusters”. In: *MNRAS* 425 (Sept. 2012), pp. 2169–2186. DOI: 10.1111/j.1365-2966.2012.21564.x. arXiv: 1201.1940 [astro-ph.CO] (cit. on p. 18).

[30] C. Giocoli, M. Bonamigo, et al. “Characterising Strong Lensing Galaxy Clusters using the Millennium-XXL and MOKA simulations”. In: *ArXiv e-prints* (Apr. 2016). arXiv: 1604.03109 (cit. on pp. 22, 39, 64).

[31] C. Giocoli, M. Meneghetti, et al. “MOKA: a new tool for strong lensing studies”. In: *MNRAS* 421 (Apr. 2012), pp. 3343–3355. DOI: 10.1111/j.1365-2966.2012.20558.x (cit. on p. 38).

[32] J. F. Hennawi, N. Dalal, et al. “Characterizing the Cluster Lens Population”. In: *ApJ* 654 (Jan. 2007), pp. 714–730. DOI: 10.1086/497362. eprint: arXiv:astro-ph/0506171 (cit. on p. 38).

[33] P. F. Hopkins, N. A. Bahcall, et al. “Cluster Alignments and Ellipticities in ΛCDM Cosmology”. In: *ApJ* 618 (Jan. 2005), pp. 1–15. DOI: 10.1086/425993. eprint: arXiv:astro-ph/0409652 (cit. on p. 18).

[34] A. Jenkins, C. S. Frenk, et al. “The mass function of dark matter haloes”. In: *MNRAS* 321 (Feb. 2001), pp. 372–384. DOI: 10.1046/j.1365-8711.2001.04029.x. eprint: astro-ph/0005260 (cit. on p. 12).

[35] Y. P. Jing and Y. Suto. “Triaxial Modeling of Halo Density Profiles with High-Resolution N-Body Simulations”. In: *ApJ* 574 (Aug. 2002), pp. 538–553. DOI: 10.1086/341065. eprint: arXiv:astro-ph/0202064 (cit. on pp. 22, 58).

[36] YP Jing and Y Suto. “Triaxial modeling of halo density profiles with high-resolution N-body simulations”. In: *The Astrophysical Journal* (2002), pp. 538–553. URL: http://iopscience.iop.org/0004-637X/574/2/538 (cit. on pp. 18, 24).

[37] E. Jullo, J.-P. Kneib, et al. “A Bayesian approach to strong lensing modelling of galaxy clusters”. In: *New Journal of Physics* 9 (Dec. 2007), pp. 447–+. DOI: 10.1088/1367-2630/9/12/447. eprint: arXiv:0706.0048 (cit. on p. 83).

[38] S. F. Kasun and A. E. Evrard. “Shapes and Alignments of Galaxy Cluster Halos”. In: *ApJ* 629 (Aug. 2005), pp. 781–790. DOI: 10.1086/430811. eprint: arXiv:astro-ph/0408056 (cit. on p. 18).

[39] J.-P. Kneib and P. Natarajan. “Cluster lenses”. In: *A&A Rev.* 19, 47 (Nov. 2011), p. 47. DOI: 10.1007/s00159-011-0047-3. arXiv: 1202.0185 [astro-ph.CO] (cit. on p. 17).

[40] C. Lacey and S. Cole. “Merger rates in hierarchical models of galaxy formation”. In: *MNRAS* 262 (June 1993), pp. 627–649 (cit. on p. 12).

[41] E. T. Lau, A. V. Kravtsov, et al. “Residual Gas Motions in the Intracluster Medium and Bias in Hydrostatic Measurements of Mass Profiles of Clusters”. In: *ApJ* 705 (Nov. 2009), pp. 1129–1138. DOI: 10.1088/0004-637X/705/2/1129. arXiv: 0903.4895 (cit. on p. 16).

[42] J. Lee and Y. Suto. “Modeling Intracluster Gas in Triaxial Dark Halos: An Analytic Ap proach”. In: *ApJ* 585 (Mar. 2003), pp. 151–160. DOI: 10.1086/345931. eprint: arXiv:astro-ph/0211007 (cit. on p. 59).

[43] M. Limousin, J. Richard, E. Jullo, et al. “Strong-lensing analysis of MACS J0717.5+3745 from Hubble Frontier Fields observations: How well can the mass distribution be constrained?” In: *A&A* 588, A99 (Apr. 2016), A99. DOI: 10.1051/0004-6361/201527638. arXiv: 1510.08077 (cit. on p. 119).

[44] M. Limousin, J. Richard, J.-P. Kneib, et al. “Strong lensing in Abell 1703: constraints on the slope of the inner dark matter distribution”. In: *A&A* 489 (Oct. 2008), pp. 23–35. DOI: 10.1051/0004-6361:200809646. arXiv: 0802.4292 (cit. on p. 83).

[45] Marceau Limousin, Andrea Morandi, et al. “The Three-Dimensional Shapes of Galaxy Clusters”. In: *Space Science Reviews* 177.1-4 (May 2013), pp. 155–194. ISSN: 0038-6308. DOI: 10.1007/s11214-013-9980-y. URL: http://link.springer.com/10.1007/s11214-013-9980-y (cit. on pp. 19, 56–58, 63).

[46] A. V. Macciò, A. A. Dutton, et al. “Concentration, spin and shape of dark matter haloes as a function of the cosmological model: WMAP1, WMAP3 and WMAP5 results”. In: *MNRAS* 391 (Dec. 2008), pp. 1940–1954. DOI: 10.1111/j.1365-2966.2008.14029.x (cit. on p. 24).

[47] A. Mahdavi, H. Hoekstra, et al. “Evidence for non-hydrostatic gas from the cluster X-ray to lensing mass ratio”. In: *MNRAS* 384 (Mar. 2008), pp. 1567–1574. DOI: 10.1111/j.1365-2966.2007.12796.x. arXiv: 0710.4132 (cit. on p. 16).

[48] P. J. Marshall, M. P. Hobson, et al. “Bayesian joint analysis of cluster weak lensing and Sunyaev-Zel’dovich effect data”. In: *MNRAS* 346 (Dec. 2003), pp. 489–500. DOI: 10.1046/j.1365-2966.2003.07111.x. eprint: arXiv:astro-ph/0307098 (cit. on p. 61).

[49] P. Mazzotta, E. Rasia, et al. “Comparing the temperatures of galaxy clusters from hydrodynamical N-body simulations to Chandra and XMM-Newton observations”. In: *MNRAS* 354 (Oct. 2004), pp. 10–24. DOI: 10.1111/j.1365-2966.2004.08167.x. eprint: astro-ph/0409618 (cit. on p. 61).

[50] M. Meneghetti, C. Fedeli, et al. “Strong lensing in the MARENOSTRUM UNIVERSE. I. Biases in the cluster lens population”. In: *A&A* 519, A90 (Sept. 2010), A90. DOI: 10.1051/0004-6361/201014098. arXiv: 1003.4544 [astro-ph.CO] (cit. on p. 38).

[51] M. Meneghetti, E. Rasia, et al. “Weighing simulated galaxy clusters using lensing and X-ray”. In: *A&A* 514, A93 (May 2010), A93. DOI: 10.1051/0004-6361/200913222. arXiv: 0912.1343 [astro-ph.CO] (cit. on p. 16).

[52] A. Morandi and M. Limousin. “Triaxiality, principal axis orientation and non-thermal pressure in Abell 383”. In: *MNRAS* 421 (Apr. 2012), pp. 3147–3158. DOI: 10.1111/j.1365-2966.2012.20537.x. arXiv: 1108.0769 [astro-ph.CO] (cit. on pp. 19, 22, 56).

[53] A. Morandi, M. Limousin, Y. Rephaeli, et al. “Triaxiality and non-thermal gas pressure in Abell 1689”. In: *MNRAS* 416 (Oct. 2011b), pp. 2567–2573. DOI: 10.1111/j.1365-2966.2011.19175.x. arXiv: 1103.0202 [astro-ph.CO] (cit. on pp. 56, 59).

[54] A. Morandi, M. Limousin, J. Sayers, et al. “X-ray, lensing and Sunyaev Zel’dovich triaxial analysis of Abell 1835 out to R200”. In: *ArXiv e-prints* (Nov. 2011). arXiv: 1111.6189 [astro-ph.CO] (cit. on pp. 56, 63).

[55] A. Morandi, K. Pedersen, et al. “Unveiling the Three-dimensional Structure of Galaxy Clusters: Resolving the Discrepancy Between X-ray and Lensing Masses”. In: *ApJ* 713 (Apr. 2010), pp. 491–502. DOI: 10.1088/0004-637X/713/1/491. arXiv: 0912.2648 (cit. on pp. 56, 59).

[56] A. Morandi, K. Pedersen, et al. “Reconstructing the Triaxiality of the Galaxy Cluster A1689: Solving the X-ray and Strong Lensing Mass Discrepancy”. In: *ApJ* 729, 37 (Mar. 2011), p. 37. DOI: 10.1088/0004-637X/729/1/37. arXiv: 1001.1656 [astro-ph.CO] (cit. on p. 56).

[57] Andrea Morandi, Kristian Pedersen, et al. “Reconstructing the Triaxiality of the Galaxy Cluster A1689: Solving the X-ray and Strong Lensing Mass Discrepancy”. en. In: *The Astrophysical Journal* 729.1 (Mar. 2011), p. 37. ISSN: 0004-637X. DOI: 10.1088/0004-637X/729/1/37. URL: http://iopscience.iop.org/0004-637X/729/1/37/article/%20http://stacks.iop.org/0004-637X/729/i=1/a=37?key=crossref.82630d5cc8dd00558616b86c72d68a31 (cit. on p. 88).

[58] J. C. Muñoz-Cuartas, A. V. Macciò, et al. “The redshift evolution of $\Lambda$ cold dark matter halo parameters: concentration, spin and shape”. In: *MNRAS* 411 (Feb. 2011), pp. 584–594. DOI: 10.1111/j.1365-2966.2010.17704.x. arXiv: 1007.0438 [astro-ph.CO] (cit. on pp. 18, 24).

[59] D. Nagai, A. Vikhlinin, et al. “Testing X-Ray Measurements of Galaxy Clusters with Cosmological Simulations”. In: *ApJ* 655 (Jan. 2007), pp. 98–108. DOI: 10.1086/509868. eprint: arXiv:astro-ph/0609247 (cit. on p. 16).

[60] J. F. Navarro, C. S. Frenk, et al. “The Structure of Cold Dark Matter Halos”. In: *ApJ* 462 (May 1996), pp. 563–+. DOI: 10.1086/177173. eprint: arXiv:astro-ph/9508025 (cit. on p. 11).

[61] A. F. Neto, L. Gao, et al. “The statistics of $\Lambda$ CDM halo concentrations”. In: *MNRAS* 381 (Nov. 2007), pp. 1450–1462. DOI: 10.1111/j.1365-2966.2007.12381.x. eprint: arXiv:0706.2919 (cit. on p. 18).

[62] M. Oguri, M. Takada, et al. “Direct measurement of dark matter halo ellipticity from two-dimensional lensing shear maps of 25 massive clusters”. In: *MNRAS* 405 (July 2010), pp. 2215–2230. DOI: 10.1111/j.1365-2966.2010.16622.x. arXiv: 1004.4214 [astro-ph.CO] (cit. on p. 18).

[63] D. J. Paz, D. G. Lambas, et al. “Shapes of clusters and groups of galaxies: comparison of model predictions with observations”. In: *MNRAS* 366 (Mar. 2006), pp. 1503–1510. DOI: 10.1111/j.1365-2966.2005.09934.x. eprint: arXiv:astro-ph/0509062 (cit. on p. 18).

[64] S. Perlmutter, G. Aldering, et al. “Measurements of Omega and Lambda from 42 High-Redshift Supernovae”. In: *ApJ* 517 (June 1999), pp. 565–586. DOI: 10.1086/307221. eprint: astro-ph/9812133 (cit. on p. 10).

[65] W. H. Press and P. Schechter. “Formation of Galaxies and Clusters of Galaxies by Self-Similar Gravitational Condensation”. In: *ApJ* 187 (Feb. 1974), pp. 425–438. DOI: 10.1086/152650 (cit. on p. 12).

[66] M. Redlich, M. Bartelmann, et al. “The strongest gravitational lenses: I. The statistical impact of cluster mergers”. In: *ArXiv e-prints* (May 2012). arXiv: 1205.6906 [astro-ph.CO] (cit. on p. 38).

[67] J. Richard, L. Pei, et al. “Keck spectroscopic survey of strongly lensed galaxies in Abell 1703: further evidence of a relaxed, unimodal cluster”. In: *A&A* 498 (Apr. 2009), pp. 37–47. DOI: 10.1051/0004-6361/200811366. arXiv: 0901.0427 [astro-ph.GA] (cit. on p. 83).

[68] A. G. Riess, A. V. Filippenko, et al. “Observational Evidence from Supernovae for an Accelerating Universe and a Cosmological Constant”. In: *AJ* 116 (Sept. 1998), pp. 1009–1038. DOI: 10.1086/300499. eprint: astro-ph/9805201 (cit. on p. 10).

[69] J. Sayers, S. R. Golwala, et al. “Cluster Morphologies and Model-independent Y $_{SZ}$ Estimates from Bolocam Sunyaev-Zel’dovich Images”. In: *ApJ* 728 (Feb. 2011a), pp. 39–+. DOI: 10.1088/0004-637X/728/1/39. arXiv: 1010.1798 [astro-ph.CO] (cit. on p. 18).

[70] Michael D Schneider, Carlos S Frenk, et al. “The shapes and alignments of dark matter halos”. In: *Journal of Cosmology and Astroparticle Physics* 2012.05 (May 2012), pp. 030–030. ISSN: 1475-7516. DOI: 10.1088/1475-7516/2012/05/030. URL: http://stacks.iop.org/1475-7516/2012/i=05/a=030?key=crossref.cc830ed75b217686133902a3b6e4b052 (cit. on p. 18).

[71] M. Sereno, S. Ettori, et al. “Shape and orientation of the gas distribution in A1689”. In: *MNRAS* 419 (Jan. 2012), pp. 2646–2656. DOI: 10.1111/j.1365-2966.2011.19914.x. arXiv: 1109.2732 [astro-ph.CO] (cit. on pp. 19, 20, 56).

[72] L. D. Shaw, D. Nagai, et al. “Impact of Cluster Physics on the Sunyaev-Zel’dovich Power Spec trum”. In: *ApJ* 725 (Dec. 2010), pp. 1452–1465. DOI: 10.1088/0004-637X/725/2/1452. arXiv: 1006.1945 [astro-ph.CO] (cit. on p. 60).

[73] R. K. Sheth, H. J. Mo, et al. “Ellipsoidal collapse and an improved model for the number and spatial distribution of dark matter haloes”. In: *MNRAS* 323.1 (May 2001), pp. 1–12. ISSN: 0035-8711. DOI: 10.1046/j.1365-8711.2001.04006.x. URL: http://mnras.oxfordjournals.org/cgi/doi/10.1046/j.1365-8711.2001.04006.x (cit. on p. 12).

[74] R. K. Sheth and G. Tormen. “Large-scale bias and the peak background split”. In: *MNRAS* 308 (Sept. 1999), pp. 119–126. DOI: 10.1046/j.1365-8711.1999.02692.x. eprint: astro-ph/9901122 (cit. on p. 12).

[75] G. Soucail, B. Fort, et al. “A blue ring-like structure, in the center of the A 370 cluster of galaxies”. In: *A&A* 172 (Jan. 1987), pp. L14–L16 (cit. on p. 18).

[76] K. Umetsu, M. Birkinshaw, et al. “Mass and Hot Baryons in Massive Galaxy Clusters from Subaru Weak-Lensing and AMiBA Sunyaev-Zel’Dovich Effect Observations”. In: *ApJ* 694 (Apr. 2009), pp. 1643–1663. DOI: 10.1088/0004-637X/694/2/1643. arXiv: 0810.0969 (cit. on p. 18).

[77] A. Vikhlinin, A. Kravtsov, et al. “Chandra Sample of Nearby Relaxed Galaxy Clusters: Mass, Gas Fraction, and Mass-Temperature Relation”. In: *ApJ* 640 (Apr. 2006), pp. 691–709. DOI: 10.1086/500288. eprint: arXiv:astro-ph/0507092 (cit. on pp. 60, 86).

[78] G. M. Voit. “Tracing cosmic evolution with clusters of galaxies”. In: *Reviews of Modern Physics* 77 (Apr. 2005), pp. 207–258. DOI: 10.1103/RevModPhys.77.207. eprint: astro-ph/0410173 (cit. on p. 12).

[79] J.-C. Waizmann, M. Redlich, et al. “The strongest gravitational lenses: II. Is the large Einstein radius of MACS J0717.5+3745 in conflict with LCDM?” In: *ArXiv e-prints* (July 2012). arXiv: 1207.0801 [astro-ph.CO] (cit. on p. 38).

[80] M. S. Warren, P. J. Quinn, et al. “Dark halos formed via dissipationless collapse. I - Shapes and alignment of angular momentum”. In: *ApJ* 399 (Nov. 1992), pp. 405–425. DOI: 10.1086/171937 (cit. on p. 18).

[81] J. S. B. Wyithe, E. L. Turner, et al. “Gravitational Lens Statistics for Generalized NFW Profiles: Pa rameter Degeneracy and Implications for Self-Interacting Cold Dark Matter”. In: *ApJ* 555 (July 2001), pp. 504–523. DOI: 10.1086/321437. eprint: arXiv:astro-ph/0007354 (cit. on p. 59).

[82] F. Zwicky. “On the Masses of Nebulae and of Clusters of Nebulae”. In: *ApJ* 86 (Oct. 1937), p. 217. DOI: 10.1086/143864 (cit. on p. 14).

# Notes

1 using the FFTW libraries: http://www.fftw.org

2 The value of 7 arcseconds ensures that the measurement of the size of the Einstein radius of the cluster is not affected nor by particle noise neither by the finite grid size of the map

# Appendices

# A. Some busy plots (AKA posterior probability distributions)

In this appendix, we show the posterior probability obtained with the triaxial analysis (from Fig. .9 to Fig. .15) and with the spherical analysis (from Fig. .16 to Fig. .22 ) as blue 2D filled contours and histograms. Dark contours show the areas that contain $39.3\%$ of the volume, lighter contours contain $86.4\%$; these are the values that correspond to $1$ and $2$ sigma for a 2D normal distribution. In the one dimensional histograms, dashed vertical lines show the median, $16\%$ and $84\%$ percentiles; these values are also shown in Table 4.2.

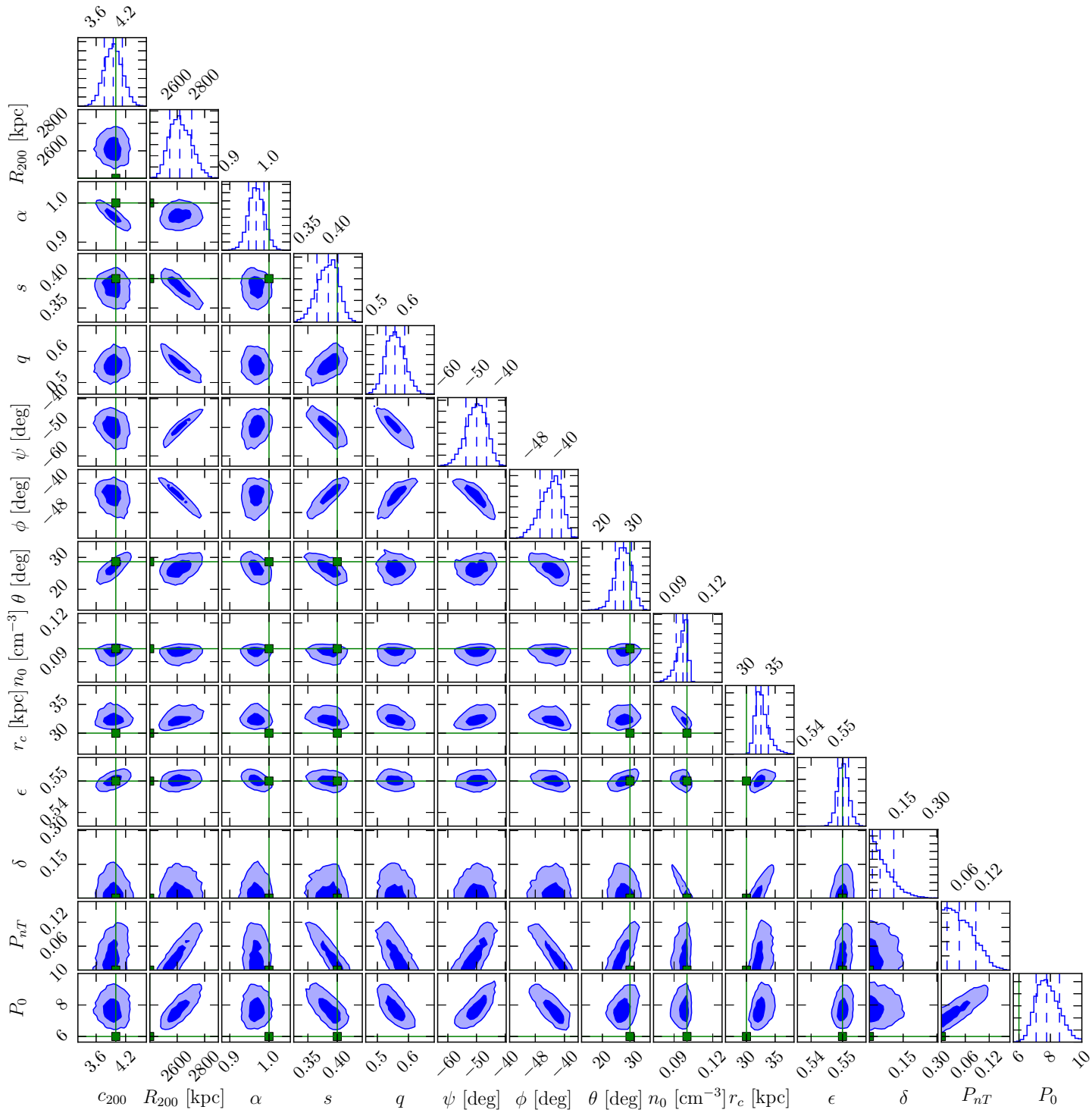


Figure .9.: Marginalised posterior probability distributions for the triaxial joint model parameters of halo 4.

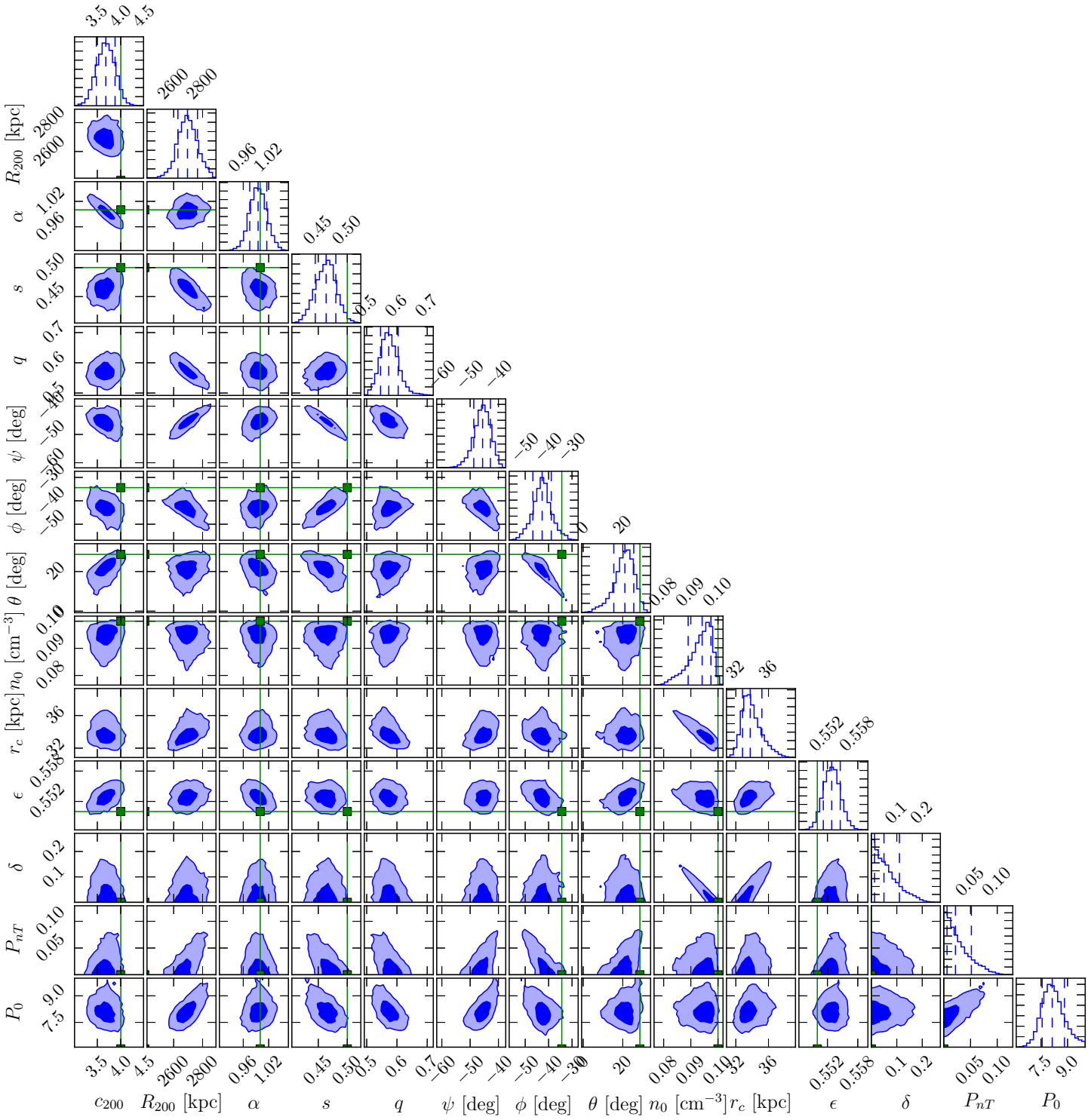


Figure .10.: Marginalised posterior probability distributions for the triaxial joint model parameters of halo 5.

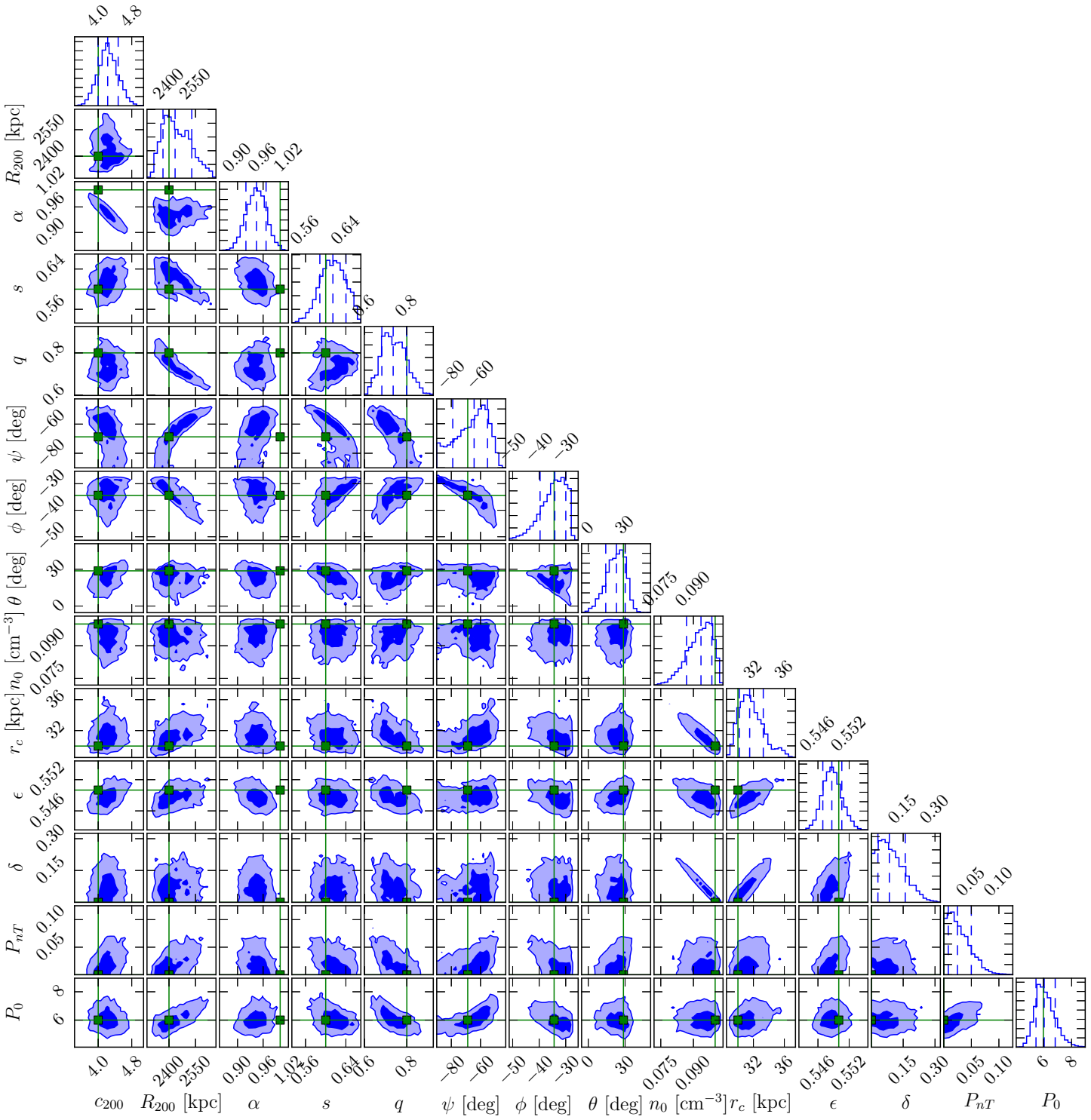


Figure .11.: Marginalised posterior probability distributions for the triaxial joint model parameters of halo 6.

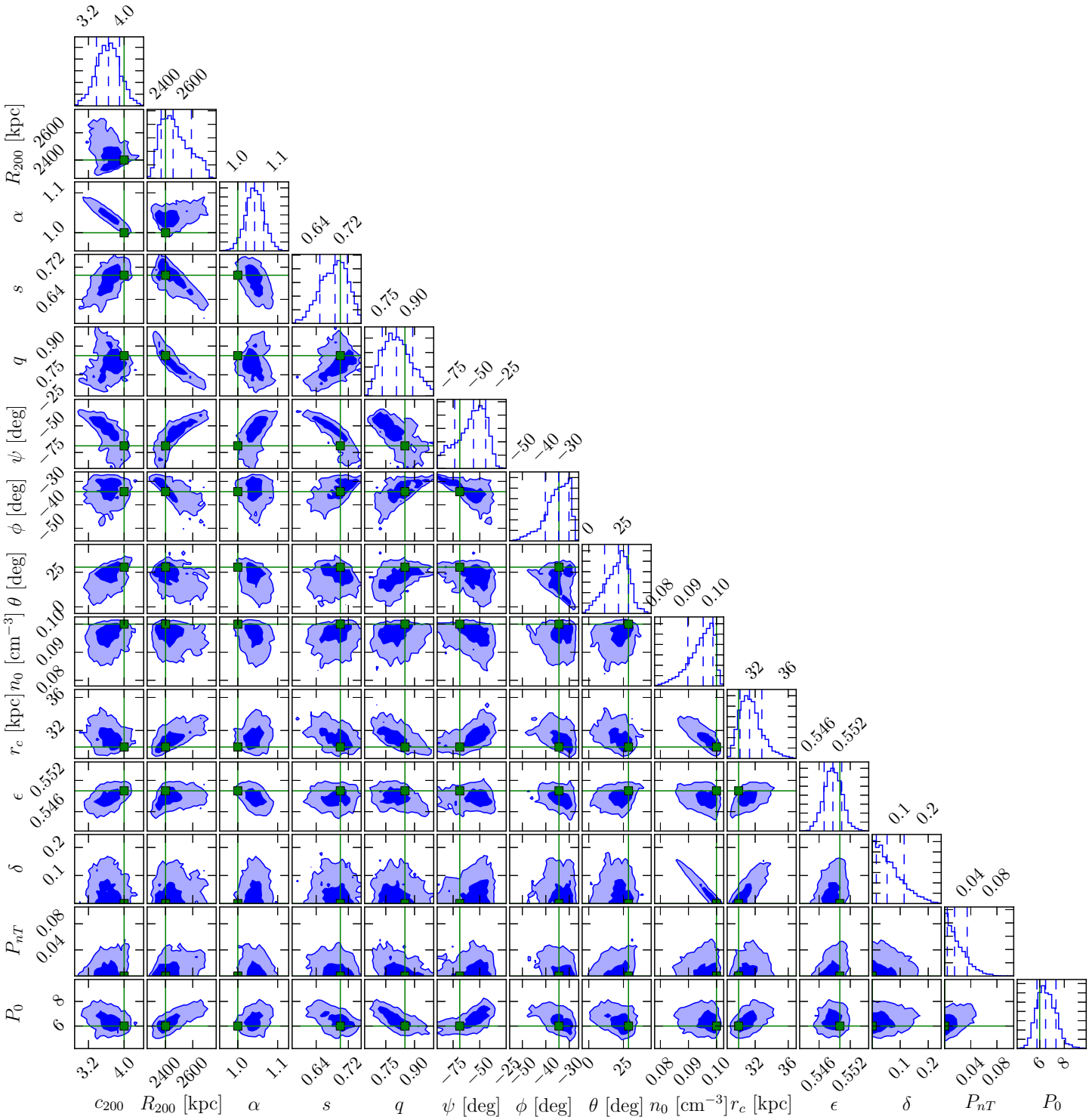


Figure .12.: Marginalised posterior probability distributions for the triaxial joint model parameters of halo 7.

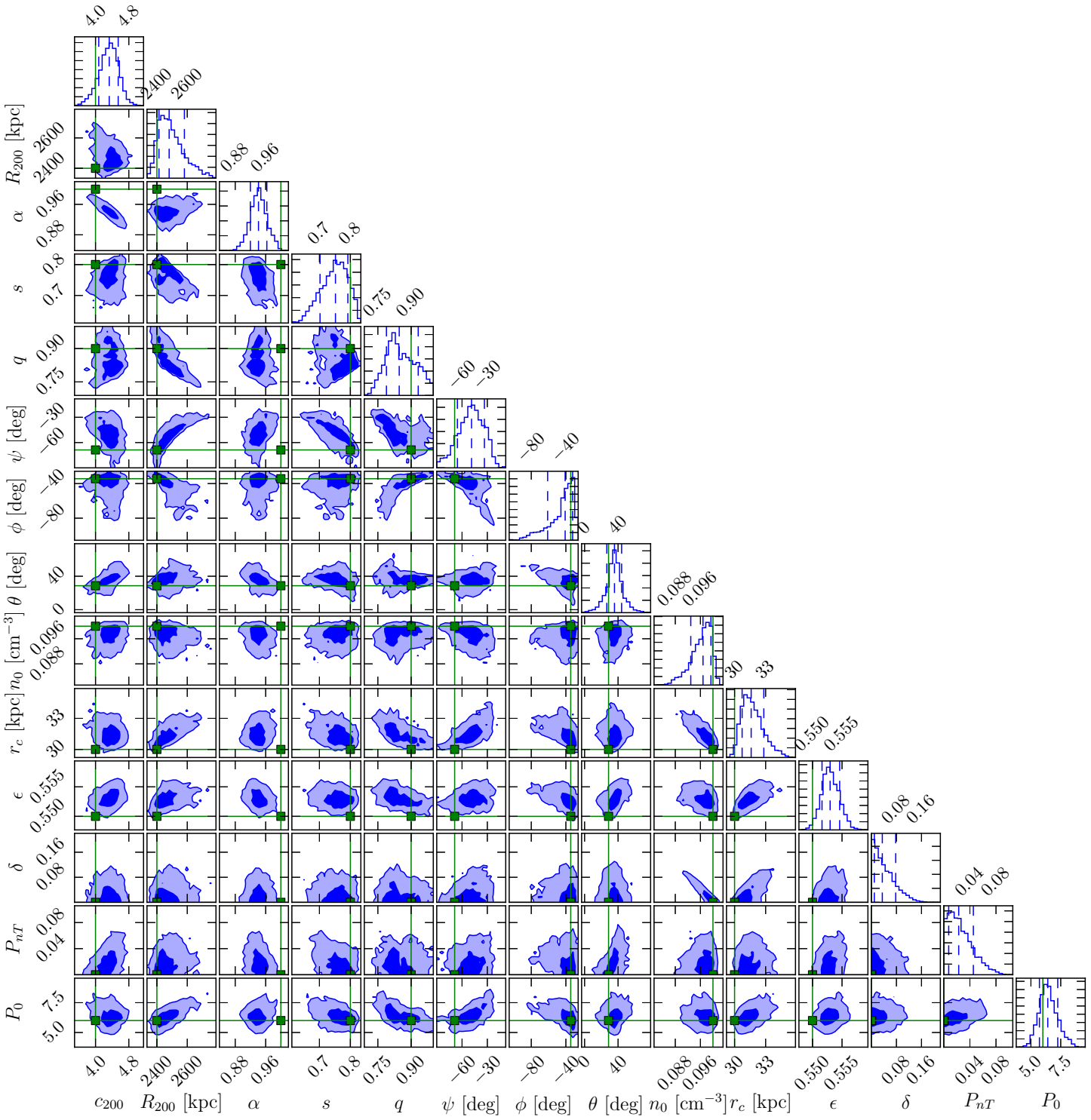


Figure .13.: Marginalised posterior probability distributions for the triaxial joint model parameters of halo 8.

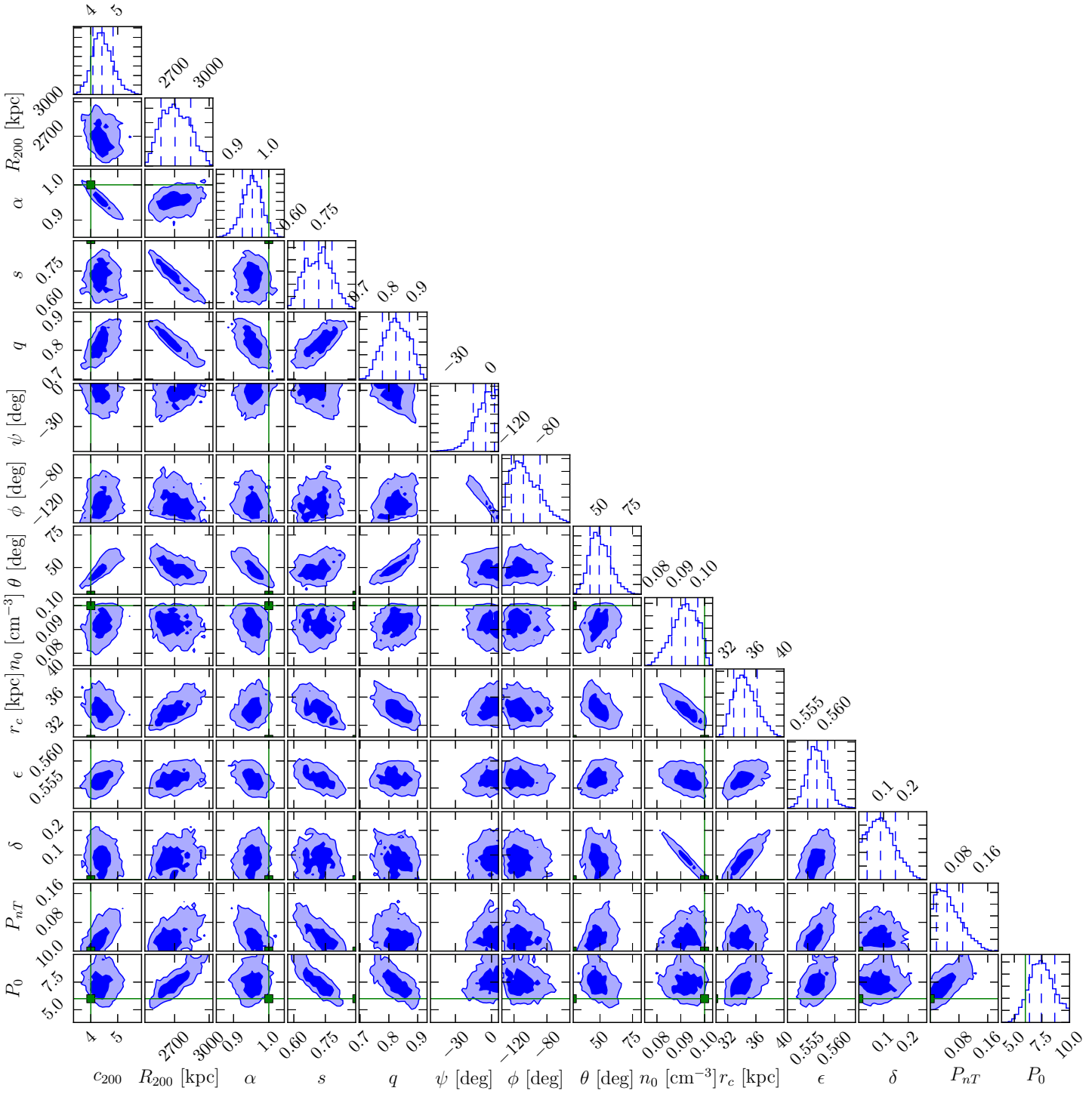


Figure .14.: Marginalised posterior probability distributions for the triaxial joint model parameters of halo 9.

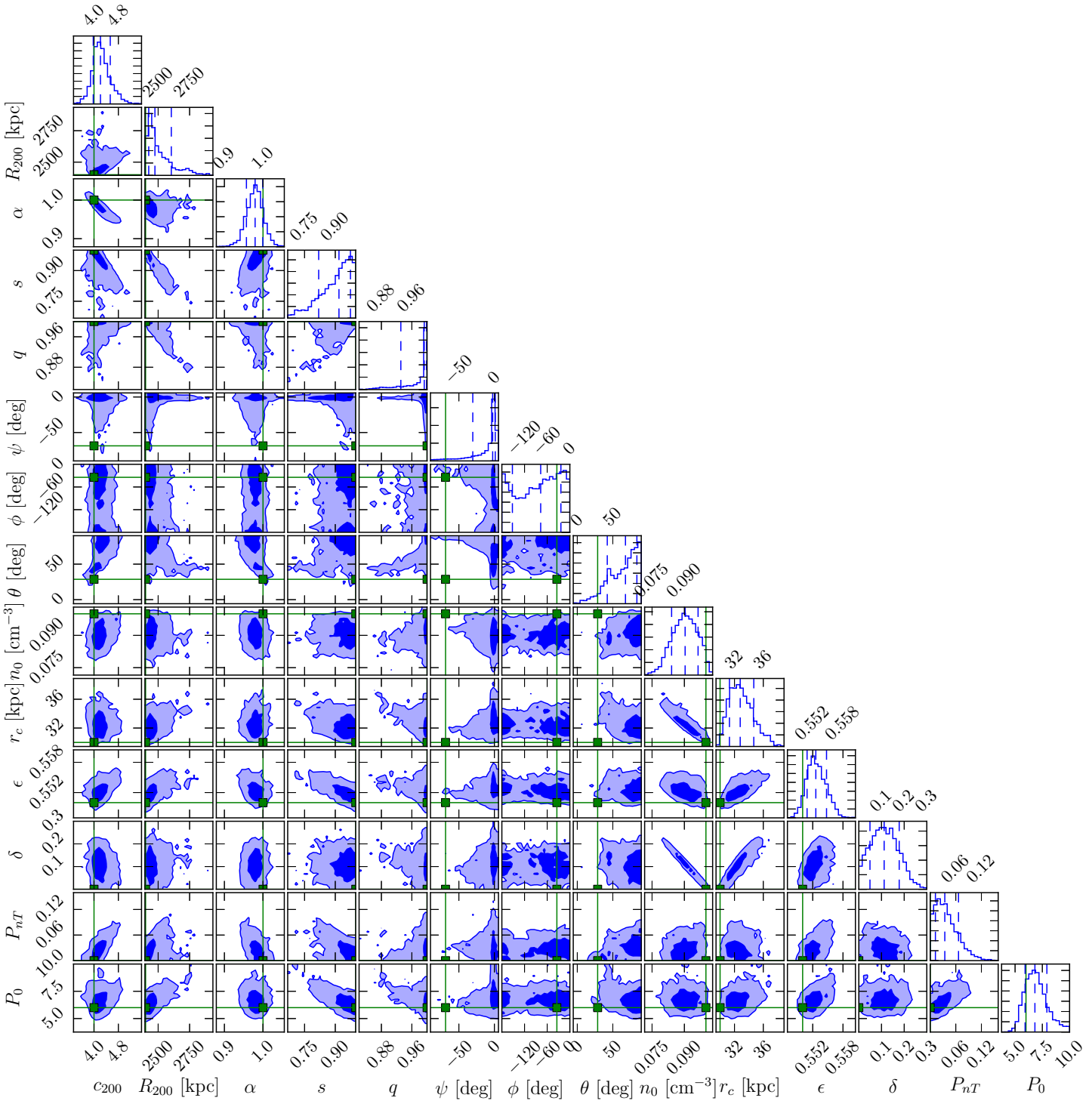


Figure .15.: Marginalised posterior probability distributions for the triaxial joint model parameters of halo 10.

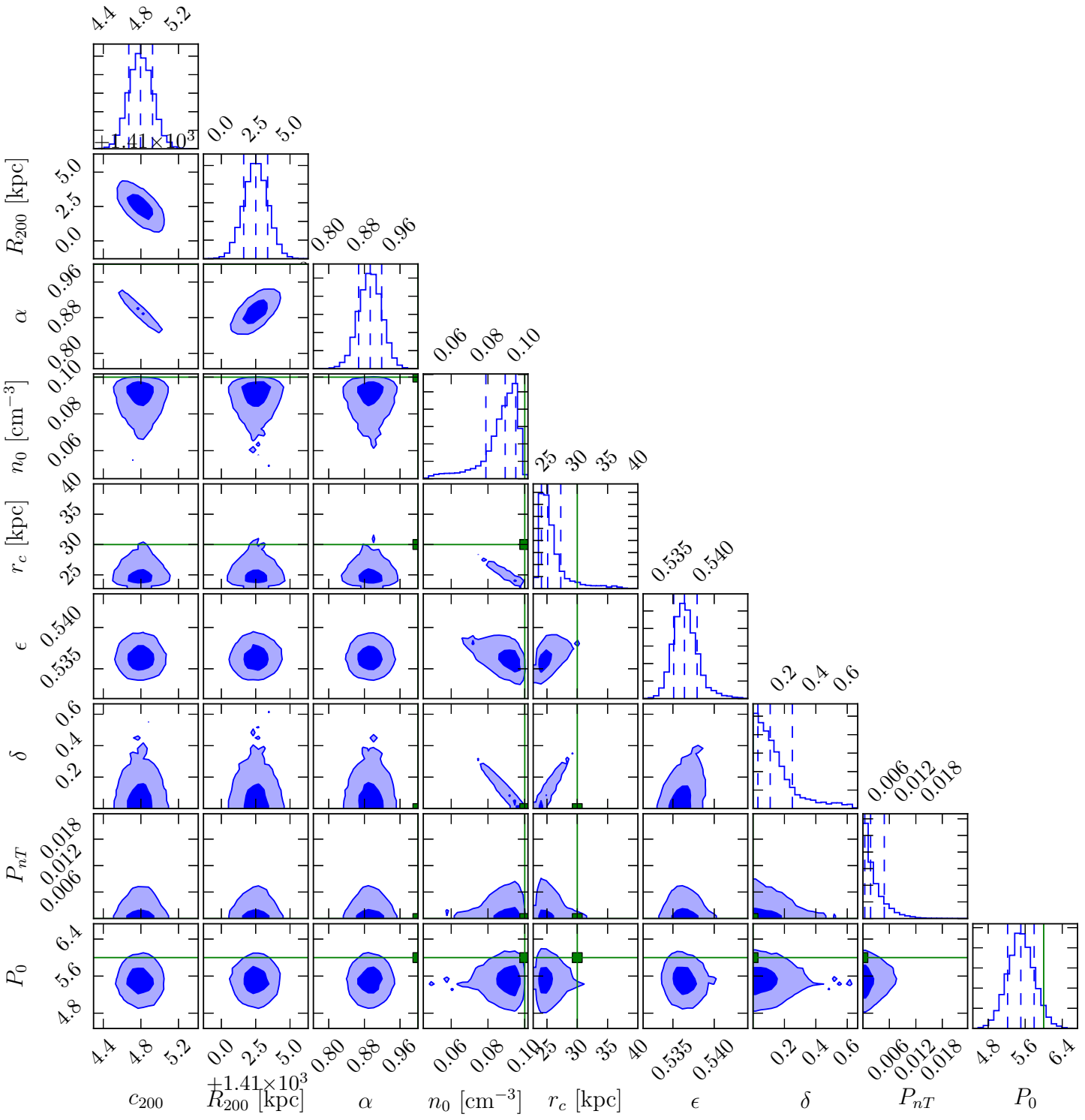


Figure .16.: Marginalised posterior probability distributions for the spherical joint model parameters of halo 4.

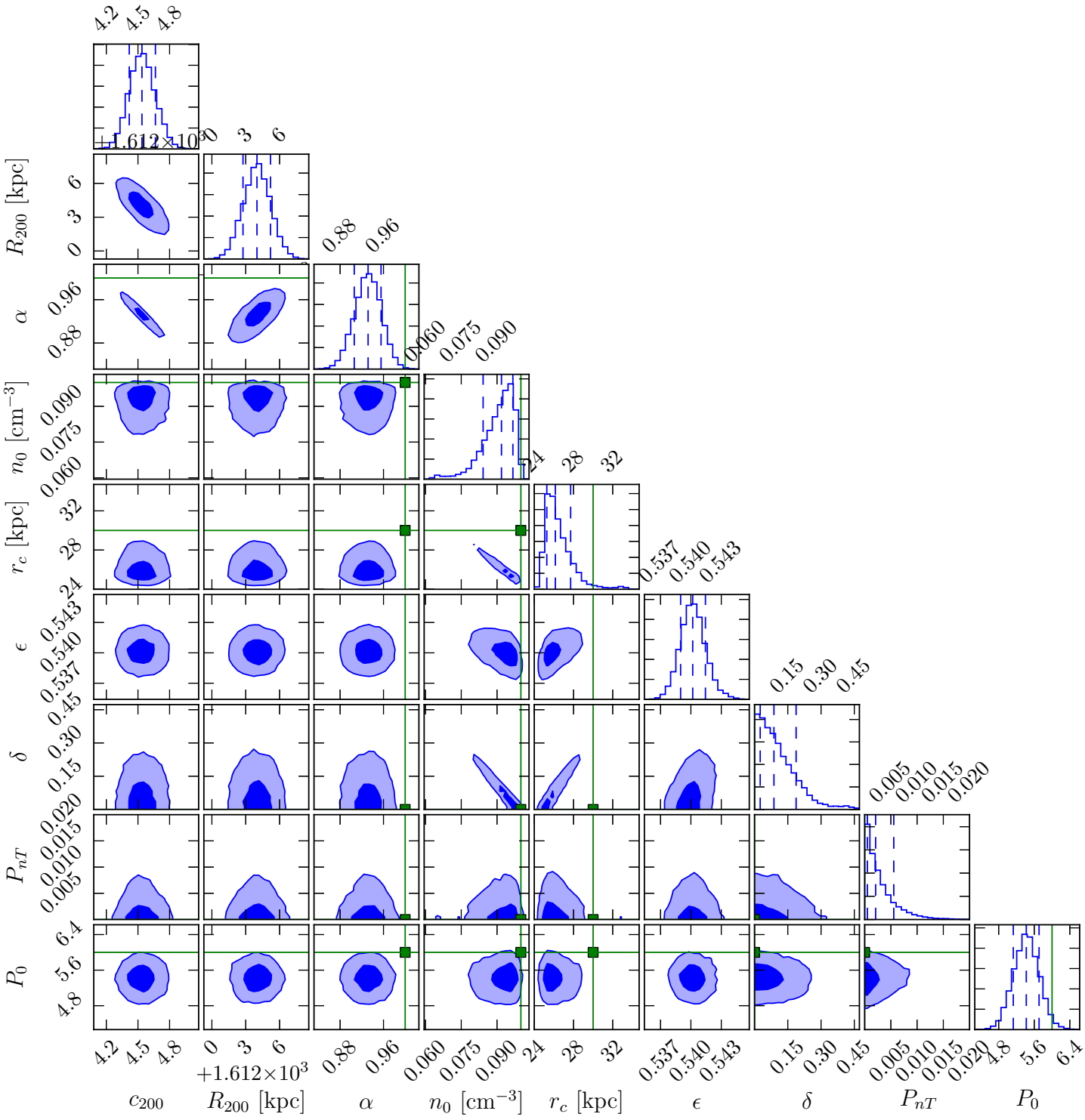


Figure .17.: Marginalised posterior probability distributions for the spherical joint model parameters of halo 5.

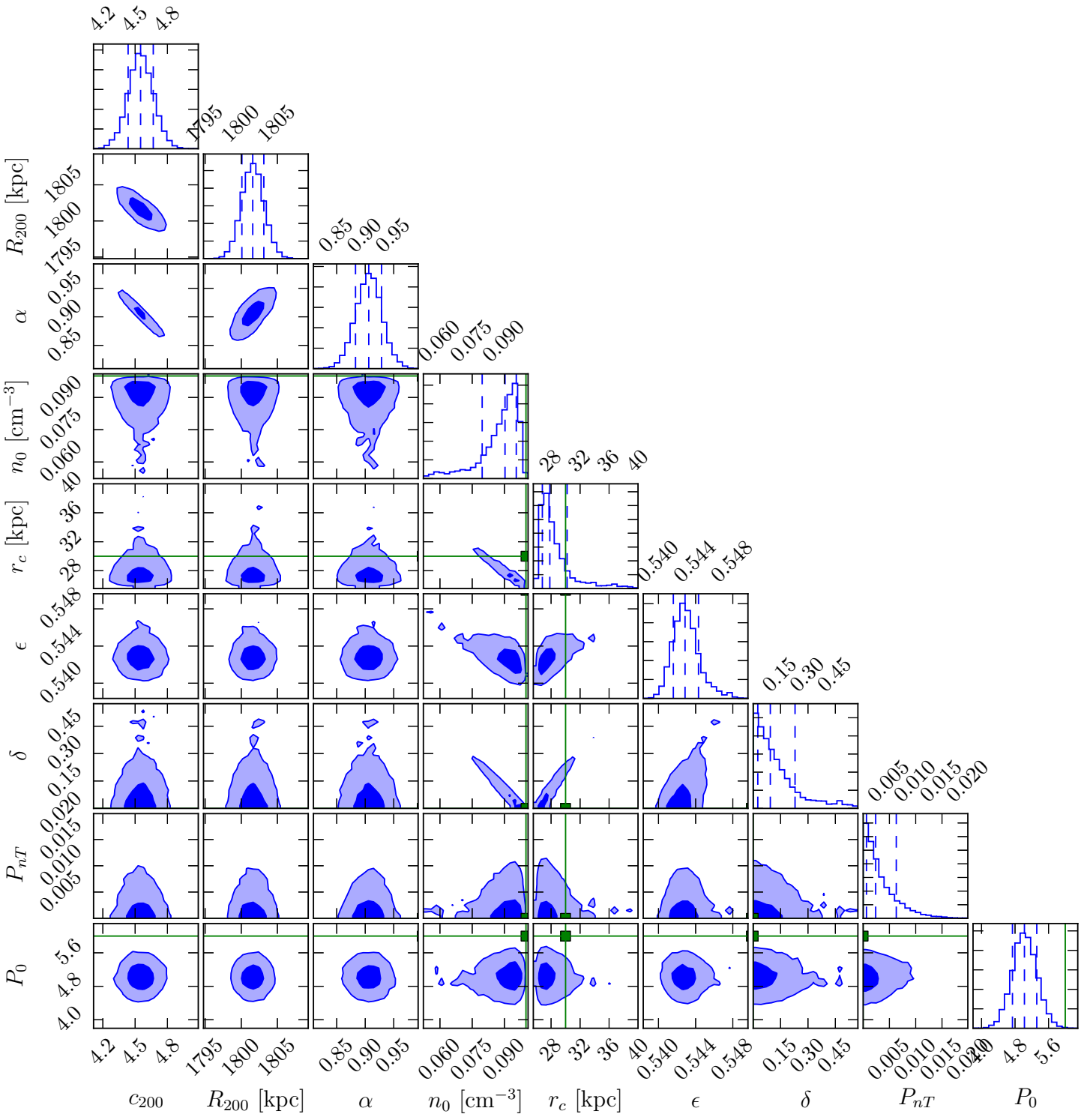


Figure .18.: Marginalised posterior probability distributions for the spherical joint model parameters of halo 6.

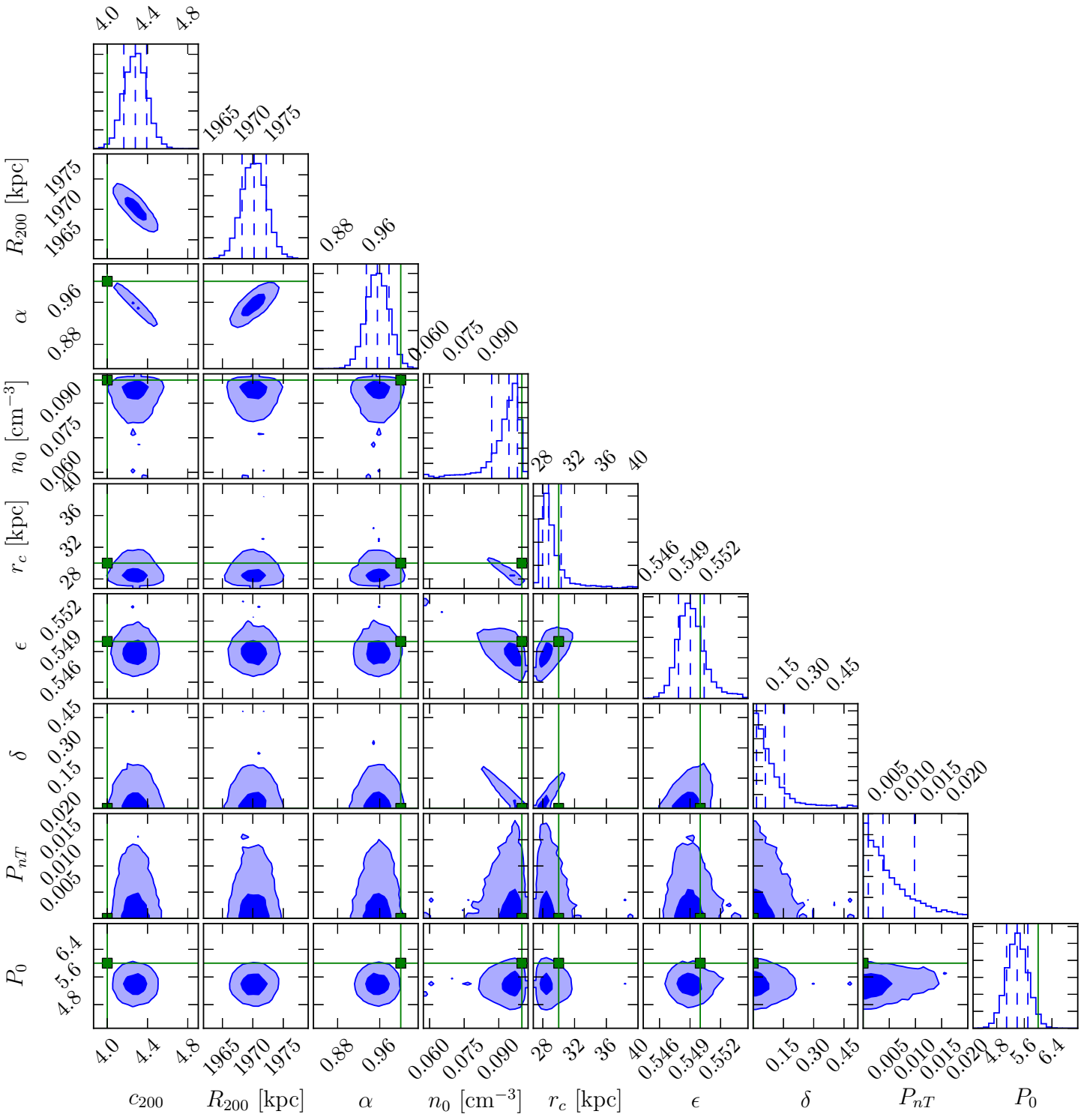


Figure .19.: Marginalised posterior probability distributions for the spherical joint model parameters of halo 7.

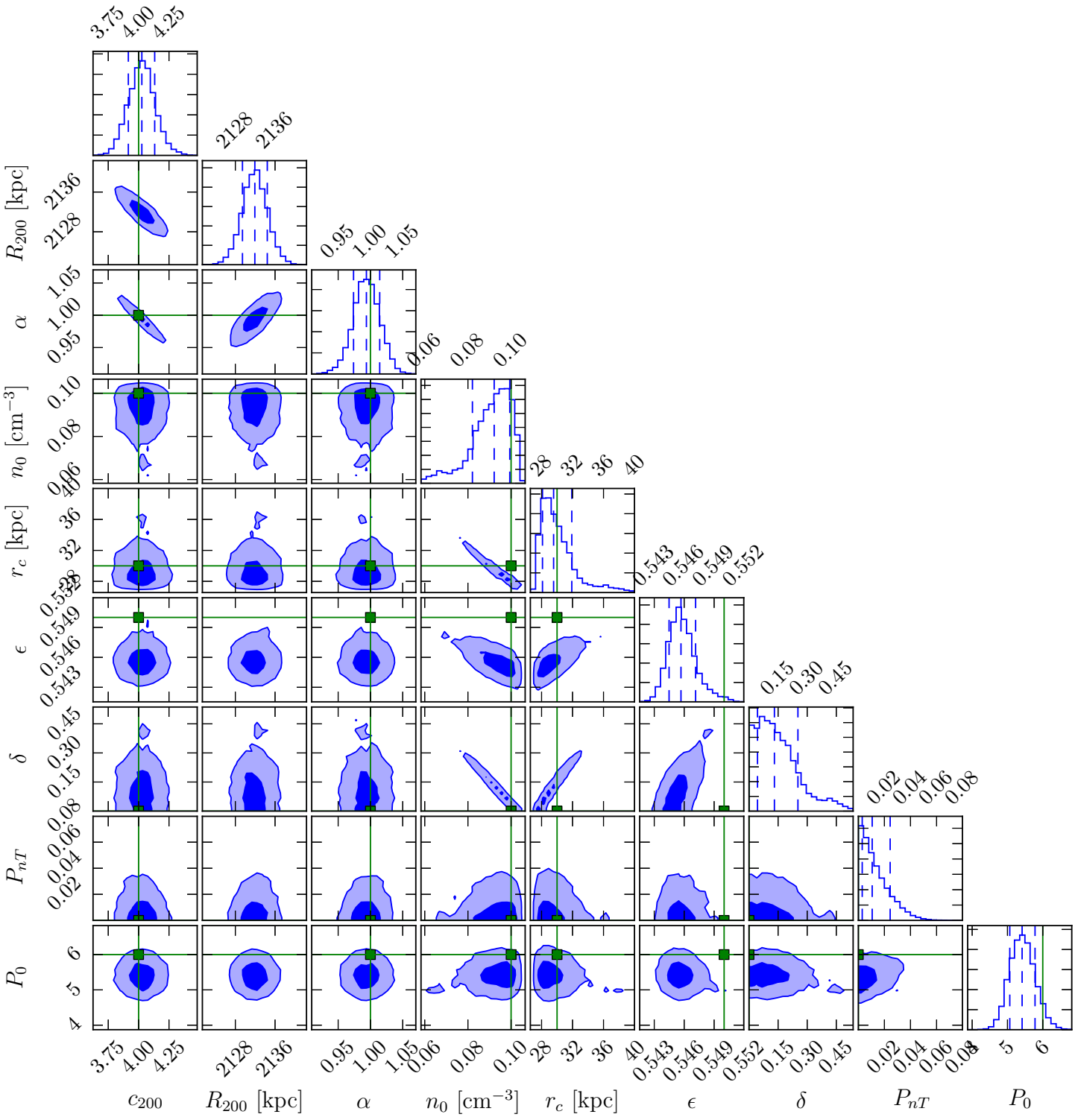


Figure .20.: Marginalised posterior probability distributions for the spherical joint model parameters of halo 8.

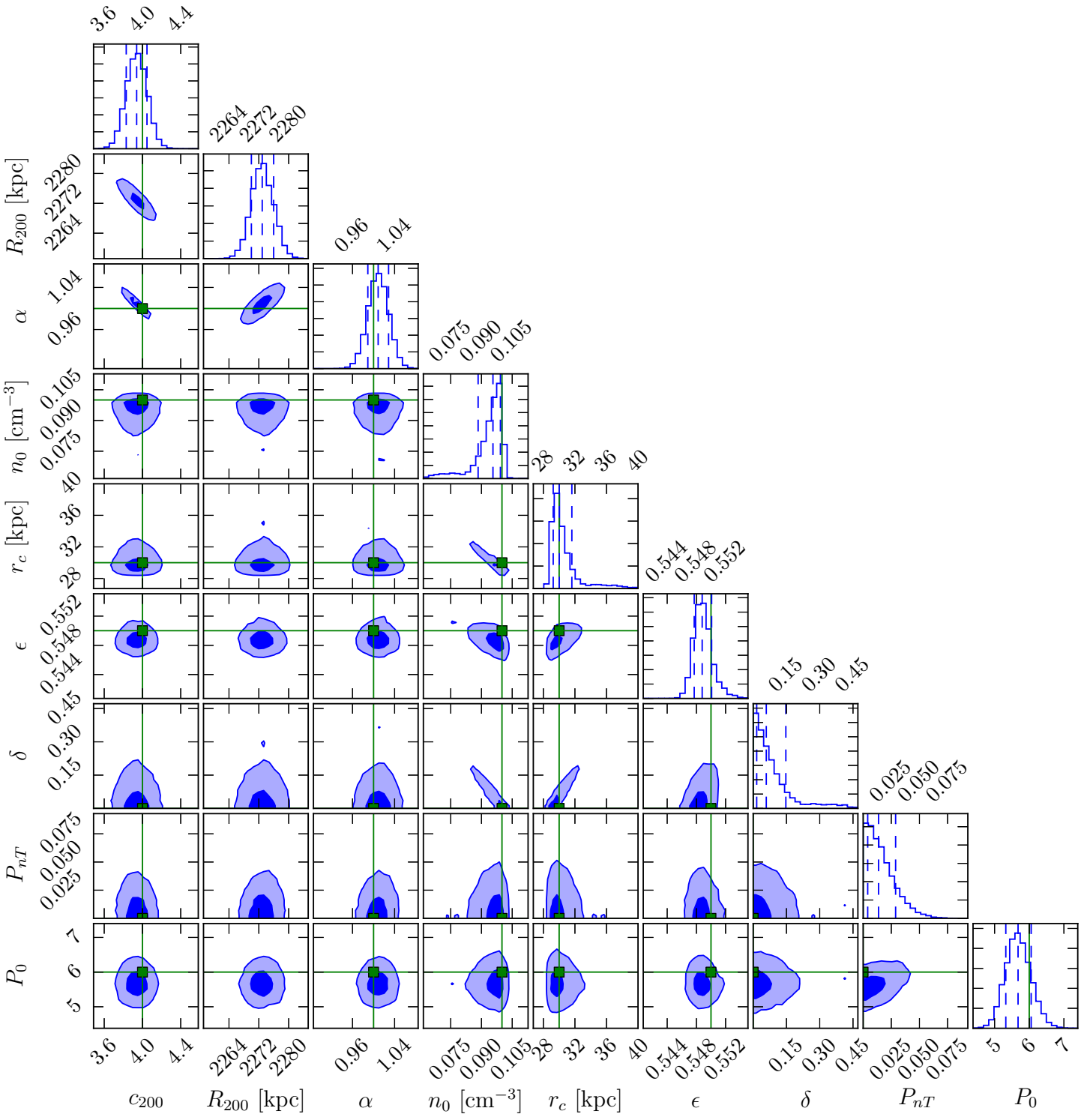


Figure .21.: Marginalised posterior probability distributions for the spherical joint model parameters of halo 9.

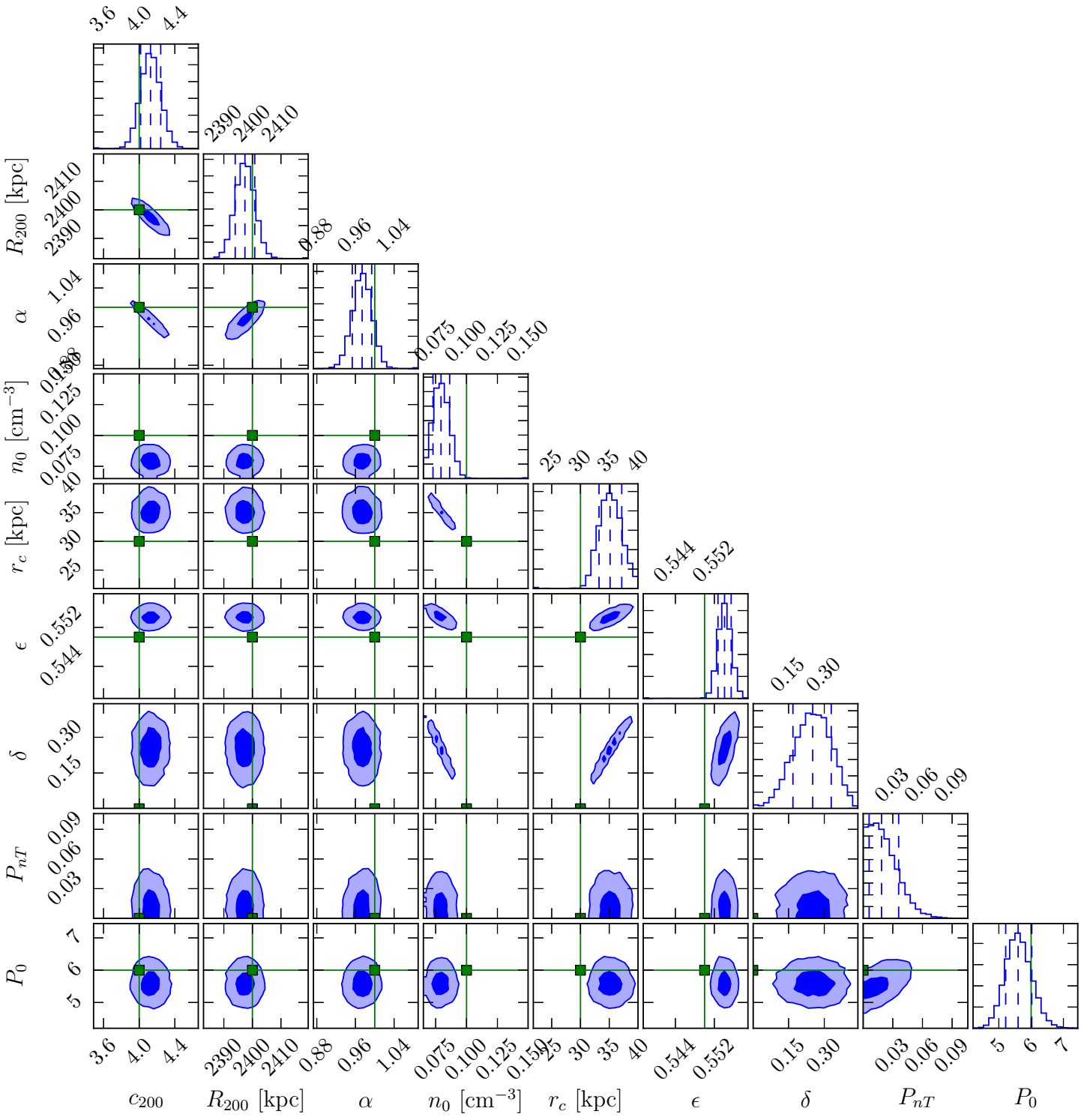


Figure .22.: Marginalised posterior probability distributions for the spherical joint model parameters of halo 10.

# B. Published papers

## B.1. Strong-lensing analysis of MACS J0717.5+3745 from Hubble Frontier Fields observations: How well can the mass distribution be constrained?

M. Limousin, J. Richard, E. Jullo, et al. "Strong-lensing analysis of MACS J0717.5+3745 from Hubble Frontier Fields observations: How well can the mass distribution be constrained?" In: *A&A* 588, A99 (Apr. 2016), A99. DOI: 10.1051/0004-6361/201527638. arXiv: 1510.08077

A&A 588, A99 (2016)
DOI: 10.1051/0004-6361/201527638


Astronomy & Astrophysics

# Strong-lensing analysis of MACS J0717.5+3745 from *Hubble* Frontier Fields observations: How well can the mass distribution be constrained?

M. Limousin[1], J. Richard[2], E. Jullo[1], M. Jauzac[3,4,5], H. Ebeling[6], M. Bonamigo[1], A. Alavi[7], B. Clément[2], C. Giocoli[1], J.-P. Kneib[8,1], T. Verdugo[9,10], P. Natarajan[11], B. Siana[7], H. Atek[8,11], and M. Rexroth[8,⋆]

[1] Laboratoire d'Astrophysique de Marseille, UMR 6610, CNRS-Université de Provence, 38 rue Frédéric Joliot-Curie, 13388 Marseille Cedex 13, France
e-mail: marceau.limousin@lam.fr
[2] CRAL, Observatoire de Lyon, Université Lyon 1, 9 avenue Ch. André, 69561 Saint-Genis Laval Cedex, France
[3] Centre for Extragalactic Astronomy, Department of Physics, Durham University, Durham DH1 3LE, UK
[4] Institute for Computational Cosmology, Durham University, South Road, Durham DH1 3LE, UK
[5] Astrophysics and Cosmology Research Unit, School of Mathematical Sciences, University of KwaZulu-Natal, 4041 Durban, South Africa
[6] Institute for Astronomy, University of Hawaii, 2680 Woodlawn Dr, Honolulu, HI 96822, USA
[7] Department of Physics and Astronomy, University of California Riverside, CA 92521, USA
[8] Laboratoire d'Astrophysique, École Polytechnique Fédérale de Lausanne, Observatoire de Sauverny, 1290 Versoix, Switzerland
[9] Universidad Nacional Autónoma de México, Instituto de Astronomía, Apdo. Postal 106, Ensenada, B.C., 22860 México, Mexico
[10] Instituto de Física y Astronomía, Universidad de Valparaíso, Avenida Gran Bretaña 1111, Valparaíso, Chile
[11] Department of Astronomy, Yale University, 260 Whitney Avenue, New Haven, CT 06511, USA

Received 25 October 2015 / Accepted 11 December 2015

**ABSTRACT**

We present a strong-lensing analysis of MACSJ0717.5+3745 (hereafter MACS J0717), based on the full depth of the *Hubble* Frontier Field (HFF) observations, which brings the number of multiply imaged systems to 61, ten of which have been spectroscopically confirmed. The total number of images comprised in these systems rises to 165, compared to 48 images in 16 systems before the HFF observations. Our analysis uses a parametric mass reconstruction technique, as implemented in the L software, and the subset of the 132 most secure multiple images to constrain a mass distribution composed of four large-scale mass components (spatially aligned with the four main light concentrations) and a multitude of galaxy-scale perturbers. We find a superposition of cored isothermal mass components to provide a good fit to the observational constraints, resulting in a very shallow mass distribution for the smooth (large-scale) component. Given the implications of such a flat mass profile, we investigate whether a model composed of "peaky" non-cored mass components can also reproduce the observational constraints. We find that such a non-cored mass model reproduces the observational constraints equally well, in the sense that both models give comparable total rms. Although the total (smooth dark matter component plus galaxy-scale perturbers) mass distributions of both models are consistent, as are the integrated two-dimensional mass profiles, we find that the smooth and the galaxy-scale components are very different. We conclude that, even in the HFF era, the generic degeneracy between smooth and galaxy-scale components is not broken, in particular in such a complex galaxy cluster. Consequently, insights into the mass distribution of MACS J0717 remain limited, emphasizing the need for additional probes beyond strong lensing. Our findings also have implications for estimates of the lensing magnification. We show that the amplification difference between the two models is larger than the error associated with either model, and that this additional systematic uncertainty is approximately the difference in magnification obtained by the different groups of modelers using pre-HFF data. This uncertainty decreases the area of the image plane where we can reliably study the high-redshift Universe by 50 to 70%.

**Key words.** gravitational lensing: strong – galaxies: clusters: individual: MACS J0717.5+3745

## 1. MACS J0717 in the *Hubble* Frontier Field era

MACS J0717, a galaxy cluster located at $z = 0.55$, is well established as one of the most massive and complex merging structures known so far, based on extensive optical (Ebeling et al. 2004, 2007; Ma et al. 2008; Ma & Ebeling 2010), radio (Edge et al. 2003; van Weeren et al. 2009; Bonafede et al. 2009; Pandey-Pommier et al. 2013), X-ray (Ma et al. 2009), and Sunyaev Zel'dovich studies (LaRoque et al. 2003; Mroczkowski et al. 2012; Sayers et al. 2013). Acting as a powerful gravitational lens, the system has been investigated both in the strong- (Zitrin et al. 2009; Limousin et al. 2012; Richard et al. 2014; Diego et al. 2015b) and in the weak-lensing regimes (Jauzac et al. 2012; Medezinski et al. 2013), further underlining its position as one of the most complex, dynamically active, and massive clusters studied to date.

As a result, MACS J0717 has been selected as a target by the CLASH program (Postman et al. 2012) and more recently by the *Hubble* Frontier Field (HFF) initiative. The HFF project constitutes the largest commitment of *Hubble* Space Telescope (HST) time ever made to the exploration of the high-redshift Universe

⋆ Based on observations obtained with the *Hubble* Space Telescope.

via gravitational lensing by massive galaxy clusters: 140 orbits of HST time have been devoted to deep imaging observations of six galaxy clusters. Each cluster is observed for 20 orbits in each of three ACS filters (*F435W*, *F606W* and *F814W*), and in each of four WFC3 passbands (*F105W*, *F125W*, *F140W* and *F160W*). More information on the HFF initiative can be found on their website[1].

In this paper, we use the full set of HFF observations in order to pursue a strong-lensing analysis of MACS J0717. Our aims are twofold: (i) first, to study the mass distribution in detail, which entails estimating the total projected mass of the core of MACS J0717, quantifying the location and shape of the mass components relative to the gas and galaxy distribution, and using the results to gain further insight into the ongoing merging processes in MACS J0717, which may have broader implications for our understanding of structure formation and evolution. (ii) Second, to provide the community with a calibrated mass model of MACS J0717, thereby enabling its use as an efficient gravitational telescope for studies of the high-redshift Universe, which is the primary scientific goal of the HFF program.

Previous analyses revealed that MACS J0717 is undergoing multiple merger events, reflected in its quadri-modal mass distribution, with a filament extending to the south-east. Using X-ray and optical data (both imaging and spectroscopy), Ma et al. (2009) were the first to identify four major concentrations of large elliptical cluster galaxies, referred to as A, B, C, and D in their work. This scenario was later confirmed in a parametric strong-lensing analysis by Limousin et al. (2012). More recently, Diego et al. (2015b), exploiting the first third of the HFF data and using a non-parametric strong-lensing technique, has again found evidence for a quadri-modal mass distribution for the smooth component, i.e., once cluster members are removed. This agreement between the results from both parametric and non-parametric, grid-based modelling approaches (the latter having much more freedom than the former) is further evidence in favour of the four-component model. Like all the above-mentioned strong-lensing studies of MACS J0717, ours also uses the original labelling by Ma et al. (2009) of these four components (see Fig. 2). In fact, we assume in this paper that the mass distribution of MACS J0717 is quadri-modal.

All our results use the ΛCDM concordance cosmology with $\Omega_M = 0.3, \Omega_\Lambda = 0.7$, and a Hubble constant $H_0 = 70\ \mathrm{km\,s^{-1}\ Mpc^{-1}}$. At the redshift of MACS J0717 this cosmology implies a scale of 6.4 kpc/″. Magnitudes are quoted in the AB system. Figures are aligned with the conventional equatorial axes, i.e. north is up, and east is left.

## 2. Multiple images

### 2.1. Previous work

Prior to the HFF observations, 16 multiple-image systems, comprising 48 individual images, had been reported (Johnson et al. 2014; Richard et al. 2014; Coe et al. 2015). The analysis by Diego et al. (2015b), using the first third of the data from the HFF observations, identified an additional 17 multiple-image systems, as well as 10 elongated features, assumed to be single images of lensed background galaxies.

More recently, at the same time as this paper, Kawamata et al. (2016) has presented a mass model for MACS J0717 based on the full depth of the HFF observations. We briefly discuss their findings in Sect. 5.4.

[1] http://www.stsci.edu/hst/campaigns/frontier-fields/

### 2.2. This work

In this work, we revisit the strong-lensing identifications by Diego et al. (2015b), agree with most of them (discarding, however, their system 30), and, using the full depth of the HFF observations, add 28 new multiple-image systems. The HFF observations thus enabled the discovery of 45 new systems (consisting of 117 images), bringing the grand total to 61 multiple-image systems in MACS J0717, comprised of 165 individual images. Here we use as constraints only a subset of 132 multiple images that we consider to be the most reliably identified ones.

For clarity, we present an overview of these images in two tables: Table A.1 lists the multiple images known before the HFF observations and is thus identical to the one published in Richard et al. (2014); the corresponding strong-lensing features are shown in red in Fig. 1. Table A.2 lists the multiple images discovered thanks to the HFF observations; they are shown in blue and cyan in Fig. 1. Where relevant, we use the notation of Diego et al. (2015b).

We note that we have not been able to securely identify counter-images for some systems. We also report two radial arcs (systems 27 and 37). It is very likely that more multiple-image systems are present in the HFF data of MACS J0717.

### 2.3. Comparison with Diego et al.

Diego et al. (2015b) identified ten elongated features, interpreted as single-image arclets. These arclets are of potential interest in the region beyond the Einstein radius where strong-lensing constraints largely disappear. Combined with photometric estimates of their redshifts, the shape of these features (elongation, orientation) may provide valuable constraints. However, in our analysis, we do not use these features.

We agree with the identifications by Diego et al. (2015b), except for the following few cases:

- image 25.3: we removed this image on the grounds of unclear morphology and colour. Adding 25.3 leads to a larger rms for this system (2″ instead of 1.3″).
- image 29.3: as for 25.3 we find the morphology and colour of 29.3 poorly determined; adding 29.3 leads to a larger rms for this system (2.6″ instead of 1.9″).
- system 30: we disagree with this identification. Image 30.1 as proposed by Diego et al. (2015b) is a faint long arc located between images 1.2 and 1.3. In Limousin et al. (2012), we previously interpreted this feature as the merged tail of 1.2 and 1.3. This merged tail corresponds to the counter image of the tail associated with 1.1, for which we measured a spectroscopic of 2.963 (labelled 1.1* in Limousin et al. 2012). In addition, our parametric mass model is not able to reproduce system 30 as proposed by Diego et al. (2015b).
- system 34: we propose an alternative identification for image 34.1 which significantly improves the rms of this system (1.6″ instead of 3.7″ when using the identification by Diego et al. 2015b). We note that Diego et al. (2015b) has already reported a possible problem with this system. The identification we propose is supported by the geometry of systems 50 and 56.
- system 39: Diego et al. (2015b) consider image 39.1 an elongated single-image feature. We associate this image with another one located on the other side of the arc, forming system 39. A third image is predicted, at least 1 mag fainter. Although we identify several candidates for this third image, none is sufficiently compelling, causing us to use only images 39.1 and 39.2 for this system.

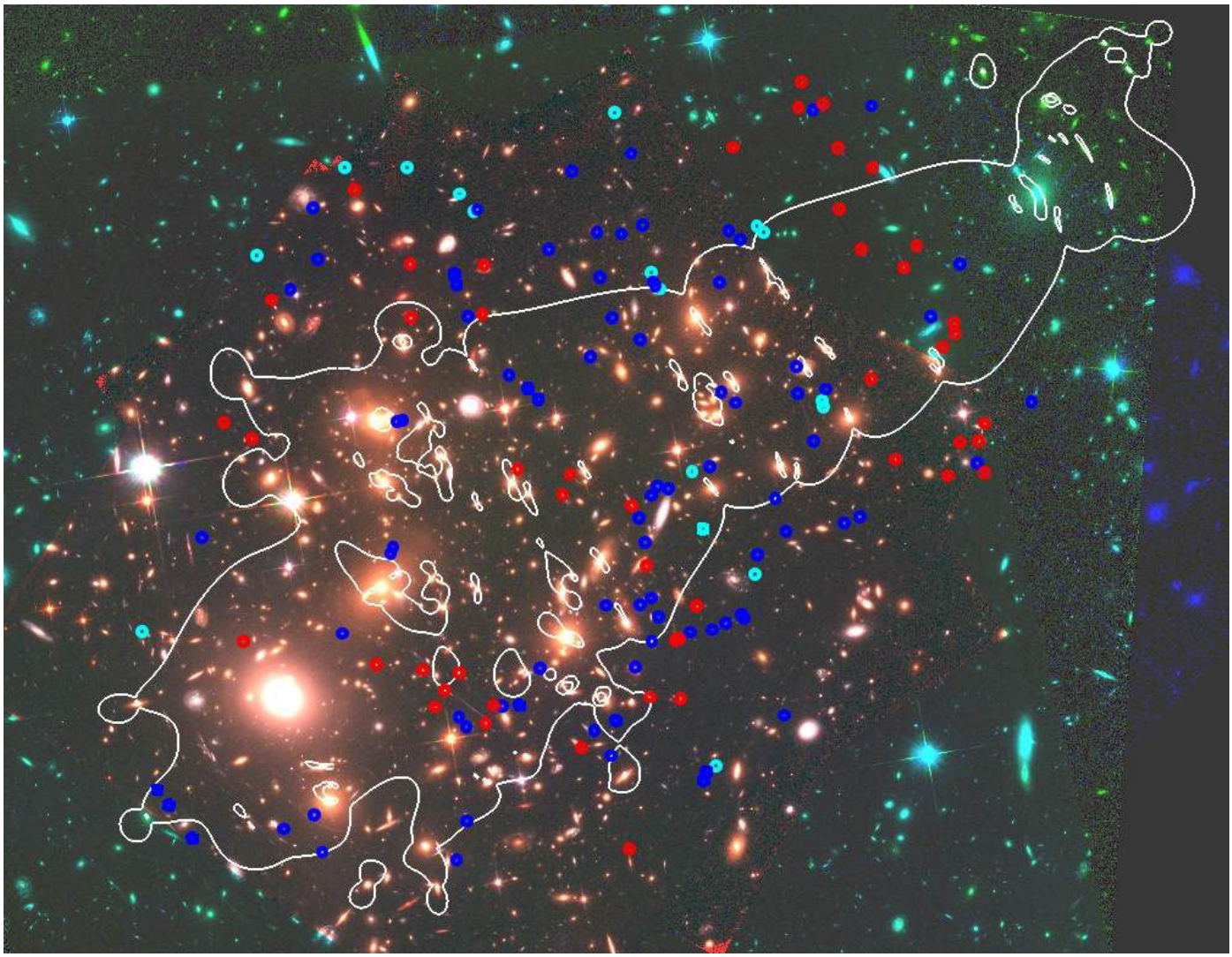

**Fig. 1.** Colour image ($240'' \times 184''$) of MACS J0717 based on HST images in the *F435W*, *F606W*, and *F814W* ACS pass bands. Multiple-image systems used in this work are marked: in red, the 48 multiple images identified prior to the HFF observations; in blue, the 84 images discovered thanks to the HFF observations; in cyan, the 33 candidate images discovered in the HFF observations. Shown in white is the critical line for a source redshift of 7.

### 2.4. Photometric redshifts

In addition to the Frontier Fields observations, we include WFC3/UVIS (*F275W*, *F336W*) photometry in our analysis in order to estimate photometric redshifts for the multiple images. The corresponding data were obtained for HST program ID 13389 (PI: B. Siana), which obtained deep UV imaging (8 orbits per filter) of three Frontier Field clusters (Abell 2744, MACS J0717, and MACS J1149.5+2223). A complete description of the data reduction and photometry catalogues will be given in Siana et al. (in prep.). Here, we briefly summarize the photometric redshift measurements; a more detailed discussion will be presented in a forthcoming paper (Alavi et al., in prep.).

We derived photometric redshifts of the galaxies using the EAZY software package (Brammer et al. 2008) with the PÉGASE (Fioc & Rocca-Volmerange 1997) stellar synthetic templates and a $\chi^2$ fitting procedure. When doing so, we included an additional spectral energy distribution (SED) template of a dusty starburst SED. EAZY parameterizes absorption from the intergalactic medium following the description presented in Madau (1995). We did not use the magnitude priors in EAZY, as the lensed galaxies are much fainter than the luminosity range covered by the priors.

We note that the resulting photometric redshift estimates (listed in Tables A.1 and A.2) are not used as constraints in the strong-lensing analysis; they are, however, very helpful for associating images with each other while looking for multiple-image systems.

## 3. Strong-lensing analysis

### 3.1. Arc spectroscopy

Previous work (Limousin et al. 2012; Schmidt et al. 2014; Vanzella et al. 2014; Treu et al. 2015) reported spectroscopic redshifts for nine multiple-image systems (systems 1, 3, 4, 6, 12, 13, 14, 15 and 19). In addition, a spectroscopic redshift of $z = 5.51$ was measured for system 68 (Clement et al., in prep.), bringing to ten the total number of multiple-image systems in MACS J0717 for which spectroscopic redshifts are available.

Treu et al. (2015) reported a "probable" redshift of $z = 0.928$ for image 5.1. We disregard this value. Given the colour and morphology of the three images constituting system 5, we are

**Table 1.** dPIE parameters inferred for the dark matter components considered in the optimization procedure: the four large-scale dark matter clumps (A, B, C, D) and the galaxy-scale component.

| Component | ΔRA | ΔDec | $e$ | $\theta$ | $r_{\rm core}$ ($''$) | $r_{\rm s}$ ($''$) | $\sigma$ (km s$^{-1}$) |
|---|---|---|---|---|---|---|---|
| C | $-9.1^{+1.5}_{-0.5}$ | $-8.7 \pm 1.4$ | $0.34 \pm 0.03$ | $54 \pm 4$ | $16.1 \pm 2.0$ | [1000] | $895 \pm 29.0$ |
| D | $26.6 \pm 0.9$ | $-19.3 \pm 1.1$ | $0.65 \pm 0.03$ | $52 \pm 3$ | $4.5 \pm 0.8$ | [1000] | $494 \pm 15$ |
| B | $37.3 \pm 3.9$ | $34.9 \pm 1.8$ | $0.50 \pm 0.06$ | $3^{+9}_{-2}$ | $27.6 \pm 2.1$ | [1000] | $800 \pm 38$ |
| A | $114.9 \pm 2.9$ | $64.7 \pm 1.1$ | $0.68 \pm 0.01$ | $9 \pm 5$ | $20.7 \pm 2.1$ | [1000] | $880 \pm 22$ |
| $L^*$ galaxy | – | – | – | – | [0.05] | $8.3 \pm 0.7$ | $250.3 \pm 8.4$ |

**Notes.** These parameters correspond to the cored mass model. Coordinates are given in arcseconds with respect to $\alpha = 109.3982, \delta = 37.745778$. The ellipticity $e$ is for the mass distribution. Error bars correspond to $1\sigma$ confidence level. Parameters in brackets are not optimized. For the scaling relations, the zero point is set to a magnitude equal to 20.66.

confident in this multiply imaged system, whose geometrical configuration does not support a low redshift as reported by Treu et al. (2015). Indeed, our model predicts a redshift around 4 (Table A.1), in agreement with the predictions from Diego et al. (2015b) and Kawamata et al. (2016). In addition, a non-detection in all filters bluer than the $B$-band can suggest a high-redshift solution ($z > 3$), as this possibility is also favoured by the CLASH survey which estimates a photometric redshift of 4.5 for images 5.1 and 5.2 (Jouvel et al. 2014).

### 3.2. Methodology

As in our previous work (see, e.g. Limousin et al. 2007b), our mass model consists of large-scale dark matter (DM) haloes, whose individual mass is larger than that of a galaxy group (typically of the order of $10^{14}$ $M_\odot$ within $50''$), and perturbations associated with individual cluster galaxies. For our analysis of MACS J0717, we consider the 90 most luminous galaxies in the ACS field as perturbers (corresponding to a magnitude limit equal to 23.4). We characterize these mass components (both on the cluster and the galaxy scale) with dual Pseudo Isothermal Elliptical Mass Distribution (dPIE, Limousin et al. 2005; Elíasdóttir et al. 2007), parametrized by a fiducial velocity dispersion $\sigma$, a core radius $r_{\rm core}$, and a scale radius $r_{\rm s}$. For the individual cluster galaxies, empirical scaling relations (without any scatter) are used to derive their dynamical dPIE parameters (central velocity dispersion and scale radius) from their luminosity (the core radius being set to a vanishingly small value of 0.3 kpc), whereas all geometrical parameters (centre, ellipticity, position angle) are set to the values measured from the light distribution. More precisely, the scaling relations are given by:

$$r_{\rm s} = r_{\rm s}^* \left(\frac{L}{L^*}\right)^{\frac{1}{2}} \quad \text{and} \quad \sigma = \sigma * \left(\frac{L}{L^*}\right)^{\frac{1}{4}}. \tag{1}$$

We allow the velocity dispersion of an $L^*$ galaxy to vary between 100 and 250 km s$^{-1}$, whereas its scale radius is forced to be less than 70 kpc, thus accounting for tidal stripping of galaxy-size dark matter haloes (see, e.g. Limousin et al. 2007a, 2009; Natarajan et al. 2009; Wetzel & White 2010, and references therein). Model optimisation is performed in the image plane using the [2] software (Jullo et al. 2007).

Positional uncertainty. The positional uncertainties of the images is an important ingredient for the $\chi^2$ computation. They affect the derivation of errors, in the sense that smaller positional uncertainties will, in general, result in smaller statistical uncertainties, which may in fact be underestimated.

In principle, deep HST images like the ones used in this paper allow compact images to be located to an astrometric precision of the order of $0\farcs05$. However, parametric cluster lens models often fail to reproduce or predict image positions to this precision, yielding instead typical image-plane rms values between $0.2''$ and a few arc seconds. Nominal positional uncertainties of $1.4''$ are usually chosen (Zitrin et al. 2015) to account for the contribution of fore- or background structures that are not included in our simple mass models (Jullo et al. 2010; D'Aloisio & Natarajan 2011; Host 2012). In this work, we use an even larger positional uncertainty of $2.0''$ (i.e., a value of the order of the image plane rms), in order to attain a reduced $\chi^2$ of order 1.

Finally, we should keep in mind that we are trying to reproduce observed and, to some extent, poorly understood structures located far away using rather simple parameterized mass models.

### 3.3. A multimodal mass model

Acknowledging previous results, we adopt and optimize a quadri-modal mass distribution for MACS J0717. Each mass component is associated with one of the four components (A, B, C and D), its location set to coincide with the corresponding light peak (red diamonds in Fig. 2). As in prior studies, we allow the positions of these components to vary within $\pm 20''$ of the associated light peak, while the ellipticity is limited to a range from 0 to 0.7 (in units of $(a^2 - b^2)/(a^2 + b^2)$). The velocity dispersion of each component is allowed to vary between 400 and 1500 km s$^{-1}$, and the core radius may take any value between 1 and $30''$. Finally, the scale radius – unconstrained by our data – is fixed at $1000''$.

## 4. Mass distribution from strong lensing

### 4.1. Cored mass components: A flat DM distribution?

Our quadri-modal mass model is able to reproduce the lensing constraints with an image-plane rms of $1.9''$. The resulting parameters of all mass components are given in Table 1; the corresponding mass contours are shown in yellow in Fig. 2.

We find that the total mass distribution (i.e., smooth DM component + galaxy-scale perturbers) follows the light distribution. The centre of each component is offset from the associated light concentration by $19''$, $27''$, $13''$, and $14''$ for components A, B, C, and D, respectively. In light of the large core radii of most of the four components ($21''$, $28''$, $21''$, and $5''$ for A, B, C, and D, respectively); however, these offsets are not necessarily significant. Specifically, our analysis does not support the hypothesis advanced by Diego et al. (2015b) that component A

[2] http://www.oamp.fr/cosmology/lenstool/

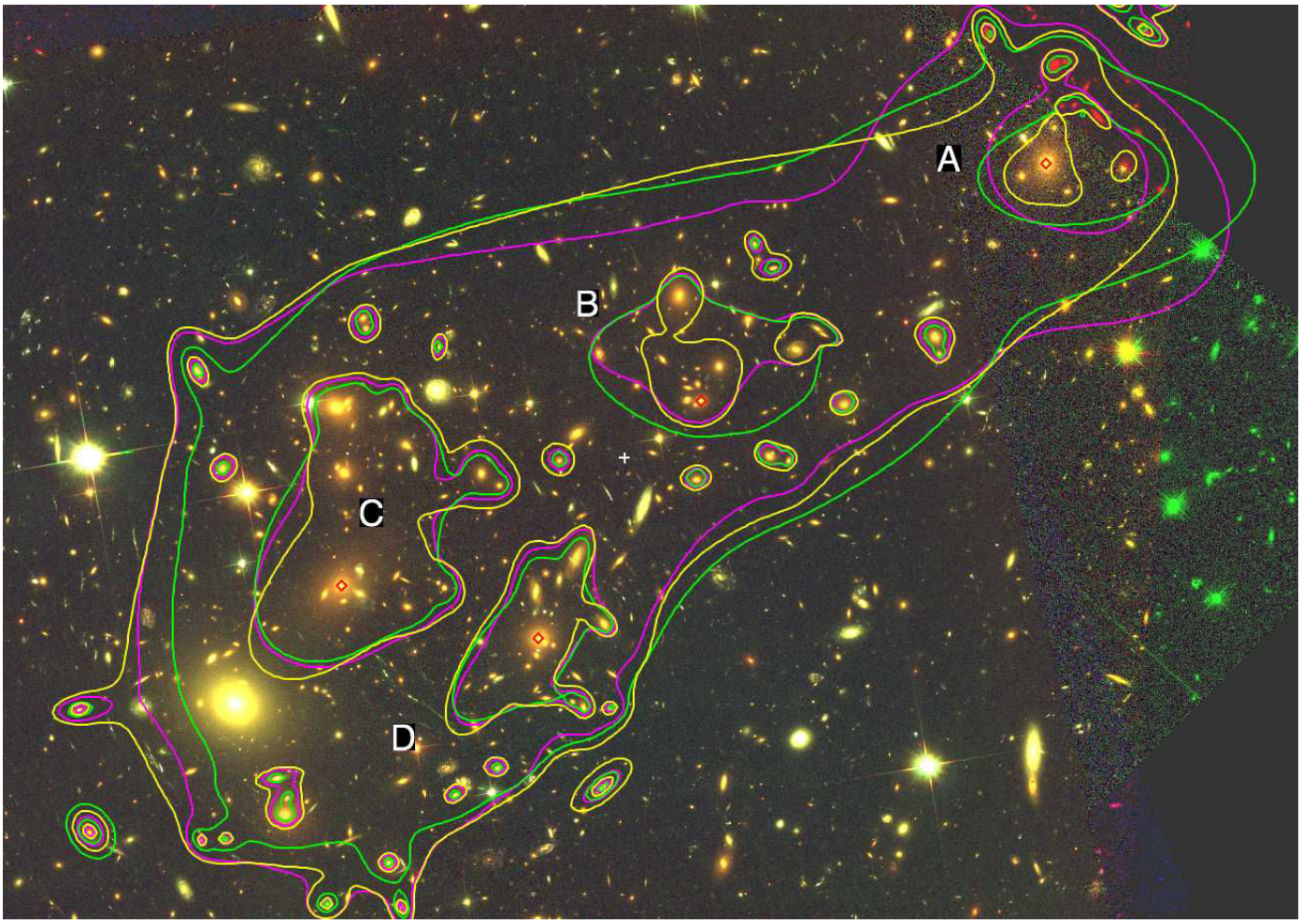


**Fig. 2.** Mass maps inferred from the cored (yellow), the non-cored (green) and the NFW (magenta) models. Contours show where the surface mass density equals 4, $7 \times 10^{10}\ M_{\odot}$ arcsec$^{-2}$. Red diamonds correspond to the light peaks associated with each mass component. The white cross shows the barycentre of the Einstein ring as estimated by Meneghetti et al. (2011) at $\alpha = 109.38002, \delta = 37.752214$. The underlying image covers an area of $236'' \times 166''$.

is significantly offset from the closest light peak. These authors argued that this offset is probably due to the lack of lensing constraints in that area.

Since three of the four components have core radii larger than 15″, i.e., larger than 100 kpc at the redshift of MACS J0717, their superposition leads to a relatively flat mass distribution. In the following, this model is referred to as the cored mass model.

Various mechanisms that could lead to such large cores have been proposed (see also Diego et al. 2015b,a, for a thorough discussion). Large cores in massive central galaxies are thought to be caused by massive black holes that clear the centre of galaxies of stars (see, e.g. López-Cruz et al. 2014). This may affect dark matter as well, but the scales on which this mechanism can be expected to be effective (less than 10 kpc) are smaller than the scale we are interested in here (∼100 kpc). Actif galactic nucleus feedback can also contribute to the flattening of the central region (Martizzi et al. 2012), but once again this mechanism is efficient only on small scales (up to 10–15 kpc). On scales of 100 kpc, large cores may result from violent interactions related to merging events in this actively evolving cluster, although several studies find that DM profiles are not strongly altered by a collision (Ricker & Sarazin 2001; Dekel et al. 2003; Molnar et al. 2010). Finally, heating of massive galaxies by dynamical friction against the diffuse dark matter distribution of the cluster can flatten the slope of the DM density profile, and sometimes even dominate over adiabatic contraction (see, e.g. El-Zant et al. 2001, 2004). Another explanation might be self-interacting dark matter particles (Natarajan et al. 2008; Rocha et al. 2013), known to flatten the cusps of cluster scale haloes on scales up to 100 kpc, or the multi-coupled Dark Energy scenario (Garaldi et al. 2016).

Given the implications of a flat mass profile for MACS J0717, we investigate its mass distribution further by testing whether large-core components are really required by the data. To this end, we explore in the next subsection a peaky, non-cored mass model.

### 4.2. Non-cored mass components: a peaky DM distribution?

The differences between the non-cored and the cored mass models lie in the shape and location of each mass component: the position of each mass component is required to lie within 5″ of the associated light peak in both right ascension and declination, and its core radius is forced to be smaller than 5″. Interestingly, we find that this non-cored mass model is also able to reproduce the observational constraints, with an image-plane rms of 2.4″, similar to that of the cored mass model. Therefore, both models fit the data equally well, in the sense that they give comparable total rms.

**Table 2.** Same as Table 1 for the non-cored mass model.

| Component | ΔRA | ΔDec | $e$ | $\theta$ | $r_{\rm core}$ ($''$) | $r_{\rm s}$ ($''$) | $\sigma$ (km s$^{-1}$) |
|---|---|---|---|---|---|---|---|
| C | –0.9 ± 0.5 | $4.9^{+0.1}_{-0.5}$ | >0.38 | 63 ± 2 | $4.9^{+0.1}_{-0.2}$ | [1000] | 889 ± 11 |
| D | 31.8 ± 0.5 | –14.5 ± 0.5 | >0.69 | 46 ± 3 | 4.8 ± 0.2 | [1000] | 617 ± 8 |
| B | 64.9 ± 1.0 | $39.9^{+0.1}_{-0.2}$ | >0.54 | 173 ± 18 | $4.9^{+0.1}_{-0.6}$ | [1000] | 733 ± 13 |
| A | $134.9^{+0.1}_{-0.7}$ | $75.0^{+0.5}_{-0.1}$ | 0.61 ± 0.03 | 12.0 ± 9 | 2.7 ± 0.4 | [1000] | 795 ± 16 |
| $L^*$ galaxy | – | – | – | – | [0.05] | 11.4 ± 1.4 | 161 ± 6 |

**Table 3.** NFW parameters inferred for the four large-scale dark matter clumps (A, B, C, D) and the dPIE parameters for the galaxy-scale component (core radius fixed to 0.3 kpc).

| Component | ΔRA | ΔDec | $e$ | $\theta$ | $c_{200}$ | $r_{\rm s}$ ($''$) | $\sigma$ (km s$^{-1}$) |
|---|---|---|---|---|---|---|---|
| C | –2.3 ± 0.6 | –0.7 ± 0.8 | 0.13 ± 0.02 | 53 ± 4 | 3.4 ± 0.2 | 81.8 ± 6.0 | – |
| D | 32.6 ± 0.4 | –13.5 ± 0.5 | 0.55 ± 0.03 | 50 ± 2 | 5.3 ± 0.3 | 25.3 ± 2.2 | – |
| B | 63.3 ± 1.2 | 44.6 ± 0.4 | 0.51 ± 0.06 | 5 ± 2 | $3.0^{+0.1}_{-0.0}$ | 63.9 ± 3.7 | – |
| A | 133.7 ± 0.9 | 77.4 ± 1.4 | 0.23 ± 0.04 | 165 ± 15 | 5.5 ± 0.3 | 32.5 ± 0.35 | – |
| $L^*$ galaxy | – | – | – | – | – | 9.2 ± 0.4 | 188 ± 9 |

**Notes.** These parameters correspond to the NFW mass model. Coordinates are given in arcseconds with respect to $\alpha$ = 109.3982, $\delta$ = 37.745778. The ellipticity $e$ is for the mass distribution. Error bars correspond to 1$\sigma$ confidence level. Concerning the scaling relations, the zero point is set to a magnitude equal to 20.66.

Best-fit parameters for this mass model are listed in Table 2. We can appreciate that they differ significantly from the best-fit parameters obtained for the cored mass model. The corresponding mass contours are shown in green in Fig. 2. Essentially, the total mass distribution of this model also follows the light distribution.

### 4.3. NFW profile

We further investigate the impact of the profile of the DM components on our model's ability to satisfy the lensing constraints by adopting an NFW profile (Navarro et al. 1996), parametrized by a scale radius $r_{\rm s}$ and a concentration parameter $c_{200}$, for each of the four cluster-scale components. We note that this exercise is not physically motivated. Although NFW profiles are well suited to describe isolated, relaxed DM haloes, they are not necessarily expected to be adequate for the parameterization of this complex merging system. While the four subclusters may have had an NFW mass profile before their collision, it is not obvious that they will keep this shape during the violent merging process acting in MACS J0717.

Here we test two NFW models. In the first, the location of each mass component is allowed to vary within ±20″ of its associated light peak (the same limits used for the cored mass model); in the second, this limitation is tightened to 5″ (the same limits used for the non-cored mass model). In both cases, the scale radius is allowed to vary between 80 and 750 kpc, and the concentration parameter between 3 and 6.

We find that the best-fit parameters derived for either NFW model agree with each other. Even when the position of the components is allowed to deviate from that of the corresponding light peak, the best-fit position ends up consistent with the light distribution. We conclude that an NFW cusp without a luminous counterpart is not favoured by the data. In light of this result, we thus only discuss further the second NFW model. It too is able to reproduce the observational constraints, with an image-plane rms of 2.2″, comparable to that of both the cored and non-cored models. Best-fit parameters for this mass model are listed in Table 3; the corresponding mass contours are shown in magenta in Fig. 2.

This test thus further confirms that a peaky DM distribution for the large-scale mass components can accommodate the strong lensing constraints.

### 4.4. A hybrid mass model

A key assumption of all models so far has been that each mass component is associated with one of the four light peaks in MACS J0717 (we note that this hypothesis is supported by previous studies, in particular by the series of "blind tests" performed in Limousin et al. 2012). Consistent with this assumption, Fig. 2 shows the light distributions corresponding to the mass components A, C, and D to be dominated by a bright elliptical galaxy; however, this is not the case for mass component B, whose light peak coincides with a group of small elliptical galaxies. Acknowledging this peculiarity, we consider a hybrid mass model that combines some of the properties of the cored and the non-cored mass models. Components A, C, and D are described by a dPIE mass profile, whose right ascension and declination are required to remain within ±5″ of the associated light peak and whose core radius is forced to be smaller than 5″, whereas component B is modelled by a dPIE mass profile whose position is allowed to vary within ±20″ of the associated light peak, and whose core radius is allowed to reach 35″. Not surprisingly, this hybrid model is also able to reproduce the observational constraints with an rms of 2.2″. The best-fit location of component B is 8.5″ away from the associated light peak, and its best-fit core radius is 20 ± 2″.

## 5. Model comparison

The small difference in rms between the cored and the non-cored model (0.5″) suggests that the observational constraints, even in the HFF era, cannot discriminate between a flat and a peaky dark matter distribution for the smooth component. This difference in rms is comparable to or smaller than that due to an image mis-identification (see, e.g. the case of image 3.3 in Abell 2744 presented in Jauzac et al. 2015), or to the difference caused by an unaccounted for structure along the line of sight (e.g. Host 2012), two effects that may also affect our analysis.

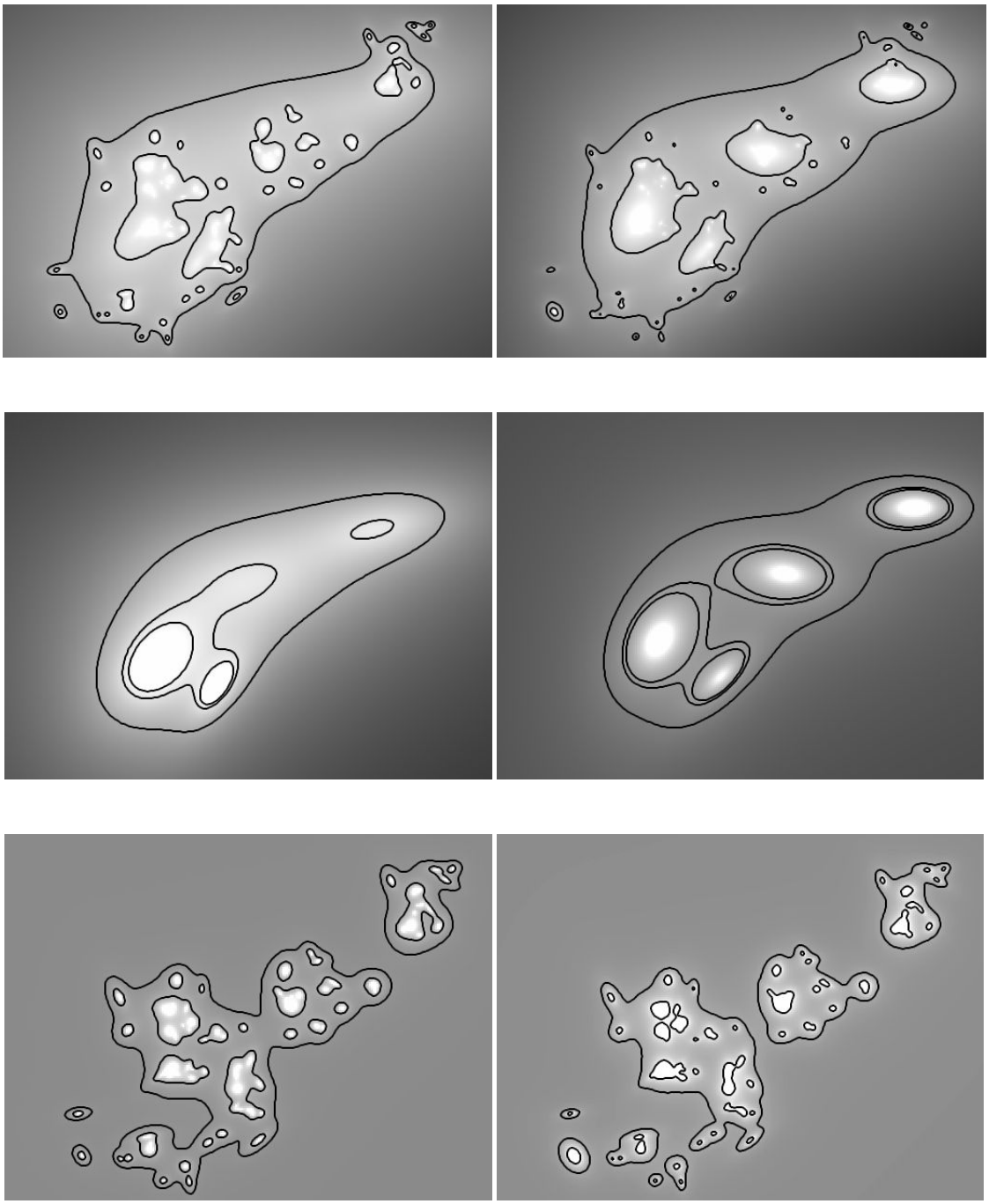

**Fig. 3.** Comparison between the mass maps of the cored (*left*) and the non-cored (*right*) mass models. *Top*: total mass (smooth component + galaxies). Contours show where the surface mass density equals 4, $7 \times 10^{10}$ $M_{\odot}$ arcsec$^{-2}$. *Middle*: contribution from the smooth component only. Contours delineate where the surface mass density equals 4, 5.5, $6.0 \times 10^{10}$ $M_{\odot}$ arcsec$^{-2}$. *Bottom*: contribution from the galaxies component only. Contours mark where the surface mass density equals 0.5, $2 \times 10^{10}$ $M_{\odot}$ arcsec$^{-2}$. We note that the galaxies gain more weight in the cored mass model, in order to compensate for the smoothness of the underlying large-scale mass components. Each panel measures $260'' \times 190''$.

### 5.1. Mass maps

Figure 3 shows that the total mass maps generated by these two mass models are quite similar (top row) and follow the light distribution. In the middle and bottom row of Fig. 3 this comparison is decomposed into the smooth component and the galaxy-scale component. In that decomposition, one can see important differences between the smooth components. It is peaky in the non-cored mass model, and the four mass components are clearly visible. By contrast, the dark matter distribution of the cored mass model is much more diffuse, leading to a very shallow mass profile. However, this effect is compensated for by the galaxy-scale component, which is much more massive in the cored mass model (lower plots of Fig. 3).

### 5.2. Convergence profile of the smooth component

Figure 4 (top left) compares the resulting convergence profile of the smooth component for the two models. Following Diego et al. (2015b), we take the centre of the profile to be the position of the most massive galaxy that is closest to the centre of group C ($\alpha = 109.3982, \delta = 37.745778$). As expected from Fig. 3, the

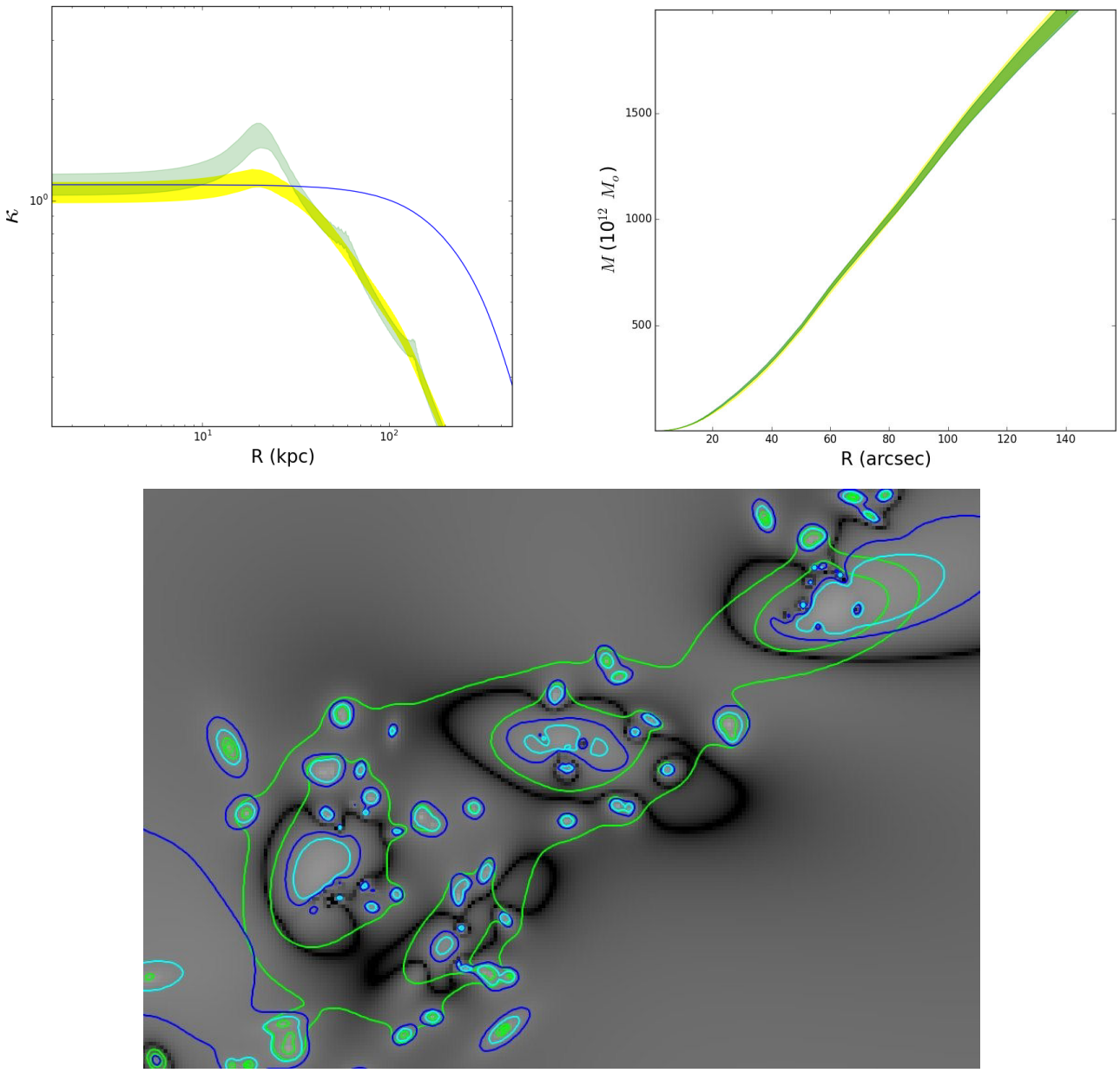


**Fig. 4.** *Top left*: surface-mass-density profile for the smooth component of the cored (yellow) and the non-cored (green) mass model. The blue line shows the same quantity, as derived by Diego et al. (2015b). Shaded areas represent $3\sigma$ uncertainties. *Top right*: cumulative two-dimensional mass profile for the cored (yellow) and the non-cored (green) mass model (abscissa in arc seconds). *Bottom*: absolute value of the relative difference between each models. Blue contours mark where the difference is 20%, and cyan contours where it is 30%. The mass contours corresponding to the non-cored model are shown in green. The size of the field is $226'' \times 155''$.

profiles differ visibly. For the cored mass model, the convergence profile is basically flat out to 20 kpc and then decreases monotonically, whereas the profile for the non-cored model features bumps corresponding to the mass components D, B, and A. For comparison, the same figure also shows the convergence profile for the smooth component inferred by Diego et al. (2015b). It resembles the profile of our cored model, but remains very flat to a much larger radius (~100 kpc) before decreasing monotonically.

### 5.3. Total mass profile

Although the large-scale (smooth) components of our two models results in noticeably different radial mass profiles, the models' cumulative total two-dimensional mass profiles are nearly indistinguishable (Fig. 4, right). Owing to the complex spatial distribution of the mass, the centre of MACS J0717 (needed to integrate the two-dimensional mass map) is not easily defined. Following Meneghetti et al. (2011), we choose the barycentre of the Einstein ring, at $\alpha = 109.38002, \delta = 37.752214$ (white cross on Fig. 2), near the centre of the ACS frame. The projected mass within 990 kpc ($156''$) of this location is found to be $M = (2.229 \pm 0.022) \times 10^{15}\ M_\odot$ for the cored model, and $M = (2.199 \pm 0.021) \times 10^{15}\ M_\odot$ for the non-cored model ($1\sigma$ statistical errors). As for other cluster mass models based on HFF data (Jauzac et al. 2015, 2016, 2014), the errors thus imply 1% precision. However, such claims disregard the additional, systematic uncertainty that we investigate here and which, based on the choice of mass model, leads to larger error bars on the mass. Averaging the two mass measurements yields $M = (2.214 \pm 0.037) \times 10^{15}\ M_\odot$. It is likely that other systematic uncertainties, not

taken into account here, further affect the reported value and its error.

A final comparison is presented in Fig. 4, which shows the absolute value of the relative difference between the mass maps inferred for the cored and the non-cored model. We find differences of 30% near massive cluster ellipticals and, importantly, also in the cores of the four large-scale components.

### 5.4. Comparison with other studies

Diego et al. (2015b), using the first third of the HFF observations, reported an image plane rms of 2.8″. More recently, Kawamata et al. (2016), using 173 images from the full depth of the HFF observations, reported an image plane rms of 0.52″. Their modelling approach is parametric. They place nine NFW components on the positions of bright cluster members (of which six have a mass larger than $10^{14}\,h^{-1}\,M_{\odot}$), plus multipole perturbations modelling the external perturbations on the lens potential and the asymmetry of the cluster mass distribution. Compared to our approach, their model involves many more parameters, which may explain why their rms is significantly smaller than ours. Their paper focusses on the detection of high-redshift galaxies, and so modelling results that allow to pursue a more detailed comparison are not provided. In particular, it is not possible to see if their best mass model is closer to our cored or to our non-cored mass model.

## 6. Discussion

Our analysis reveals that two very different models (in term of mass component parameters) are able to reproduce all observational constraints equally well, in the sense that the total rms is comparable. While we can state that the mass distribution in MACS J0717 is quadri-modal, further insights remain limited; in particular, we are not able to constrain the shape and the precise location of the four mass clumps, even with the exquisite data provided by the HFF project. Although this problem is likely exacerbated by the complexity of the mass distribution in MACS J0717, it is likely to affect and limit our understanding of the mass distribution in other clusters too.

In the following we discuss ways to discriminate between these models.

### 6.1. Stellar velocity dispersions

As our two models lead to different mass distributions for the galaxy-scale component (see Fig. 3), here we investigate the role of the galaxy-scale perturbers in an attempt to find ways to discriminate between the two models.

The parameters characterizing the galaxy-scale perturbers, the velocity dispersion $\sigma$ and the scale radius $r_{\rm s}$, differ noticeably: we find $\sigma = 250\,{\rm km\,s^{-1}}$ and $r_{\rm s} = 53\,{\rm kpc}$ for the cored mass model, and $\sigma = 161\,{\rm km\,s^{-1}}$ and $r_{\rm s} = 73\,{\rm kpc}$ for the non-cored mass model (for a magnitude of 20.66). Both of these parameters can be constrained independently by weak and strong galaxy-galaxy lensing in clusters, and by measurements of the stellar velocity dispersion from low-resolution spectroscopy. Recently, Monna et al. (2015) conducted the latter type of investigation for the galaxies in Abell 383 and also presented a compilation of similar measurements in the literature (Fig. 11 of their paper). The parameter $\sigma$ is found to range from 80 to 300 $\rm km\,s^{-1}$ and $r_{\rm s}$ from 5 to 85 kpc, which are consistent with the values obtained for both of our two models. Measurements of these parameters for a significant number of individual galaxies in MACS J0717 may allow us to discriminate between the cored and the non-cored mass model.

### 6.2. Redshift estimates and measurements

In principle, the redshift predictions of either model might prove useful to discriminate between them. However, all estimated redshifts predicted by the different mass models (listed in Tables A.1 and A.2) agree with each other at the $3\sigma$ confidence level. We also note that for all systems but one (system 39), these model-based estimates agree with the photometric redshifts.

### 6.3. Beyond strong lensing

Using different probes beyond strong lensing might also allow us to at least alleviate the degeneracies between the cluster- and galaxy-scale mass components. Measuring the weak-lensing shear around cluster members is a very interesting avenue in this context, in particular in the flexion regime, which is well suited to probe galaxy-scale dark matter haloes. Although flexion is challenging to measure, its signal has already been detected in much shallower space-based images than the ones provided by the HFF (see, e.g. Leonard et al. 2007, on Abell 1689).

## 7. Implications for magnification estimates

The primary science goal of the HFF campaign is to use clusters as gravitational telescopes in order to probe deeper into the high-redshift Universe. Whether, or how well, this goal can be achieved depends critically on the accuracy with which one can recover the amplification that allows us to convert observed into intrinsic properties of said high-redshift objects.

Not surprisingly, the cored and the non-cored mass models presented in this paper lead to different magnification estimates, thus adding a systematic error that is in general larger than the statistical error derived from a single mass model. This systematic error is defined as the difference between the amplification derived from the best-fit cored model and the amplification derived from the best-fit non-cored model. It can sometimes be larger than the difference between the magnification values obtained by the different groups of modellers, using pre-HFF data. To quantify the effect for a given image, we compute the amplifications obtained by the different groups of modellers using pre-HFF data[3] and take the difference between the smallest and largest value as the "modellers" uncertainty.

For a given source redshift, the implications of these systematic uncertainties for magnification estimates depends on where one looks through the cluster. To illustrate this, for a few multiply imaged galaxies we list the following informations in Table 4: the amplification with associated error bars and signal-to-noise ratio (in square brackets), for the cored and the non-cored models; the difference between these two amplifications (the systematic error developed in this paper), and the previously mentioned modellers uncertainty. The images used for this exercise were chosen to represent a wide range of magnifications: several are located far from the critical lines (images 19.3, 68.2, 71.2, and 61.2), one is close to the critical line in one model but not in the other (image 57.1), and another one lies close to the critical lines in both models (23.2).

In regions where the amplification is estimated with high confidence, we note how the amplification difference between

[3] http://archive.stsci.edu/prepds/frontier/lensmodels/

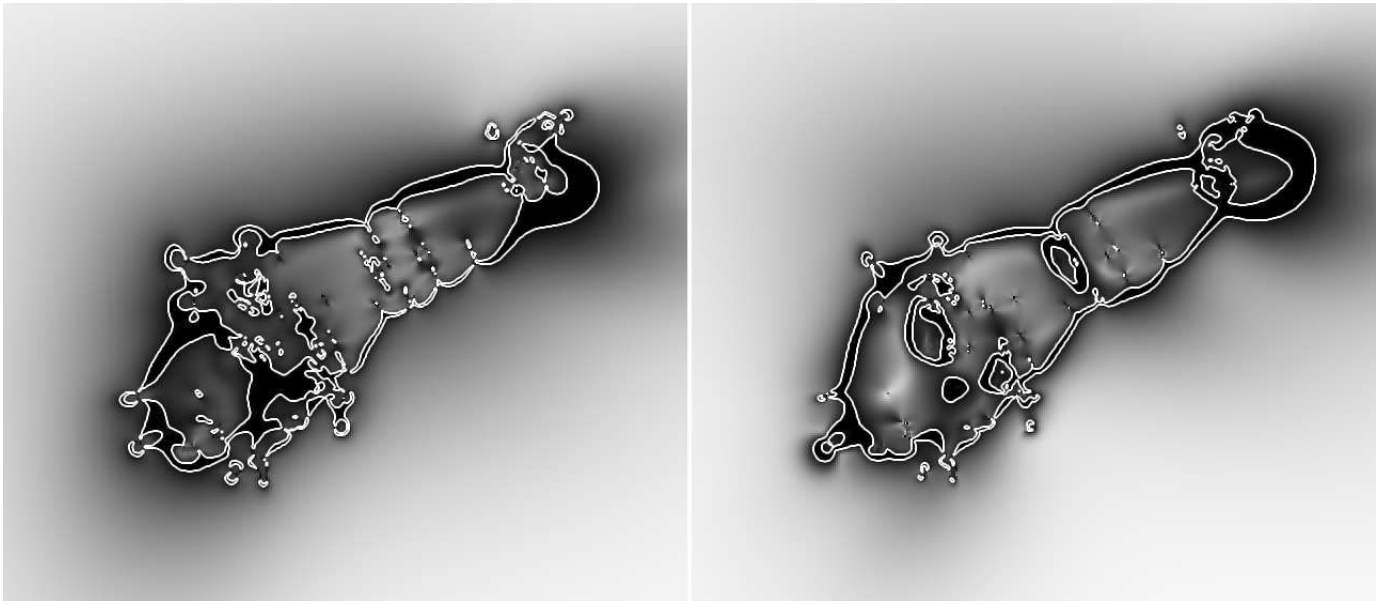

**Fig. 5.** Map (310″ × 310″) of the signal-to-noise ratio of the amplification, for the cored (*left*) and the non-cored (*right*) mass models. White lines indicate where the signal-to-noise ratio equals 3. Darker areas interior to these lines correspond to regions where the signal-to-noise ratio is less than 3.

**Table 4.** Illustration of the implication of the systematic uncertainty on magnification estimates.

| ID | Ampli (cored) | Ampli (non-cored) | Δ [cored – noncored] | Δ [pre-HFF] |
|---|---|---|---|---|
| 19.3 | 3.2 ± 0.15 [21] | 2.8 ± 0.07 [40] | 0.4 | 1.7 |
| 68.2 | 24 ± 2.0 [12] | 8.7 ± 0.6 [14.5] | 15.3 | 4.0 |
| 71.2 | 12.0 ± 1.4 [8.5] | 10.0 ± 0.7 [14] | 2.0 | 63.5 |
| 61.2 | 2.3 ± 0.2 [11.5] | 1.6 ± 0.1 [16] | 0.7 | 1.62 |
| 57.1 | 12.3 ± 6.0 [2] | 32.4 ± 846 [<1] | >100 | 205 |
| 23.2 | 1083 ± 9167 [<1] | 21.8 ± 2.5 [<1] | >1000 | 69 |

**Notes.** For different multiple images, the value of the amplification with associated errors and signal-to-noise ratio (in brackets), for the cored and the non-cored model; the difference in amplification between the cored and the non-cored mass model; the difference in amplification considering pre-HFF data and the different modelling/group software. Magnifications computed for $z = 3.0$.

the cored and the non-cored models is larger than the error associated with a given model and comparable to the modellers uncertainty. In the case of image 57.1, we also note how the amplification is reasonably well constrained in the cored model (signal-to-noise ratio of 2), but essentially unconstrained in the non-cored model.

This additional systematic uncertainty needs to be taken into account in all practical applications of a gravitational telescope, as it will decrease the area of the image plane where amplifications are well determined enough for credible studies of the high-redshift Universe. We quantify this effect by computing the area of the image plane for which the signal-to-noise ratio on the amplification is less than 3 for a source redshift of 7. We find 1.1 and 1.3 arcmin$^2$ for the cored and non-cored models, respectively. When both models are considered valid descriptions, thus adding the above-mentioned systematic error, this area increases to 1.9 arcmin$^2$, i.e., by 50 and 70%, respectively. A graphic presentation of this change in area is provided by Fig. 5 which shows the signal-to-noise ratio for the cored and the non-cored mass models; the white line marks a value of 3.

## 8. Conclusion

We present a strong-lensing analysis of MACS J0717 based on the full depth of the HFF data.

We find that the lensing constraints can be equally well satisfied by a mass model with a shallow large-scale DM component and one for which this component is peaky. Given the clear physical difference between the two models, we conclude that our insights into the DM distribution remain limited, even in the HFF era. One way to discriminate between the two models would be to model the mass distribution while constraining simultaneously the large-scale smooth component and the galaxy-scale component, i.e. the two ingredients of our mass models that display generic degeneracies.

Our findings have important implications for magnification estimates. We show that the ambiguity between the two models leads to an additional systematic error that varies with position and needs to be taken into account when looking at the high-redshift Universe through MACS J0717. Generally speaking, it decreases the area available for studying the high-redshift Universe by 50–70%.

*Acknowledgements.* M.L. thanks Jose M. Diego for helpful exchanges during the writing of this paper. M.L. acknowledges the Centre National de la Recherche Scientifique (CNRS) for its support. This work was performed using facilities offered by CeSAM (Centre de donnéeS Astrophysique de Marseille-(http://lam.oamp.fr/cesam/). This work was granted access to the HPC resources of Aix-Marseille Université financed by the project Equip@Meso (ANR-10-EQPX-29-01) of the program "Investissements d'Avenir" supervised by the Agence Nationale pour la Recherche (ANR). We acknowledge support

from the Programme National de Cosmologie et Galaxie (PNCG). C.G. is grateful to CNES for financial support. This work was carried out with support of the OCEVU Labex (ANR-11-LABX-0060) and the A*MIDEX project (ANR-11-IDEX-0001-02) funded by the "Investissements d'Avenir" French government program managed by the ANR. M.J. is supported by the Science and Technology Facilities Council [grant number ST/L00075X/1 & ST/F001166/1]. This work used the DiRAC Data Centric system at Durham University, operated by the Institute for Computational Cosmology on behalf of the STFC DiRAC HPC Facility (www.dirac.ac.uk [www.dirac.ac.uk]), using equipment funded by BIS National E-infrastructure capital grant ST/K00042X/1, STFC capital grant ST/H008519/1, and STFC DiRAC Operations grant ST/K003267/1 and Durham University. DiRAC is part of the National E-Infrastructure. This study used gravitational-lensing models produced by PIs Bradac, Ebeling, Merten & Zitrin, Sharon, and Williams funded as part of the HST Frontier Fields program conducted by STScI. STScI is operated by the Association of Universities for Research in Astronomy, Inc. under NASA contract NAS 5-26555. The lens models were obtained from the Mikulski Archive for Space Telescopes (MAST); we thank Dan Coe for kindly making them available to the community. PN acknowledges support from the National Science Foundation through grant AST-1044455.

## References

Bonafede, A., Feretti, L., Giovannini, G., et al. 2009, A&A, 503, 707
Brammer, G. B., van Dokkum, P. G., & Coppi, P. 2008, ApJ, 686, 1503
Coe, D., Bradley, L., & Zitrin, A. 2015, ApJ, 800, 84
D'Aloisio, A., & Natarajan, P. 2011, MNRAS, 411, 1628
Dekel, A., Devor, J., & Hetzroni, G. 2003, MNRAS, 341, 326
Diego, J. M., Broadhurst, T., Molnar, S. M., Lam, D., & Lim, J. 2015a, MNRAS, 447, 3130
Diego, J. M., Broadhurst, T., Zitrin, A., et al. 2015b, MNRAS, 451, 3920
Ebeling, H., Barrett, E., & Donovan, D. 2004, ApJ, 609, L49
Ebeling, H., Barrett, E., Donovan, D., et al. 2007, ApJ, 661, L33
Edge, A. C., Ebeling, H., Bremer, M., et al. 2003, MNRAS, 339, 913
El-Zant, A., Shlosman, I., & Hoffman, Y. 2001, ApJ, 560, 636
El-Zant, A. A., Hoffman, Y., Primack, J., Combes, F., & Shlosman, I. 2004, ApJ, 607, L75
Elíasdóttir, Á., Limousin, M., Richard, J., et al. 2007, ArXiv e-prints [arXiv:0710.5636]
Fioc, M., & Rocca-Volmerange, B. 1997, A&A, 326, 950
Garaldi, E., Baldi, M., & Moscardini, L. 2016, J. Cosmol. Astropart. Phys., 1, 050
Host, O. 2012, MNRAS, 420, L18
Jauzac, M., Jullo, E., Kneib, J.-P., et al. 2012, MNRAS, 426, 3369
Jauzac, M., Clément, B., Limousin, M., et al. 2014, MNRAS, 443, 1549
Jauzac, M., Richard, J., Jullo, E., et al. 2015, MNRAS, 452, 1437
Jauzac, M., Richard, J., Limousin, M., et al. 2016, MNRAS, 457, 2029
Johnson, T. L., Sharon, K., Bayliss, M. B., et al. 2014, ApJ, 797, 48
Jouvel, S., Host, O., Lahav, O., et al. 2014, A&A, 562, A86
Jullo, E., Kneib, J.-P., Limousin, M., et al. 2007, New J. Phys., 9, 447
Jullo, E., Natarajan, P., Kneib, J.-P., et al. 2010, Science, 329, 924
Kawamata, R., Oguri, M., Ishigaki, M., Shimasaku, K., & Ouchi, M. 2016, ApJ, 819, 114
LaRoque, S. J., Joy, M., Carlstrom, J. E., et al. 2003, ApJ, 583, 559
Leonard, A., Goldberg, D. M., Haaga, J. L., & Massey, R. 2007, ApJ, 666, 51
Limousin, M., Kneib, J.-P., & Natarajan, P. 2005, MNRAS, 356, 309
Limousin, M., Kneib, J. P., Bardeau, S., et al. 2007a, A&A, 461, 881
Limousin, M., Richard, J., Jullo, E., et al. 2007b, ApJ, 668, 643
Limousin, M., Sommer-Larsen, J., Natarajan, P., & Milvang-Jensen, B. 2009, ApJ, 696, 1771
Limousin, M., Ebeling, H., Richard, J., et al. 2012, A&A, 544, A71
López-Cruz, O., Añorve, C., Birkinshaw, M., et al. 2014, ApJ, 795, L31
Ma, C., & Ebeling, H. 2010, MNRAS, 1646
Ma, C.-J., Ebeling, H., Donovan, D., & Barrett, E. 2008, ApJ, 684, 160
Ma, C.-J., Ebeling, H., & Barrett, E. 2009, ApJ, 693, L56
Martizzi, D., Teyssier, R., Moore, B., & Wentz, T. 2012, MNRAS, 422, 3081
Medezinski, E., Umetsu, K., Nonino, M., et al. 2013, ApJ, 777, 43
Meneghetti, M., Fedeli, C., Zitrin, A., et al. 2011, A&A, 530, A17
Molnar, S. M., Chiu, I.-N., Umetsu, K., et al. 2010, ApJ, 724, L1
Monna, A., Seitz, S., Zitrin, A., et al. 2015, MNRAS, 447, 1224
Mroczkowski, T., Dicker, S., Sayers, J., et al. 2012, ApJ, 761, 47
Natarajan, P., Croton, D., & Bertone, G. 2008, MNRAS, 388, 1652
Natarajan, P., Kneib, J.-P., Smail, I., et al. 2009, ApJ, 693, 970
Navarro, J. F., Frenk, C. S., & White, S. D. M. 1996, ApJ, 462, 563
Pandey-Pommier, M., Richard, J., Combes, F., et al. 2013, A&A, 557, A117
Postman, M., Coe, D., Benítez, N., et al. 2012, ApJS, 199, 25
Richard, J., Jauzac, M., Limousin, M., et al. 2014, MNRAS, 444, 268
Ricker, P. M., & Sarazin, C. L. 2001, ApJ, 561, 621
Rocha, M., Peter, A. H. G., Bullock, J. S., et al. 2013, MNRAS, 430, 81
Sayers, J., Mroczkowski, T., Zemcov, M., et al. 2013, ApJ, 778, 52
Schmidt, K. B., Treu, T., Brammer, G. B., et al. 2014, ApJ, 782, L36
Treu, T., Schmidt, K. B., Brammer, G. B., et al. 2015, ApJ, 812, 114
van Weeren, R. J., Röttgering, H. J. A., Brüggen, M., & Cohen, A. 2009, A&A, 505, 991
Vanzella, E., Fontana, A., Zitrin, A., et al. 2014, ApJ, 783, L12
Wetzel, A. R., & White, M. 2010, MNRAS, 403, 1072
Zitrin, A., Broadhurst, T., Rephaeli, Y., & Sadeh, S. 2009, ApJ, 707, L102
Zitrin, A., Fabris, A., Merten, J., et al. 2015, ApJ, 801, 44

**Table A.1.** Multiple-image systems found before the FF observations.

| ID | RA | Dec | $z_{spec}$ | $z_{model}$ (non-cored, cored, NFW) | $z_{phot}$ |
|---|---|---|---|---|---|
| 1.1 | 109.39534 | 37.741178 | – | – | 3.07 ± 0.06 |
| 1.2 | 109.39382 | 37.740095 | 2.963 | – | 2.91 ± 0.09 |
| 1.3 | 109.39098 | 37.738280 | 2.963 | – | 2.72 ± 0.17 |
| 1.4 | 109.38436 | 37.736945 | – | – | 3.11 ± 0.06 |
| 1.5 | 109.40578 | 37.761378 | – | – | 3.11 ± 0.07 |
| 2.1 | 109.39281 | 37.741010 | – | 2.6 ± 0.3, 2.2 ± 0.4, 3.0 ± 0.3 | 2.72 ± 0.12 |
| 2.2 | 109.39043 | 37.739245 | – | – | 2.72 ± 0.07 |
| 3.1 | 109.39855 | 37.741495 | 1.855 | – | 1.87 ± 0.04 |
| 3.2 | 109.39446 | 37.739176 | 1.855 | – | 1.84 ± 0.04 |
| 3.3 | 109.40715 | 37.753827 | 1.855 | – | 1.84 ± 0.04 |
| 4.1 | 109.38088 | 37.750127 | 1.855 | – | 1.93 ± 0.05 |
| 4.2 | 109.37644 | 37.744696 | 1.855 | – | 1.84 ± 0.04 |
| 4.3 | 109.39109 | 37.763296 | 1.855 | – | 1.82 ± 0.04 |
| 5.1 | 109.37991 | 37.746861 | – | 4.1 ± 0.2, 3.8 ± 0.2, 3.7 ± 0.1 | – |
| 5.2 | 109.37791 | 37.742810 | – | – | – |
| 5.3 | 109.40003 | 37.767399 | – | – | – |
| 6.1 | 109.36436 | 37.757091 | 2.393 | – | 2.37 ± 0.06 |
| 6.2 | 109.36271 | 37.752693 | 2.393 | – | 2.27 ± 0.07 |
| 6.3 | 109.37388 | 37.769711 | 2.393 | – | – |
| 7.1 | 109.36657 | 37.766343 | – | 1.9 ± 0.1, 2.0 ± 0.1, 2.0 ± 0.1 | – |
| 7.2 | 109.36505 | 37.764125 | – | – | – |
| 7.3 | 109.35905 | 37.751780 | – | – | 2.23 ± 0.13 |
| 8.1 | 109.36665 | 37.769694 | – | 2.5 ± 0.1, 2.9 ± 0.2, 2.8 ± 0.1 | – |
| 8.2 | 109.36208 | 37.763125 | – | – | – |
| 8.3 | 109.35652 | 37.751928 | – | – | – |
| 12.1 | 109.38516 | 37.751844 | 1.699 | – | 1.62 ± 0.05 |
| 12.2 | 109.37762 | 37.742878 | 1.699 | – | 1.73 ± 0.06 |
| 12.3 | 109.39122 | 37.760626 | 1.699 | – | 1.71 ± 0.05 |
| 13.1 | 109.38567 | 37.750733 | 2.547 | – | 2.47 ± 0.06 |
| 13.2 | 109.37756 | 37.739627 | – | – | 2.54 ± 0.07 |
| 13.3 | 109.39621 | 37.763333 | 2.540 | – | 2.61 ± 0.09 |
| 14.1 | 109.38879 | 37.752163 | 1.855 | – | 1.84 ± 0.04 |
| 14.2 | 109.37966 | 37.739707 | 1.855 | – | 1.84 ± 0.04 |
| 14.3 | 109.39619 | 37.760427 | 1.855 | – | 1.84 ± 0.02 |
| 15.1 | 109.36766 | 37.772059 | 2.405 | – | – |
| 15.2 | 109.35862 | 37.760127 | – | – | – |
| 15.3 | 109.35654 | 37.754641 | – | – | 3.40 ± 0.08 |
| 16.1 | 109.36916 | 37.773279 | – | 3.2 ± 0.3, 3.6 ± 0.3, 3.1 ± 0.1 | – |
| 16.2 | 109.35856 | 37.759558 | – | – | – |
| 16.3 | 109.35694 | 37.753691 | – | – | – |
| 17.1 | 109.36938 | 37.771869 | – | 2.7 ± 0.2, 2.8 ± 0.2, 2.7 ± 0.1 | – |
| 17.2 | 109.35938 | 37.758792 | – | – | – |
| 17.3 | 109.35822 | 37.753609 | – | – | 3.15 ± 0.14 |
| 18.1 | 109.36425 | 37.768628 | – | 2.0 ± 0.1, 2.6 ± 0.5, 2.2 ± 0.1 | – |
| 18.2 | 109.36121 | 37.764326 | – | – | – |
| 19.1 | 109.40906 | 37.754681 | 6.40 | – | – |
| 19.2 | 109.40772 | 37.742731 | 6.40 | – | – |
| 19.3 | 109.38105 | 37.731391 | 6.40 | – | – |

**Notes.** Uncertainties quoted for redshifts predicted by our model, $z_{model}$, correspond to the $1\sigma$ confidence level. They are given for the non-cored, the cored, and the NFW models. In the last column, we show the estimate of the photometric redshift, when possible, together with the $1\sigma$ error bars.

**Table A.2.** Multiple-image systems found after the FF observations.

| ID | RA | Dec | $z_{spec}$ | $z_{model}$ (non-cored, cored, NFW) | $z_{phot}$ |
|---|---|---|---|---|---|
| 20.1 | 109.37420 | 37.7651450 | – | 3.4 ± 1.0, >2.6, uncons. | – |
| 20.2 | 109.37340 | 37.7646610 | – | – | – |
| 21.1* | 109.37241 | 37.746392 | – | – | 2.61 ± 0.16 |
| 21.2* | 109.37673 | 37.752029 | – | – | 2.65 ± 0.12 |
| 22.1* | 109.36773 | 37.755897 | – | – | 0.87 ± 0.11 |
| 22.2* | 109.36769 | 37.755556 | – | – | 0.93 ± 0.05 |
| 23.1* | 109.37958 | 37.762879 | – | – | – |
| 23.2* | 109.37897 | 37.761983 | – | – | – |
| 24.1 | 109.392290 | 37.732946 | – | 2.7 ± 0.1, 2.5 ± 0.1, 2.5 ± 0.1 | – |
| 24.2 | 109.410560 | 37.748427 | – | – | – |
| 25.1 | 109.380290 | 37.744746 | – | 4.0 ± 0.1, 3.8 ± 0.1, 3.8 ± 0.2 | – |
| 25.2 | 109.379510 | 37.742762 | – | – | – |
| 25.3 | 109.402910 | 37.766411 | – | – | – |
| 27.1 | 109.397390 | 37.747883 | – | 1.6 ± 0.9, 3.0 ± 1.1, uncons. | 2.95 ± 0.18 |
| 27.2 | 109.397560 | 37.747567 | – | – | 2.17 ± 0.32 |
| 29.1 | 109.400870 | 37.743174 | – | 1.7 ± 0.1, 1.7 ± 0.1, 1.7 ± 0.1 | 1.45 ± 0.07 |
| 29.2 | 109.392840 | 37.738612 | – | – | 1.62 ± 0.06 |
| 31.1 | 109.374720 | 37.756347 | – | 1.6 ± 0.1, 1.6 ± 0.1, 1.6 ± 0.1 | 1.55 ± 0.08 |
| 31.2 | 109.371000 | 37.750538 | – | – | 1.52 ± 0.06 |
| 31.3 | 109.381610 | 37.764973 | – | – | 1.57 ± 0.08 |
| 32.1 | 109.369500 | 37.757729 | – | 2.3 ± 0.1, 2.8 ± 0.1, 2.5 ± 0.1 | – |
| 32.2 | 109.380950 | 37.769382 | – | – | – |
| 32.3 | 109.366250 | 37.749210 | – | – | 2.40 ± 0.05 |
| 33.1 | 109.383770 | 37.758259 | – | 3.5 ± 0.3, 3.7 ± 0.2, 3.7 ± 0.1 | – |
| 33.2 | 109.386620 | 37.764144 | – | – | – |
| 33.3 | 109.370370 | 37.738712 | – | – | – |
| 34.1 | 109.391580 | 37.766308 | – | 2.6 ± 0.2, 2.7 ± 0.2, 2.6 ± 0.1 | – |
| 34.2 | 109.379110 | 37.751227 | – | – | 1.03 ± 0.05 |
| 34.3 | 109.373300 | 37.744211 | – | – | 1.11 ± 0.09 |
| 36.1 | 109.364330 | 37.771976 | – | 2.4 ± 0.2, 2.9 ± 0.2, 2.6 ± 0.1 | – |
| 36.2 | 109.358240 | 37.763325 | – | – | – |
| 36.3 | 109.353290 | 37.755808 | – | – | – |
| 37.1 | 109.397090 | 37.754736 | – | 3.8 ± 0.8, 3.3 ± 0.7, 3.3 ± 0.4 | – |
| 37.2 | 109.396720 | 37.754793 | – | – | – |
| 39.1 | 109.402270 | 37.731234 | – | 4.3 ± 0.3, 4.1 ± 0.3, 4.1 ± 0.3 | 1.82 ± 0.04 |
| 39.2 | 109.404950 | 37.732519 | – | – | 2.14 ± 0.19 |
| 39.3* | 109.414740 | 37.743276 | – | – | – |
| 45.1 | 109.389820 | 37.739214 | – | 2.7 ± 0.1, 2.7 ± 0.1, 2.6 ± 0.1 | – |
| 45.2 | 109.383480 | 37.737879 | – | – | – |
| 45.3 | 109.404470 | 37.761960 | – | – | – |
| 49.1 | 109.402800 | 37.733260 | – | >4.8, 4.1 ± 0.3, 3.8 ± 0.2 | 3.40 ± 0.08 |
| 49.2 | 109.393000 | 37.730812 | – | – | 3.54 ± 0.06 |
| 50.1 | 109.374440 | 37.743736 | – | 3.7 ± 0.4, 3.6 ± 0.3, 3.6 ± 0.2 | 3.19 ± 0.10 |
| 50.2 | 109.379580 | 37.750708 | – | – | – |
| 50.3* | 109.392800 | 37.767181 | – | – | – |
| 52.1 | 109.368380 | 37.771761 | – | 3.0 ± 0.2, 3.3 ± 0.2, 3.3 ± 0.3 | – |
| 52.2 | 109.360230 | 37.760497 | – | – | – |
| 52.3 | 109.357040 | 37.752486 | – | – | – |
| 55.1 | 109.373760 | 37.755778 | – | 2.2 ± 0.1, 2.4 ± 0.1, 2.4 ± 0.1 | – |
| 55.2 | 109.370240 | 37.748743 | – | – | 2.17 ± 0.11 |
| 55.3 | 109.385020 | 37.768411 | – | – | – |
| 56.1 | 109.373150 | 37.744015 | – | 3.2 ± 0.2, 3.2 ± 0.2, 3.0 ± 0.1 | – |
| 56.2 | 109.378400 | 37.751095 | – | – | – |
| 56.3* | 109.391820 | 37.766216 | – | – | – |
| 57.1 | 109.379030 | 37.744097 | – | 1.7 ± 0.1, 1.8 ± 0.2, 1.7 ± 0.1 | – |
| 57.2 | 109.379530 | 37.745110 | – | – | – |
| 58.1 | 109.379420 | 37.762383 | – | 4.2 ± 1.4, 4.2 ± 1.2, uncons. | 3.03 ± 0.34 |
| 58.2 | 109.379260 | 37.762129 | – | – | – |
| 59.1 | 109.376840 | 37.743245 | – | 3.4 ± 0.8, 4.2 ± 0.5, 3.6 ± 0.5 | 3.11 ± 0.23 |
| 59.2 | 109.379960 | 37.748146 | – | – | – |
| 59.3* | 109.400700 | 37.768628 | – | – | – |

**Notes.** Images with (*) are the ones we propose as candidates and that are not used as constraints in the mass model. Uncertainties quoted for redshifts predicted by our model, $z_{model}$, correspond to the $1\sigma$ confidence level. They are given for the non-cored, the cored, and the NFW model. uncons means unconstrained, i.e. when the output PDF is flat. In the last column, we show the estimate of the photometric redshift, when possible, together with the $1\sigma$ error bars.

**Table A.2.** continued.

| ID | RA | Dec | $z_{spec}$ | $z_{model}$ (non-cored, cored, NFW) | $z_{phot}$ |
|---|---|---|---|---|---|
| 62.1 | 109.372220 | 37.747464 | – | 2.7 ± 0.3, 2.9 ± 0.3, 2.7 ± 0.3 | 2.23 ± 0.08 |
| 62.2 | 109.375510 | 37.752276 | – | – | 2.23 ± 0.06 |
| 63.1 | 109.369420 | 37.756278 | – | 1.3 ± 0.1, 1.6 ± 0.1, 1.7 ± 0.1 | 2.20 ± 0.24 |
| 63.2 | 109.368360 | 37.753695 | – | – | 2.20 ± 0.18 |
| 64.1* | 109.372250 | 37.765391 | – | – | – |
| 64.2* | 109.371790 | 37.765066 | – | – | – |
| 65.1 | 109.383120 | 37.762595 | – | 5.4 ± 0.3, >4.6, >5.0 | – |
| 65.2 | 109.382250 | 37.760394 | – | – | – |
| 66.1 | 109.383310 | 37.765079 | – | >6.5, 6.4 ± 0.8, 6.5 ± 0.4 | – |
| 66.2 | 109.380290 | 37.759228 | – | – | – |
| 67.1 | 109.367470 | 37.756509 | – | 3.0 ± 0.1, 4.2 ± 0.9, 4.5 ± 0.5 | – |
| 67.2 | 109.365120 | 37.749544 | – | – | – |
| 67.3* | 109.382090 | 37.771629 | – | – | – |
| 68.1 | 109.392330 | 37.738083 | 5.51 | – | – |
| 68.2 | 109.382350 | 37.736508 | – | – | – |
| 68.3* | 109.406780 | 37.763803 | – | – | – |
| 69.1 | 109.380400 | 37.749467 | – | 3.4 ± 0.5, 3.3 ± 0.4, 3.1 ± 0.4 | – |
| 69.2 | 109.375320 | 37.743383 | – | – | – |
| 69.3* | 109.396440 | 37.768591 | – | – | – |
| 70.1 | 109.392210 | 37.760496 | – | 3.7 ± 0.4, 3.1 ± 0.2, 3.9 ± 0.3 | 2.72 ± 0.06 |
| 70.2 | 109.389380 | 37.757279 | – | – | 3.11 ± 0.07 |
| 70.3* | 109.375110 | 37.735945 | – | – | 2.14 ± 0.09 |
| 71.1 | 109.382700 | 37.744711 | – | 3.0 ± 0.1, 2.6 ± 0.1, 2.6 ± 0.1 | 2.91 ± 0.10 |
| 71.2 | 109.380650 | 37.741346 | – | – | 1.82 ± 0.04 |
| 71.3 | 109.402550 | 37.763610 | – | – | 2.65 ± 0.16 |
| 71.4 | 109.387210 | 37.741295 | – | – | – |
| 72.1 | 109.380120 | 37.765496 | – | >4.1, >4.0, 3.9 ± 0.4 | 3.32 ± 0.14 |
| 72.2 | 109.374810 | 37.762346 | – | – | 3.32 ± 0.22 |
| 73.1* | 109.375970 | 37.748883 | – | – | – |
| 73.2* | 109.375500 | 37.748483 | – | – | – |
| 73.3* | 109.391470 | 37.767033 | – | – | – |
| 74.1* | 109.370890 | 37.751182 | – | – | 1.52 ± 0.06 |
| 74.2* | 109.383420 | 37.769708 | – | – | – |
| 74.3* | 109.371310 | 37.751974 | – | – | 1.60 ± 0.15 |
| 75.1 | 109.382000 | 37.738429 | – | 3.6 ± 0.4, 4.7 ± 0.4, 4.3 ± 0.5 | – |
| 75.2 | 109.388640 | 37.739263 | – | – | – |
| 75.3* | 109.40496 | 37.764678 | – | – | – |
| 76.1 | 109.411230 | 37.731990 | – | 4.5 ± 0.4, 5.4 ± 0.3,3.7 ± 0.4 | – |
| 76.2 | 109.412840 | 37.733789 | – | – | – |
| 76.3 | 109.413660 | 37.734646 | – | – | – |
| 77.1* | 109.377000 | 37.736456 | – | – | – |
| 77.2* | 109.386260 | 37.751928 | – | – | – |
| 77.3* | 109.399110 | 37.764959 | – | – | – |
| 78.1* | 109.371840 | 37.742478 | – | – | – |
| 78.2* | 109.379010 | 37.752778 | – | – | – |
| 79.1 | 109.393150 | 37.762795 | – | 3.7 ± 0.3, 3.4 ± 0.2,3.7 ± 0.3 | – |
| 79.2 | 109.387350 | 37.755963 | – | – | – |
| 79.3 | 109.375740 | 37.735628 | – | – | – |
| 80.1 | 109.390940 | 37.733628 | – | 3.7 ± 0.3, 3.3 ± 0.1, 3.8 ± 0.2 | 2.37 ± 0.15 |
| 80.2 | 109.400250 | 37.738496 | – | – | 2.50 ± 0.11 |
| 80.3 | 109.410080 | 37.753576 | – | – | 2.40 ± 0.14 |
| 81.1* | 109.408320 | 37.728127 | – | – | – |
| 81.2* | 109.409010 | 37.728544 | – | – | – |
| 81.3* | 109.410160 | 37.729344 | – | – | – |
| 82.1* | 109.383660 | 37.766146 | – | – | 2.65 ± 0.48 |
| 82.2* | 109.379500 | 37.756303 | – | – | 2.72 ± 0.21 |

## B.2. A look to the inside of haloes: a characterisation of the halo shape as a function of overdensity in the Planck cosmology

G. Despali, C. Giocoli, M. Bonamigo, et al. “A look to the inside of haloes: a characterisation of the halo shape as a function of overdensity in the Planck cosmology”. In: *ArXiv e-prints* (May 2016). arXiv: 1605.04319

Mon. Not. R. Astron. Soc. **000**, 1–15 (2010) Printed 17 May 2016 (MN LATEX style file v2.2)

# A look to the inside of haloes: a characterisation of the halo shape as a function of overdensity in the Planck cosmology

Giulia Despali[1⋆], Carlo Giocoli[2], Mario Bonamigo[2], Marceau Limousin[2], Giuseppe Tormen[3]

[1] *Max Planck Institute for Astrophysics, Karl-Schwarzschild-Strasse 1, 85740 Garching, Germany*
[2] *Aix Marseille Université, CNRS, LAM (Laboratoire d'Astrophysique de Marseille) UMR 7326, 13388, Marseille, France*
[3] *Dipartimento di Fisica e Astronomia, Università degli Studi di Padova, vicolo dell'Osservatorio 3, 35122, Padova, Italy*



**ABSTRACT**

In this paper we study the triaxial properties of dark matter haloes of a wide range of masses extracted from a set of cosmological $N$-body simulations. We measure the shape at different distances from the halo center (characterised by different overdensity thresholds), both in three and in two dimensions, discussing how halo triaxiality increases with (*i*) mass, (*ii*) redshift and (*iii*) overdensity. We also examine how the orientation of the different ellipsoidal shells are aligned with each other and what is the gradient in internal shapes for halos with different virial configurations. Our findings highlight that the internal part of the halo retains memory of the violent formation process keeping the major axis oriented toward the preferential direction of the infalling material while the outer part becomes rounder due to continuous isotropic merging events; this effect is clearly evident in high mass haloes - which formed recently - while it is more blurred in low mass haloes. We present simple distributions that may be used as priors for various mass reconstruction algorithms, operating in different wavelengths, in order to recover a more complex and realistic dark matter distribution of isolated and relaxed systems.

**Key words:** galaxies: halos - cosmology: theory - dark matter - methods: numerical

## 1 INTRODUCTION

Different wide field surveys, observing at various wavelengths, are revealing that most of the matter density content of our Universe is in form of collisionless particles (Amara et al. 2012; Guzzo et al. 2014; Covone et al. 2014). These particles do not emit radiation and interact only gravitationally with the surrounding density field: they are generally termed Dark Matter. In addition to these, various analyses are revealing that another dark component dominates the energy budget of the Universe – approximately 70%, responsible for the late time acceleration of the spacetime metric (Perlmutter et al. 1999; Riess et al. 2004, 2007; Schrabback et al. 2010): Dark Energy (Komatsu et al. 2011; Planck Collaboration et al. 2014; Cappi et al. 2015). To the ordinary matter – planets, stars, hot and cold intergalactic medium etc. – is attributed only approximately 5% of the energy budget (Ettori et al. 2009, 2013): commonly called baryos.

Following the standard scenario of structure formation, dark matter drives the structure evolution processes: systems up to proto-galactic scales form as consequence of gravitational collapse and then merge together, along the cosmic time, forming the more massive ones (White & Rees 1978; Tormen 1998; Springel et al. 2001b; Tormen et al. 2004). Galaxy clusters sit at the top of this hierarchical pyramid being the most massive and late forming virialised structures of our Universe (Frenk et al. 1990; Borgani & Kravtsov 2011; Angulo et al. 2012).

Various studies of time evolving isolated perturbations seeding in the dark matter density field have lead many scientist to the development of the spherical collapse theory (White & Silk 1979; Press & Schechter 1974; Pace et al. 2010). A density perturbation grows with the expansion of the Universe in concentric shells and, if it is dense enough, will pull away from the background expansion, and will collapse after reaching a maximum size characterised by null kinetic energy. The collapse happens when the perturbation exceeds the predicted critical value by the spherical collapse model forming a so called dark matter halo (Bond et al.

⋆ E-mail: gdespali@gmail.com

1991; Eke et al. 1996; Bryan & Norman 1998). The improvement of the computational facilities and the development of faster computers have allowed many scientists to perform high resolution cosmological simulations. Those have given the possibility to many researchers to follow the collapse, the creation and the formation of a large number of dark matter haloes in a variety of environments (Springel et al. 2001a, 2005; Angulo et al. 2009; Angulo et al. 2012). The main conclusion is that density perturbations from which haloes form are not independent with each other nor isolated, but during the expansion and collapse perturbations are pulled, stretched and sheared by the surrounding density field (Doroshkevich 1970; Despali et al. 2013). All these also translate in a mass dependence of the collapse threshold (Eisenstein & Loeb 1995; Sheth & Tormen 1999; Sheth et al. 2001; Sheth & Tormen 2002) and in the formation of haloes that are typically triaxial, more in particular prolate (Jing & Suto 2002; Despali et al. 2014; Bonamigo et al. 2015).

In addition to these, the standard spherical modelling of the dark matter, stars, inter-galactic and the intra-cluster medium is only a rough approximation and in particular both theory and observations agree on the general picture that haloes in which galaxies and clusters live are very well approximated by a triaxial ellipsoid (Morandi et al. 2011, 2012; Sereno & Zitrin 2012; Limousin et al. 2013). The study of the asphericity of galaxy clusters is growing, in light of the analyses performed on different numerical simulations during the last years (Angrick & Bartelmann 2010; Rossi et al. 2011a,b; Despali et al. 2014). In this paper we aim to discuss the dependence of the halo shape on the distance from the centre. Other previous works (Allgood et al. 2006; Bailin & Steinmetz 2005) have measured shapes at different fractions of the virial radius. For reasons that are linked to the different halo mass definitions, $M_{500}$, $M_{200}$ or $M_{vir}$ (Despali et al. 2015) and so on and so forth – as we will better discuss later in the text – we chose to present our results in term of different overdensity thresholds: we define halos as triaxial regions enclosing a desired multiple of the critical density of the Universe and, for each halo identified using $\Delta_{vir}$, we measure the triaxial shape at other four overdensity thresholds, multiples of the critical density of the Universe $\rho_c$ (200, 500, 1000 and 2000). This choice is also motivated by the fact that, typically, the X-ray community adopts as mass definition that associated to the region enclosing 500 times the critical density, while weak lensing and dynamical analyses usually prefer 200 times the critical density. On the other side, strong lensing researchers make use of the very central region of clusters or galaxies, where critical lines emerge; in this case we can refer to observe a region enclosing at least 1000 times the critical density of the Universe (Broadhurst et al. 2005b; Coe et al. 2012; Zitrin et al. 2011). In light of the various observational analyses, it is important to underline that a study of the degree of alignment of the mass density distribution at different distances from the centre can help us to understand dark matter and baryonic properties in which the various physical processes are taking place.

Warren et al. (1992) using dissipationless simulations has found that a typical halo is a triaxial spheroid which tends to be more often prolate than oblate, and that halo shapes are primarily supported by anisotropic velocity dispersion. In addition Bailin & Steinmetz (2005) has discussed the fact that shapes of haloes in $N$-body simulations are correlated internally and are aligned with respect to the location and properties of the surrounding systems; their measured shape properties are also in agreement with the computed cluster shape from weak-lensing by Hoekstra et al. (2004). Hopkins et al. (2005) have studied the shape properties of haloes extracted from a light-cone up to redshift $z = 3$ constructed from a large-scale high-resolution $N$-body simulation. They discuss that the mean halo ellipticity increases with redshift as $\langle\epsilon\rangle = 0.33 + 0.05z$ and with the cluster mass, as also found by Despali et al. (2014); Bonamigo et al. (2015). For Hopkins et al. (2005) the cluster ellipticity decreases with radius in disagreement with other results (Bailin & Steinmetz 2005; Hayashi et al. 2007; Vera-Ciro et al. 2011; Velliscig et al. 2015). In particular Vera-Ciro et al. (2011), studying the $N$-body haloes from the Aquarius simulation (Springel et al. 2008), found that the evolution in halo shape correlates well with the distribution of the infalling material: prolate configurations arise when haloes are fed through narrow filaments whereas triaxial/oblate configurations result as the accretion turns more isotropic at later times. The geometrical properties of haloes at different epochs are not lost: haloes retain memory of their structure at earlier times. This memory is imprinted in their present-day shape trends with radius, which change from typically prolate in the inner (earlier collapsed) regions to a triaxial in the outskirts (corresponding to the shells that have collapsed last and are now at the virial radius). Analysing the results of dissipational and dissipationless simulations Kazantzidis et al. (2004) have noticed that the firsts produce significantly rounder halos. This happens because the gas cooling causes an average increase in halo principal axis ratios of $\sim 0.2-0.4$ in the inner regions and a systematic shift that persists out to the virial radius. Haloes in Dark-Matter (DM) only simulations are more triaxial, where there is cooling there is transportation of angular momentum of the substructures that survive more toward the central region, making haloes more round. However, it is worth to mention that the interplay between dissipative gas physics and dark matter is still ambiguous and may depends both on the baryonic physic implementations and on the gas treatment. Velliscig et al. (2015) have noticed that the stellar distributions exhibit a median misalignment of about 45-50 degrees with respect to their host haloes, studying the shapes of stars and dark matter in galaxy scale haloes extracted from the EAGLE and the cosmo-OWLS simulations. The authors have also presented some fitting functions and tabulated values for the probability distribution of galaxy-halo misalignment to enable a straightforward inclusion of their results into models of galaxy formations based on purely collisionless N-body simulations

In this work we will present a study of the shape properties of haloes extracted from DM only simulations. We underline that our results do not account for the presence of baryons – mainly influencing the most internal shells – and could eventually be adapted to their presence using precalibrated analytical recipes.

The paper is organised as follows: (*i*) Section 2 describes the numerical simulations and the halo catalogues; (*ii*) in Section 3 we discuss how we selected the halos for the following sections and which are the best criteria to avoid contaminations from unrelaxed or irregular haloes; (*iii*) our results

are presented in Sections 4 and 5, which show respectively the distributions derived in three or two dimensions; (*iv*) Section 6 is dedicated to summarise our results and draw our conclusions.

## 2 THE NUMERICAL SIMULATIONS

### 2.1 Le SBARBINE simulations

Le SBARBINE simulations are six cosmological simulations which have been run in Padova using the publicly available code GADGET-2 (Springel 2005); these are part of a series of new simulations which have been presented in a previous work (Despali et al. 2015). The adopted cosmology follows the recent Planck results (Planck Collaboration et al. 2014), in particular we have set: $\Omega_m = 0.307$, $\Omega_\Lambda = 0.693$, $\sigma_8 = 0.829$ and $h = 0.677$. The initial power spectrum was generated with the code CAMB (Lewis et al. 2000) and initial conditions were produced perturbing a glass distribution with N-GenIC (`http://www.mpa-garching.mpg.de/gadget`). They all follow $1024^3$ collisionless particles in a periodic box of variable length (we refer the reader to Table 1 for more details).

### 2.2 Halo catalogues

At each stored snapshot, we identified the dark matter haloes using the Ellipsoidal Overdensity algorithm, as described in Despali et al. (2013, 2014, 2015) and Bonamigo et al. (2015). This algorithm identifies ellipsoidal haloes in numerical simulations: it works similarly to the more common Spherical Overdensity criterion (Lacey & Cole 1994; Tormen et al. 2004; Planelles & Quilis 2010; Knebe et al. 2011, 2013), with the difference that the halo shape is refined using an iterative procedure to find the best triaxial ellipsoid that follows the mass density distribution - instead of forcing a spherical shape. For example, at the present time we used the virial overdensity $\Delta_{vir} \simeq 319$ as a density threshold for the main halo catalogues (Eke et al. 1996; Bryan & Norman 1998). Then, we identified the haloes at other four overdensity thresholds, corresponding to 200, 500, 1000 and $2000\rho_c$ (as in Despali et al. (2015)); each run has been made independently, so that the resulting shape and direction of each shell is not influenced by the virial value.

We calculate halo shapes using eigenvalues of the mass tensor, defined as:

$$M_{\alpha,\beta} = \frac{1}{N}\sum_{i=1}^{N} r_{i,\alpha} r_{i,\beta}, \qquad (1)$$

where $r_i$ is the position vector of the $i$-the particle and $\alpha$ and $\beta$ are the tensor indexes. By diagonalizing $M_{\alpha,\beta}$ we obtain the eigenvalues and eigenvector: the axes of the ellipsoid ($a \leqslant b \leqslant c$) are then defined as the square roots of the eigenvalues .

## 3 HALO SELECTION

Since the purpose of this work is to provide reliable prediction of the halo shapes as a function of radius – and overdensities, we decided to restrict our halo catalogue in order to exclude irregular, merging or highly unrelaxed haloes. First of all we applied one of the common criteria to define relaxed haloes (Neto et al. 2007; Macciò et al. 2008) - *method 1*: we calculated the distance between the position of the minimum of potential and the centre of mass of the halo; then, we maintain only systems in which this difference is less than 5% of the corresponding halo virial radius. As seen in Bonamigo et al. (2015), this criterion is able to exclude most of the irregular haloes – meaning those that cannot be reliably described by one single triaxial ellipsoid – and their fraction increases with the mass, due to the fact that high mass haloes, forming later (Giocoli et al. 2007; Zhao et al. 2009; Giocoli et al. 2012b), are still in a merging phase. As a second criterion - *method 2*, we calculated the total energy of haloes – as a sum of the kinetic and potential energies of the constituting particles – and discarded those with positive energy, getting rid of some other irregular systems. In Figure 1 (left panels – top and bottom panels refer to $z = 0$ and $z = 1$, respectively) we illustrate the effect of these two selection criteria on the halo catalogue: showing the percentage of irregular haloes detected (and those excluded) by each method and by their combination.

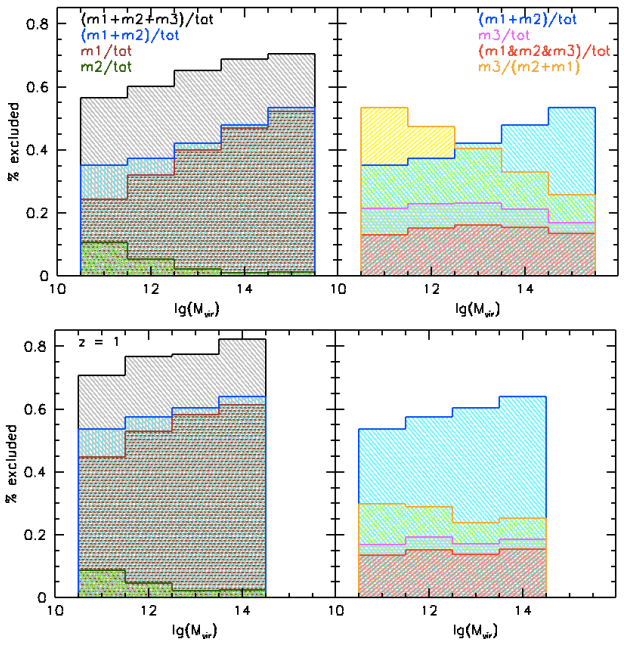


**Figure 1.** Fraction of haloes excluded by each selection criterion - or by their combination - for different mass bins. *Left*: the brown histogram shows the percentage of irregular or "unrelaxed" haloes detected by *method 1* (*m1*), the green colour stands for those detected with *method 2* (*m2*), the association of the two criteria is shown in blue and finally the combination with *method 3* (*m3*) is shown in black. At $z = 0$ (top panels), our remaining catalogue contains roughly 60 % of haloes of $10^{12} M_\odot h^{-1}$ and 40% of high mass haloes of $10^{15} M_\odot h^{-1}$; at $z = 1$ (bottom panels) the percentage of selected haloes is further reduced.

Nevertheless, after this first selection, we noticed that some irregular haloes were still present in our catalogues, as for example the halo displayed on top panel of Figure 2. This halo was chosen randomly between those exhibiting extremely low virial axial ratios ($ar1 = a/c \leqslant 0.2$), who were not excluded by the first selections: it is clearly an unrelaxed

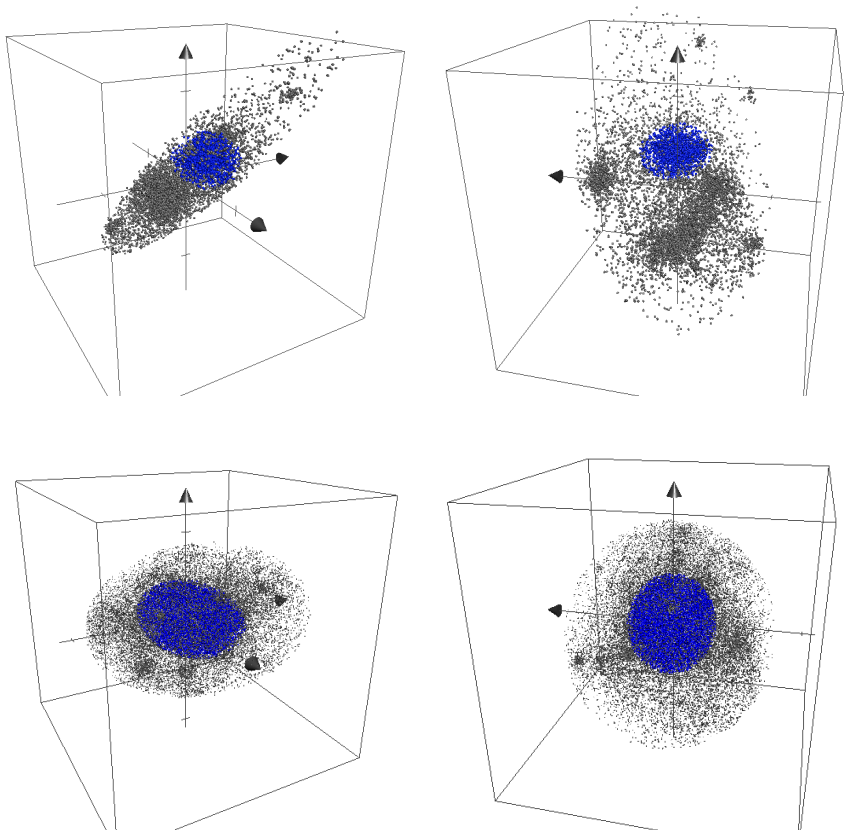

**Figure 2.** *Top panels*: spatial distribution of particles of an irregular halo, which is not excluded by *method 1* and *method 2*. It has a virial mass $M_{vir} \simeq 1.37 \times 10^{14} M_{\odot} h^{-1}$ and it is clearly still in a merging phase, being composed by multiple mass clumps. The black dots show the virial particles, while those identified at $500\rho_c$ are in blue, located around the centre of mass and the most massive clump. In this case, while $ar1_{vir} = (a/c)_{vir} = 0.21$, the axial ratio in the inner shell is $ar1_{500} = 0.68$, causing an irregular shape profile. This halo is successfully excluded by *method 3*. *Bottom panels*: for comparison, we show the particle distribution of a regular halo; in this case the axial ratios at both overdensities are about 0.3.

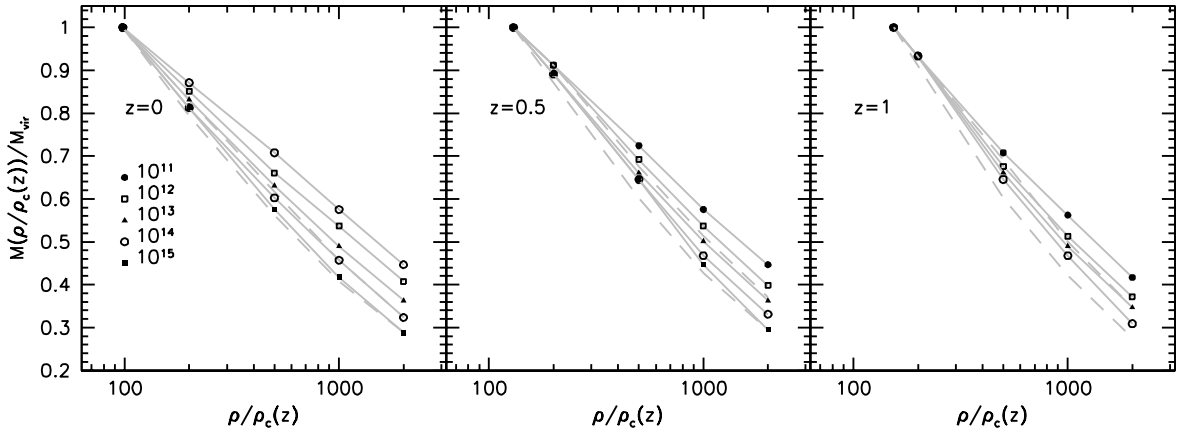


**Figure 3.** Mass fraction in each shell, with respect to the total mass at the virial overdensity. Different points show the median result for different mass bins: in all cases the mass fraction decreases similarly to the centre, but with different slopes determined by the differences in the density profiles and thus in the concentration. As an example, the two dashed lines show the 25% and 75% quartiles for the mass bin associated to $10^{14} M_{\odot} h^{-1}$.

| name | box [Mpc $h^{-1}$] | $z_i$ | $m_p[M_\odot h^{-1}]$ | soft [kpc $h^{-1}$] | $N_{h-tot}(z=0)$ | $N_{h>1000}(z=0)$ |
|---|---|---|---|---|---|---|
| **Ada** | 62.5 | 124 | $1.94 \times 10^7$ | 1.5 | 2264847 | 36561 |
| **Bice** | 125 | 99 | $1.55 \times 10^8$ | 3 | 2750411 | 44883 |
| **Cloe** | 250 | 99 | $1.24 \times 10^9$ | 6 | 3300880 | 54467 |
| **Dora** | 500 | 99 | $9.92 \times 10^9$ | 12 | 3997898 | 58237 |
| **Emma** | 1000 | 99 | $7.94 \times 10^{10}$ | 24 | 4739379 | 38636 |
| **Flora** | 2000 | 99 | $6.35 \times 10^{11}$ | 48 | 5046663 | 5298 |

**Table 1.** Main features of the simulations. The last two columns report the total number of haloes with more than 10 and 1000 particles ($N_h$)), at redshift $z = 0$.

halo, being composed by multiple mass clumps and in a merging phase. It survived through the previous selection because (even if it may not be clear from the figure due to the projection effect and the colour combination) its main clump is still more massive than the other, keeping the centre of mass near the minimum of potential. From the figure, we can notice how the shape of the $500\rho_c$ shell (shown in blue) is very different from the overall virial shape (black dots): while $ar1_{vir} = (a/c)_{vir} = 0.21$, the axial ratio in the inner shell is $ar1_{500} = 0.68$, in contrast with the common finding that inner shells are more elongated than the outer ones (see Section 4.1). For comparison, the two bottom panels, show the case of a relaxed halo with similar mass: its axial ratios do not change dramatically as a function of radius and the shell enclosing $500\rho_c$ is clearly larger and more massive than in the previous case.

In order to capture this kind of systems, we propose and use a third selection criterion (*method 3*), based on the discreet measurement of the density profile of the halo computed on elliptical shell of well defined overdensities. In particular, we measure the mass fraction contained in each overdensity shell, with respect to the total virial mass. Figure 3 shows the mass enclosed by each overdensity threshold, as a function of the overdensity with respect to the critical one. The points show the median values in each mass bin: the mass decreases with overdensity, with a mass dependent slope because smaller haloes are more concentrated than the more massive ones (Giocoli et al. 2012; Meneghetti et al. 2014). In those haloes which are in a merging phase, the central clump can be expected to be less massive than in relaxed haloes, since a significant part of the mass still resides in the infalling clumps. Thus, this median density profile can be used as a selection criterion, in particular to characterise a relaxed sample in addition to the *method 1* and *method 2*: we exclude also all haloes for which the mass fraction $M_X/M_{vir}(\rho/\rho_c)$ always lies in the lower quartile ($\leqslant 25\%$ of the distribution) for all the four shells. We remind the reader that this last selection criterion is very analogous to the substructure mass fraction method adopted by Neto et al. (2007) to characterise relaxed and unrelaxed haloes. The fraction of haloes excluded only by *method 3* is shown by the pink histogram in Figure 1 (right panels): they are approximately 20% of the whole halo sample both at $z = 0$ and $z = 1$. In the same plot, the yellow histogram shows how many of the haloes excluded by *method 1*+*method 2* are also excluded by the *method 3*; finally the red histogram displays the haloes that satisfy all the three conditions. This means that, adding *method 3* as an exclusion criterion, we are able to discard some irregular haloes that are not identified by the first two methods: the final cut in the halo catalogue is shown by the black histogram in the left panel of Figure 1. The relaxed halo in the bottom panels of Figure 2 satisfy all our selection criteria, thus proving to be relaxed and regular – in all considered overdensities, while the top one is successfully excluded from the whole sample by *method 3*.

## 4 3D SHAPE AS A FUNCTION OF OVERDENSITY

In this section we analyse how the three-dimensional shape of relaxed haloes changes as a function of the overdensity, and characterise the variation as a function of mass and redshift at fixed shape at the virial radius. First, we confirm that halo shapes are not self-similar as a function of radius (Allgood et al. 2006; Vera-Ciro et al. 2011; Jing & Suto 2002; Bailin & Steinmetz 2005), both in terms of axial ratios and orientations. Usually this dependence is explored by measuring halo shapes at different fractions of the virial radius; analogously – and consistently with how our ellipsoidal halo finder works – we chose to use the overdensity as an alternative to the radius, also in order to produce results more easily comparable with observational studies and selection criteria. Then, we will proceed to analyse conditional shape distributions, in order to give more detailed predictions of the properties of individual haloes. A general colour/style code is used through the paper: (*i*) different overdensities are represented by various colours (from black for the virial case to red for the innermost one, going through green, blue and magenta) and (*ii*) $z = 0$ results are shown by solid lines, while at $z = 1$ we chose dashed lines – we mention that for better display our data and results we do not show the case $z = 0.5$ that lays in the middle between $z = 0$ and $z = 1$. We start by showing how the overall distribution of shapes depends on overdensity (for different masses and redshifts) and then we explore the conditional distribution of shapes, binning in the virial axial ratio: in this way we can give realistic prediction of the change in shape within individual halos. Finally, we address the misalignment between the shells and show how it depends on mass and an the virial shape properties.

### 4.1 General distributions

Figure 4 shows how the axial ratios varies as a function of the virial mass for our five overdensity thresholds. We remind the reader that the three dimensional ellipticity is defined as

$$e = \frac{c-a}{2(a+b+c)} \tag{2}$$

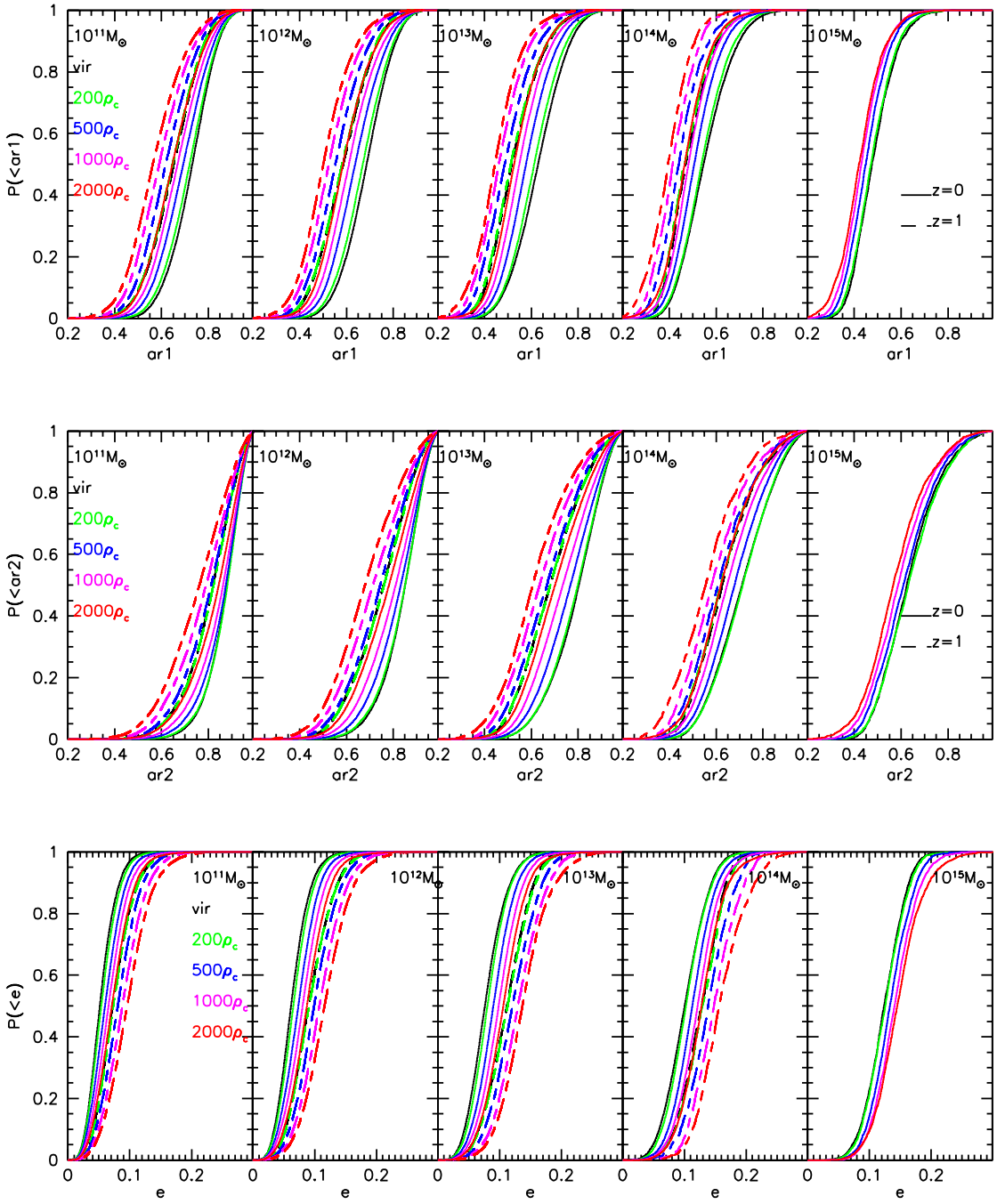


**Figure 5.** Cumulative distributions of axial ratios and ellipticity for different overdensity thresholds; each panel shows the results for haloes in a certain mass bin, centred in $10^{11}M_\odot h^{-1}$ - $10^{15}M_\odot h^{-1}$, at redshift 0 (solid) and 1 (dashed).

(with $a \leqslant b \leqslant c$) and it is equal to zero for a spherical system. Apart from the well known dependence on mass (Allgood et al. 2006; Despali et al. 2014; Bonamigo et al. 2015), we notice how the dependence on overdensity is almost the same and regular for all relaxed masses, with inner shells being more triaxial than the outermost virial one, shown in black. The same behaviour can be observed at $z = 1$ (dashed lines): at this time, for a given mass bin, haloes are generally more triaxial, but the inner ordering is unaltered. Note that the black and green dashed lines (virial and $200\rho_c$) almost coincide, since at this redshift the two overdensities are very close to each other (Despali et al. 2015). The analogous distributions for unrelaxed haloes at $z = 0$ are shown in Appendix A, proving why unrelaxed haloes cannot be easily described by simple relations, and a regular trend is absent. This highlight the fact that the morphological prop-

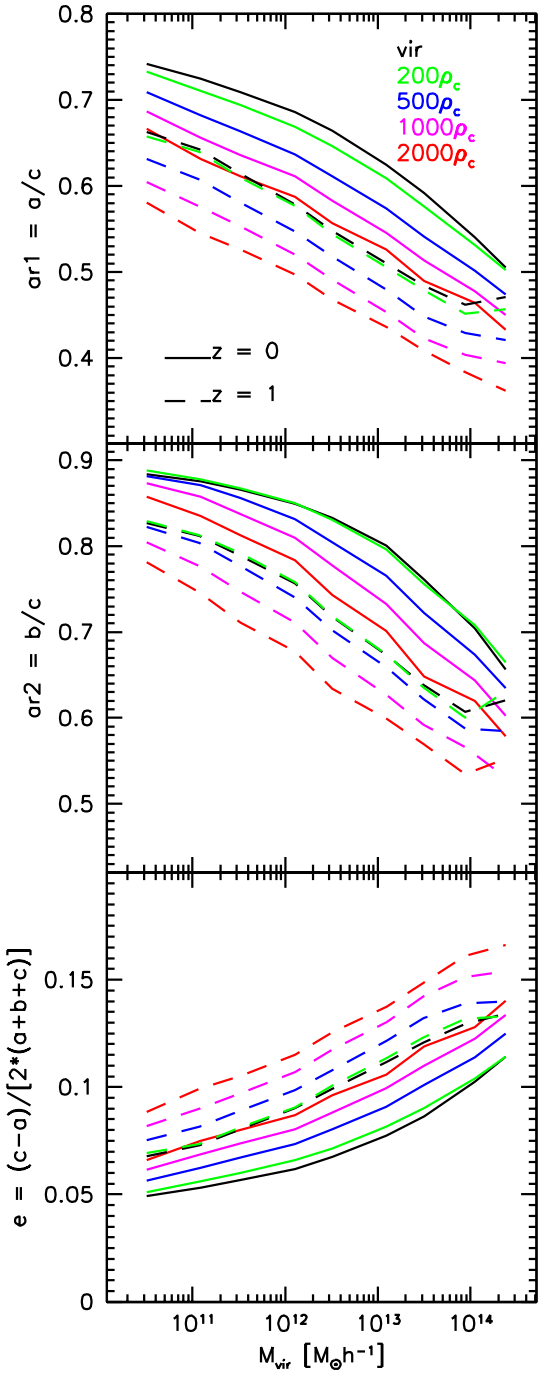


**Figure 4.** Axial ratios and ellipticity as a function of halo mass, for different overdensity thresholds. The lines show the median values of the distributions for $ar1 = a/c$, $ar2 = b/c$ and $e = (c-a)/[2*(a+b+c)]$ with $a \leqslant b \leqslant c$)..

erties of galaxies and clusters at different radii may be used to infer the state of relaxation (Donahue et al. 2016) and that our relations for relaxed haloes do not hold for some of the recently observed clusters, which appear unrelaxed and presents multiple components.

In Figure 5 we present the shape distributions in more details: we consider five mass bins, centred on masses from $10^{11}M_{\odot}h^{-1}$ to $10^{15}M_{\odot}h^{-1}$ and outline the cumulative distributions of the shapes – axial ratios and ellipticities – for different overdensities. From the figure we notice that all trends are very regulars both in mass and overdensities. Comparing the distributions at $z = 0$ and $z = 1$ we notice that at higher redshifts haloes of same mass are more triaxial, once the mass is fixed – the case $z = 0.5$ would lay in the middle between $z = 0$ and $z = 1$ not shown here avoiding to overcrowd the panels. As described in Despali et al. (2014) the redshift dependence can be removed comparing haloes possessing the same peak-height $\nu = \delta_c(z)/S(M)$, which is beyond the scope of this work.

### 4.2 Conditional distributions

Figure 6 shows conditional distribution of the axial ratios, for different mass bins and redshifts $z = 0$ and $z = 1$, using solid and dashed line styles, respectively. In order to characterise more precisely the shape variation inside individual haloes, we bin the axial ratio distributions using the computed values at the virial overdensity: each colour shows the median distribution of the axial ratios for haloes in a certain bin of virial axial ratio. Each bin in $ar1$ or $ar2$ has a width of 0.1. Thus, the virial axial ratios of haloes represented by the yellow lines are contained in the interval [0.9, 1], the green ones in [0.8,0.9] and so on and so forth. The lowest axial ratios $ar1/2$ =[0.3,0.4] are represented in purple colour. Objects with even lower axial ratios are excluded by our selection criteria, since extreme elongations often coincide with haloes in a merging phase, as already discussed above in the text. A new feature, that was not visible in the previous figures, emerges from the conditional distributions: the variation of shape with overdensity – or radius – depends on their outer shape. While triaxial haloes with axial ratios ($ar1 \simeq 0.5, ar2 \simeq 0.6$) are self-similar in their inner parts, the more spherical ones present a greater shape variation, becoming considerably more triaxial inside. This effect is present for all masses, even if it may be caused by different phenomena: in general, it has been argued that the outer parts of haloes become rounder due to the interactions with the surrounding density field, which take place after their formation, while the inner parts maintain the original triaxiality due to the collapse process. This is true in particular for low mass haloes, which formed earlier and are more influenced by the surrounding tidal field or by encounters with more massive structures. For high-mass haloes, apart from the few with high formation redshifts, the physical explanation of this dependence may be different: it is possible that, while matter is still in an accretion phase from many directions onto a $10^{15}M_{\odot}h^{-1}$ halo - as they live at the intersection of filaments, the centre already collapsed in a well defined triaxial object.

To summarise, our results highlight that the internal part of the halo retains memory of the violent formation process keeping the major axis oriented toward the pref-

| $M_{vir}[M_{\odot}h^{-1}]$ | $\rho_{vir}$ | $200\rho_c$ | $500\rho_c$ | $1000\rho_c$ | $2000\rho_c$ |
|---|---|---|---|---|---|
| $10^{11}$ | (0.732,0.878,0.052) | (0.720,0.882,0.054) | (0.693,0.874,0.060) | (0.669,0.863,0.066) | (0.646,0.844,0.071) |
| $10^{12}$ | (0.687,0.851,0.061) | (0.670,0.851,0.066) | (0.637,0.832,0.074) | (0.611,0.810,0.081) | (0,585,0.782,0.087) |
| $10^{13}$ | (0.629,0.803,0.076) | (0,612,0.798,0.080) | (0.577,0.767,0.090) | (0.549,0.735,0.099) | (0.506,0.701,0.106) |
| $10^{14}$ | (0.546,0.710,0.100) | (0.537,0.713,0.102) | (0.506,0.678,0.113) | (0.481,0.646,0.121) | (0.465,0.620,0.128) |
| $10^{15}$ | (0.475,0.624,0.124) | (0.471,0.631,0.126) | (0.449,0.610,0.133) | (0.430,0.587,0.141) | (0.420,0.566,0.145) |

**Table 2.** Median values of (ar1,ar2,e) at different overdensity $z = 0$ thresholds for five mass bins.

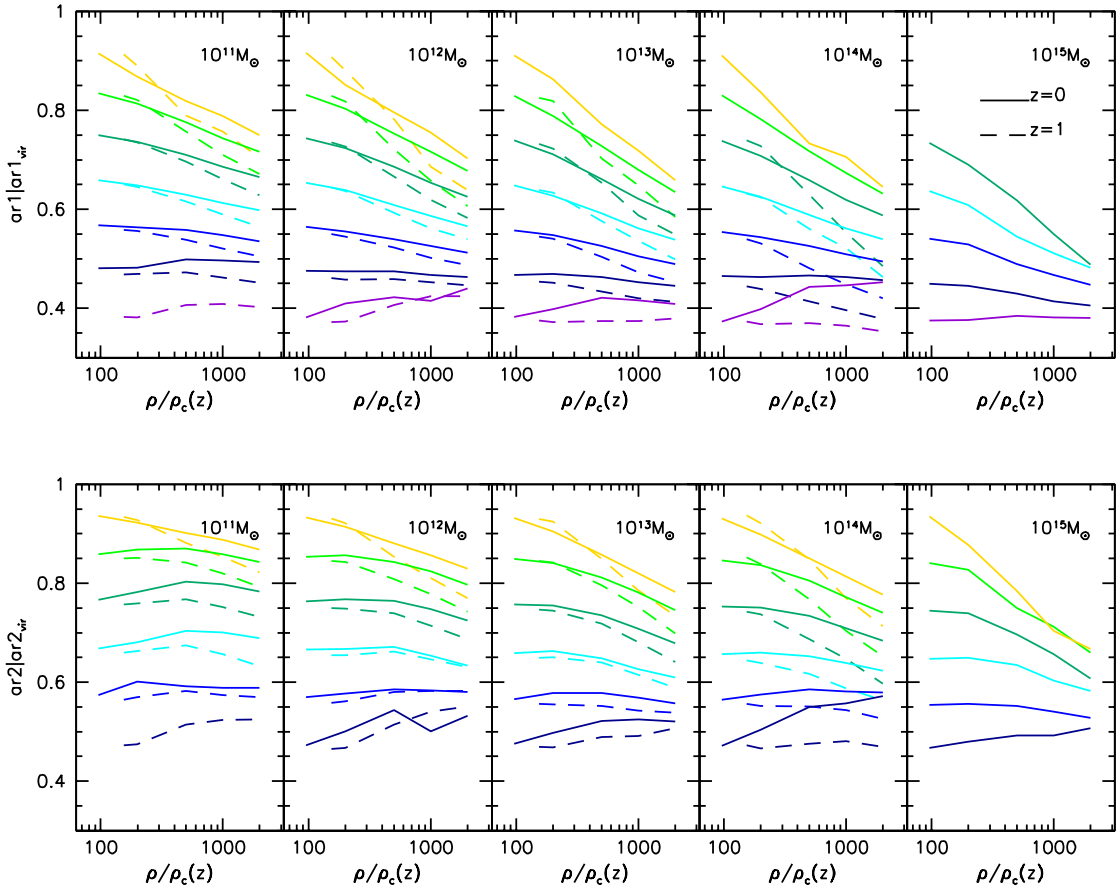


**Figure 6.** Conditional distributions of the axial ratios. Each colour shows the median axial ratio as a function of density for the haloes with a certain value of the virial axial ratio. For example, the haloes represented by the yellow have $0.9 < a/c \leqslant 1$, while for the purple curve $0.3 < a/c \leqslant 0.4$. The same holds for the second axial ratio $b/c$ in the right panel. Solid lines represent the results at $z = 0$ and dashed ones those for $z = 1$.

erential direction of the infalling material, the outer part become rounder due to continuous isotropic merging events. (Zhang et al. 2009; Vera-Ciro et al. 2011)

We underline that these distributions are useful to generate mock mass density distributions of dark matter in galaxies and clusters producing for example more realistic lens models (Giocoli et al. 2012a).

### 4.3 Misalignment of the different shells

It has been previously shown that shapes measured at different radii within the same halo are not perfectly aligned with each other. Having independently measured the triaxial shapes of four inner shells, we can easily compare their relative orientations – with respect to a predefined direction of the three dimensional ellipsoid – in a way to better understand how on average the different shells are misaligned with each other. We remind the reader that our shape measurements include all the components of haloes and do not discriminate between the main smooth component and the

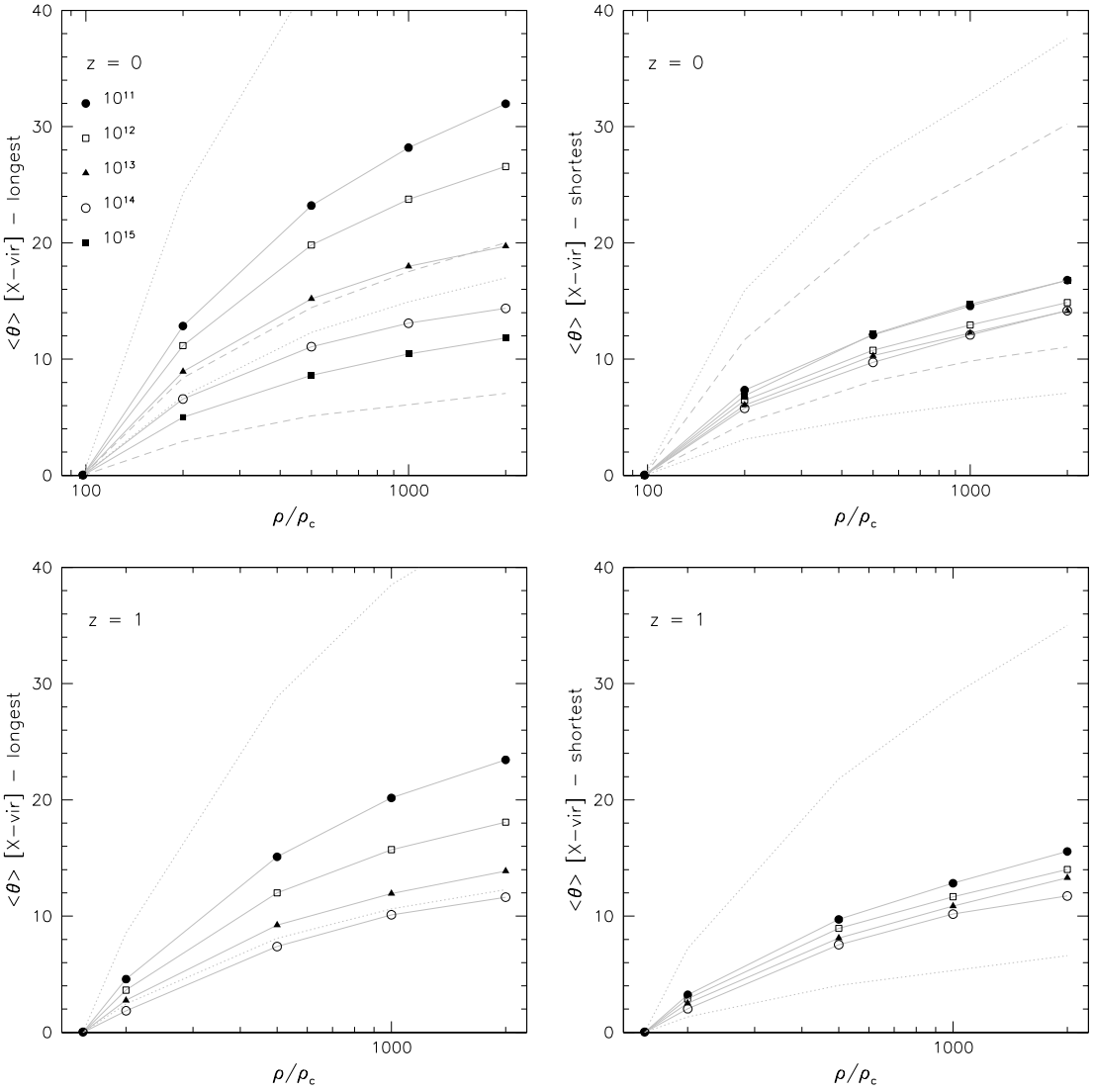


**Figure 7.** Misalignment angle of the four inner shells with respect to the virial one, as a function of halo mass. The upper panel shows the the median angle between the two longest axes, while the lower one the median misalignment between the two shortest axes. Different mass bins are represented by different point types; the dashed and the dotted lines show the 25% and 75% quartiles of the distribution for $10^{15} M_{\odot} h^{-1}$ and $10^{11} M_{\odot} h^{-1}$, respectively.

substructures, as has been done in other previous works (as for example Vera-Ciro et al. 2011). In Figure 7 we show the median misalignment angle between the four inner shells with respect to the virial one – that we view as reference; we considered the misalignment between the two longest (*left*) and the two shortest axes (*right*) of the 3D mass ellipsoid – to give an idea of the deformation of the triaxial mass ellipsoid. The measurements are divided in five mass bins, represented by different point types. From the figure we notice that while the median misalignment at $200\rho_c$ is around 10 degrees only, it becomes larger when going toward the halo centre. We stress that there is a considerable dispersion in the data, which increases for low mass haloes: to give an idea about this, the dashed (dotted) lines show the 25% and 75% quartiles associated with the highest (lowest) mass bin - thus $10^{15}$ ($10^{11}$). The median misalignment appears to depend on mass: in particular, for cluster size haloes, which formed very recently – or are in their formation phase, the shells are aligned with each other within 10 degrees - probably to the direction of compression of the gravitational collapse, while low mass haloes – that formed typically at higher redshifts (Lacey & Cole 1993; Giocoli et al. 2007) – present greater variations, again due to the interactions with the surrounding field and their evolution after the formation time (more evident is the halo to halo variation) – also being less gravitationally strong they tend to be more influenced by the surrounding density field. As shown in Despali et al. (2014), the ellipticity anti-correlates with the formation redshift and so more elongated haloes formed more recently. Also, this mass dependence may hide a geometrical shape dependence: low mass halos are rounder and thus the axes direction at the virial radius may be less

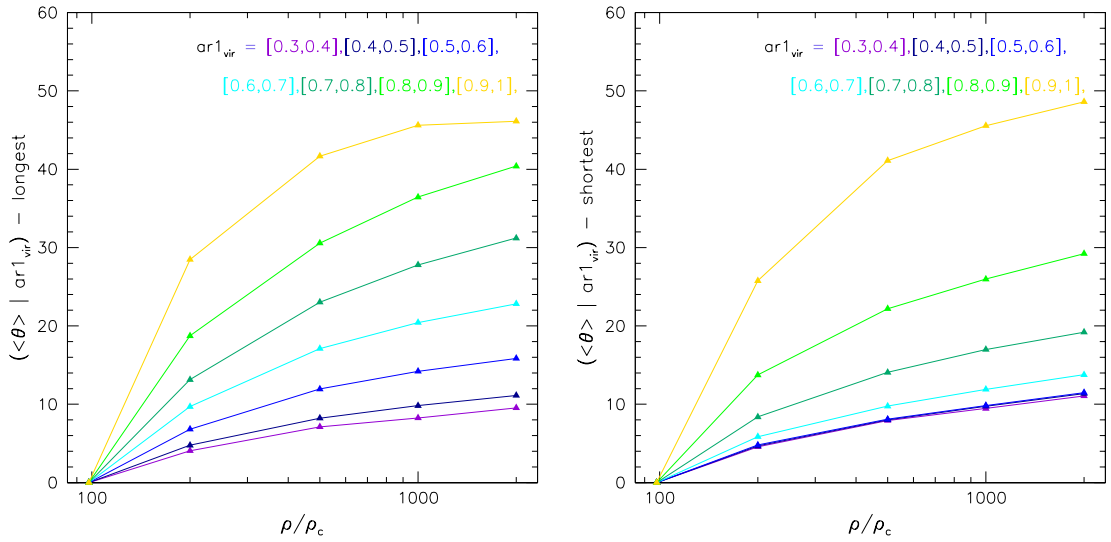


**Figure 8.** Conditional misalignment of the different shells. Different colours show angles corresponding to haloes with a certain $ar1_{vir}$, as was done for the axial ratios in Figure 6. Since binned results where almost the same for the five mass bins of the previous figure, we decided to not bin in mass in this case: this proves how the scatter of Figure 7 between different halo masses is due to the different distribution of shapes.

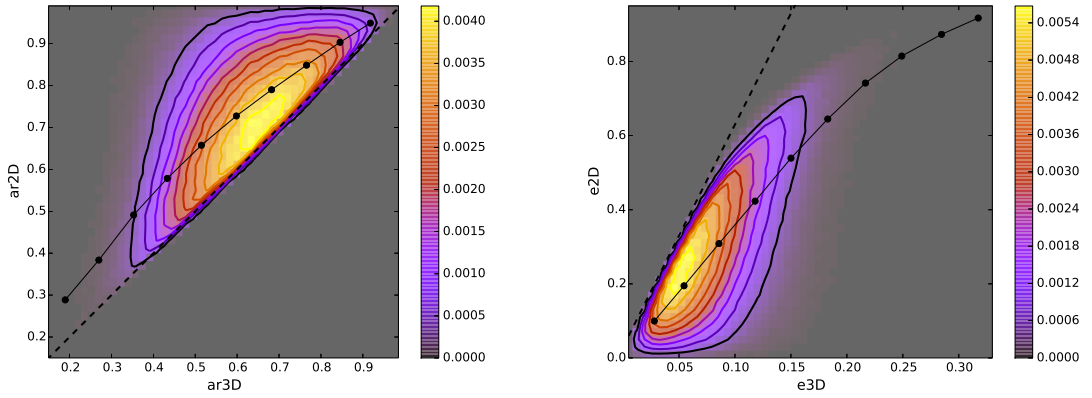


**Figure 9.** Correlation between the 3D and 2D shapes. For each real halo, we calculated three two dimensional projections and here we plot all of them. In both cases, the axes have been calculated from the inertia tensor, in three or two dimension, but the ellipticities follow two different formula: $(c-a)/(2*(a+b+c))$ in 3D and $(a^2-b^2)/(a^2+b^2)$ for 2D. In both cases, $e=0$ corresponds to a sphere. We used the first axial ratio and so, for simplicity in this particular case, ar3D is what was called previously ar1. Since the projection is just a geometrical effect, here we show the points corresponding to all the density thresholds.

defined than in a very elongated system. This seems to be supported also by the results of Figure 8, where we display the conditional distributions of the misalignment of the different shells. The data are divided according to the virial axial ratio $ar1$, as in Figure 6. From this figure it appears more clear that for very triaxial haloes all the shells are well aligned, probably due to the phase of collapse or a recent formation, while this is not true for rounder haloes. This figure shows all the masses together, as we noticed that the conditional distribution are very similar for different mass bins, reinforcing our framework and our explanations.

Together with the results on conditional axial ratios presented at the beginning of this section, these distribution can be used to produce self-consistent mock mass density distribution of realistic triaxial and perturbed haloes.

## 5 PROJECTED 2D SHAPE AS A FUNCTION OF OVERDENSITY

After the discussion presented in the previous section about three dimensional shapes, we proceed analysing the shapes in two dimensions (2D), which can be more directly related with observed quantities. We project each halo along three random directions in particular along the three axes of the coordinate system of the simulation ($x$,$y$,$z$) – considering each projection a random measure of the 2D shape of the

halo ellipsoid. Since we already have a relatively large number of haloes we do not consider necessary to project each object along different possible random line of sights. We then look at the distributions of halo shapes and orientations for different overdensities and masses, as done and discussed for the 3D case. In 2D we calculate the ellipticity as

$$e = \frac{a^2 - b^2}{a^2 + b^2}, \tag{3}$$

we notice that the ranges in which $e_{2D}$ and $e_{3D}$ changes are different, even though both tend to zero for more spherical cases.

As general result, 2D-distributions maintain the same properties and ordering of the 3D ones, but they become shallower due to projection effects. The extreme cases, such as very elongated shapes, are blurred by being the halo ellipsoid projected in random directions. This general effect can be seen in Figure 9 where the contours show the point density of the relationship between the axial ratios (left) and ellipticities (right) as measured in 2D versus the 3D ones. The black points show the median of the distribution at a fixed 3D value. From the figure we notice that the 2D axial ratio is always higher than the corresponding 3D value ($ar1$ in this case) for all haloes, as marked by the dashed lines that indicate the exclusion regions in the two panels.

In Figure 10 we present the cumulative probability distribution of axial ratios (top panel) and ellipticities (bottom panel) for haloes of different masses and at redshift $z = 0$ (solid curves) and $z = 1$ (dashed curves). The figure underlines that in projections high mass haloes are still on average more elongated than low mass ones, at all redshifts. Also the ordering due to the different overdensity definitions is not altered when one looks at two dimensional quantities (Figure 11), even if the low-axial ratios tail is reduced in comparison with the three dimensional quantities, as presented in Figure 5.

Same considerations also holds for the conditional distributions as presented in Figure 12, where we show the 2D axis ratios at various overdensities binning the haloes in term of the 2D axis ratios at the virial definition. In Figure 13 we present the misalignment angle in the plane of the sky of the projected mass ellipsoids at the various overdensities. We notice that in projection the misalignment angle of the inner shell may reach values of the order of 15-20 degrees with respect to the virial direction - lower than the median values of 40 degrees as measured in the 3D case.

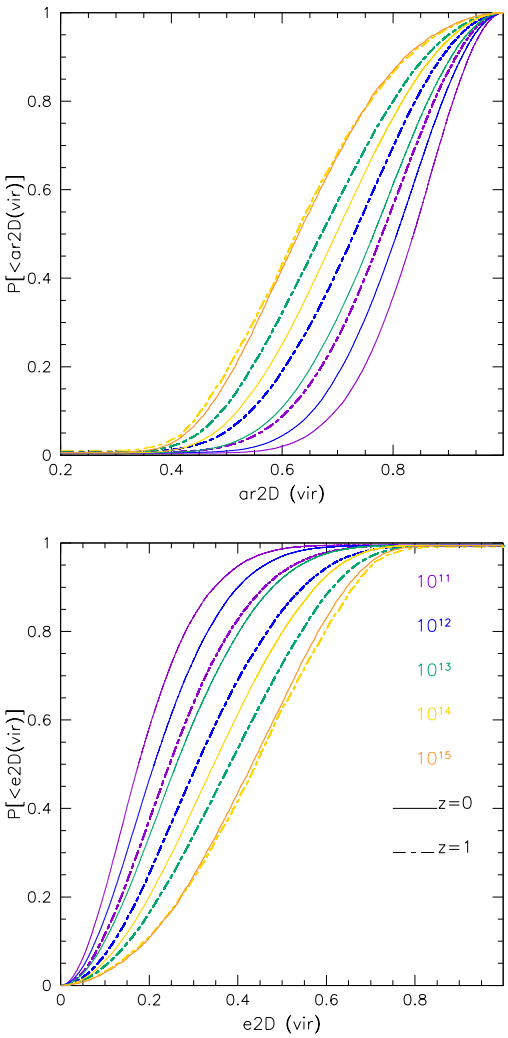


**Figure 10.** Projected axial ratios and ellipticities in 2D at the virial overdensity. The different colours show various halo masses while solid and dashed curves refer to redshift $z = 0$ and $z = 1$, respectively

## 6 SUMMARY AND CONCLUSIONS

The aim of this work is to provide simple and clear estimates of how the shape of relaxed haloes changes as a function of overdensity, mass and redshift. We looked at five different shells, enclosing various overdensities, and measured their shape in three and two dimensions. The main results of our work can be summarised as follows:

(i) general distributions: we confirm that, as found in other previous works (Jing & Suto 2002; Allgood et al. 2006), dark matter haloes are more elongated near the centre than in the outskirts; this is true for a wide range in halo masses (from $10^{11}$ to $10^{15} M_{\odot} h^{-1}$).

(ii) conditional distributions: the rate at which the shape varies through the halo depends on that at the virial radius; very triaxial haloes show a similar shape at all the overdensity shells and the shells are quite well aligned with each other, while for rounder haloes the inner shells are, proportionally, both more misaligned and more triaxial than the virial one.

(iii) 2D projections: we calculated projected shapes by taking three different projections for each halo; the conclusions coming from projected quantities are similar to the 3D ones, even though the differences between shell ellipticities and orientations are shallower due to projection effects.

Our findings are consistent with the standard picture of structure formation, in which the central part of haloes may maintain its original triaxiality longer than the outskirts which are subjected to stronger interactions with the surrounding field; also, haloes formed recently will be still aligned with the direction of the last merger or of the filament along which matter accreted onto the halo, and so their

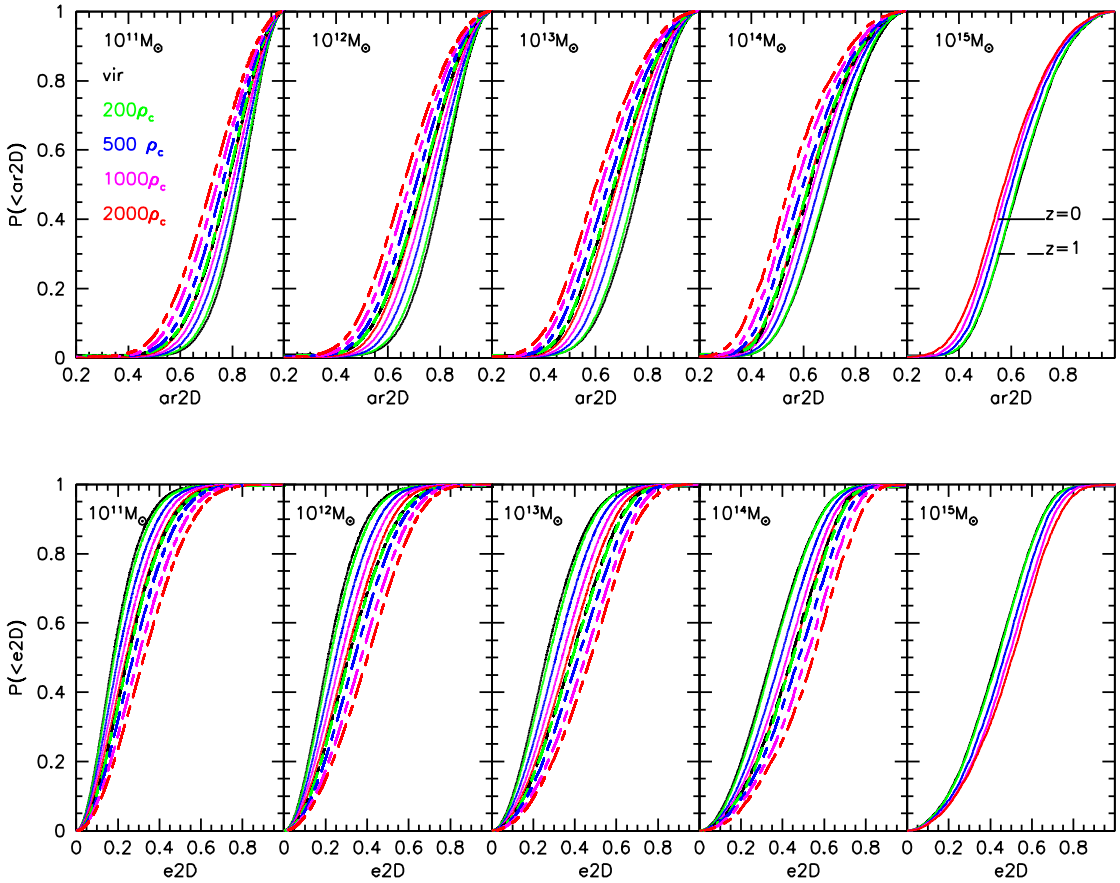


**Figure 11.** Cumulative distributions of projected axial ratios and ellipticities. The panel from left to right show the results for various host halo masses while the colours refer to different overdensities: virial in black, green 200, blue 500, magenta 1000 and red $2000\rho_c$. Solid and dashed line styles refer to redshift $z = 0$ and $z = 1$ respectively.

whole shape will probably be well aligned. The distributions presented in this work may be used as priors for mass reconstruction algorithms working in different wavelengths, in order to recover a more realistic triaxial matter distribution of galaxies and clusters.

## ACKNOWLEDGMENTS

CG thanks CNES for financial support. ML acknowledges the Centre National de la Recherche Scientifique (CNRS) for its support. This work was performed using facilities offered by CeSAM (Centre de donneS Astrophysique de Marseille-(http://lam.oamp.fr/cesam/). This work was granted access to the HPC resources of Aix-Marseille Universite financed by the project Equip@Meso (ANR-10-EQPX-29-01) of the program *Investissements d'Avenir* supervised by the Agence Nationale pour la Recherche (ANR). This work was car- ried out with support of the OCEVU Labex (ANR- 11- LABX-0060) and the A*MIDEX pro ject (ANR-11-IDEX- 0001-02) funded by the *Investissements d'Avenir* French government program managed by the ANR.

## APPENDIX A: UNRELAXED HALOES

In the analysis preformed in our paper we have chosen to discard unrelaxed and irregular haloes from our sample, because they tend to introduce more scatter in the distributions, not easily to explain and model in the same way for all the objects. In the various cases, the analyses should take into account the specific features of each system and of the field surrounding it. Figure A1 shows the analogous of Figure 4 for unrelaxed haloes, showing clearly why they cannot be modelled together with the more relaxed ones; in particular, the ellipticity trend is completely reversed, leading to more triaxial shapes in the outer shells (instead of the inner ones), probably due to the presence of multiple components or infalling material along a preferential direction at the observing time.

## REFERENCES

Allgood B., Flores R. A., Primack J. R., Kravtsov A. V., Wechsler R. H., Faltenbacher A., Bullock J. S., 2006, MNRAS, 367, 1781

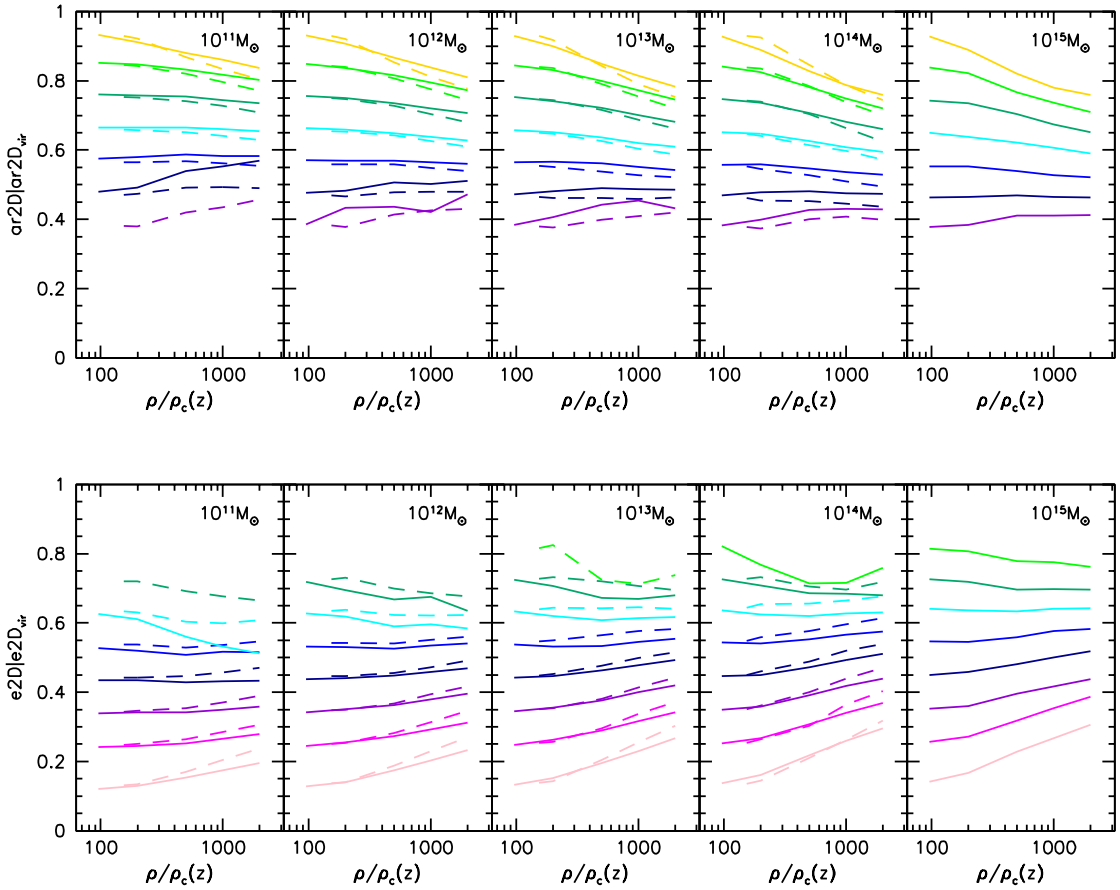


**Figure 12.** Conditional distributions of the projected 2D axial ratios and ellipticities. Each colour shows the median axial ratio as a function of density for the haloes with a certain value of the virial axial ratio.

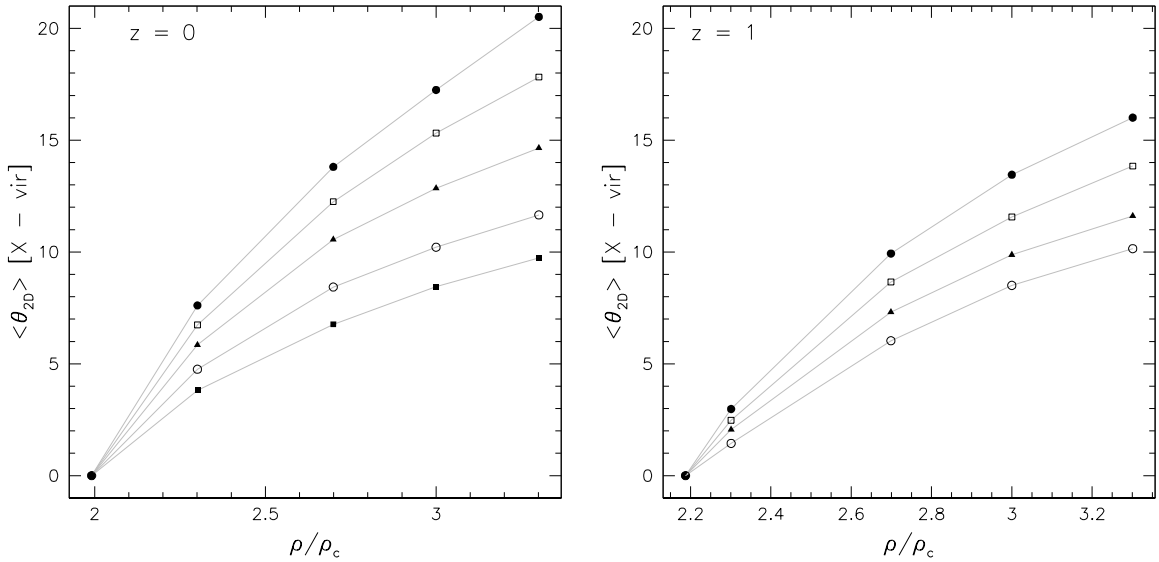


**Figure 13.** Misalignment of the ellipsoids of the 2D mass density distribution enclosed in different overdensities with respect to the direction of the virial ellipsoid. Left and right panels show the results for redshift $z = 0$ and $z = 1$, respectively. The different data points indicate the misalignment angle for different host halo masses as in Fig. 7.

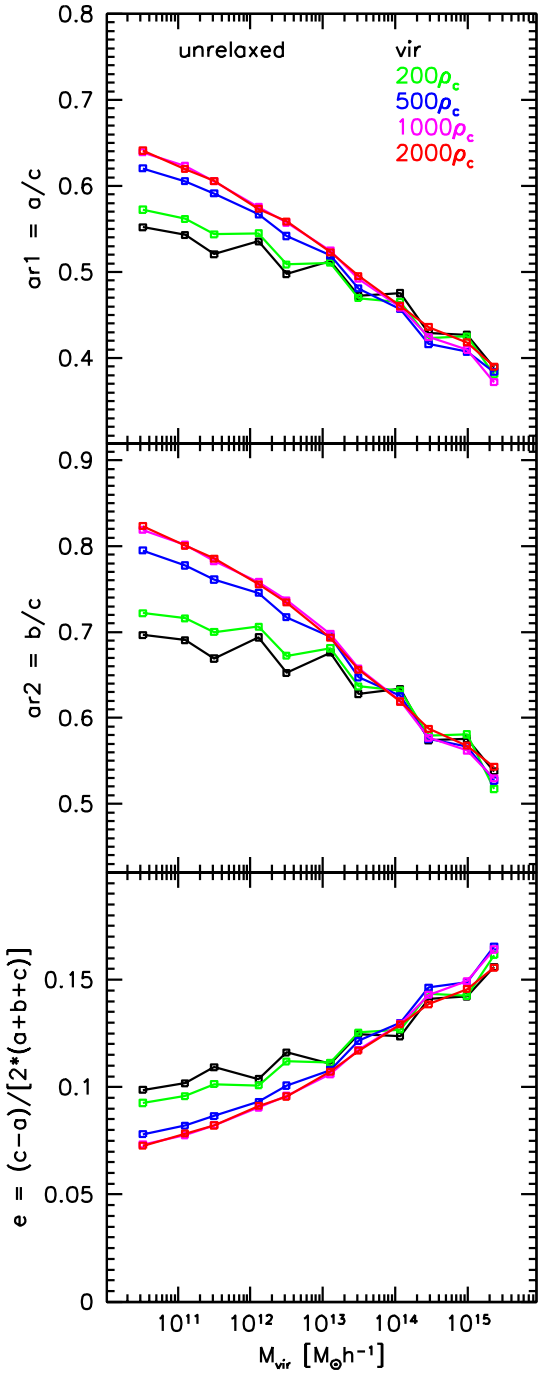


**Figure A1.** Axial ratios and ellipticity as a function of halo mass, for different overdensity thresholds for the unrelaxed halo sample. The points show the median values of the distributions for $ar1 = a/c$, $ar2 = b/c$ and $e = (c-a)/[2*(a+b+c)]$) with $a \leqslant b \leqslant c$).

Amara A., Lilly S., Kovač K., Rhodes J., Massey R., Zamorani G., Carollo et al. 2012, MNRAS, 424, 553
Angrick C., Bartelmann M., 2010, A&A, 518, A38
Angulo R. E., Lacey C. G., Baugh C. M., Frenk C. S., 2009, MNRAS, 399, 983
Angulo R. E., Springel V., White S. D. M., Jenkins a., Baugh C. M., Frenk C. S., 2012, MNRAS, 426, 2046
Bailin J., Steinmetz M., 2005, ApJ, 627, 647
Bonamigo M., Despali G., Limousin M., Angulo R., Giocoli C., Soucail G., 2015, MNRAS, 449, 3171
Bond J. R., Cole S., Efstathiou G., Kaiser N., 1991, ApJ, 379, 440
Borgani S., Kravtsov A., 2011, Advanced Science Letters, 4, 204
Broadhurst T., Benítez N., Coe D., Sharon K., Zekser K., White R., Ford H., et al. B., 2005b, ApJ, 621, 53
Bryan G. L., Norman M. L., 1998, ApJ, 495, 80
Cappi A., Marulli F., Bel J., Cucciati O., Branchini E., de la Torre S., Moscardini L., et al. 2015, A&A, 579, A70
Coe D., Umetsu K., Zitrin A., Donahue M., Medezinski E., Postman M., Carrasco M., Anguita T., et al. 2012, ApJ, 757, 22
Covone G., Sereno M., Kilbinger M., Cardone V. F., 2014, ApJ, 784, L25
Despali G., Giocoli C., Angulo R. E., Tormen G., Sheth R. K., Baso G., Moscardini L., 2015, ArXiv e-prints
Despali G., Giocoli C., Tormen G., 2014, MNRAS, 443, 3208
Despali G., Tormen G., Sheth R. K., 2013, MNRAS, 431, 1143
Donahue M., Ettori S., Rasia E., Sayers J., Zitrin A., Meneghetti M., Voit G. M., Golwala S., Czakon N., Yepes G., Baldi A., Koekemoer A., Postman M., 2016, ApJ, 819, 36
Doroshkevich A. G., 1970, Astrophysics, 6, 320
Eisenstein D. J., Loeb A., 1995, ApJ, 439, 520
Eke V. R., Cole S., Frenk C. S., 1996, MNRAS, 282, 263
Ettori S., Donnarumma A., Pointecouteau E., Reiprich T. H., Giodini S., Lovisari L., Schmidt R. W., 2013, Space Sci.Rev., 177, 119
Ettori S., Morandi A., Tozzi P., Balestra I., Borgani S., Rosati P., Lovisari L., Terenziani F., 2009, A&A, 501, 61
Frenk C. S., White S. D. M., Efstathiou G., Davis M., 1990, ApJ, 351, 10
Giocoli C., Meneghetti M., Bartelmann M., Moscardini L., Boldrin M., 2012a, MNRAS, 421, 3343
Giocoli C., Meneghetti M., Ettori S., Moscardini L., 2012, MNRAS, 426, 1558
Giocoli C., Moreno J., Sheth R. K., Tormen G., 2007, MNRAS, 376, 977
Giocoli C., Tormen G., Sheth R. K., 2012b, MNRAS, 422, 185
Guzzo L., Scodeggio M., Garilli B., Granett B. R., Fritz A., Abbas U., Adami C., Arnouts et al. 2014, A&A, 566, A108
Hayashi E., Navarro J. F., Springel V., 2007, MNRAS, 377, 50
Hoekstra H., Yee H. K. C., Gladders M. D., 2004, ApJ, 606, 67
Hopkins P. F., Bahcall N. A., Bode P., 2005, ApJ, 618, 1
Jing Y. P., Suto Y., 2002, ApJ, 574, 538
Kazantzidis S., Kravtsov A. V., Zentner A. R., Allgood B.,

Nagai D., Moore B., 2004, ApJ, 611, L73
Knebe A., Knollmann S. R., Muldrew S. I., Pearce F. R., Aragon-Calvo M. A., Ascasibar Y., Behroozi P. S., Ceverino D., et al. 2011, MNRAS, 415, 2293
Knebe A., Pearce F. R., Lux H., Ascasibar Y., Behroozi P., Casado J., Moran C. C., Diemand J., et al. 2013, MNRAS, 435, 1618
Komatsu E., Smith K. M., Dunkley J., Bennett C. L., Gold B., Hinshaw G., Jarosik N., Larson D., Nolta M. R., et al. 2011, ApJS, 192, 18
Lacey C., Cole S., 1993, MNRAS, 262, 627
Lacey C., Cole S., 1994, MNRAS, 271, 676
Lewis A., Challinor A., Lasenby A., 2000, Astrophys. J., 538, 473
Limousin M., Morandi A., Sereno M., Meneghetti M., Ettori S., Bartelmann M., Verdugo T., 2013, Space Sci.Rev.
Macciò A. V., Dutton A. A., van den Bosch F. C., 2008, MNRAS, 391, 1940
Meneghetti M., Rasia E., Vega J., Merten J., Postman M., Yepes G., Sembolini F., Donahue M., Ettori S., Umetsu K., Balestra et al. 2014, ArXiv e-prints
Morandi A., Limousin M., Sayers J., Golwala S. R., Czakon N. G., Pierpaoli E., Jullo E., Richard J., Ameglio S., 2012, MNRAS, 425, 2069
Morandi A., Pedersen K., Limousin M., 2011, ApJ, 729, 37
Neto A. F., Gao L., Bett P., Cole S., Navarro J. F., Frenk C. S., White S. D. M., Springel V., Jenkins A., 2007, MNRAS, 381, 1450
Pace F., Waizmann J.-C., Bartelmann M., 2010, MNRAS, 406, 1865
Perlmutter S., Aldering G., Goldhaber G., Knop R. A., Nugent P., Castro P. G., Deustua S., Fabbro S., Goobar A., et al. 1999, ApJ, 517, 565
Planck Collaboration Ade P. A. R., Aghanim N., Alves M. I. R., Armitage-Caplan C., Arnaud M., Ashdown M., Atrio-Barandela F., Aumont J., Aussel H., et al. 2014, A&A, 571, A1
Planelles S., Quilis V., 2010, A&A, 519, A94
Press W. H., Schechter P., 1974, ApJ, 187, 425
Riess A. G., Strolger L., Casertano S., Ferguson H. C., Mobasher B., Gold B., Challis P. J., Filippenko A. V., Jha S., Li W., et al. 2007, ApJ, 659, 98
Riess A. G., Strolger L.-G., Tonry J., Casertano S., Ferguson H. C., Mobasher B., Challis P., Filippenko A. V., et al. 2004, ApJ, 607, 665
Rossi G., Sheth R. K., Tormen G., 2011a, MNRAS, 416, 248
Rossi G., Sheth R. K., Tormen G., 2011b, MNRAS, 416, 248
Schrabback T., Hartlap J., Joachimi B., Kilbinger M., Simon P., Benabed K., Bradač M., Eifler T., Erben et al. 2010, A&A, 516, A63+
Sereno M., Zitrin A., 2012, MNRAS, 419, 3280
Sheth R. K., Mo H. J., Tormen G., 2001, MNRAS, 323, 1
Sheth R. K., Tormen G., 1999, MNRAS, 308, 119
Sheth R. K., Tormen G., 2002, MNRAS, 329, 61
Springel V., 2005, MNRAS, 364, 1105
Springel V., Wang J., Vogelsberger M., Ludlow A., Jenkins A., Helmi A., Navarro J. F., Frenk C. S., White S. D. M., 2008, MNRAS, 391, 1685
Springel V., White S. D. M., Jenkins A., Frenk C. S., Yoshida N., Gao L., Navarro J., Thacker R., Croton D., Helly J., Peacock J. A., Cole S., Thomas P., Couchman H., Evrard A., Colberg J., Pearce F., 2005, Nature, 435, 629
Springel V., White S. D. M., Tormen G., Kauffmann G., 2001b, MNRAS, 328, 726
Springel V., Yoshida N., White S. D. M., 2001a, New Astronomy, 6, 79
Tormen G., 1998, MNRAS, 297, 648
Tormen G., Moscardini L., Yoshida N., 2004, MNRAS, 350, 1397
Velliscig M., Cacciato M., Schaye J., Bower R. G., Crain R. A., van Daalen M. P., Dalla Vecchia C., Frenk C. S., Furlong M., McCarthy I. G., Schaller M., Theuns T., 2015, ArXiv e-prints
Vera-Ciro C. A., Sales L. V., Helmi A., Frenk C. S., Navarro J. F., Springel V., Vogelsberger M., White S. D. M., 2011, MNRAS, 416, 1377
Warren M. S., Quinn P. J., Salmon J. K., Zurek W. H., 1992, ApJ, 399, 405
White S. D. M., Rees M. J., 1978, MNRAS, 183, 341
White S. D. M., Silk J., 1979, ApJ, 231, 1
Zhang Y., Yang X., Faltenbacher A., Springel V., Lin W., Wang H., 2009, ApJ, 706, 747
Zhao D. H., Jing Y. P., Mo H. J., Bnörner G., 2009, ApJ, 707, 354
Zitrin A., Broadhurst T., Barkana R., Rephaeli Y., Benítez N., 2011, MNRAS, 410, 1939